Dublin City University
School of Physical Sciences

Photoemission Studies of Surface Preparation and Passivation of InGaAs

Lalit Chauhan
Doctor of Philosophy

June 2013

Supervised by Professor Greg Hughes

Dedication and Acknowledgements

I would like to express my gratitude to my supervisor, Prof. Greg Hughes, for his co-operation, inspiring guidance, discussion and constant help at all stages of my project work. His constant encouragement and concern during the execution of the work would be remembered with gratefulness for all times to come. I am sure that the knowledge gained through my association with my supervisor shall go a long way in helping me to realize my goals in life.

I would also like to give thanks to Paul Hurley and everyone I collaborated on the ‘FORME’ project. I, also, sincerely thanks to Prof. Navakanta Bhat for providing me an opportunity to work in his research lab at Center for Nano Science and Engineering (CENSE), Indian Institute of Science (IISc) Bangalore, India.

Many thanks to Dr. David McNeill and Durga Rao Gajula for the collaborated work during this project and arranging my research visit to their laboratory at Queens University Belfast UK.

I would like to thank everyone in the Surface and Interfaces Research Group for all of their help over the past 4 years; to Rajesh, Kumar, Justin, Lee, Barry, Anthony, Paddy and Rob. I am also very thankful to Pat Wogan and Des Lavelle for all of their help on the technical side of things.

I would also give thanks to all of my friends especially Pradeep Kumar Singh, Suman and Gurusharan for their support and encouragement to maintain a level of sanity throughout my PhD.

I would like to acknowledge Science Foundation Ireland for the financial support of this work.

Most importantly, I am grateful to my family for all of their teachings, love, support and blessings. I thank to my father and late mother for showing me the value and importance of education and I dedicate this thesis to them.

Declaration

I hereby certify that this material, which I now submit for assessment on the programme of study leading to the award of Doctor of Philosophy is entirely my own work, that I have exercised reasonable care to ensure that the work is original, and does not to the best of my knowledge breach any law of copyright, and has not been taken from the work of others save and to the extent that such work has been cited and acknowledged within the text of my work.

Signed: __________________________ (Candidate)

ID No. : 58126775

Date :

Abstract

This thesis investigates a range of surface and interface preparation procedures for the ternary III-V semiconductor, InGaAs which has potential applications in high speed metal-oxide-semiconductor field effect transistors (MOSFETs). Various chemical methods of passivating the InGaAs surface prior to high-k dielectric deposition have been studied. Both conventional x-ray photoelectron spectroscopy (XPS) and high resolution synchrotron radiation based photoemission spectroscopy (HSRPES) have been used to investigate the chemical interactions at the high-k/InGaAs interface while electrical characterisation studies have been made by current-voltage (I-V) and capacitance-voltage (C-V) measurements. A systematic study of in-situ sulphur passivation of the atomically clean InGaAs surface has been performed and a comparison has been made with wet chemical ex-situ preparations methods. High temperature thermal stability experiments were also performed to establish a threshold decomposition temperature for these surfaces. In addition, high temperature thermal stability studies were carried out on interfaces between ultrathin atomic layer deposited (ALD) Al_2O_3 layers and differently prepared InGaAs surfaces. The interface formation between an in-situ deposited MgO dielectric layer and the atomically clean InGaAs surface was studied by high resolution synchrotron radiation based photoemission. Finally, the effectiveness of the insertion of ultrathin ALD deposited Al_2O_3 dielectric layers on the Schottky barrier formed at the interface between different work function metals and the InGaAs surface was also investigated.

Publications arising from this work

High resolution synchrotron radiation based photoemission study of the in-situ deposition of molecular sulphur on the atomically clean InGaAs surface
Lalit Chauhan and Greg Hughes,
J. Appl. Phys. 111, 114512 (2012)

Thermal stability studies on atomically clean and sulphur passivated InGaAs surfaces
Lalit Chauhan and Greg Hughes
Phys. Stat. Sol. A, 210, 3 (2013)

Synchrotron radiation photoemission study of interface formation between MgO and the atomically clean n-InGaAs surface
Lalit Chauhan and Greg Hughes
(Under review in J. Vac. Sci. Tech. A)

High temperature thermal stability investigations of ammonium sulphide passivated InGaAs and interface formation with Al2O3 studied by synchrotron radiation based photoemission
Lalit Chauhan, Greg Hughes, Durga Gajula, David McNeill
(under review in J. Phys. D : Appl. Phys.)

Synchrotron radiation photoemission study of the high temperature thermal stability of the ammonium sulphide passivated InGaAs and InAs surface
Lalit Chauhan, Greg Hughes
(Manuscript in preparation)
Modification of Metal – InGaAs Schottky barrier height by atomic layer deposition of ultrathin Al_2O_3 interlayers
Lalit Chauhan, Suman Gupta, Piyush Jaiswal, Navakanta Bhat, S.A. Shivashankar and Greg Hughes
(Manuscript in preparation)

Contributed Conferences

High resolution synchrotron radiation based photoemission study of the insitu deposition of molecular sulphur on the atomically clean InGaAs surface
Lalit Chauhan, Greg Hughes
Interdisciplinary Surface Science Conference (ISSC-18), University of Warwick, UK, 4-7 April 2011

Synchrotron radiation photoemission study of interface formation between MgO and the atomically clean n-InGaAs surface
Lalit Chauhan, Greg Hughes
42nd IEEE Semiconductor Interface Specialists Conference (SISC) Arlington, VA, USA, December 1-3, 2011

Synchrotron radiation photoemission study of interface formation between high-k layer and the atomically clean n-InGaAs surface
Lalit Chauhan Greg hughes
Intel European Research and Innovation Conference (ERIC) 2011, Leixlip Ireland.

High resolution photoemission comparison study of atomic hydrogen cleaned and decapped InGaAs substrates
Barry Brennan, Kumar Kumarappan, Lalit Chauhan and Greg Hughes
38th International Symposium on Compound Semiconductors (ISCS) May 22 – 26, 2011 Berlin, Germany

Modification of Metal – InGaAs Schottky Barrier Height by Atomic Layer Deposition of Ultrathin Al_2O_3 Interlayers
Lalit Chauhan, Suman Gupta, Piyush Jaiswal, Navakanta Bhat. S.A. Shivashankar, G.J. Hughes
AVS 59th Annual International Symposium and Exhibition October 28 – November 2, 2012 Tampa Florida, USA

Table of contents

Dedication and acknowledgement…………………………………..1

Declaration……………………………………………………..2

Abstract…………………………………………………………...3

Publications arising from this work…………………………………4

Contributed Conferences……………………………………………5

Table of Contents………………………………………………….6

Figure Captions…………………………………………………....12

Chapter 1………………………………………………………....21

Introduction…………………………………………………….. 21

1.1 Need for high-k dielectrics in nanoelectronics ……………….. 21
1.2 Choice of high-k dielectrics………………………………….24
1.3 High-k dielectrics incompatibility with Si : Call for new channel material…… 26
1.4 InGaAs based MOSFET…………………………………….. 28
1.5 Surface Passivation………………………………………….29
1.6 Thesis organisation…………………………………………..30
1.7 References ……………………………………………………..31

Chapter 2..…………………………………………………….39

Experimental details ……………………………………………39

2.1 X-ray photoemission spectroscopy (XPS)………………………39
  2.1.1 Principle of Photoemission Spectroscopy……………………40
  2.1.2 Binding energy reference…………………………………42
  2.1.3 XPS peak width…………………………………….…….43
2.2 Interpretation of the XPS spectra……………………………44
2.3 Inelastic mean free path………………………………………..46
2.4 Core level chemical shift ………………………………………48

2.5 Quantification……………………………………………………………… …..50
2.6 Angle resolved XPS…………………………………………………… ……52
2.7 Thickness Calculations………………………………………………… …...54
2.8 Synchrotron radiation photoemission…………………………………… ….55
    2.8.1 The ASTRID synchrotron…………………………………………….…..56
2.9 Electrical Characterisation…………………………..……………………….57
    2.9.1 MOS diode C-V characteristics……………………………………… ….58
    2.9.2 Schottky diode I-V characteristics…………………………… ……63
2.10 Vacuum system description…………………………………………... ….65
2.11 Synchrotron vacuum system at ASTRID Aahrus, Denmark…………………. ….69
2.12 Deposition techniques………………………………………………………..70
    2.12.1 Atomic layer deposition……………………………………… …..70
    2.12.2 Thermal evaporation………………………………………………………71
2.13 Surface preparation methods………………………………………………… ...72
2.14 Sulphur Cell……………………………………………………………………….72
2.15 References…………………………………………………………………… ...69

Chapter 3………………………………………………………………………………76

High resolution synchrotron radiation based photoemission studies of the sulphur treated InGaAs surface

3.1 Introduction………………………………………………………………….. 76
    3.1.1 InGaAs surface passivation……………………………………….. 76
3.2 Preparation of atomically clean InGaAs surface by thermal desorption of a protective As cap………………………………………………………….....79
    3.2.1 Sample preparation…………………………………………………....80
    3.2.2 Atomically Clean InGaAs Surface…………………………... ……..…80
    3.2.3 Thermal annealing of atomically clean surface at high temperature…..... 82
3.3 In-situ sulphur passivation of InGaAs and thermal anneals…………………... …...86
    3.3.1 Impact on As 3d spectra………………………………………… …...86
    3.3.2 Impact on In 4d /Ga 3d spectra…………………………………….…87
    3.3.3 Impact on sulphur spectra following thermal anneals……….......... ….92
    3.3.4 Indium desorption from surface at higher temperature anneals……... ….93
    3.3.5 Angle resolved measurements……………………………………………95

3.3.6 Fermi level position as a function of treatment from valance band measurement……………………………………………………………………97
3.3.7 Change in InGaAs work function with sulphur deposition and anneal….100
3.4 Native oxide and wet chemical sulphur passivated InGaAs surfaces investigation by synchrotron radiation based photoemission……………………………………103
3.4.1 Sample preparation…………………………………………… ……103
3.4.2 Synchrotron radiation photoemission study of wet chemical sulphur passivated InGaAs surface………………………………… ……103
3.4.2.1 Impact on As 3d spectra …………………………… ……103
3.4.2.2 Impact on In 4d/ Ga 3d spectra…………………… ……...106
3.4.3 Thermal stability of the wet chemical sulphur passivated InGaAs surface at high temperature….………………………………………………….109
3.4.3.1 Thermal annealing……………………………………….....109
3.4.3.2 Impact on As 3d spectra………………………………….…111
3.4.3.3 Impact on In 4d/ Ga3d spectra…………………………..….112
3.5 Thermal stability comparison between differently prepared InGaAs surfaces…. .118
3.6 Conclusion…………………………………………………………………..120
3.8 References………………………………………………….……… ……121

Chapter 4……………………………………………………………………..125

Interface characterisation of Al_2O_3 deposition on differently prepared InGaAs surfaces by x-ray photoemission and synchrotron radiation based photoemission spectroscopy……………………………………………………………. …….125

4.1 Introduction……………………………………………………… …….125
4.2 Experimental…………………………………………………………………126
4.3 Advantage of synchrotron technique over convention XPS…………….……..133
4.4 High temperature thermal stability studies of 1nm Al_2O_3 deposited on native oxide and sulphur passivated InGaAs surface…………………………………...…133
4.4.1 Impact on As 3d Spectra……………………………………………..136
4.4.2 Impact on In 4d/Ga 3d Spectra……………………………….… ...138
4.5 Al_2O_3 film thermal stability…………………………………………………144
4.6 Growth of Al_2O_3 layer on InGaAs surface…………………….……… ….…145
4.6.1 As 3d spectra……………………….…………………..………….….…..146

4.6.2 In 4d/Ga 3d spectra……………………………………………………... ….149
4.7 Conclusion……………………………………………………………….. ……152
4.8 References…………………………………………………………………..… ….153

Chapter 5..…………………………………………………………………. ………156

Interfacial oxide formation study of in-situ deposition of MgO on atomically clean InGaAs surface by HRSPES ………………………………………………..……156

5.1 Introduction………………………………………………………………… …….143
5.2 Experimental details……………………………………………………………… …157
5.3 MgO growth on atomically clean InGaAs…………………………………… …..157
5.3.1 As 3d spectra……..………………………………………………… ……157
5.3.2 In 4d/G 3d Spectra…………………………………….…… ……….161
5.3.3 O 1s spectra……………………………………………………… ………163
5.3.4 Valance band spectra and energy band diagram……….………..... …….164

Chapter 6…………………………………………………….……………… ….167

Modification of metal – InGaAs Schottky barrier height by atomic layer deposition of ultrathin Al_2O_3 interlayers and fabrication of MOS structures on InGaAs…..167

6.1 Introduction……………………………………………….………… ……167
6.2 Experiments details…..…………………………………………….……………168
6.3 Schottky J-V characteristics…………………………………………… ………169
6.3.1 P-type……………………………………………………..……………169
6.3.2 N-type…………………………………………………….. ……………172
6.3.3 Discussion……………………………………………………………174
6.4 MOS capacitors…………………………………………………...… ………175
6.4.1 $Al/Al_2O_3/n\text{-}In_{0.53}Ga_{0.47}As/Al$ capacitor fabrication with and without sulphur passivation……………………………………………………175
6.5 Conclusions……………………………………………………..……… ………...177
6.6 References …………………………………………………………… ……..…177

Chapter 7……………………………………………………………………. …...…179
Conclusions and future work……………………………………………… ……179

Figure captions

Figure 1.1 For thick and thin potential barriers, the wave function of an electron as it reaches a potential barrier …………………………....... ………..22

Figure 1.2 Band gap versus static dielectric constant for candidate gate oxide materials…………………………………………………………………..... ….24

Figure 1.3 Schematic illustrations of reasons contributing to carrier mobility degradation in a high-k oxide layer ……..……………………………………… …….27

Figure 1.4 (a) Flat- band (b) when bias is applied Fermi level move inducing band bending means (c) In absence of bias the band bending at n type semiconductor with filled surface states upto Fermi level (d) Applied bias can not move the Fermi level i.e. Fermi level is pinned...…………………………………………………………………29

Figure 2.1 Schematic diagram of the photoemission experimental arrangement………37

Figure 2.2 Schematic diagram of the photoemission process……………………… ….39

Figure 2.3 Energy level diagram for the photoemission process showing a sample and spectrometer in electrical contact……………………………………… ……………40

Figure 2.4 Survey spectra of InGaAs sample……………………………… ………..43

Figure 2.5 Diagram showing paths of various electron emissions during photoemission process………………………………………………………………..... …..….44

Figure 2.6 Universal mean free path (MFP) curve, showing a range of materials… ….45

Figure 2.7 Probability of unscattered electron emission as a function of depth…… ….46

Figure 2.8 Si 2p spectrum showing a 4 eV chemical shift between component peaks which indicates the presence of Si and SiO_2………………………....... …………..47

Figure 2.9 Schematic of angle resolved XPS at normal emission and $\theta > 0$ shadow shows the information depth from which electron escape from the surface……… ….51

Figure 2.10 Si 2p spectra taken from a 5.4 nm SiO_2 layer on silicon showing the increased surface sensitivity using ARXPS…………………………………… ……52

Figure 2.11 Diagram of the ASTRID synchrotron in Aarhus, Denmark……....... …..56

Figure 2.12 Typical C-V characteristics of 12 nm Al_2O_3 on p-type InGaAs……… …..57

Figure 2.13 Energy band diagram for ideal p-type MOS capacitor ………………..…59

Figure 2.14 Application of a negative voltage on the metal gate causes the accumulation of holes at the semiconductor/oxide interface which results in a maximum capacitance value within the measured C-V profile……………………………………………....60

Figure 2.15 Energy band diagram showing depletion in MOS capacitors. Application of a positive voltage depletes the semiconductor surface of majority carriers………..…61

Figure 2.16 Energy band diagram showing depletion in MOS capacitors. Application of a positive voltage depletes the semiconductor surface of majority carriers…………62

Figure 2.17 Energy band diagram of metal/p-type semiconductor (a) thermal equilibrium, (b) positive bias and (c) reverse bias ……………………………………64

Figure 2.18 I-V characteristics of Al-InGaAs Schottky diode ……………….. ………65

Figure 2.19 XPS analysis chamber………………………………………..……...66

Figure 2.20 Diagram showing the operation of a dual anode X-ray source……......... 67

Figure 2.21 Schematic diagram of an XPS analysis system, showing how electrons are focused into the analyser system……………………………........ ……………...68

Figure 2.22 Vacuum end station on the SX700 beamline at the ASTRID synchrotron in Aarhus, Denmark…………………………………………………….......……….69

Figure 2.23 Graphic representation of one full ALD cycle starting with (a) a bare substrate, (b) introducing an organo-metallic precursor, (c) saturating the surface with one organo-metallic layer, (d) purging remaining gas and introducing an oxygen source, (e) reaction to form a metal oxide and (f) formation of one atomic layer of metal oxide……………………………………………………….....……………..71

Figure 2.24 A schematic illustration of the electrochemical sulphur source …………..68

Figure 3.1 shows the photoemission spectra for In 4d/Ga 3d core levels for clean InGaAs surface at different photon energy (a) 69 eV, (b) 130 eV and (c) 300 eV highlighting the change in the relative intensity due to photo-ionisation cross-sectional area by varying the photon energy……………………………………………....... ……..78

Figure 3.2 Photoemission spectra of As 3d peak acquired at a photon energy of 92 eV of the (a) 100 nm As capped surface (b) annealed at 340 °C showing evidence of elemental arsenic and (c) the atomically clean surface annealed at 410 °C……......... ..81

Figure 3.3 Photoemission spectra of the raw data of In 4d/Ga 3d peak acquired at a photon energy of 69 eV of the (a) Annealed at 340 °C (b) atomically clean surface annealed at 410 °C……………………………………………………...... ……………82

Figure 3.4 Normalised As 3d photoemission spectra acquired at a photon of energy 92 eV during the thermal annealing sequence showing no change in the peak profile…………………………………………………………………......………….83

Figure 3.5 (a) Curve fitted As 3d spectra at a photon of energy 92 eV at 410 °C, 530 °C and 560 ° C (b) curve fitted area showing the As intensity and As dimer signal as a function of thermal anneals…………………………………………………………. ……84

Figure 3.6 top (a) and (b) Curve fitted spectra of In4d/Ga 3d spectra at a photon of energy 130 eV and 300 eV at 410 °C, 530 °C and 560 ° C , (bottom) (c) and (d) Curve fitted area of In 4d and Ga 3d signal as a function of thermal anneals…………………………………………………………………..... ………..79

Figure 3.7 Normalised photoemission spectra for the As 3d peaks at 92 eV photon energy showing the evolution of the peak shape with the removal of the As cap, sulphur deposition and anneal……………………………………………………..... ………86

Figure 3.8 As 3d curve fitted photoemission spectra for p-type InGaAs at photon energy 92 eV for (a) Clean surface (b) Sulphur exposed at room temperature (c) Sulphur + 400 °C anneal……………………………………………........ …………87

Figure 3.9 Normalised In4d/Ga3d spectra at the three different photon energies of 69 eV, 130 eV, and 300 eV on p-type InGaAs a) clean surface, (b) sulphur exposed at room temperature and (c) Sulphur + 400 °C anneal…………………………......... ………..88

Figure 3.10 In 4d and Ga 3d curve fitted photoemission spectra for p-type InGaAs at photon energy 69 eV for (a) clean surface, (b) sulphur exposed at room temperature and (c) sulphur + 400 °C anneal………………………………………........ ……………89

Figure 3.11 In 4d and Ga 3d curve fitted photoemission spectra for p-type InGaAs at photon energies of 130 eV and 300 eV for (a) clean surface, (b) sulphur exposed at room temperature and (c) sulphur + 400 °C anneal……………………......... ………..90

Figure 3.12 Area plot for (a) As 3d at a photon energy of 92 eV, In 4d and Ga 3d for p type at photon energy (b) 69 eV, c) 130 eV and (d) 300 eV for surface treatment 340 °C, 410 °C, 410 °C +S, S+400 °C, 480 °C, 530 °C…………………………....... …….92

Figure 3.13 S 2p curve fitted spectra acquired at 220 eV photon energy for room temperature deposition and following 400°C anneal. The high binding energy component peak at 163 eV, which is removed by the 400C anneal, is attributed to an As-S bonding. …………………………………………………………....... …..93

Figure 3.14 The loss of In as a function of thermal anneal is apparent in these spectra acquired at a photon energy of 105 eV (a) normalised spectra (b) curve fitted spectra……………………………………………………………………....... …….94

Figure 3.15 The magnitude of the changes in the intensity of the indium bulk, S-In and S-Ga components as a function of thermal anneal ……........... …95

Figure 3.16 Ga : As and S:As ratios at normal emission and 60^0 off normal showing that sulphur replaces the As in the near surface region………………………......... ……96

Figure 3.17 Valence band spectra for clean surface, sulphur exposed at RT and Sulphur + 400 °C anneal surface………………………………………………....... ……..98

Figure 3.18 Fermi level position for both n and p doped substrates as a function of surface treatment…………………………………………………………...... …..99

Figure 3.19 Band bending diagram for both doping type (a) and (b) ideal condition, (c) and d) clean surface after As decapping, (e) and (f) sulphur deposited surface…………………………………………………………………………......……100

Figure 3.20 Change in work function value on sulphur deposition and following thermal anneals…………………………………………………………………………........101

Figure 3.21 Comparison of As 3d and In 4d /Ga 3d curve fitted photoemission spectra acquired at photon energies of 92eV and 69 eV on air exposed surface and native oxide surface…………………………………………………………………………...... …102

Figure 3.22 Normalised As 3d spectra acquired at a photon energy of 92 eV for native oxide and sulphur passivated surface showing the effectiveness of the $(NH_4)_2S$ treatment in removing the oxide……………………………………........………104

Figure 3.23 Curve fitted As 3d spectra at photon energy of 92 eV for native oxide and sulphur passivated surface showing the effectiveness of the treatment in removing the native oxide………………………………………………………………........………105

Figure 3.24 Normalised O 1s Spectra at a photon energy of 600 eV for native oxide and sulphur passivated InGaAs surface……………………………………........…….106

Figure 3.25 Curve fitted spectra for In 4d and Ga 3d at different photon energy of (a) 69 eV (b) 105 eV (c) 130 eV the sulphur passivated InGaAs surface………….……107

Figure 3.26 Oxide to bulk ratio comparison for native oxide and sulphur pasivated surface……………………………………………………………………......………..108

Figure 3.27 Normalised As 3d spectra at a photon energy of 92 eV for sulphur passivated surface as a function of thermal anneal…………………………….…..109

Figure 3.28 Photoemission spectra for the In 4d and Ga 3d peaks at photon energies of (a) 69 eV (b) 105 eV (c) 130 eV (d) and 300 eV after annealing up to 700 °C….. ….110

Figure 3.29 Curve fitted core level spectra of As 3d at photon energy of 92 eV on sulphur passivated InGaAs surface following thermal…………………........ ……111

Figure 3.30 Magnitude of the changes in the intensity of arsenic components as a function of thermal anneal are clearly observed……………………….......………112

Figure 3.31 Curve fitted core level spectra of In 4d/Ga 3d at a photon energy of 69 eV on sulphur passivated InGaAs surface following thermal anneals………........ …..113

Figure 3.32 The magnitude of the changes in the intensity of In and Ga components as a function of thermal anneal are clearly observed……………………....... ………114

Figure 3.33 (a) Curve fitted core level spectra of In 4d/Ga 3d at photon energy of 130 eV on sulphur passivated InGaAs surface following thermal anneals (b) the magnitude of the changes in the intensity of In and Ga components as a function of thermal anneal are clearly observed…………………………………………………......……115

Figure 3.34 Curve fitted core level spectra of In 4d/Ga 3d at photon energy of 105 eV on sulphur passivated InGaAs surface following thermal anneals b) the magnitude of the changes in the intensity of In and Ga components as a function of thermal anneal are clearly observed…………………………………………………....……………116

Figure 3.35 Changes in the O 1s at a photon energy of 600 eV signal as a function of thermal anneals…………………………………………………………....…….117

Figure 3.36 Changes in the S 2p signal at a photon energy of 220 eV as a function of thermal anneals…………………………………………………………....…….118

Figure 4.1 Comparison of the As 3d spectra for (a) synchrotron based photoemission (92 eV) photon energy and (b) conventional XPS for different surfaces/interfaces : 1nm Al_2O layer on sulphur passivated surface (A1) and native oxide surface (A2), bare native oxide surface (A3) (no overlayer)……………………………........... ……..128

Figure 4.2 Comparison of oxidation states in curve fitted core level spectra of As 3d and In 4d/ Ga3d by XPS and HRSPES for Al_2O_3 deposited on sulphur passivated and native oxide surface using XPS (a) As 3d and (b) In 4d/ Ga3d (XPS), and using HRSPES (c) As 3d and (d) In 4d/ Ga3d………………………………........ ..……129

Figure 4.3 Comparison of oxidation states in curve fitted core level spectra of As 3d and In 4d/ Ga3d by XPS and HRSPES for Al_2O_3 deposited on sulphur passivated and native oxide surface (a) As 3d and (b) In4d/Ga3d (XPS) , (c) As 3d and (d) In 4d/ Ga3d (HRSPES)……………………………………………………......... ……..131

Figure 4.4 Comparison of oxide to bulk ratio measured by HRSPES and XPS for (a) Al_2O_3 on sulphur passivated surface (A2) and (b) native oxide surfaceb(A2)..........…..132

Figure 4.5 Normalised photoemission spectra by HRSPES and XPS for the Al 2p and O1s peaks at photon energies of 120 eV and 600 eV, respectively, for Al_2O_3 on sulphur passivated (A1) and native oxide surfaces(A2)………………........…………..133

Figure 4.6 Normalised photoemission spectra for As 3d peaks at photon energy 92 eV after annealing at temperatures incrementing from RT to 700 °C for Al_2O_3 on (a) sulphur passivated surface(A1) and (b) native oxide surface(A2) ……….........……..134

Figure 4.7 Normalised photoemission spectra for the In 4d and Ga 3d peaks at photon energies of 69 eV, 105 eV and 130 eV after annealing at temperatures incrementing from RT to 700 °C for Al_2O_3 on sulphur passivated surface (left) and native oxide surface (right)…………………………………………………………....……….135

Figure 4.8 Curve fitted photoemission spectra for the As 3d peaks at photon energy of 92 eV after annealing at RT, 545 °C, 635 °C and 700 °C for Al_2O_3 on sulphur passivated sample and native oxide surface……………………………......... …….136

Figure 4.9 Arsenic oxidation states component to arsenic bulk ratio highlighting changes in the oxide composition as a function of thermal anneals (a) for Al_2O_3 on sulphur passivated InGaAs surface (b) for Al_2O_3 on native oxide InGaAs surface…………………………………………………………........………..137

Figure 4.10 Curve fitted core level spectra In 4d/Ga 3d at 105 eV following thermal anneals (a) for Al_2O_3 on sulphur passivated InGaAs surface (b) for Al_2O_3 on native oxide InGaAs……………………………………………………...... ……139

Figure 4.11 Core level spectra of S2p peak at photon energy of 230 eV for Al_2O_3 on sulphur passivated surface…………………………………………………......... …...140

Figure 4.12 In and Ga oxidation states component to bulk ratio highlighting changes in the oxide composition as a function of thermal anneals (a) for Al_2O_3 on sulphur passivated InGaAs surface (b) for Al_2O_3 on native InGaAs surface………….......... ..141

Figure 4.13 Curve fitted photoemission spectra for the In 4d and Ga 3 peaks at photon energy of 69 eV and 300 eV after annealing at (a) RT (b) 545 °C (c) 635 °C and (d) 700 °C for Al_2O_3 on sulphur passivated sample and native oxide surface…......... ..142

Figure 4.14 Indium and gallium components to bulk ratio highlighting changes in oxide composition and thermal stability at various photon energy of 69 eV and 300 eV as a function of annealing temperature for both : 1nm Al_2O_3 on sulphur passivated surface and on native oxide surface……………………………………………….…... ……143

Figure 4.15 Ga : In ratios at different photon energies as a function of annealing temperature for (a) sulphur passivated and (b) unpaasivated Al_2O_3/InGaAs…..........…144

Figure 4.16 Normalised photoemission spectra by HRPES for the Al 2p and O1s peaks at photon energies of 120 eV and 600 eV respectively following thermal anneals for Al_2O_3 on sulphur passivated…………………………………………....... ……..145

Figure 4.17 Normalised As 3d core level spectra for Al_2O_3/InGaAs interface of different chemically treated surfaces…………………………………… …………147

Figure 4.18 (a) Curve fitted As 3d core level spectra (b) oxide to bulk ratio, for Al_2O_3/InGaAs interface of different chemically treated surfaces………….........…..147

Figure 4.19 Normalised In 4d/Ga 3d core level spectra for Al_2O_3/InGaAs interface of different chemically treated surfaces………………………………………… …….148

Figure 4.20 (a) Curve fitted In 4d/Ga 3d core level spectra (b) oxide to bulk ratio, for Al_2O_3/InGaAs interface of different chemically treated surfaces………….........…..149

Figure 4.21 Graph displays the curve fitted area of O 2s signal verses surface treatments showing the growth rate of Al_2O_3.. 150

Figure 4.22 (a) Al 2p and (b) O1s spectra showing the uniform composition on all the samples…………………………………………………………….….. …………152

Figure 5.1 Curve fitted core level spectra of As3d at 92eV for the atomically clean InGaAs surface and after each MgO deposition, anneal and Mg deposition, To show the actual presence of weak interfacial oxides enlargement (Magnification x 2) of the oxides peak was used…………………………………………………………..........……….158

Figure 5.2 As 3d absolute intensity plot as a function of successive MgO depositions and anneal…………………………………………………………………………….....……….160

Figure 5.3 Individual As oxide to As substrate intensity ratios for the atomically clean InGaAs surface and after each MgO deposition, anneal and metallic Mg deposition………..……..….160

Figure 5.4 Curve fitted core level spectra of In 4d/Ga 3d at 92eV for the atomically clean InGaAs surface and after each MgO deposition, anneal and Mg…………………….... ……..161

Figure 5.5 (a) In 4d absolute intensity plot as a function of successive MgO depositions and anneal (b) InO and GaO to In and Ga substrate ratio respectively, for the atomically clean InGaAs surface and after each MgO deposition, anneal………………………….. ……….162

Figure 5.6 O1s core level spectra following MgO deposition, thermal anneal and subsequent Mg deposition………………………………………………………………... ……….163

Figure 5.7 (a) Valence band spectra acquired at 69 eV showing the change in the valence band offset resulting from the MgO deposition on atomically clean InGaAs surface. (b) Band diagram of MgO / InGaAs. Valance band (VB) offset is (3.2 ± 0.3) eV and conduction band (CB) offset is (3.8 ± 0.3) eV…………...........……………164

Figure 6.1 Typical J-V characteristics of p-type Al/InGa As and Al/Al_2O_3/InGaAs junctions (a) native oxide (b) sulphur passivated surface…………………...............…170

Figure 6.2 Typical J-V characteristics of p-type Pt/InGaAs and Pt Al_2O_3/InGaAs junctions (a) native oxide (b) sulphur passivated surface junctions……........... …..171

Figure 6.3 Typical J-V characteristics of n-type Al/InGa As and Al /Al_2O_3/InGaAs junctions (a) native oxide and (b) sulphur passivated surface……………….........….172

Figure 6.4 Typical J-V characteristics of n-type Pt/InGaAs and Pt/Al_2O_3/InGaAs junctions (a) native oxide and (b) sulphur passivated surface……………......... …173

Figures 6.5 Schematic diagram of Al/Al_2O_3/n-InGaAs capacitors……….......... ….175

Figure 6.6 show the capacitance-voltage measurements on un-passivated and sulphur passivated Al/Al_2O_3/n-InGaAs capacitors respectively measured at room temperature with a frequency range of 1 KHz-1MhZ. The Hysteresis behaviour at 1 MHz is also shown in these figures…………………………………………...............................……176

Chapter 1

Introduction

1.1 Need for high-k dielectrics in nanoelectronics

Dimensional scaling of silicon based complementary metal oxide semiconductor (CMOS) technology has been at the heart of Moore’s law. In 1965, Gordon Moore [1] predicted that for silicon-based integrated circuits, the number of transistors per square centimetre would double every 12-18 months. Indeed the number of transistors per chip has been increased from a few hundred in the 1970’s to billions in current processor technology. As the number of transistor devices per unit area continues to increase, the dimensions of the transistor devices must decrease accordingly. The scaling of the MOS-devices has become the driving force for the semiconductor industries. The challenges which the semiconductor device industry faces include reduced power consumption and high speed operation at a low cost. A critical factor in the performance of a metal oxide semiconductor field effect transistor (MOSFET) is the thickness of the gate dielectric. For the last three decades of MOSFETs fabrication, SiO_2 has been used as the dielectric material on the Si substrate because of its excellent material and electrical properties. It is relatively easy to thermally grow high quality layers of controlled thickness on the Si substrate, it has good electrical insulation properties and forms a highly stable interface with silicon. At the Si/SiO_2 interface of high quality MOS structures the interface state defect density is $\sim10^{10}/cm^2$ and hard breakdown fields in excess of 10 MV/cm are routinely achievable. However, with continued dimensional scaling, these ultrathin SiO_2 dielectrics suffer heavily from reliability and high power consumption issues caused in part by charge trapping and quantum tunnelling through the dielectric which manifests itself as leakage current. In MOSFETs the gate capacitance would decrease with the reduction in the channel length and the gate area which can be compensated by decreasing oxide thickness in order to prevent short channel effects. Therefore a replacement of the SiO_2 must be found. According to the International Technology Roadmap for Semiconductor (ITRS) [2], after reaching the oxide thickness of 1.2 nm the scaling in Si CMOS has more or less stopped which results in a substantial undesirable leakage current due to quantum mechanical tunnelling [3].

The mechanism of direct quantum tunnelling across the insulating dielectric of thick and thin barrier (d) in MOS capacitors is graphically represented in Figure 1.1

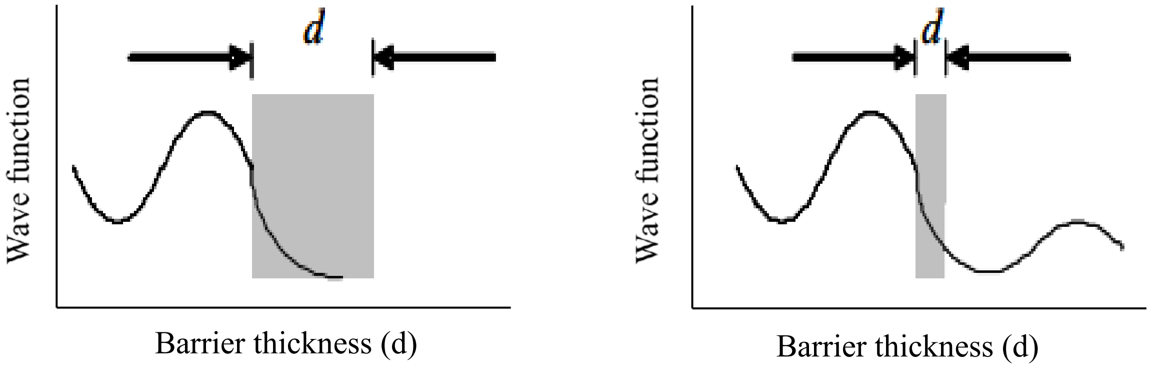

Figure 1.1 For thick and thin potential barriers, the wave function of an electron as it reaches a potential barrier

The tunnelling current J_{DT} in a MOS structure increase exponentially with decreasing oxide thickness and is given by the equation

$$J_{DT} = \frac{q^2}{2\Pi h t_{ox}^2} \emptyset \, exp\left(\frac{-8\Pi}{h}(2m_e)^{1/2} \, t_{ox} \, \emptyset^{1/2}\right) \tag{1.1}$$

Where q is the charge of the electron m_e is the effective mass of the direct tunnelling electrons, t_{ox} is the thickness of the oxide.

This equation shows the strong dependence on oxide thickness and barrier height at the interface.

$$\emptyset = \emptyset_B - \frac{E_{ox} t_{ox}}{2} \tag{1.2}$$

where $\emptyset_B$ is barrier height at the metal oxide semiconductor interface and E_{ox} is the electric field across the oxide. With a physical thicknesses of SiO_2 below 1 nm, quantum mechanical tunnelling would allow gate leakage currents of 1 A/cm^2 at 1 V, while it is desirable that it does not exceed 1.5 x 10^{-2} A/cm^2. Therefore new dielectric materials which have higher dielectric constants must be used to reduce the leakage current. The capacitance of a parallel plate capacitor cane be written as

$$C = \frac{\epsilon_o \, k \, A}{t} \tag{1.3}$$

where ε_0 is the permittivity of free space, k is the relative permittivity of the dielectric material, A is the area of the device and t is the thickness of the dielectric layer. In device scaling, when the area A of the structures decrease, in order to maintain the same capacitance the thickness t of the dielectric layers must also decrease which leads to undesirably large gate leakage currents. Hence, the solution to the tunnelling problem is to replace SiO_2 with a physically thicker layer of a new material of higher dielectric constant (permittivity) k in order to retain the same equivalent capacitance at reduced leakage currents.

In successive generations of device scaling all FET dimensions reduce proportionately. When new gate dielectric materials are introduced it is convenient to define an 'electrical thickness' of the new gate oxide material in terms of its equivalent silicon dioxide thickness or 'equivalent oxide thickness' (EOT) as

$$t_{ox} = \mathrm{EOT} = \frac{3.9 * t_{\mathrm{highk}}}{k} \tag{1.4}$$

where 3.9 is the static dielectric constant of SiO_2 and t_{highk} is thickness of the high k dielectric layer For a material of a k value of roughly 20, a 5 nm thick layer would have the same dielectric properties as 1 nm of SiO_2 and would significantly reduce any leakage current. An important objective in continued microprocessor development is therefore the introduction of high-k oxides which allow scaling to continue to ever lower values of EOT.

1.2 Choice of high-k dielectrics

One of the main challenges with high-k oxide integration is to achieve a high quality interface between the high-k film and the semiconductor substrates. At the Si/SiO_2 interface of high quality MOS structures, the interface state defect density is ~10^{10}/cm^2. The search for alternative high-k oxides that could offer stable interfaces with a low density of electrically active defects has become a topic of major interest. Beyond silicon dioxide (SiO_2) and silicon nitride (Si_3N_4), a number of high-k dielectric candidates such as aluminium oxide (Al_2O_3) [4-6], gadolinium oxide (Gd_2O_3) [6], magnesium oxide (MgO) [7-9], erbium oxide (Er_2O_3) [10], lanthanum aluminium oxide ($LaAlO_3$), La_2O_3(lanthanum oxide) [11, 12], tantalum pentoxide (Ta_2O_5) [13, 14, 15], zirconium dioxide (ZrO_2) [16,17], zirconium silicate ($ZrSiO_4$)[18], hafnium oxide (HfO_2) [19-22] hafnium silicate ($HfSiO_4$) [23], and strontium titanate ($SrTiO_3$), have been proposed and investigated, with HfO_2 and Al_2O_3 getting special attention. Table 1.1 and Figure 1.2 shows that the k value of candidate oxides tends to vary inversely with the band gap value.

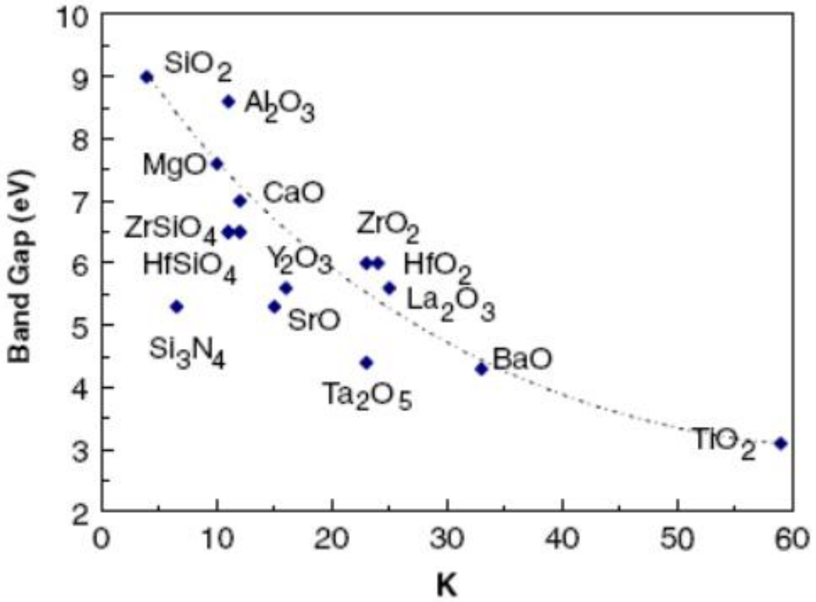

Figure 1.2 Band gap versus static dielectric constant for candidate gate oxide materials [24]

Table 1.1 Static dielectric constant (k) and experimental band gap of high-k oxides [25].

Dielectric	k value	Band gap (eV)
SiO_2	3.9	9
Si_3N_4	7	5.3
HfO_2	25	5.8
Al_2O_3	9	8.8
TiO_2	80	3.5
Ta_2O_5	22	4.4
$SrTiO_3$	2000	3.2
ZrO_2	25	5.8
$HfSiO_4$	11	6.5
La_2O_3	30	6
Y_2O_3	15	6
$LaAlO_3$	30	5.6

For a good quality semiconductor/dielectric interface the required properties for a new high-k oxide according to John Robertson [24]:

1. It must have a high enough ‘k’ that it will be used for a reasonable number of generations of scaling. It is reported that a k value between 25-30 is required [24], and while there are several available candidates with k values as large and larger than this (30-110) Ta_2O_5 , $SrTiO_3$ [24] and TiO_2 [25] these materials do not satisfy some of the following criteria such as band offsets, large leakage current and poor

thermal stability [26]. Robertson reports that, in general, the bandgap of materials decreases as the dielectric constant increases as shown in Figure 1.2

2. The dielectric material must be thermodynamically stable to withstand the high temperature annealing steps in device fabrication (1000 ^{o}C for 5 seconds).

4. It must act as an insulator, by having band offsets relative to channel and gate over 1 eV to minimise carrier injection into its bands.

5. It must form a good electrical interface with the semiconductor channel.

6. It must have few electrically active bulk defects.

Ideally the gate oxide film should be a single amorphous structure for a given composition, no dislocations or grain boundaries and a continuous random linkage which tends to minimize electrically active defects. While a variety of different deposition techniques can be used to deposit the dielectric films in a controlled way; atomic layer deposition (ALD) is one of the principal methods for the deposition of high-k dielectrics for MOSFET applications. ALD is a layer by layer growth process carried out at low temperature (100- 400 ^{o}C). It provides outstanding film thickness control and near perfect conformity because of its surface saturating character. There are two factors which causes the saturation of the surface: steric hindrance of the ligands and the number of reactive the surface sites. Steric hindrance of the ligands can cause the ligands of the chemisorbed species to protect the surface from being accessible to the reactant. Now the surface can be considered full and no bonding sites are available to access.

1.3 High-k dielectrics incompatibility with Si: Call for new channel material

High-k dielectric materials processing is an important issue for the incorporation of these materials with the conventional Si MOSFET technology. It was observed that high-k processing on Si resulted in reduced reliability because of the high defect concentrations, particularly O vacancies, which resulted in charge trapping, transient threshold and voltage shifts. Another issue of importance in considering any gate oxide, and high-k dielectric is the channel carrier mobility degradation due to Coulombic scattering as schematically shown in the Figure 1.3 is taken from [26].

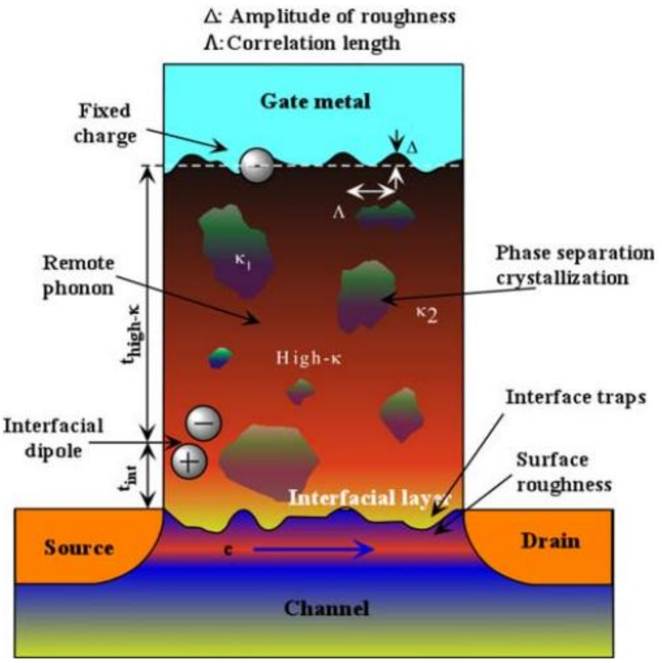

Figure 1.3 Schematic illustrations of reasons contributing to carrier mobility degradation in a high-k oxide layer [26]

Therefore progress in scaling of MOSFETs is not limited to the high-k materials issues only in that the search is on for new possible channel materials with better transport properties than Si. A range of alternative semiconductor materials are being considered in order to obtain better transport properties and to drive for technologies beyond the 16 nm CMOS fabrication node. The integration of high-mobility conduction channels such as InGaAs for n-channel and Ge for p-channel devices with novel high-k gate dielectrics is being intensively investigated. The electron and hole mobility values for Si, GaAs and $In_{0.53}Ga_{0.47}As$ are given in Table 2 and explain the motivation for using these III-V materials for high speed device applications.

Table 1.2 Band gap (E_g), electron mobility (μe) and electron saturation velocity (υ_{sat}) for Si, GaAs and $In_{0.53}Ga_{0.47}As$ of semiconductor materials. [27]

	Si	**GaAs**	**$In_{0.53}Ga_{0.47}As$**
E_g (eV)	1.12	1.42	0.75
μe (cm^2/V-s)	800	4000	7000
υ_{sat}(cm/s)	8×10^6	8×10^6	7×10^6

1.4 InGaAs based MOSFET

The integration of certain III-V semiconductors into MOSFET devices offers the opportunity to benefit from their high electron mobility and high transconductance [28]. However, a largely unresolved issue relating to achieving this objective for all III-V semiconductors is the high density of defect states (D_{it}) at the III-V/dielectric interface. This high density of defect states is thought to arise from the presence of native oxides, surface contamination, dimers and dangling bonds at the semiconductor surface which results in the Fermi level being effectively pinned in the semiconductor bandgap [29, 30]. Surface states in the semiconductor bandgap can act as donors or acceptors. The crystallographic density of surface atoms is approximately 10^{14} /cm^2. Fermi level pinning at the semiconductor surface is explained in the band diagram shown in Figure 1.4 (a) - (d). Figure 1.4 (a) shows a flat band condition of the n- type semiconductor. When a positive bias is applied to the n- type semiconductor, the Fermi level moves, inducing the band bending shown in Figure 4.1(b). Figure 4.1 (c) shows the band diagram of the n type semiconductor with surface states filled up to the Fermi level showing band bending, even in the absence of an applied bias. If the density of these surface states is high enough, an applied bias cannot move the Fermi level, therfore it is pinned as shown in Figure 4.1(d). To overcome these problems, surface passivation treatments have been developed to reduce D_{it} in order to facilitate the inversion of the semiconductor [31-34]. A range of approaches to control D_{it} have been employed including interface control layers, wet chemical passivation treatments and forming gas anneals (FGA) with varied levels of success [35-43].

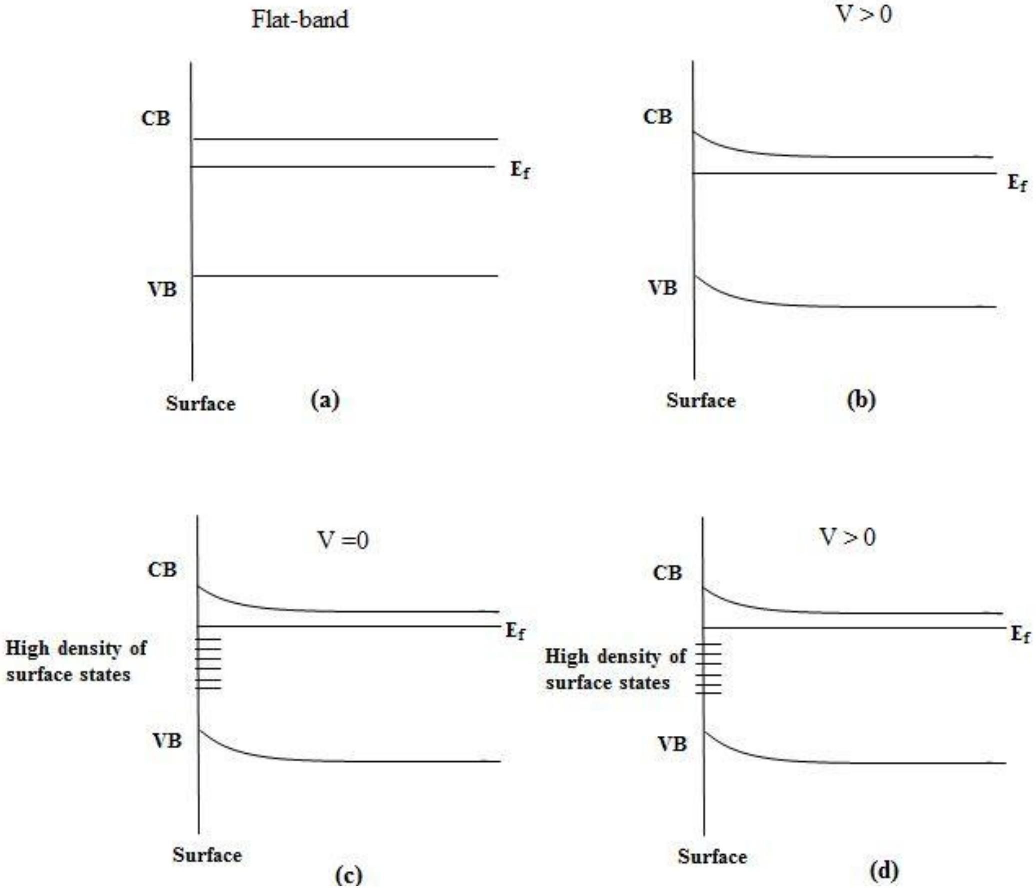

Figure 1.4 (a) Flat- band (b) when bias is applied Fermi level move inducing band bending means (c) In absence of bias the band bending at n type semiconductor with filled surface states upto Fermi level (d) Applied bias can not move the Fermi level i.e. Fermi level is pinned

1.5 Surface passivation

Semiconductor surface passivation technology must address two problems. Firstly, it must prevent the clean semiconductor surface from oxidising either in air or at the dielectric interface which is referred to as chemical passivation. Secondly, it must significantly reduce the interfacial state density at the dielectric interface which is effective electrical passivation.

Sulphur passivation of III-V compound semiconductors has been performed in two distinct ways

1) Passivation from solutions

2) Passivation from the gas phase

There have been many efforts of sulphur passivation by H_2S, molecular sulphur and $(NH_4)_2S$, which show good results in terms of chemical passivation [47, 56-58]. The wet chemical solution based passivation methods reported in the literature have been shown to be able to fully remove the native oxides from InP and GaAs. However, the surface passivation has not been as successful as that of Si/SiO_2 based devices due to complexities in achieving a high quality interface between the high-k film and these semiconductors. Among them sulphur passivation of III-V semiconductors has been extensively explored since the 1990's [43-52] and has been shown to be effective in improving the electrical properties of MOS and MOSFET devices [53-56]. In addition, these treatments reduce the rate of re-oxidation upon exposure to the atmosphere. Surface and interfacial defects arise from the presence of native oxides, surface contamination, dimers and dangling bonds at the semiconductor surface. Sulphur allows both chemical and electronic passivation of a surface and is therefore a promising method in III–V semiconductor technology. On the one hand, chalcogenide passivation (S, Se etc.) makes it possible to decrease substantially the density of surface states in the band gap thereby decreasing the surface recombination velocity and, as a result, improving many characteristic features of the devices. On the other hand, it makes it possible to slow down the re-oxidation of a clean semiconductor surface upon exposure to the atmosphere.

GaAs surfaces have been passivated in aqueous solutions of K2Se as well as in the solutions Na_2S+$RuCl_2$ [59], Na_2Se/NH_4OH [60], SeS_2[61], S_2Cl_2 [62] and Se/NH_4OH [63]. Later, $(NH_4)_2S$ solution was found most effective in reducing thesurface state densities. Many of these investigations utilize similar surface treatments to those employed for GaAs surfaces. Later, the technology of sulphide passivation from solutions has led to the development of alternative sulphur based passivation including H_2S and ultra high vacuum based electrochemical cell deposition methods. Electrochemical sulphide passivation has made it possible to obtain a relatively thick sulphide coating on a GaAs surface [64]. H2S/H2mixture, obtained by decomposition of copper sulphide in hydrogen, was used as the sulphur containing gas including H2S. Adsorption of H_2S on the surface of strongly doped n-GaAs grown immediately prior to the experiment by molecular-beam epitaxy, was investigated [65]. A mixture consisting of atomic hydrogen and hydrogen sulphide molecules, was decomposed by means of a microwave discharge, which resulted in the production of atomic sulphur that was adsorbed on the GaAs surface at 60–70 °C [66].

InGaAs is a prime candidate for incorporation into future devices replacing silicon and has been the subject of extensive research due to its previous use in high electron mobility transistors (HEMT) high power devices and detailed processing protocols exist from this application [67]. Recently, large numbers of passivation techniques have been proposed for the passivation of InGaAs eg. in-situ high-k oxide on InGaAs [68] atomic layer deposition (ALD) of Al_2O_3 [68,69], amorphous ultrathin Si or Ge [70,71]. In fact, ALD of Al_2O_3 on InGaAs received a lot of attention due to the effects associated with the use of tri methyl aluminum (TMA) molecule, which reduces the Ga and As native oxides [,68]. An in-situ deposited amorphous Si interface passivation layer (IPL) of at least 1.5 nm thicknesses can be used to reduce interface state density and prevent the Fermi level pinning at InGaAs interface [38]. In the literature it has also been reported recently that different thermal treatments like post deposition forming gas annealing (FGA) at temperatures of 400-500 ^{o}C can be used to improve the electrical characteristics of Al_2O_3/InGaAs based MOS structures [72,73].

The principal aims of this work were (a) to examine various surface preparation methods for InGaAs substrates in terms of the removal of the native oxides and surface contamination, (b) investigate interface formation with high-κ dielectric materials and (c) study the high temperature thermal stability of these layers. The principle techniques used in this study High resolution synchrotron radiation photoemission spectroscopy (HRSPES) and x-ray photoemission spectroscopy (XPS). However, the higher surface sensitivity of the synchrotron radiation photoemission measurements provides a great advantage in determining the extent of oxide formation at the surfaces and interfaces investigated. Electrical measurements were also performed to observe the effects of chemical passivation treatments. These studies have highlighted a number of problems that need to be addressed for the process optimisation of high speed InGaAs based MOSFET devices.

1.6 Thesis organisation

Chapter 2 introduces the analysis techniques used in this study, along with the principles behind their operation. In first part of the chapter, the technique of x-ray photoelectron spectroscopy is described. XPS based on conventional laboratory based x-ray source and a synchrotron radiation source are considered. The electrical characterisation techniques used on the fabricated MOS structures are also described. In second part of the chapter, the ultra-high vacuum (UHV) systems used for these experiments, along with the thin film deposition and semiconductor surface preparation procedures employed throughout the study are outlined. The deposition techniques used in this study include atomic layer deposition and thermal deposition. The fabrication processes for both MOS and Schottky diode structure are also described.

Chapter 3 focuses on the production of the atomically clean InGaAs surface in an ultra high vacuum (UHV) environment. Systematic studies of in-situ and ex-situ sulphur passivation were carried out to observe the differences between these passivation strategies. High temperature stability studies of the passivated surfaces were also undertaken.

Chapter 4 presents the advantages of high surface sensitivity synchrotron radiation based photoemission over conventional XPS to characterise 1nm Al_2O_3 layers deposited on the native oxide and sulphur passivated InGaAs surfaces. High temperature annealing studies were also carried out to observe the chemical changes induced at the interfaces. The growth of Al_2O_3 layers by ALD on different chemically treated InGaAs surfaces characterised by conventional XPS is also presented.

Chapter 5 presents the investigation of the interfacial oxide formation and improvements during the stepwise deposition of the MgO layer on atomically clean InGaAs surface.

Chapter 6 presents the results of electrical measurements on MOS and Schottky diode structures formed on the differently prepared InGaAs surfaces. In this chapter sulphur passivation effects were investigated by C-V and I-V measurements and showed that a reduction in the defect state densities at the interface resulted in limited Fermi level movement within the band gap for both p-type and n-type substrates. This chapter investigates the effectiveness of the insertion of ultrathin ALD deposited Al_2O_3 dielectric layers on the Schottky barrier formed at the interface with metals of different work function metals. MOS structures ($Al/Al_2O_3/InGaAs$) formed on native oxide covered and sulphur passivated InGaAs surfaces are also investigated by capacitance measurements.

Chapter 7 presents an overall summary of the results and outlines the future research directions which this work could lead.

Each of the experimental results chapters are sub-divided into sections, which relate to different aspects of the study. At the end of each section a brief summary is given in an attempt to highlight the main results and place them in context within the chapter.

1.7 References

[1] G.E. Moore, Daedelus 125, 55 (1964); G.E. Moore, Cramming more components onto integrated circuits. Electronics38, 114–116 (1965)

[2] J.N. Burghartz (ed.), Ultra-thin Chip Technology and Applications, Chapter 2, page 13 (2011)

[3] D.R. Wolters, H.L. Peek, Solid-State Electronics, 30, 835 (1987)

[4] V. Naumann, M. Otto, R. B. Wehrspohn, C. Hagendorf, J. Vac. Sci. Technol. A 30, 04D106 (2012)

[5] Z. Liu, Sharon Cui, P. Shekhter, Xiao Sun, Lior Kornblum, Jie Yang, Eizenberg, K. S. Chang-Liao, T. P. Ma Appl. Phys. Lett. 99, 222104 (2011)

[6] K. Xu, H. Sio, O. A. Kirillov, L. Dong, M. Xu, P. D. Ye, D. Gundlach, and N. V. Nguyen J. Appl. Phys. 113, 024504 (2013)

[7] M. Czernohorsky, E. Bugiel, H.J. Osten, A. Fissel, O. Kirfel, Appl. Phys. Lett.88, 152905 (2006).

[8] P. Casey. G Hughes, Appl. Surf. Sci. 256, 24 (2010)

[9] Hsing-Yi Chou, V. V. Afanas’ev, A. Stesmans, H. C. Lin, P. K. Hurley, S. B. Newcomb, Appl. Phys. Lett. 97, 132112 (2010)

[10] S. Chen, Y. Zhu, R. Xu, Y.Q. Wu, X.J. Yang, Y.L. Fan, Z. M. Jiang, J. Zou, Appl. Phys. Lett.88, 222902 (2006)

[11] S. Guha, E. Cartier, M.A. Gribelyuk, N.A. Bojarczuk, M.C.Copel, Appl. Phys. Lett. 77, 2710 (2000)

[12] Y.H. Wu, M.Y. Yang, C.M. Kwei, IEEE Electron Device Lett.21, 341 (2000).

[13] I. C. Kizilyalli, R. Y. S. Huang, and P. K. Roy, IEEE Electron Device Letters. 19, 423(1998)

[14] J.L. Autran, R. Devine, C. Chaneliere, B. Ballard, IEEE Electron Device Lett.18, 447 (1997)

[15] D. Pach, Y.C. King, Q. Lu, T.J. King, C. Hu, A. Kalnitsky, S.P.Tay, C.C. Cheng, IEEE Electron Device Lett.19, 441 (1998)

[16] S. Shao, Z. Fan, J. Shao, H. He, Thin Solid Films 445,59 (2003)

[17] M. Copel, M. Giberyuk, E. Gusev, Appl. Phys. Lett.76, 436 (2000)

[18] W.J. Qi, R. Neih, E. Dharmarajan, B.H. Lee, Y. Jeon, L. Kang,K. Onishi, J.C. Lee, Appl. Phys. Lett.77, 1704 (2000)

[19] C. H. An, Y. C. Byun, M. H. Cho, H Kim, Phys. Stat. Sol. RRL 6, 247 (2012)

[20] B.H. Lee, L. Kang, R. Neeh, W.J. Qi, J.C. Lee, Appl. Phys. Lett.76, 1926 (2000)

[21] R. Suzuki, N. Taoka, M. Yokoyama, S. H. Kim, T. Hoshii, T. Maeda, T. Yasuda, Osamu Ichikawa, N. Fukuhara, M. Hata, M. Takenaka, S. Takagi, J. Appl. Phys. 112, 084103 (2012)

[22] N. Goel, P. Majhi, C. O. Chui, W. Tsai, D. Choi, J. S. Harris, Appl. Phys. Lett. 89, 163517 (2006)

[23] G.D. Wilk, R.M. Wallace, J.M. Anthony, J. Appl. Phys.87, 484 (2000)

[24] J. Robertson, Reports on Progress in Physics, 69, 327 (2006)

[25] J. Robertson, Eur. Phys. J. Appl. Phys.28, 265 (2004)

[26] M. Wu, Y. I. Alivov, H. Morkoc, J Mater Sci: Mater Electron 19, 915 (2008)

[27] A. Erol, Semiconductor properties Dilute III-V Nitride Semiconductors and Material Systems: Physics and Technology, Springer (2008)

[28] W. Liu, Fundamentals of III–V Devices, Wiley (1999)

[29] O.L. Krivanek, Z. Liliental, J.F. Wager, R.G. Gan, S.M. Goodnick, C.W. Wilmsen, J. Vacuum Sci. Tech. B, 3, 1081 (1985)

[30] M. Passlack, M. Hong, J. P. Mannaerts, J. R. Kwo, 53rd DRC Late News Technical Digest IEEE, New York, 13 (1995)

[31] B. Shin, D. Choi, J. S. Harris, and P. C. McIntyre, Appl. Phys. Lett. 93, 052911 (2008)

[32] N. Goel, P. Majhi, C. O. Chui, W. Tsai, D. Choi, and J. S. Harris, Appl. Phys. Lett. 89, 163517 (2006)

[33] Y. C. Chang, M. L. Huang, K. Y. Lee, Y. J. Lee, T. D. Lin, M. Hong, J. Kwo, T. S. Lay, C. C. Liao, and K. Y. Cheng, Appl. Phys. Lett. 92, 072901 (2008)

[34] C. L. Hinkle, A. M. Sonnett, E. M. Vogel, S. McDonnell, G. Hughes, M. Milojevic, B. Lee, F. S. Aguirre-Tostado, K. J. Choi, J. Kim, and R. M. Wallace, Appl. Phys. Lett. 91, 163512 (2007)

[35] A. Molle, G. Brammertz, L. Lamagna, M. Fanciulli, M. Meuris, S. Spiga, Appl. Phys. Lett. 95, 023507 (2009)

[36] S. Koveshnikov,W. Tsai, I.Ok, J. Lee, V. Torkanov, M. Yakimov, and S. Oktyabrsky, Appl. Phys. Lett. 88, 022106 (2006)

[37] Zuoguang Liu, Sharon Cui, Pini Shekhter, Xiao Sun, Lior Kornblum, Jie Yang, Moshe Eizenberg, K. S. Chang-Liao, and T. P. Ma, Appl. Phys. Lett. 99,222104 (2011)

[38] Akazawa, M., Hasegawa, H. Applied Surface Science 256, 5708 (2010)

[39] J.S. Herman, F.L. Terry Jr., Appl. Phys. Lett. 60, 716 (1992)

[40] G. Hughes, C. Springer, U. Resch, N. Esser, and W. Richter, J. Appl. Phys. 78**,** 1948 (1995)

[41] L. Geelhaar, R.A. Bartynski, F. Ren, M. Schnoes, D.N. Buckley, J. Appl. Phys. 80, 199 3076 (1996)

[42] C.I. Kuo, E.Y. Chang, H.T. Hsu, C.C. Chen, C.Y. Chang, Jpn. J. Appl. Phys. 47, 3441 (2008)

[43] J. Shin, K. M. Geib, and C. W. Wilmsen, J. Vac. Sci. Technol. B 9, 2337 (1991)

[44] T. Ohno, K. Shiraishi, Phys. Rev. B 42, 11194 (1990)

[45] X. Y, Hou, W Z. Cai, Z. Q. He, P. H. Hao, Z. S. Li, X. M. Ding, X. Wang Appl . Phy s. Lett. 60, 2252 (1992)

[46] V. N. Bessolve, M.V. Lebedev, E. B. Novikov, and B.V. Tsarenkov, J. Vac. Sci. Techno. B 11, 1 (1993).

[47] N. Barbouth, Y. Berthier, J. Oudar, J. M. Moison and M. Bensoussan J. Electrochem. Soc., Solid State Science and Technology, 1663 (1986)

[48] K. C. Hwang and S. S. Li, J. Appl. Phys. 67, 2162 (1990)

[49] B. A. Kuruvilla, G. V. Ghaisas, A. Datta, S. Banerjee, and S. K. Kulkarni, J. Appl. Phys. 73, 4384 (1993)

[50] Z. S. Li, W. Z. Cai, R. Z. Su, G. S. Dong, D. M. Huang, X. M. Ding, X. Y. Hou, and X. Wang, Appl. Phys. Lett. 64, 3425 (1994)

[51] Y. Wang, Y. Darici, and P. H. Holloway, J. Appl. Phys. 71, 2746 (1992)

[52] R. S. Besser, C. R. Helms, J. Appl. Phys. 65, 11 (1989)

[53] É. O'Connor, B. Brennan, V. Djara, K. Cherkaoui, S. Monaghan, S. B. Newcomb, R.Contreras, M. Milojevic, G. Hughes, M. E. Pemble, R. M. Wallace, and P.K. Hurley. J Appl. Physics, 109, 024101 (2011)

[54] E. O'Connor, R. D. Long, K. Cherkaoui, K. K. Thomas, F. Chalvet, I. M. Povey, M. E. Pemble, and P. K. Hurley, B. Brennan and G. Hughes, S. B. Newcomb Appl. Phys. Lett. 92**,** 022902 (2008)

[55] C.L. Hinkle, **M**. Milojevic, E.M. Vogel and R.M. Wallace. Microelectronic Engineering 86**,** 1544 (2009)

[56] H.C. Lin , W. Wang, G. Brammertz, M. Meuris, M. Heyns, Microelectronic Engineering 86, 1554 (2009)

[57] V. N Bessolovy, M. V Lebedevy, N. M. Binhz, M. Friedrichz and D. R. T. Zahnz, Semicond. Sci. Technol. 13, 611 (1998)

[58] Li, Zheshen , WZ Su, RZ Dong, GS Huang, DM Ding, XM Hou, XY Wang,Applied Physics Letters, 64 (1994)

[59] M. G. Mauk, S. Xu, D. J. Arent, R. P. Mertens, and G. Borghs, Appl. Phys. Lett. 54, 213, (1989)

[60] C. J. Sandroff, M. S. Hegde, L. A. Farrow, R. Bhat, J. P. Harbison, and C. C. Chang J. Appl. Phys. 67, 586, (1990)

[61] B. A. Kuruvilla, G. V. Ghaisas, A. Datta, S. Banerjee, and S. K. Kulkarni J. Appl. Phys. 73, 4384, (1993)

[62] Li, Zheshen , W Z Su, R Z Dong, G S Huang, D M Ding, XM Hou, XY Wang Appl. Phys. Lett. 73, 4384, (1993)

[63] K. Tsuchiya, M. Sakata, A. Funyu, and H. Ikoma J. Appl. Phys. 34, 5926, (1995)

[64] X. Y. Hou, W. Z. Cai, Z. Q. He, P. H. Hao, Z. S. Li, X. M. Ding, and X. Wang Appl. Phys. Lett. 60, 2252 (1992)

[65] Chan‐Hwa Chung, Sang I. Yi, and W. Henry Weinberg Appl. Phys. Lett. 69, 3369(1996)

[66] G. Y. Gu, E. A. Ogryzlo, P. C. Wong, M. Y. Zhou, and K. A. R. Mitchell J. Appl. Phys. 72, 762, (1992)

[67] S. Oh, H. S. P.Wong, IEEE Trans. Electron. Devices 56, 1161 (2009)

[68] InJo Ok, H. Kim, M. Zhang, F. Zhu, S. Park, and J. Yum, S. Koveshnikov, W.Tsai, V. Tokranov, M. Yakimov, S. Oktyabrsky, Jack C. Lee, J. Vac. Sci.Technol. B 25, 1491 (2007)

[69] L. Lamagna a, M. Fusi, S. Spiga, M. Fanciulli, G. Brammertz, C. Merckling, M.Meuris, A. Molle, Microelectronic Engineering 88, 431 (2011)

[70] H. Hasegawa, Thin Solid Films 367, 58 (2000)

[71] A. Molle, G. Brammertz, L. Lamagna, M. Fanciulli, M. Meuris, S. Spiga Appl. Phys. Lett. 95**,** 023507(2009)

[72] H. D. Trinh, E. Y. Chang, P. W. Wu, Y. Y. Wong, C. T. Chang, Y. F. Hsieh, C. C. Yu, H. Q. Nguyen,Y. C. Lin, K. L. Lin, and M. K. Hudait, Appl. Phys. Lett. 97, 042903 (2010)

[73] J. Hu and H. S. Philip Wong J. Appl. Phys.111, 044105 (2012)

Chapter 2

Experimental Details

This chapter outlines the principles and experimental details of the analytical techniques used in this work including the primary surface science techniques of x-ray photoemission and high resolution synchrotron radiation based photoemission spectroscopy. It also describes the details of the ultra-high vacuum (UHV) systems and deposition tools used to prepare the surfaces/interfaces.

2.1 X-ray photoemission spectroscopy (XPS)

The typical experimental set up for conventional XPS analysis is shown in Figure 2.1, consisting of an x-ray source, a sample under analysis, electron collection optics, electron kinetic energy analyser and a detection system connected to a computer to display output signal.

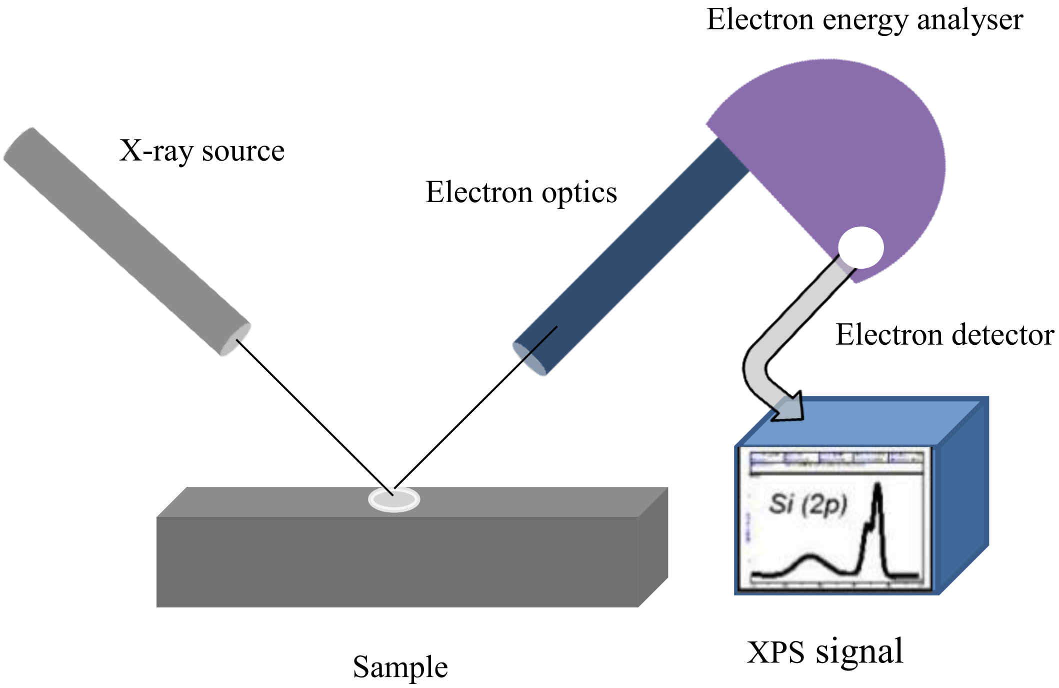

Figure 2.1 Schematic diagram of the photoemission experimental arrangement

2.1.1 Principle of Photoemission Spectroscopy

Photoemission spectroscopy involves the analysis of electrons emitted from atoms of a sample which has been irradiated with photons (X-ray, UV). The kinetic energy of photoemitted electrons is related to the photon energy of the incident x-ray and the electronic structure of the atom or molecule from which it is photo excited. The number of electrons emitted is proportional to the concentration of the emitting atoms in a material. The complete photoelectron process takes place as follows;

Photoionization (photoelectron formation)

$$A + h\nu = A^+ + e^- \qquad (2.1)$$

Where A is an atom and hν is the energy of the incident photon.

Conservation of energy requires

$$E(A) + h\nu = E(A^+) + E(e^-) \qquad (2.2)$$

Since the ejected photoelectron is free, the kinetic energy (E_{kin}) of photoelectron can be written as follows

$$E_{kin}(e^-) = h\nu - [E(A^+) - E(A)] \qquad (2.3)$$

$[E(A^+) - E(A)]$ represents the energy difference between the ionised atom and the neutral atom and is called the binding energy E_B (BE) of the electrons and leads to the following equation

$$E_{kin} = h\nu - E_B \qquad (2.4)$$

Thus, the binding energy can be obtained by measuring the kinetic energy of the emitted electron, as the energy of the x-ray photon source is known.

The principle of photoemission process is shown in Figure 2.2 and is based on the photoelectric effect [1].

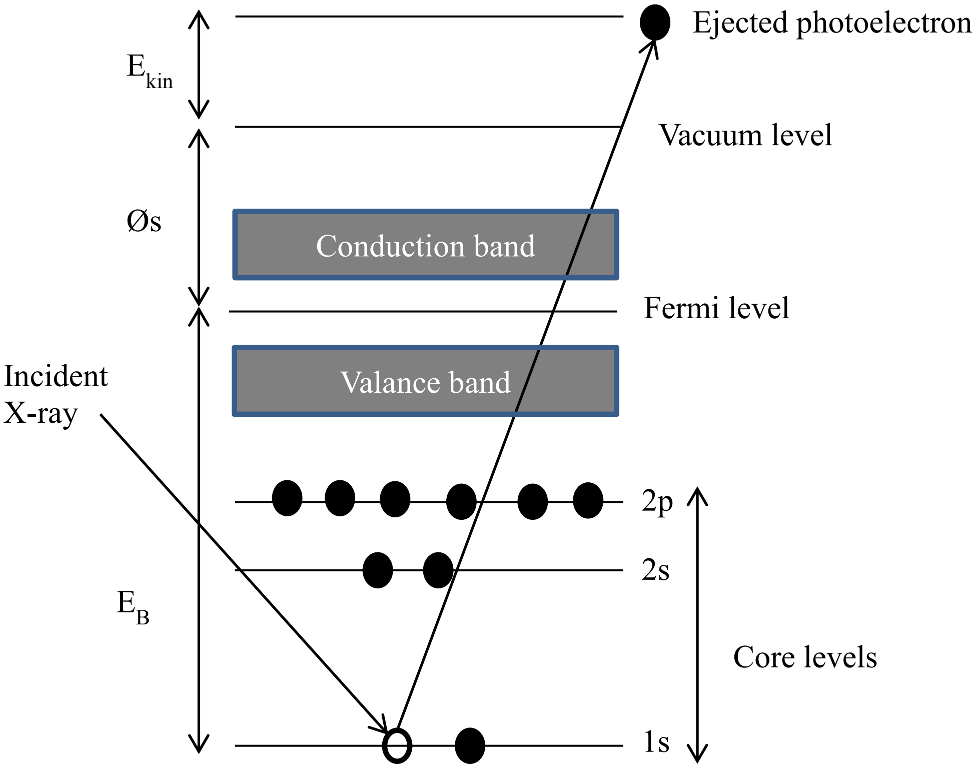

Figure 2.2 Schematic diagram of the photoemission process

XPS spectra can be acquired from gases, liquids and solids. For gases, the binding energy of an electron in a given orbital is identical to the ionization energy or first ionization potential of that electron. In solids, the influence of the surface is felt, and an additional energy component is required to eject an electron from the surface [2]. Therefore the binding energy E_B of the electron is written as

$$E_B = h\nu - E_{kin} - \O_s \qquad (2.5)$$

Where $\O_s$ is the work function of sample material as shown in Figure 2.2, which is the difference in energy between the Fermi level and the vacuum level.

2.1.2 Binding energy reference

From the previous section it is clear that the electron binding energy in a solid is calculated from the measured kinetic energy of the emitted photoelectron. To do this, a reference spectrometer is required for calibration and placed in electrical contact with a conductive sample. The Figure 2.3 shows the energy level diagram when conducting sample and spectrometer are in electrical contact.

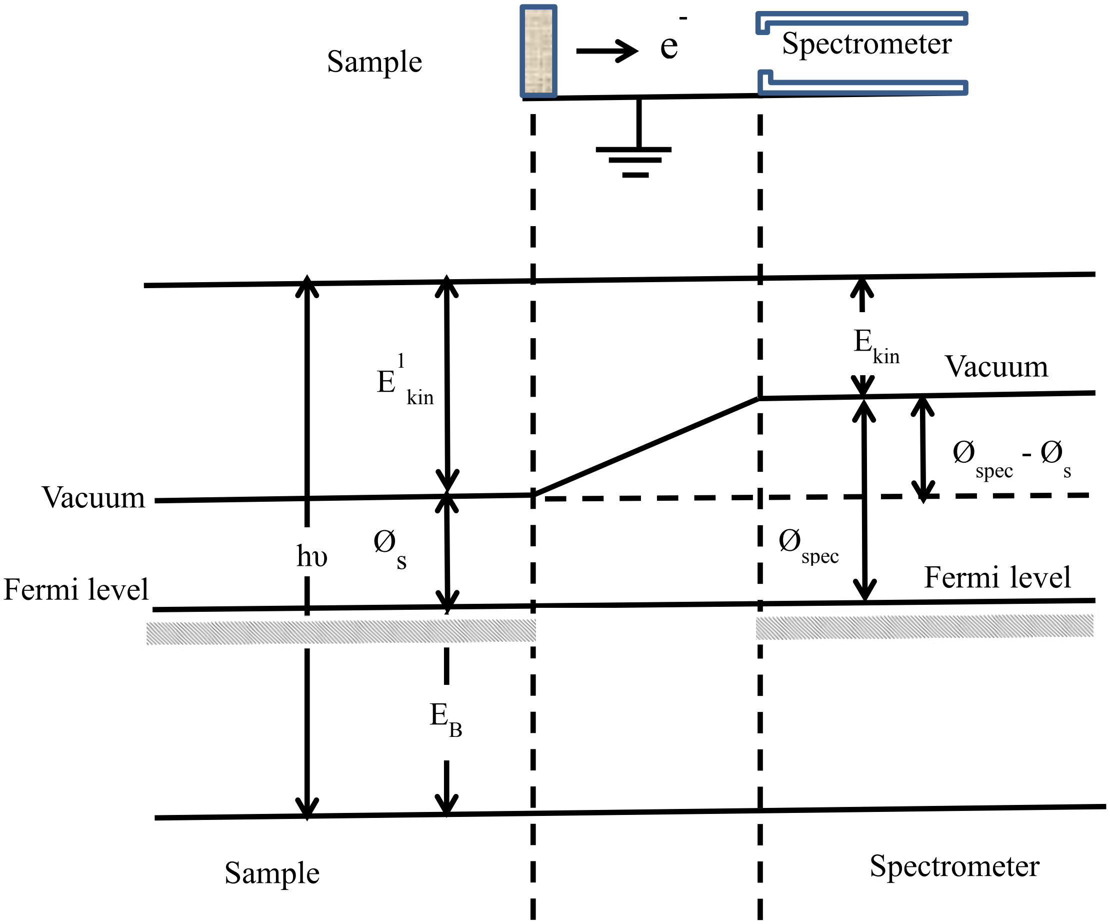

Figure 2.3 Energy level diagram for the photoemission process showing a sample and spectrometer in electrical contact [3]

When the sample is placed in electrical contact with a spectrometer, Fermi levels of both sample and spectrometer are aligned. From Figure 2.3 we can see the sum of the kinetic energy E_{kin} and binding energy (E_B) is not equal to the incident X-ray. Then the kinetic energy of the photoelectrons is measured from the Fermi level of the spectrometer. Therefore photoemission equation is as follows

$$E_{kin} = h\nu - E_B - Ø_s \tag{2.6}$$

$$E_{kin} = h\nu - E_B - Ø_s - (Ø_{spec} - Ø_s) \tag{2.7}$$

$$E_{kin} = hv - E_B - Ø_{spec} \tag{2.8}$$

$$E_B = hv - E_{kin} - Ø_{spec} \tag{2.9}$$

From above equation it is clear that we only need to know the spectrometer work function, $Ø_{spec}$ to calculate E_B. The spectrometer's work function can be calibrated by measuring the Au standard sample in the spectrometer and adjusting the instrument setting until the binding energy for Au is attained. The linearity of the binding energy scale may then be calibrated by adjusting the energy difference between two widely spaced spectral lines of known values (e.g., 2p and 3p photolines of Cu at 933eV and 75eV respectively)

In the case of insulating samples a relative surface charge potential (E_{ch}) build up at the spectrometer which raises the Fermi level of the spectrometer relative to the sample resulting in an apparent increase in binding energy and is given by following equation

$$E_B = hv - E_{kin} - Ø_{spec} - E_{ch} \tag{2.10}$$

To compensate the potential developed by positive surface charges, a mono-energetic source of low energy electrons (flooded gun) is required by which electrons (2~ 20 eV) can be flooded onto the sample.

2.1.3 XPS peak width

The peak width ΔE of a given photoelectron peak is defined as the full width at half maximum (FWHM) and is composed of a number of different contributions,

$$\Delta E = (\Delta E^2_n + \Delta E^2_p + \Delta E^2_a)^{1/2} \qquad (2.11)$$

Where

ΔE_n = lifetime width of the core hole level

ΔE_p = width of the photon source (X-ray line)

ΔE_a = analyser resolution

The ΔE_n is calculated by the Heisenberg uncertainty principle

$$\Delta E_n = \hbar/\tau \qquad (2.12)$$

Where ħ is the Planck constant and τ is core hole life time and is larger for inner shell orbitals verses outer shell electrons because inner shell electrons can be filled by the outer electrons shells when electrons are emitted from the inner shell, therefore the deeper the orbital the shorter the life time and larger the intrinsic peak width. Instrument effects that broaden the peak are the photon source width and the analyser resolution. Typically it is assumed that the line shape due to the core hole lifetime is Lorentzian and the instrumental contribution to the peak is a Gaussian line shape.

The Lorentzian peak width will be expected to increase with atomic number and for higher binding energy core levels. For example, for the Ag 3d peak with a natural line width of ~0.37 eV, this equates to a lifetime of ~1.1 x 10^{-14} s. If the lifetime were to decrease to ~6 x 10^{-15} s, this would increase the Lorentzian value to 0.7 eV, effectively doubling the natural line width.

2.2 Interpretation of the XPS spectra

The core level peak assignment of an InGaAs sample is shown in the survey spectrum in Figure 2.4 and generally scanned from 0-1000 or 1400 eV depending on the elements present in the sample. The plot has characteristic peaks for each element found on InGaAs surface of the sample.

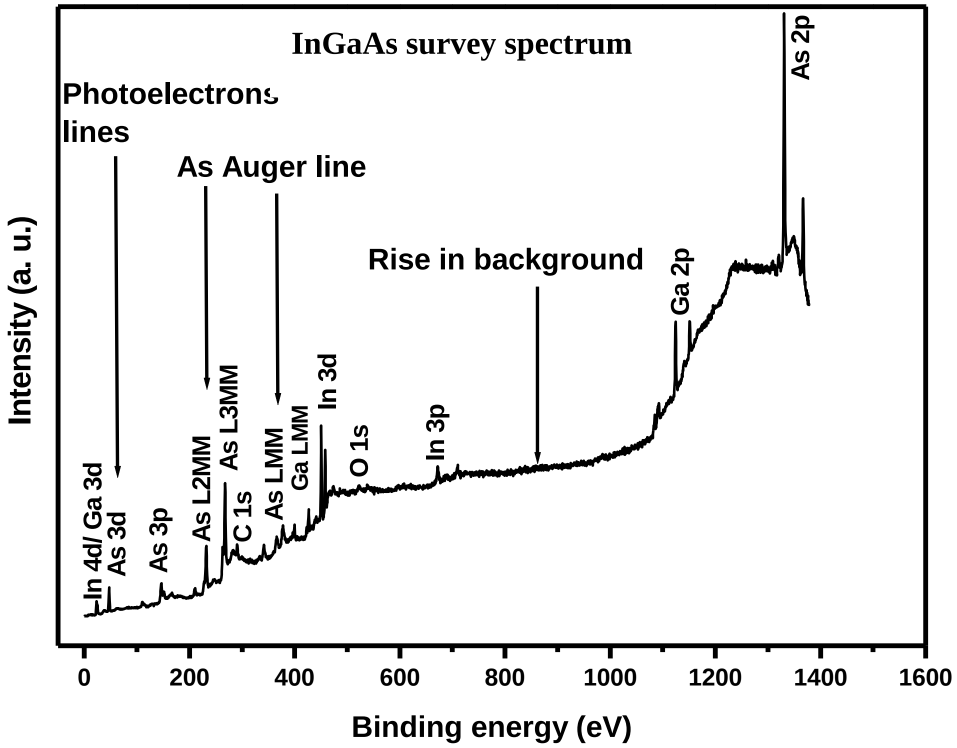

Figure 2.4 Survey spectrum of InGaAs sample

In this spectrum we can see photoemission and x-ray Auger induced emission peaks. Photoemission peaks are well defined intense spectral lines which have not suffered any energy loss in inelastic collision within the sample. They relate to the specific core level binding energies and can be identified using tabulation of binding energy values [4]. The electrons which have lost energy during the photoemission process give rise to a background signal which is continuous and rising in nature.

Where ambiguity exits in identifying a peak it is useful to look for the all photoemission lines of the same elements. For example, in InGaAs, the strongest emission are In 4d at 18.2 eV and other strong emission lines are the doublet In $3d_{3/2}$ at 443.0 eV and In $3d_{5/2}$ at 449.0 eV. The valence band (4d, 5s) emission occurs at a binding energy of 0 ~ 8 eV (measured with respect to the Fermi level). The remaining peaks are Auger peaks which are labelled in the spectra as As $L_2M_{45}M_{45}$ and As $L_3M_{45}M_{45}$ and Ga $L_3M_{45}M_{45}$. These lines can be readily distinguished by changing the energy of the x-ray source (Mg and

Al K_{α}) as the kinetic energy of the Auger lines will remain the same while the photoemission lines will shift by the energy difference between the Mg and Al K_{α} lines.

2.3 Inelastic mean free path

Typically the penetration depth of x-rays of approximately 1 keV photon energy is of the order of several microns into the solid and the photoemission process can occur down to these depths. However, the actual sampling depth in an XPS experiment is typically less than 10 nm. This difference is due to the fact that inelastic collisions can otherwise occur within the solid before the photo-excited electrons emerge from the surface. Electrons which suffer one or more inelastic collisions before being emitted from the solid do not provide any useful information about the electronic structure of the solid as the photoelectric equation is no longer valid.

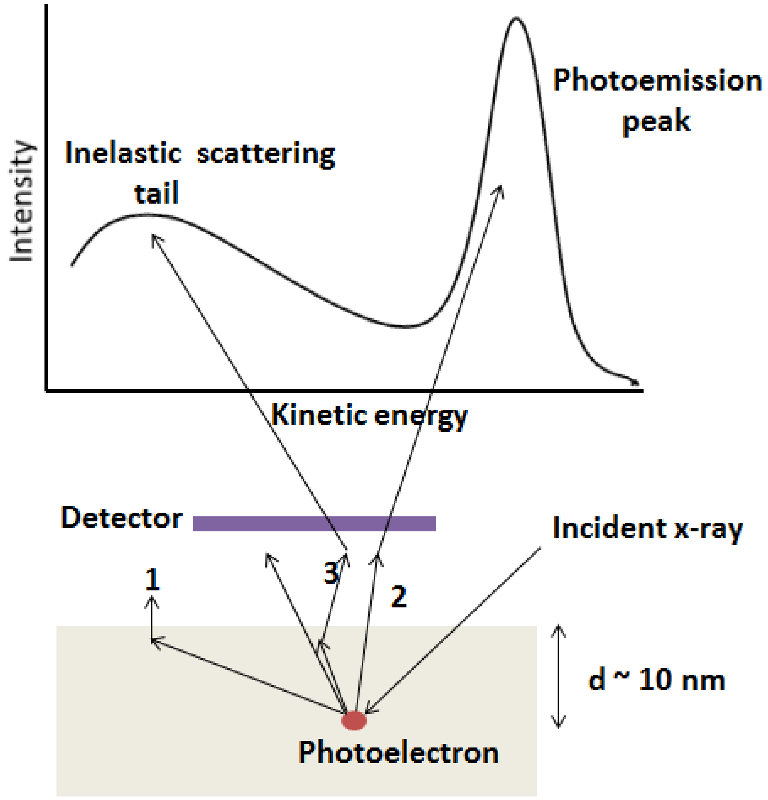

Figure 2.5 Diagram showing paths of various electron emissions during photoemission process

The different paths of photoemitted electrons from the sample surface are schematically shown in Figure 2.5 where electrons 1 and 3 have suffered scattering events which means that they contribute to background of the XPS spectrum while electron 2 reaches the detector without any energy loss thereby contributing to the photoemission peak. Therefore, in photoemission experiments useful information may only be obtained from the first 5 – 10 nm of the surface, making the technique highly surface sensitive.

The probability of such interactions can be statistically predicted based on the inelastic mean free path (IMFP) of the given material, which is dependent on the initial kinetic energy of the electron of the material and nature of the solid shown in the universal mean free path curve in Figure 2.6.

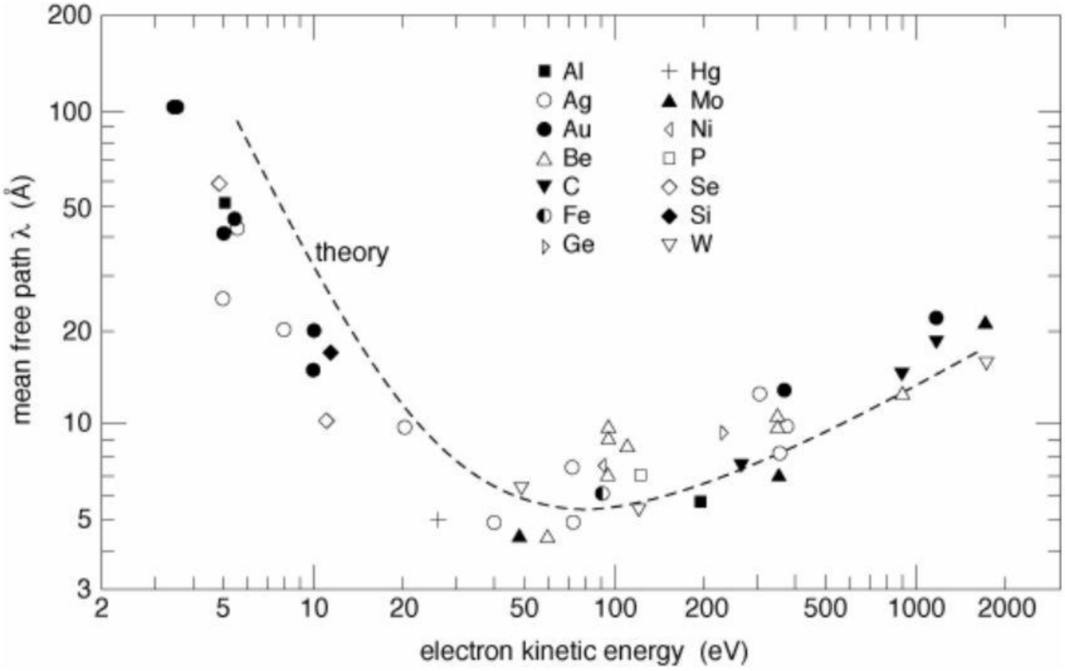

Figure 2.6 Universal mean free path (MFP) curve, showing a range of materials [5].

Therefore the IMFP is a measure of the average distance travelled by an electron through a solid before it is inelastically scattered. The IMFP may be expressed as

$$P(x) = \exp(-x/\lambdabar) \tag{2.13}$$

Where P(x) is the probability of any single electron travelling a distance x through a solid and ƛ is inelastic mean free path of electron for a given energy. Figure 2.7 shows the probability decays very rapidly and essentially becomes zero when $x > 5ƛ$.

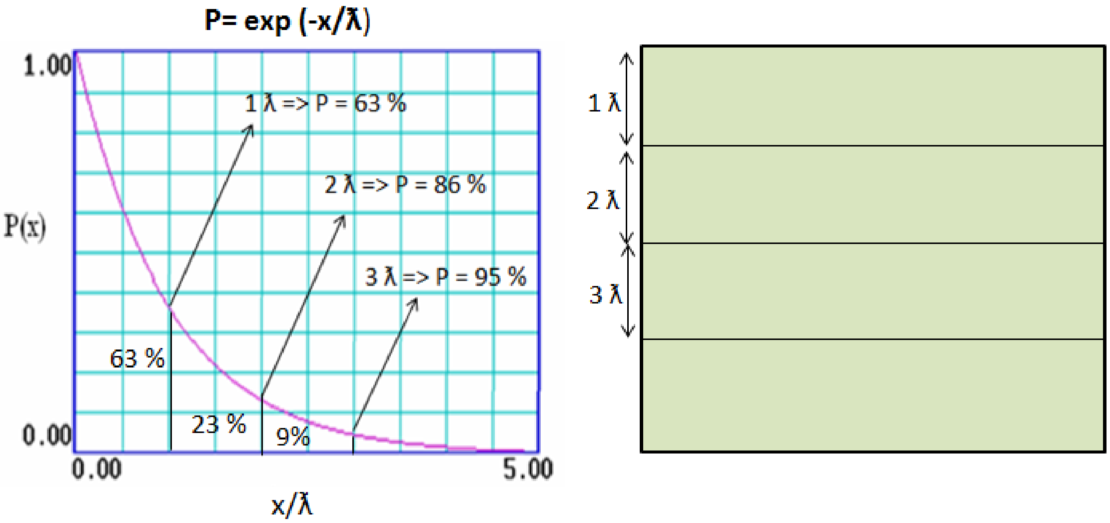

Figure 2.7 Probability of unscattered electron emission as a function of depth [6]

When x = ƛ, P = exp (-1) = 0.37, i.e. escape of the electron in a direction to the normal of surface and without inelastic scattering occurs with a 37 %.

When x = 2ƛ, P = exp (-2) = 0.14, i.e. escape of the electron in a direction to the normal of surface and without inelastic scattering occurs with a 14 %.

When x = 3ƛ, P = exp (-3) = 0.05, i.e. escape of the electron in a direction to the normal of surface and without inelastic scattering occurs with a 5%.

In conclusion, we can see virtually all the signal of unscattered electrons comes from within 3ƛ of the surface and therefore the sampling depth of XPS is defined as three times the IMFP.

2.4 Core level chemical shift

One of the most important aspects of XPS is that the core level energy depends on the chemical state of the atom. Changes in the local charge density around a particular atom resulting from the formation of a chemical bond can result in a shift in core level binding energies. The chemical shift occurs due the electronegativity effect and is correlated with the overall charge on an atom and its magnitude is influenced by

(i) Number and type of surrounding atoms

(ii) Electronegativity of atoms

(iii) Oxidation state of the atom

Withdrawal of valence electron charge (oxidation) from an atom gives rise to an increase in the binding energy of the photoemitted electrons. Conversely, the addition of valence electron charge results in a decrease in the binding energy position. Atoms of a higher positive oxidation state exhibit a higher binding energy due to the extra Coulombic interaction between the photoemitted electron and the ion core. This ability to discriminate between different oxidation states and chemical environments is one of the major strengths of the XPS technique. An example of chemical shift for the silicon/silicon dioxide system, using the Si 2p spectrum is shown in Figure 2.8.

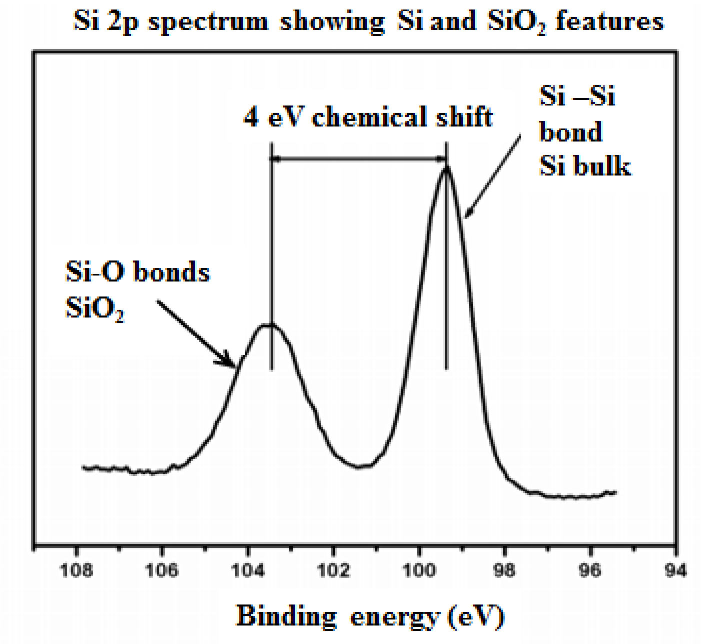

Figure 2.8 Si 2p spectrum showing a 4 eV chemical shift between component peaks which indicates the presence of Si and SiO_2 [7]

Figure 2.8 shows a Si 2p spectrum taken from a thin (~ 4 nm) SiO_2 layer which was thermally grown on a Si (111) substrate. It can be seen that electrons excited from the Si substrate appear at a binding energy of ~ 99.3 eV, while those from the SiO_2 over layer appear at a higher binding energy position, chemically shifted from the Silicon bulk by ~ 4 eV. This is due to the different bonding environment present within the two chemical species. The covalent Si-Si bonding system seen within the Si bulk allows the valence electrons to be shared equally among each of the Si atoms involved in the bond structure. However, the incorporation of O atoms, which have considerably higher electronegativity than Si, results in the transfer of electron density toward the O atoms. As such, Si-O bonds are more ionic and electrons which are excited from these silicon atoms are leaving an atom which has a slightly greater positive charge than those within the Si bulk. The effect of this positive charge is to reduce the kinetic energy of the emitted electrons, which is apparent from the increased binding energy of the SiO_2.

2.5 Quantification

Analysis of the relative intensity of strong core-level peaks from the different elements present in a sample can be used to yield semi-quantitative information on the relative atomic concentrations in the film. However, there are a number of factors which must be taken into account in order to accurately quantify chemical composition using XPS peak intensities. The XPS peak intensity [8] is given by

$$I_{ij} = n_i \mathrm{K}\ \mathrm{T}\ (KE)\ L_{ij}\ \sigma_{ij} \lambda (KE)\ \cos\Theta \tag{2.14}$$

Where I_{ij} is the peak area of the peak j present in the i element, n_i is the atomic concentration of element assuming the compound is homogenous, K is the instrument constant that contains x-ray flux and the area of the sample from which photoelectrons are detected, T(KE) is the transmission function of the analyser, L_{ij} is the angular asymmetry factor of orbital j of element i which depends on the type of atomic orbital the photoelectron is emitted from, σ_{ij} is the photoionization cross section of peak j of element i which is the probability that an electron of that core-level will be excited, λ (KE) is the inelastic mean free path, and $\cos\Theta$ is the emission angle

The atomic concentration of n_i of an element i is given by

$$n_i = \frac{n_i}{\sum n_i} \tag{2.15}$$

$$n_i = \frac{I_{ij}/\sigma_{ij}\ ƛ(KE)}{\sum I_{ij}/\sigma_{ij}\ ƛ(KE)} \tag{2.16}$$

$$S_i = \sigma_{ij}\, ƛ(KE) \tag{2.17}$$

S_i is called the atomic sensitivity factor. Therefore n_i is dependent on the peak area and sensitivity factor

$$n_i = \frac{I_{ij}/S_i}{\sum I_i/S_i} \tag{2.18}$$

Using all these contributions it is possible to determine relative sensitivity factors (RSF's) for each core-level associated with each element present and from these it is possible to determine the relative atomic concentrations in a material. Published values for these RSF's are available from XPS reference manuals and the use of these factors can yield semi-quantitative analysis. The strongest core-level peak from each detected element is 'normalised' by dividing the integrated intensity by the relevant RSF. The total sum of all normalised peak areas is then defined as 100% and the atomic percentages can be easily calculated.

An example to calculate the element concentration is explained below

Suppose a compound has 4 elements present in it (C, Si, N and O), the concentration of the Si is calculated as follows and defined in the table

$$n_{Si} = \frac{I_{Si}/S_{Si}}{I_{Si}/S_{Si} + I_N/S_N + I_C/S_C + I_O/S_O} = 0.21$$

Element	**RSF(S)**	**Peak area**	**Area/RSF(S)**	**Atomic %**
C	1	2944	2944	30
O	2.85	12754	4471.92	46
N	1.77	475	258.19	3
Si	0.83	1663	2003.61	21

2.6 Angle resolved XPS

Angle resolved XPS (ARXPS) allows non-destructive depth profiling to be achieved for a thickness into the sample surface which is comparable to the sampling depth. Therefore, the maximum sampling depth is achieved by aligning the sample so that the electrons which emerge normal to the surface are detected by the analyser. However, electrons emerging from shallower angles with respect to the surface may also be analysed by rotating the sample relative to the analyser. This is graphically represented in Figure 2.9.

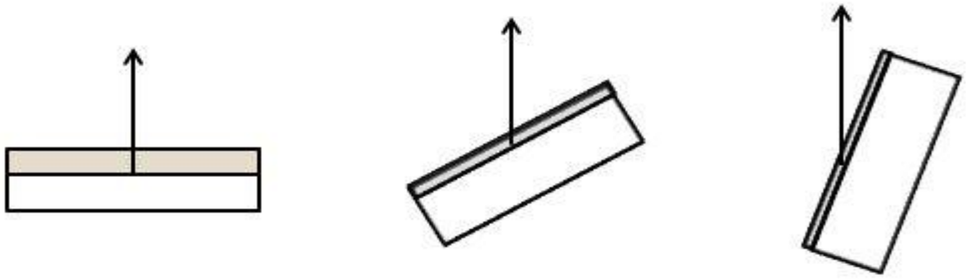

Figure 2.9 Schematic of angle resolved XPS at normal emission and θ > 0, shading shows the information depth from which electron can escape from the surface

Plotting the relative intensities of different photoemission peaks as a function of the emission angle allows for a depth profile of a region equal to the maximum sampling depth for that material. An example of a SiO_2 film on silicon analysed at two different angles in Figure 2.10 shows an increase in the intensity of the overlayer SiO_2 signal as the detector angle with respect to the surface normal is increased. However, when the sample is rotated by increasing the detector angle, the perpendicular depth from which the electrons escape from the surface is considerably less than for normal emission. This effectively enhances the surface sensitivity of the core level spectra over those taken at normal emission. This is further evidenced by Si 2p spectra in Figure 2.10 which are taken from an SiO_2 layer (~ 5.4 nm) on a silicon substrate at emission angles equal to 0 ° (normal emission) and 60°. It can be clearly seen that the spectrum taken at 60° shows an increased intensity from the Si oxide overlayer.

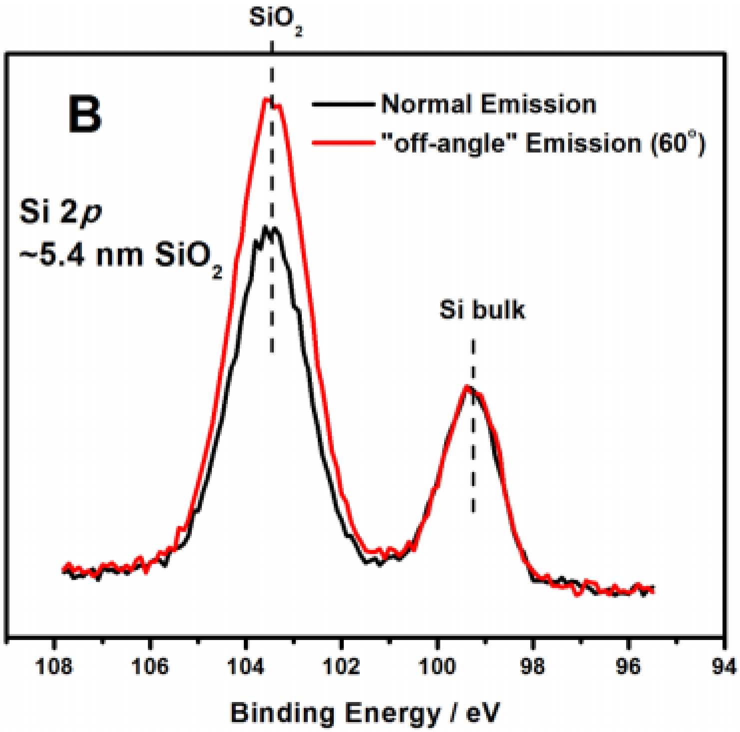

Figure 2.10 Si 2p spectra taken from a 5.4 nm SiO_2 layer on silicon showing the increased surface sensitivity using ARXPS [7]

2.7 Thickness Calculations

XPS can be a useful tool for estimating the thickness of overlayers which are less than 10 nm thick by comparing the attenuation in the intensity of a core level feature from an element in the substrate resulting from the presence of an overlayer. XPS thickness calculations used in this study can be divided into two categories. The overlayer thickness can be estimated based on the suppression of the substrate peak by the presence of an overlayer. When the same element is present in distinguishably different chemical environments in the overlayer and substrate, the overlayer thickness calculations are simplified.

For a sample of material A which forms a thin uniform layer of thickness d on a substrate of material S, the following equation can be written for the relative intensity of the substrate (I_S) and overlayer (I_A) XPS signals (assuming exponential attenuation of the overlayer) [9,10].

$$\frac{I_A}{I_S} = \frac{I_A^{\infty} exp\left\{1 - \left(\frac{-d}{\lambda_{A,A}\,(\cos\theta)}\right)\right\}}{I_S^{\infty} exp\left(\frac{-d}{\lambda_{S,A}\ cos\ \theta}\right)} \tag{2.19}$$

The angle θ in this equation is the emission angle of the photoemitted electrons and is measured with respect to the surface normal. Factors I_A^{∞} and I_S^{∞} are peak intensities taken from the overlayer and substrate of effectively infinite thickness. The parameters $\lambda_{A,\,A}$ and $\lambda_{S,\,A}$ are the effective attenuation lengths of electrons emerging from the overlayer and the substrate respectively [11]. The effective attenuation length (EAL) is known to differ from the inelastic mean free path (IMFP) due to elastic-scattering which causes the photoelectron signal to decay in a non-exponential manner [12]. This variation from the IMFP value is dependent on the composition of the sample but, in general, changes in physical properties such as an increased density will result in a reduction of the EAL.

For the case of SiO_2 on Si, where the kinetic energy of the substrate and overlayer signals differ by approximately 4 eV the values $\lambda_{A,A}$ and,$\lambda_{S,A}$ are approximately equal and can be replaced by a single term λ [11], making d the subject of the expression equation 2.19 is found

$$d = \lambda\, cos\theta\, ln\left[1 + \frac{\frac{I_A}{I_A^{\infty}}}{\frac{I_S}{I_S^{\infty}}}\right] \tag{2.20}$$

$\frac{I_S^{\infty}}{I_A^{\infty}}$ can be referred to as K [11, 13, 14] leaving;

$$d = \lambda\, cos\theta \ln\left[1 + K\left(\frac{I_A}{I_S}\right)\right] \tag{2.21}$$

As stated earlier, equation 2.20 relates only to situations where the kinetic energy of the substrate and overlayer peaks are comparable. A value for λ can be found in the literature [11]. Thickness calculations based on this method can be achieved using software such as NIST Electron EAL Database [15].

2.8 Synchrotron radiation photoemission

The method of providing increased resolution and surface sensitivity is by using synchrotron radiation to carry out photoemission studies as presented in this thesis. Synchrotron radiation is electromagnetic radiation generated by the acceleration of ultra relativistic (i.e., moving near the speed of light) charged particles through magnetic fields. The radiation produced may range over the entire electromagnetic spectrum, from radio waves to infrared light, visible light, ultra-violet light, X-rays, and gamma rays. It is distinguished by its characteristic polarization and broad featureless wavelength spectrum. The synchrotron radiation emitted by an electron storage ring is an intense spectral continuum, from which photons of the desired energy can be selected by means of a suitable monochromator while the conventional laboratory based x-ray line sources suitable for photoemission emit photons at fixed energy sources. The synchrotron radiation source is linearly polarized while the conventional line x-ray sources are not. However, high resolution synchrotron radiation photoelectron spectroscopy (HRSPES) allows for considerably improved resolution and greater surface sensitivity than conventional XPS.

Synchrotron radiation is characterised by:

- High brightness and high intensity, many orders of magnitude greater than that offered by x-rays produced in conventional x-ray source.

- High brilliance, exceeding other natural and artificial light sources by many orders of magnitude: 3rd generation sources typically have a brilliance greater than 10^{18} photons/s/mm^2/mrad/0.1% BW, where 0.1% BW denotes a bandwidth 10^{-3} ω centred on the frequency ω.

- High collimation, i.e. small angular divergence of the beam

- Low emittance, i.e. the product of source cross section and solid angle of emission is small

- Widely tuneable in energy/wavelength by monochromatisation (sub eV up to the MeV range)

- High level of polarization (linear or elliptical)

- Pulsed light emission (pulse durations at or below one nanosecond, or a billionth of a second)

2.8.1 The ASTRID synchrotron

A schematic diagram of the ASTRID synchrotron in Aarhus, Denmark is shown in Figure 2.11. A linear accelerator is used to inject electrons into a storage ring which is designed to maintain the electron beam circulating in the ring for many hours at a time. Storage rings are typically made up of a series of straight sections connected in a polygon arrangement. The change in momentum of the electron beam as it negotiates the curved sections results in the concentrated emission of synchrotron radiation at these points. The radiation is extracted through a series of beamlines connected to the ring at these points of centripetal acceleration, bringing the radiation to different user stations where it can be used in a range of different analysis techniques.

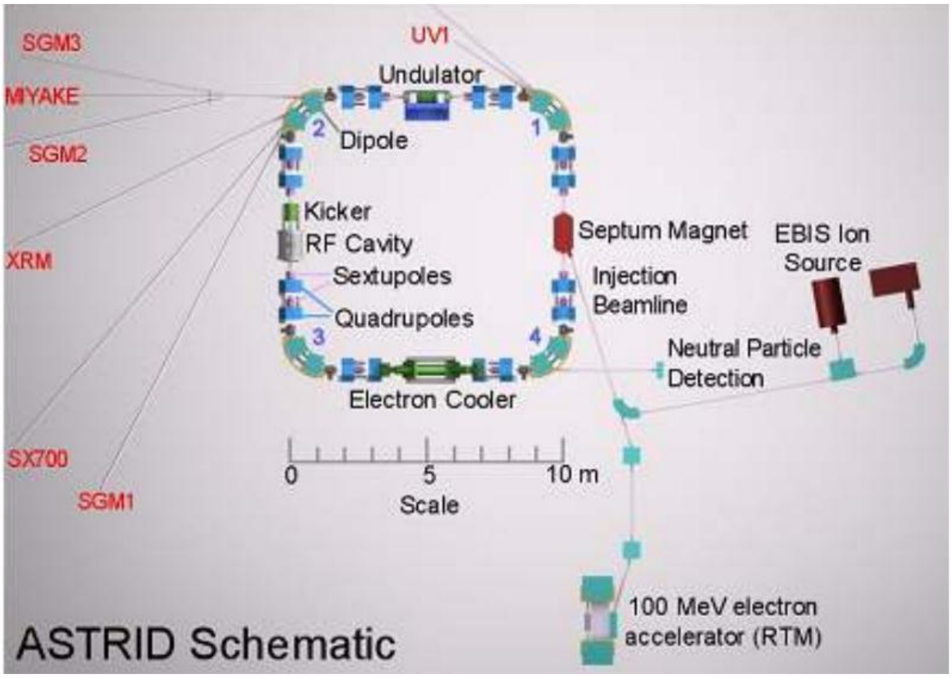

Figure 2.11 Diagram of the ASTRID synchrotron in Aarhus, Denmark

2.9 Electrical Characterisation

The two electrical characterisation techniques used in this study were current-voltage (I-V) and capacitance-voltage (C-V) measurements. Schottky barrier formation between a metal and a semiconductor substrate, with some structures having a thin deposited dielectric interlayer was studies by I-V measurements. Capacitor structures formed by high-k deposition on semiconductor substrates followed by the deposition of an appropriate metal were characterised by C-V measurements. In the experimental setup used, an electrical probe was brought into contact with a metal gate while the back of the sample was in electrical contact with the ‘chuck’ of the probe station.

2.9.1 MOS diode C-V characteristics

Figure 2.12 shows an example of a C-V sweep for an HfO_2 dielectric layer deposited a p-type silicon substrate [16]. When plotting capacitance versus voltage, the capacitance measured on different sized devices can be normalised once the area of the device size is known and quoted as capacitance per unit area. By drawing majority carriers to the semiconductor/insulator interface, the capacitor structure is brought into ‘accumulation’ and the maximum measured capacitance is achieved due to their being the lowest possible physical distance between the charges across the dielectric material. By pushing the majority carriers away from the interface the channel region is said to be in ‘depletion’ and the capacitance drops to a minimum due to the larger distance between the “plates” of the capacitor.

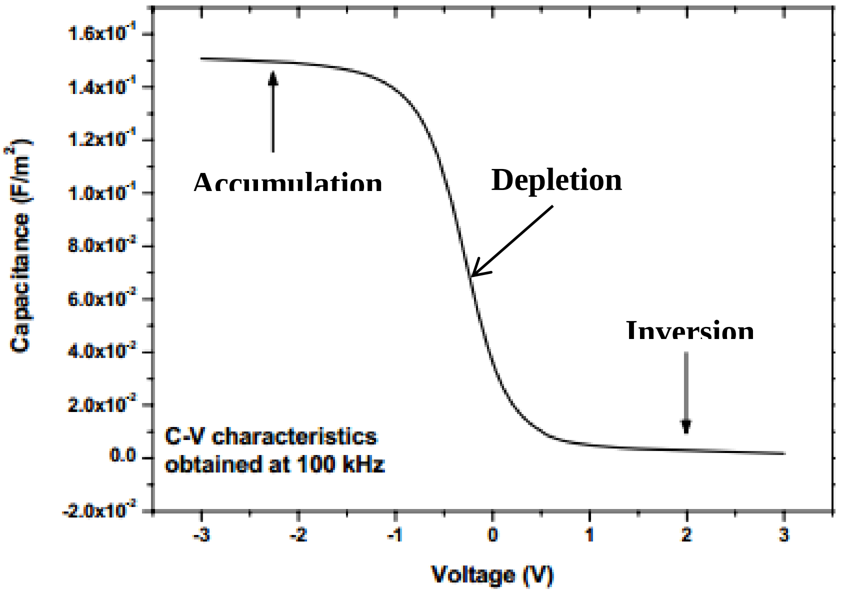

Figure 2.12 Typical C-V characteristics of 12 nm HfO_2 on p-type Si [16].

The concept of accumulation, depletion and inversion within a MOS device can be described using electron energy band diagrams. Initially it is best to consider the idealised case of a perfect MOS device and subsequently discuss the problems caused by real surfaces. Figure 2.13 shows the band diagram for an ideal p-type MOS device, which may be essentially viewed as a parallel plate capacitor.

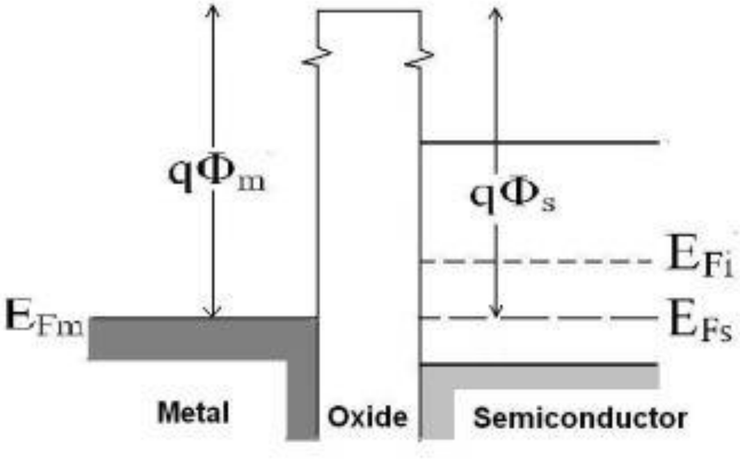

Figure 2.13 Energy band diagram for ideal p-type MOS capacitor

While the work function of a metal is usually defined as the energy required to move an electron from the electron Fermi level (E_{Fm}) to outside the metal, in this case it is more relevant to define a modified work function ($q\Phi_m$) measured from E_{Fm} to the conduction band of the oxide. It should be noted that in this idealised case the metal and semiconductor work functions are taken to be equal ($q\Phi_m= q\Phi_s$) . Given that this is a p-type semiconductor it can be seen that its Fermi level (E_{Fs}) lies close to the valence band and below the intrinsic level (E_{Fi}). This is of some importance to subsequent discussions, as it is the Fermi level position relative to the intrinsic level which defines the conduction properties of the device.

If the polarity of the voltage is changed the Fermi level of the metal is lowered with respect to that of the semiconductor, tilting the oxide conduction band in the opposite direction to that seen previously in Figure 2.14

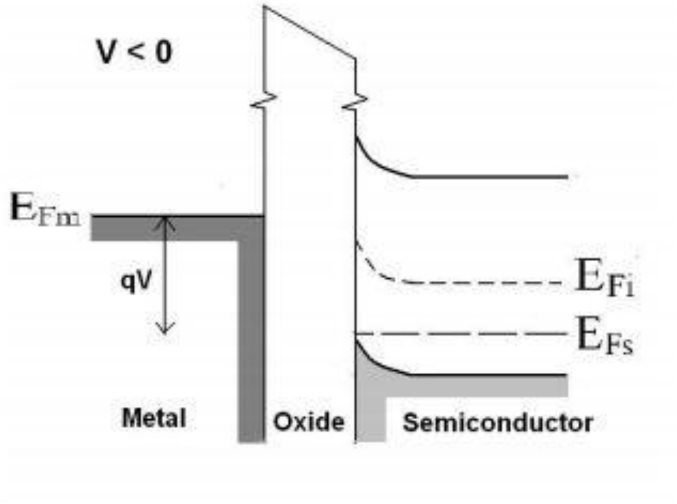

Figure 2.14 Application of a negative voltage on the metal gate causes the accumulation of holes at the semiconductor/oxide interface which results in a maximum capacitance value within the measured C-V profile.

Accumulation in MOS capacitors is evidenced by a maximum capacitance (C_{max}) level in the C-V curve (Figure 2.11). In the ideal case the C_{max} in accumulation should be determined by the dielectric properties of the oxide, allowing the dielectric constant (k) of the oxide to be obtained using the simple parallel plate capacitor equation

$$C_{max} = C_{ox} = \frac{\epsilon_o \, k \, A}{d} \qquad (2.22)$$

where A is the device area, d is the thickness of the oxide and ε_0 is the permittivity of free space.

If the polarity of the voltage is changed, the conduction band and intrinsic Fermi level moves closer to the Fermi level, tilting the oxide conduction band in the opposite direction to that seen previously (Figure 2.15)

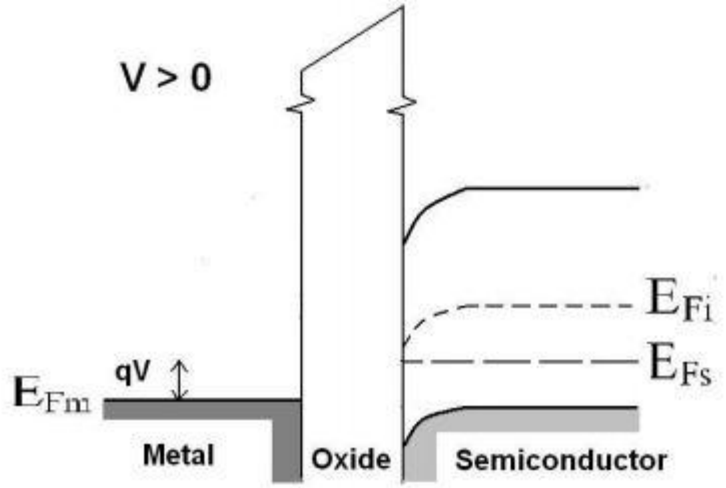

Figure 2.15 Energy band diagram showing depletion in MOS capacitors. Application of a positive voltage depletes the semiconductor surface of majority carriers

This voltage applies a positive charge to the metal plate, and attempts to form a corresponding negative charge at the semiconductor-oxide interface. As electrons are the minority carriers in p-type semiconductors this negative charge is formed by the "depletion" of holes from the region near the surface, which leave behind uncompensated, negatively charged acceptors. The creation of hole/electron pairs forms a depletion region which is analogous to that seen for p-n junction diodes. The formation of this deletion region means that the concentration of holes at the semiconductor surface is reduced. This causes E_i to be lowered closer to E_F, If the strength of this voltage is further increased the bands continue to bend, causing E_i to bend below E_F as shown in Figure 2.16

Now the surface of the semiconductor is inverted. This results in an inversion region at the semiconductor surface which is separated from the p–type bulk by a depletion region. The case of strong inversion occurs when the surface region becomes as strongly n-type as the bulk material is p-type. Therefore, by moving the semiconductor Fermi level with respect to the intrinsic position, a p-type device may be converted into an n-type device (or vice-versa) by simply applying a voltage. Depletion and inversion are shown by a reduction in the measured capacitance of the C-V curve. In the ideal case the minimum capacitance value indicates strong inversion, which occurs at a threshold inversion V_T (Figure 2.12). Thus far the operation of MOS capacitors has been discussed in terms of ideal structures.

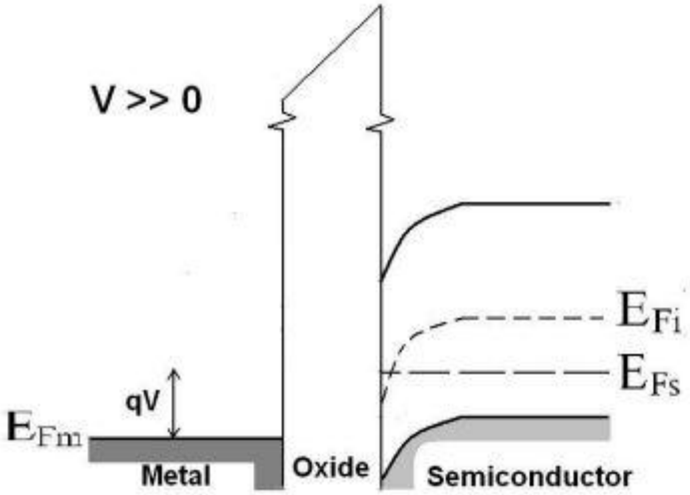

Figure 2.16 Energy band diagram showing depletion in MOS capacitors. Application of a positive voltage depletes the semiconductor surface of majority carriers

In the ideal case, shown in Figure 2.12, it can be seen that no band bending occurs prior to the application of an external voltage. However, factors such as differences in the metal and semiconductor work functions, and the presence of interfacial charge, can result in band bending under equilibrium conditions (V = 0). Therefore, a voltage must be applied in order to return the device to flat band conditions. The voltage required to achieve this is referred to as the flatband voltage (V_{FB}).

Defects at the semiconductor-oxide interface may create a measurable capacitance that may be viewed as another parallel plate capacitor, in series with the oxide capacitance and in parallel with that of the semiconductor. While the measured capacitance in accumulation will still be dominated by the oxide properties, if the density of interfacial defects (D_{it}) is sufficiently large it may contribute to the measured total capacitance during depletion and inversion. This deforms the profile of the C-V curve. C-V characterisation is also commonly used to measure the effects of Fermi level pinning in MOS devices. As shown previously, in order to achieve inversion the semiconductor Fermi level must be moved through the band gap with respect to the intrinsic level. However, the presence of defect energy states within the bandgap may prevent this movement, acting to "pin" the Fermi level. As such, the device may not be able to reach accumulation or inversion or indeed both, depending on the density and energy position of defect states within the bandgap. This is evidenced by a reduction in the difference between the maximum and minimum capacitance values measured from the C-V curve [17]. Therefore, in pinned devices, the C_{min} value may not represent true inversion in the device, and may simply present the lowest level of depletion achievable. Similarly, C_{max} values taken from pinned devices may not represent the dielectric properties of the oxide layer as the Fermi level may not be free to move across the band gap and allow majority carriers to accumulate at the interface. Fermi level pinning is most commonly seen subsequent to metal oxide deposition onto III-V semiconducting materials, and is indicative of high interface state density (D_{it}) and poor interface quality [18,19].

2.9.2 Schottky diode I-V characteristics

One of the most interesting properties of the metal-semiconductor (MS) interface is its Schottky barrier height (SBH). At a metal/n-type semiconductor interface the SBH is the difference between the conduction band minimum and the metal Fermi level. Conversely, for a p-type MS interface, the SBH is the difference between the valance band maximum of the semiconductor and the metal Fermi level as shown in Figure 2.17 (a). In case of p-type semiconductors, when applying a forward bias to a MS-contact (meaning a positive potential on the semiconductor) as shown in Figure 2.17 (b), the potential drop across the interface region results in a reduction in the potential barrier seen by mobile holes flowing from S→M allowing for an exponential increase in current (turn on voltage) as shown in Figure 2.17. Applying a reverse bias as shown in Figure 2.17 (c), which increases the potential barrier across the MS interface, results in a exponentially reduced current in the S→M direction. Furthermore since the SBH or Φ_B

is not influenced by the reverse applied bias there is always a constant cross barrier M→S electron flow. The current flow in a Schottky diode is determined primarily by the height of the Schottky barrier [20, 21]. From a purely theoretical point of view, low reverse leakage current could be achieved by increasing the barrier height however, in practice this is not easy to do. The Schottky barrier height depends on the work function of the metal.

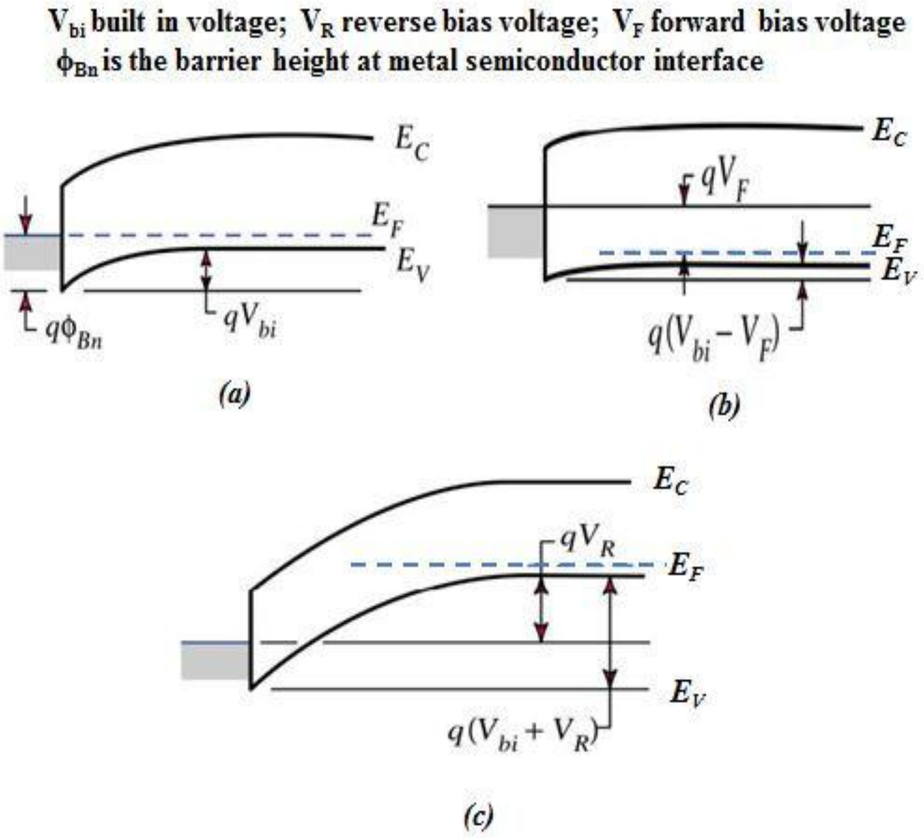

Figure 2.17 Energy band diagram of metal/p-type semiconductor (a) thermal equilibrium, (b) positive bias and (c) reverse bias.

The current-voltage J-V characteristics obtained for the Schottky devices fabricated on passivated p-type substrates are shown in Figure 2.18.

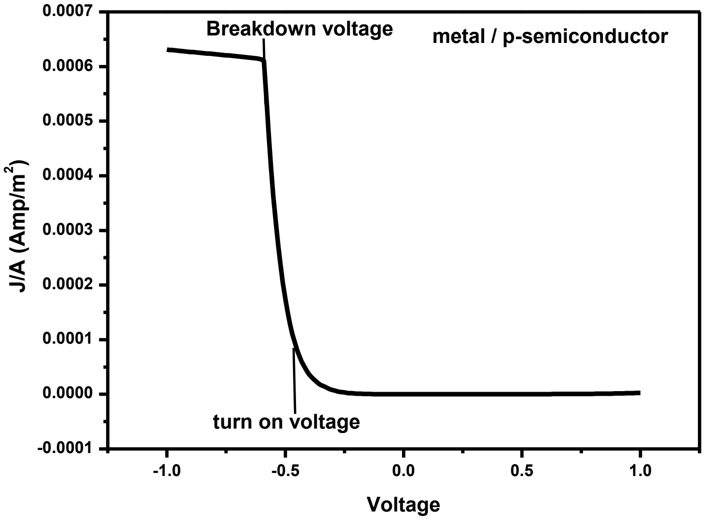

Figure 2.18 J-V characteristics of Al-InGaAs Schottky diode

The thermionic emission current is given as

$$J = A^{*}T^{2}\exp\left(\frac{-q\phi_B}{K_B T}\right) * \exp\left(\frac{qV}{nK_B T} - 1\right) \tag{2.22}$$

Where A^* is the Richardson constant, T is the temperature, q is the electron charge, $Ø_B$ is the effective Schottky barrier height (SBH), K_B is the Boltzmann constant, n is the ideality factor (≤ 1), and V is the applied forward voltage. In this study Schottky diode has been fabricated with and without passivation to study the density of oxide–semiconductor interface states by measuring the SBH.

2.10 Vacuum system description

Figure 2.19 is the XPS system used in these studies and consists of a stainless steel vacuum chamber with oil diffusion pumps capable of attaining ultra-high vacuum (UHV), a twin anode x-ray source, an electron lens, an electron energy analyser and detection system and an external computer system to display the detector output. The system consists of three vacuum chambers: a small load lock maintained at 10^{-2} mbar for the introduction of multiple samples, a preparation chamber at 10^{-7} mbar for in-situ anneals up to 500°C, and an analysis chamber at 10^{-10} mbar equipped with a twin anode X-ray source (Mg and Al), and a VG CLAM electron energy analyser with a triple channeltron detector. The system is pumped using diffusion pumps backed by rotary pumps and was used as a dedicated XPS analysis system, as no surface preparation or thin film deposition was carried out in this chamber.

Figure 2.19 XPS analysis chamber

A graphic representation of the X-ray source is shown in Figure 2.20.

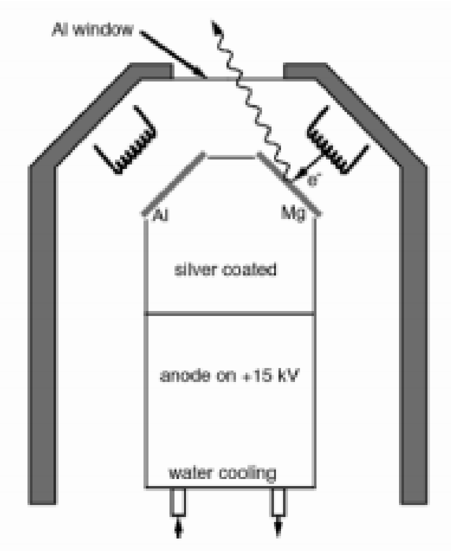

Figure 2.20 Diagram showing the operation of a dual anode X-ray source [22]

The x-ray source consists of a silver, anode target coated with thin films of aluminium and magnesium that can be selected independently. Electrons accelerated through high voltage (10 - 15 kV) bombard the Mg and Al anodes creating the characteristics x-rays on a continuous Bremstrahlung energy background. The Bremshtralung radiation produced is partially removed by placing an Al foil (~ 2 μm thick) at the exit aperture of the X-ray source, while radiation which is not removed adds to the background of the spectrum. The anode source must be water cooled during operation in order to avoid damage due to excess heating. X-rays are emited at peak intensities from the respective sources (Mg Kα = 1253.6 eV and Al Kα = 1486.6 eV). While the use of an X-ray monochromator can reduce the line width to ~ 0.3 eV, the non-monochromated system used in these studies has a line width of ~ 0.7 eV for the Mg source and ~ 0.85 eV for the Al source [2].

X-rays striking the sample surface result in the emission of photoelectrons, as described earlier in section 2.1. These photoelectrons are collected and analysed using a VG CLAM electron energy analyser, similar to that schematically shown in Figure 2.16. The electrostatic field generated by a system of two electron lenses acts to successively focus electrons to a point within the analyser system [20]. As the kinetic energy of the electrons greatly affects the focal point of the lens system, electrons first pass through a fine mesh grid which is held at a negative potential known as the retarding voltage. This restricts the kinetic energy of the electrons to a range called the pass energy, which is in this study was 20 eV. Given that the kinetic energy of electrons emitted from the sample commonly varies by up to ~ 1100 eV, the retarding voltage applied to the grid must be continually changed in order to ensure that all electrons have the same pass energy which is essential to achieve uniform resolution across the spectrum. Electrons focused by the lens system then enter a hemispherical electron energy analyser, as shown in Figure 2.21. The voltage applied to the two hemispheres is adjusted to ensure that only electrons which enter the analyser with the correct pass energy are allowed through the analyser to be detected and amplified in the channeltron. Electrons which enter with kinetic energies different from the pass energy are lost to collisions within the hemispheres, and as such do not contribute to the measured photoelectron signal.

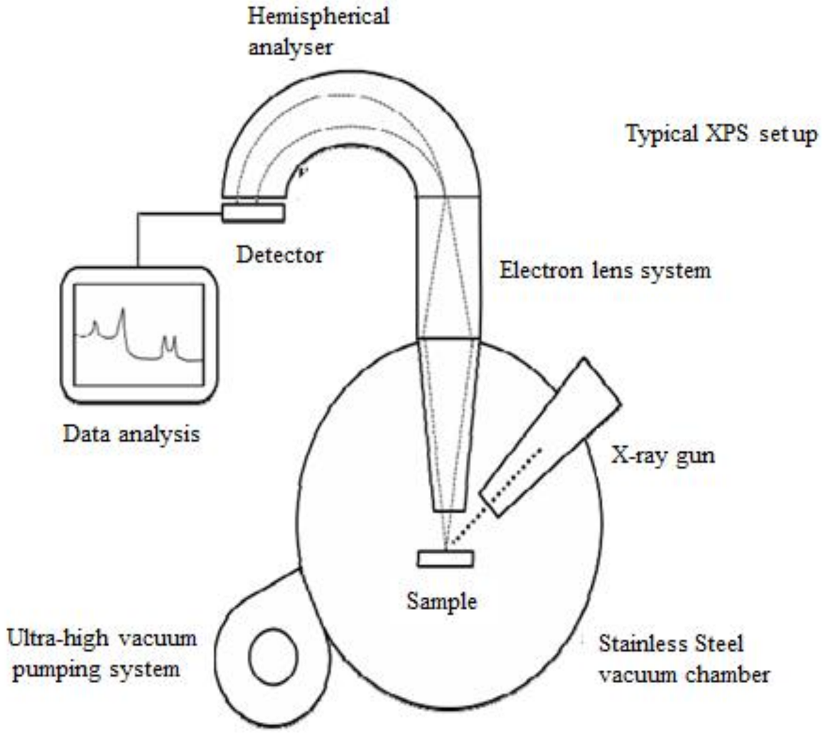

Figure 2.21 Schematic diagram of an XPS analysis system [23]

2.11 Synchrotron vacuum system at ASTRID Aahrus, Denmark

The vacuum system used at the SX700 beamline at the ASTRID Synchrotron in the University of Aarhus, Denmark, for the photoemission studies presented in Chapter 3, 4 and 5 is shown in Figure 2.22. The ultrahigh vacuum system consists of a preparation chamber (5 × 10^{-10} mbar) and an analysis chamber where a base pressure of better than 10^{-10} mbar was routinely achieved after a bake out procedure with pumping carried out by a turbo molecular pump backed by a rotary roughing pump. Sample temperatures up to 1000 °C were measured by calibrating a thermocouple attached directly to the sample holder. Therefor the system is very useful for high temperature annealing measurements. Deposition can also be carried out on this system by installing thermal evaporation sources.

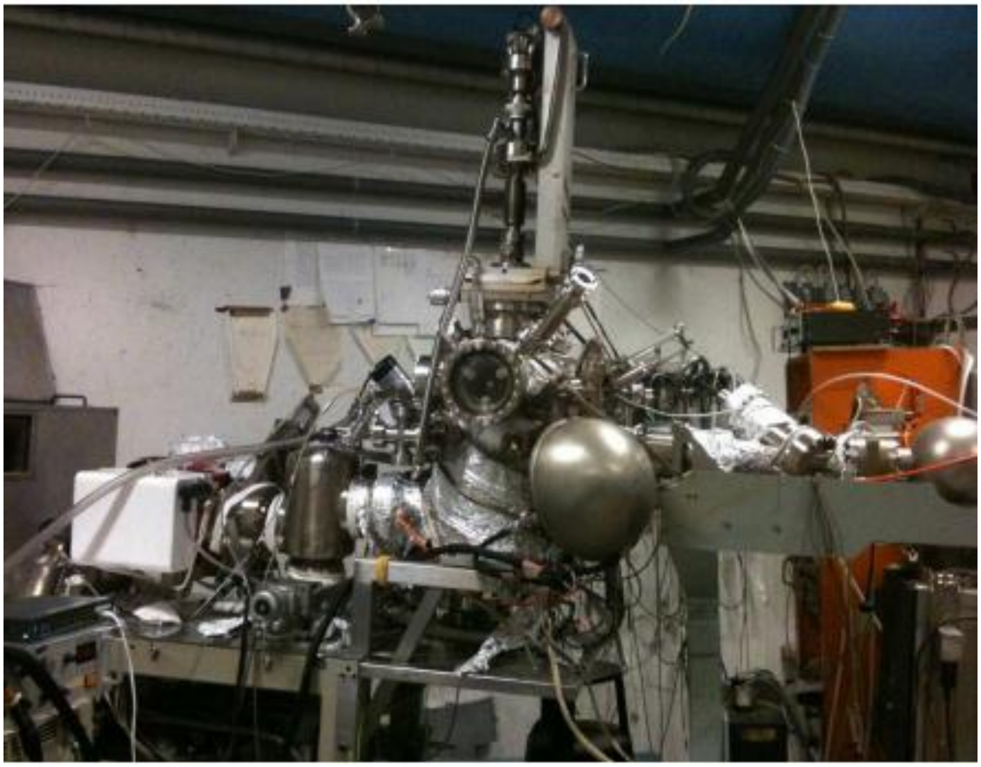

Figure 2.22 Vacuum end station on the SX700 beamline at the ASTRID synchrotron in Aarhus, Denmark

2.12 Deposition techniques

2.12.1 Atomic layer deposition

Atomic layer deposition (ALD) is a thin film deposition technique that is based on the sequential use of a gas phase chemical process. ALD is a chemical vapour deposition process distinct from the typical CVD process in that it is a strictly layer by layer growth process with reactions taking place at the sample surface. Unlike CVD, there is less need of reactant flux homogeneity, which gives large area (large batch and easy scale-up) capability. The surface–controlled reactions give rise to excellent conformality which can produce thin dense and smooth films in a highly reproducible fashion. These advantages make the ALD method attractive for microelectronic device manufacture for future generations of integrated circuits

Figure 2.23 shows a schematic representation of Al_2O_3 ALD deposition. Starting with a clean surface (oxide and contaminant free as much as possible) usually hydroxyl terminated, during the first pulse of trimethyl-aluminium (TMA), it reacts with hydroxyls groups on the substrate in one of two ways. The aluminium can bond to one oxygen atom and remain bonded to two CH_3 groups liberating one hydrogen atom from the hydroxyl and one CH_3 which forms methane (CH_4). Alternatively, the aluminium can also bond to two oxygen atoms and remain bonded to only one CH_3 group. This liberates two hydrogen atoms and two CH_3 groups which form two methane molecules. This process continues until the whole surface is covered with a monolayer of methylated Al atoms such that no more are able to interact with the surface. Any surplus TMA along with the methane is then purged by nitrogen and the oxygen containing water pulse is then injected. During this pulse, the water reacts with any CH_3 groups that are still bonded to aluminium resulting in the formation of Al-O bonds, with the released hydrogen bonding to CH_3 This results in the formation of methane which is then removed along with any surplus water by another nitrogen pulse. This complete sequence is referred to as one ALD cycle. This process is repeated until a film of the desired thickness is deposited.

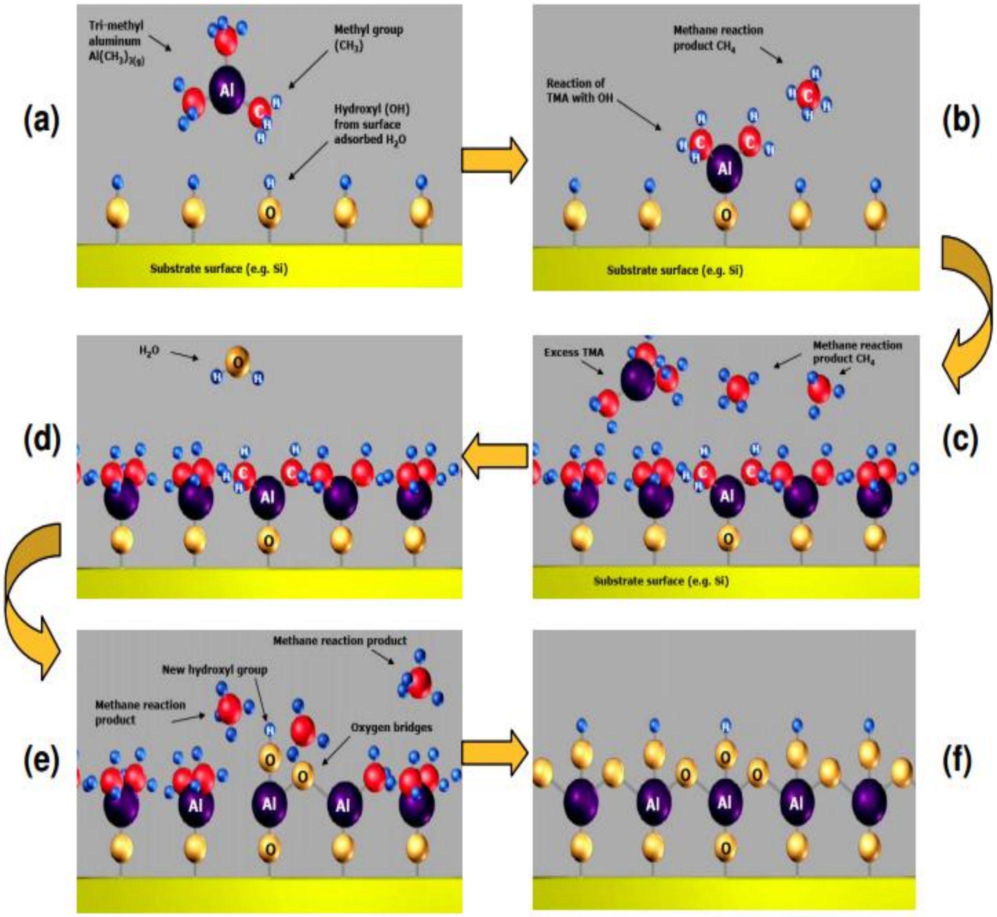

Figure 2.23 Graphic representation of one full ALD cycle starting with (a) a bare substrate, (b) introducing an organo-metallic precursor, (c) saturating the surface with one organo-metallic layer, (d) purging remaining gas and introducing an oxygen source, (e) reaction to form a metal oxide and (f) formation of one atomic layer of metal oxide [24]

2.12.2 Thermal evaporation

In this process a low melting point source material is contained in a tantalum pouch which is wrapped in a tungsten or tantalum filament, and resistively heated by passing a current through the filament [25]. This thermal deposition method is appropriate for metals with low melting temperatures (e.g. Mg), and the use of high purity (typically >99.9%) source material results in the deposition of highly pure thin films. Metal oxide films were grown by the evaporation of metals in an oxygen background pressure (5 × 10^{-7} mbar) which allows the metal to oxidise on the sample surface and form metal oxide films, which were measured to be stoichiometric using conventional XPS. In this study, in-situ deposition of MgO films on InGaAs was achieved by evaporating metallic Mg in an oxygen partial pressure using this deposition method.

2.13 Surface preparation methods

For III-V semiconductors surface cleaning is an important step in device fabrication as exposure to ambient conditions results in the formation of oxides and carbon based impurities. Since the quality of the interface between the gate dielectric insulator and the InGaAs substrate is of critical importance, ensuring that the insulator layer is grown on a clean substrate is vital. In this study the organic cleaning method used before XPS studies consisted of successive 1 minute dips in acetone, methanol and isopropyl alcohol (IPA), with samples being subsequently dried in an N_2 gas flow before being loaded into the vacuum vessel. The different chemical cleaning methods used in this work to remove the oxides from the InGaAs substrate (e.g. 2 stage etch, HCl, sulphur passivation) will be outlined in subsequent chapters.

2.14 Sulphur Cell [26]

A schematic illustration of the electrochemical sulphur source is shown in Figure 2.19. The cell was prepared from a compressed pellet of powders of silver (Ag), silver iodide (AgI) and silver sulphide placed between two sheets of platinum mesh. The pellet sits into the glass chimney with the electrical contacts made to the front and back end of the pellet. The glass chimney is surrounded by a sheet of tantalum, which is heated radiatively by passing a suitable current (~ 6 A) through the exterior tungsten wire which is wrapped into a helical coil. The hot tantalum sheet then uniformly heats the pellet. When heated to approximately 200^0C an electrochemical potential of 200 mV exits across the cell.

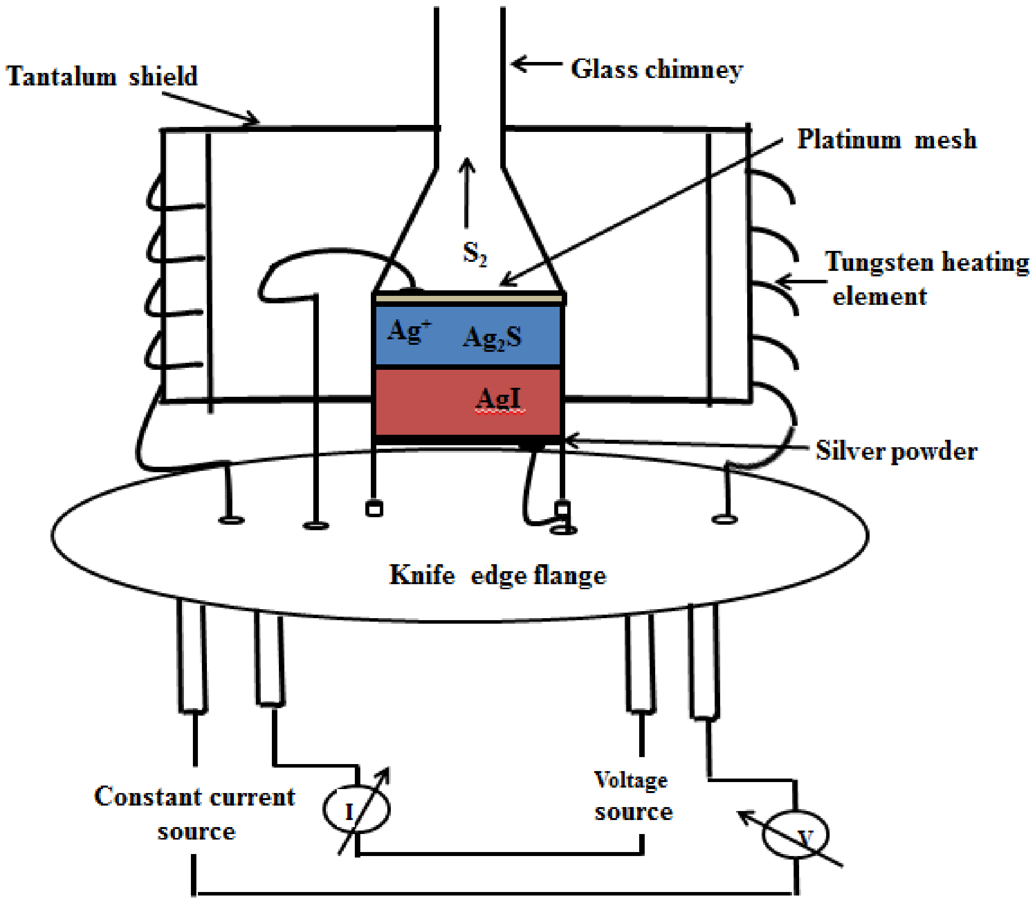

Figure 2.19 A schematic illustration of the electrochemical sulphur source

As silver iodide becomes an ionic conductor at this temperature, applying a suitable negative bias to the back of the cell under constant current conditions results in Ag^+ ions flowing from the silver sulphide through the silver iodide to the back silver electrode. Molecular sulphur effuses from the throat of the chimney in direct relation to the Ag ion current flowing in the cell in a controlled fashion.

2.15 References

[1] D. P. Woodruff and T. A. Delchar, Modern Techniques of Surface Science Cambridge Solid State Science Series (1986)

[2] J. C. Vickerman, Surface Analysis: The Principle Techniques, J. C. Vickerman, Ed. Wiley (1997)

[3] L. C. Feldman and W. Meyer, Fundamentals of surface and thin film analysis Elsevier Science Publishing Co. Inc. (1986)

[4] J. F. Moulder, W. F. Stickle, P. E. Sobol, and K. D. Bomden, Handbook of X-Ray Photoelectron Spectroscopy, J. Chastain, Ed. United States of America: Perkin-Elmer Corporation, Physical Electronics Division, (1992), XPS Handbook

[5] D. Brigggs and J. T. Grant, Surface Analysis by Auger and X-ray Photoelectron. IM Publications (2003) Chichester, UK

[6] http://www.chem.qmul.ac.uk/surfaces/scc/

[7] Casey, Patrick (2010*)* Growth and Characterisation studies of MgO and Mg silicate dielectric layers on Si and InP surfaces. PhD thesis, Dublin City University Ireland

[8] http://www2.cemr.wvu.edu/~wu/mae649/xps.pdf

[9] M. P. Seah and S. J. Spencer, "Ultrathin SiO2 on Si II. Issues in quantification of the oxide thickness ," Surf. Interface Anal., 33, 640 (2002)

[10] D. Briggs and M. P. Seah, Practical Surface Analysis: Volume 1, Auger and X-ray Photoelectron Spectroscopy. Wiley (1990)

[11] R. G. Vitchev, et al., Appl. Surf. Sci., 235, 21 (2004)

[12] A. Jablonski and C. J. Powell, Surface Science Reports, 47, 33 (2002)

[13] R. G. Vitchev, et al., Journal of Electron Spectroscopy and Related Phenomena, 149, 37, (2005)

[14] F. J. Himpsell, F. R. McFreely, A. Taleb-Ibrahimi, J. A. Yarmoff, and G. Hollinger, Phys. Rev. B, 38, 6084 (1988)

[15] NIST Database. [Online]. http://srdata.nist.gov/xps/

[16] McDonnell, Stephen (2009) Spectroscopic characterisation of high dielectric constant materials on semiconducting surfaces. PhD thesis, Dublin City University Ireland

[17] Z. Fu, S. Kasai, H. Hasegawa, Applied Surface Science 190, 298 (2002)

[18] M. Passlack, J. K. Abrokwah, R. Droopad, Yu Zhiyi, C Overgaard, S. In Yi, M. Hale, J. Sexton, A.C. Kummel, Electron Device Letters, IEEE 23, 9, 508 (2003)

[19] J. Robertson, Reports on Progress in Physics, 69, 327(2006)

[20] Moongyu Jang and Junghwan Lee, ETRI Journal, 24, 6, 455 (2002)

[21] M.P. Lepselter and J.M. Andrews, “Ohmic Contacts to Silicon,” The Electrochemical Society Symposium Series, New York, 159 (1969)

[22] Twin anode x-ray source. [Online]. http://eapclu.iap.tuwien.ac.at/~werner/images/t_exp_photo.gif

[23] http://iramis.cea.fr/Images/astImg/508_2.jpg

[24] R. L. Puurunen, Appl. Surf. Sci. 245, 6 (2005)

[25] J.S. Corneille, J.W. He, D.W. Goodman, Surf. Sci., 306, 269 (1994)

[26] W. Heegemann, K Miester, E. Bechtold, K. Hayek, Surface 49, 161(1975)

Chapter 3

High resolution synchrotron radiation based photoemission studies of the sulphur treated InGaAs surface

3.1 Introduction

Controlling the interface properties of InGaAs with dielectric materials is one of the major challenges for the future of high speed electronic devices. Poor electronic properties of the InGaAs/oxide interface in metal oxide semiconductor (MOS) devices is attributed to the presence of a high density of defect states D_{it} which pin the Fermi level and consequently make it difficult to invert the semiconductor. Therefore there is need for some kind of passivation to reduce defect states as described in chapter one. In next section 3.1.1 passivation methods reported in the literature for InGaAs will be outlined as well the methods used in this study.

3.1.1 InGaAs surface passivation

In the specific case of InGaAs various surface preparation methods are currently under investigation, including wet chemical approaches [1-5], thermal vacuum annealing [6-9], As-capping and decapping [10-13], silane and ammonia passivation [15], exposure to H-plasma cleaning and atomic H exposure to molecular species [15,16], including H_2S [17]. In addition, surface passivation strategies need to be developed which prevent re-oxidation of the surface following ambient exposure. In recent years sulphide passivation from solutions has led to the development of alternative passivation in which $(NH4)_2S$ solutions were found to be most effective in reducing the surface state densities [18-20]. However, relative to GaAs and InP, the details on the surface passivation of InGaAs are less well established. Further studies can help to identify the common factors and trends in the sulphur based passivation of InGaAs surfaces as a way of developing the most effective method for device fabrication. Hence, understanding of the chemical passivation performed by the in-situ dry sulphur and wet ex-situ chemically sulphur treated surfaces, and their thermal stabilities at higher temperature need to be addressed. However, despite this breadth of work, the underlying role of sulphur in acting as a surface passivant is not fully understood.

Therefore the principal aim of this chapter is to characterise the effects of in-situ and ex-situ sulphur passivation of InGaAs surfaces on the surface chemical composition.
The focus of this chapter is divided into four sections:

- Preparation of the atomically clean InGaAs surface and thermal stability studies of this surface at high temperature.
- In-situ gaseous sulphur passivation of the atomically clean InGaAs surface and thermal stability study.
- Ex-situ sulphur (ammonium solution based) passivation of the native oxide covered InGaAs surface and thermal stability study.
- Comparison between the different surface preparations in terms of high temperature thermal stability.

The main technique used in this study was high resolution synchrotron radiation based photoemission spectroscopy (HRSPES). Photon energies of 69 eV and 92 eV were chosen for the In 4d/Ga 3d and As 3d core level spectra, respectively, to give comparable electron escape depths and high surface sensitivity, as photoemitted electrons from both core levels will have kinetic energies of approximately 50 eV thereby maximizing surface sensitivity. The photoionization cross section for the Ga 3d at 69 eV photon energy is significantly smaller than for the In 4d core level. Acquiring these two closely spaced peaks at a photon energy of 130 eV reversed the relative intensities due to changes in cross sectional effects making it easier to identify sulphur and oxygen bonding interactions with gallium. Spectra are also recorded at photon energies 105 eV and 300 eV to investigate the variation in the peak intensities with incident photon energy. This is illustrated in Figure 3.1 in the raw data of In 4d and Ga 3d peak at three different photon energies of 69 eV, 130 eV and 300 eV. These intensity changes assist in the deconvolution of the various spectra as it permits a more accurate identification of the component peaks by changing their relative intensities.

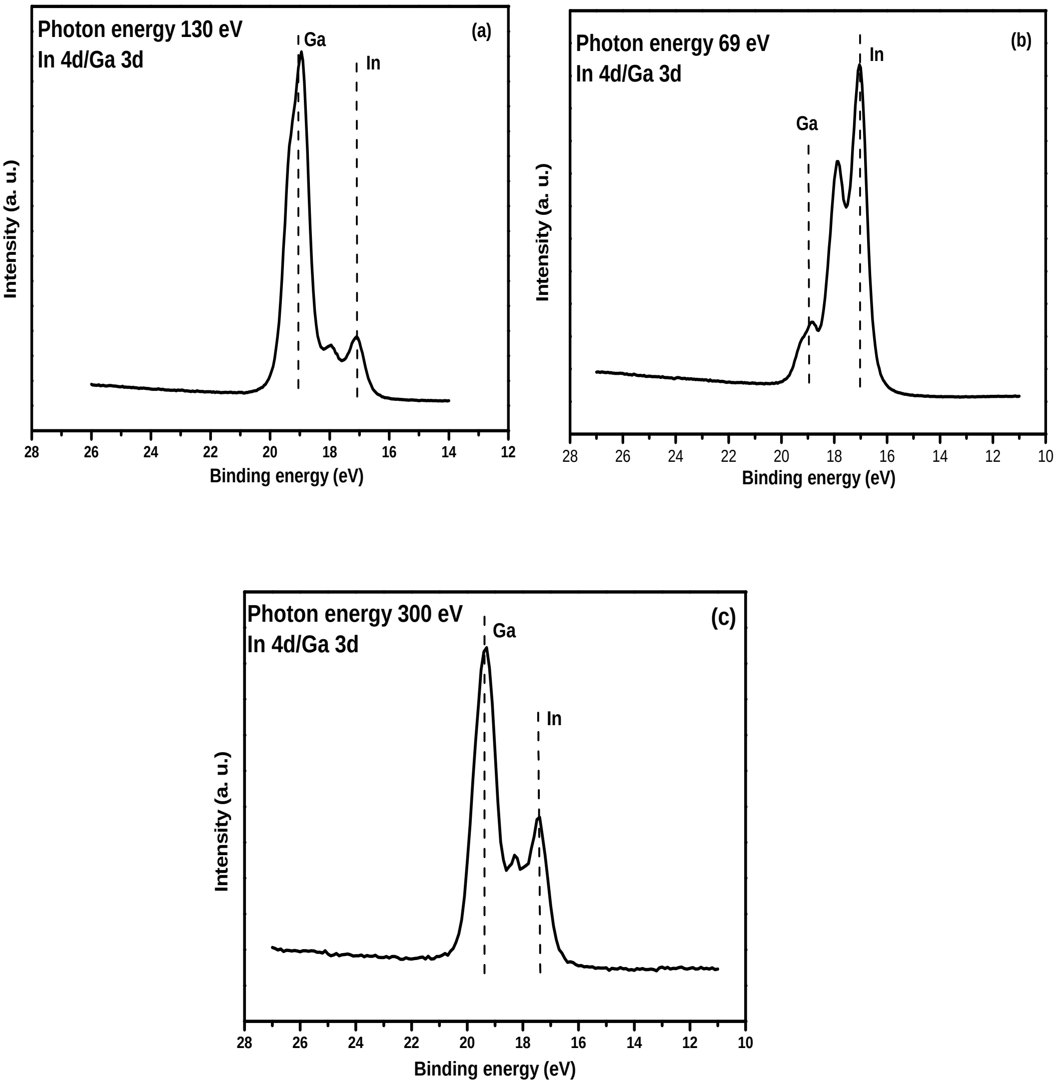

Figure 3.1 shows the photoemission spectra for In 4d/Ga 3d core levels for clean InGaAs surface at different photon energy (a) 69 eV, (b) 130 eV and (c) 300 eV highlighting the change in the relative intensity due to photo-ionisation cross-sectional effects

In the first section of this chapter, atomically clean InGaAs surfaces were prepared by desorbing a protective arsenic cap and this surface was studied by a high resolution synchrotron radiation based photoemission. A subsequent systematic study of in-situ dry sulphur deposition and thermal anneal of this InGaAs surface was then carried out on both n and p-type InGaAs and resultant changes in the surface chemical composition, Fermi level position and work function were recorded.

3.2 Preparation of atomically clean InGaAs surface by thermal desorption of a protective As cap

3.2.1 Sample preparation

The soft x-ray photoemission experiments were carried out on the SX700 beam line at the Astrid synchrotron in the University of Aarhus in an ultrahigh vacuum (UHV) system which had a base pressure of $5\text{x}10^{-10}$ mbar. Two 100 nm As capped samples, 0.5 μm thick p-type Be doped $In_{0.53}Ga_{0.47}As(100)$ epilayer ($5\text{x}10^{17}$ cm^{-3}) and 0.5 μm thick n-type Si doped $In_{0.53}Ga_{0.47}As(100)$ epilayer ($5 \text{ x } 10^{17}$ cm^{-3}) lattice matched to InP substrates, were secured to a molybdenum holder before being loaded into the vacuum system. Samples were decapped by annealing at 410 °C for 30 minutes and allowed to cool to room temperature prior to acquiring spectra. After removal of the As cap and the acquisition of clean surface spectra, the sulphur deposition was carried out at room temperature by exposing the surfaces to a beam of molecular sulphur for 30 minutes from an electrochemical cell [21]. Photoemission spectra were subsequently acquired for all core levels following thermal anneals at 400 °C, 480 °C and 530 °C. The spectra were curve fitted using Voigt profiles composed of Gaussian and Lorentzian line shapes and using a Shirley-type background. The reference fitting parameters for different core levels were acquired from the atomically clean surfaces and these were used to curve fit the InGaAs spectra following the changes induced by the sulphur deposition and anneal. The use of AAnalyzer fitting software for the analysis of the photoemission spectra attained after these thermal and chemical changes to the oxidation states allows for simultaneous fitting of up to 10 spectra at one time, ensuring the maximum correlation of the fitting parameters possible between all the spectra. It systematically applies any variation in the fit parameters seen to develop in one spectra to all the others in the series so that the highest level of consistency possible between them collectively is attained. The fitting procedure was an iterative process whereby all peaks were fitted concurrently with peak widths initially fixed to the values determined from the decapped sample. The peak width of all oxide peaks were allowed to vary as the level of oxide present changed as a result of the various chemical and thermal processes. Both Gaussian and Lorentzian contributions to the line shape were correlated as well as the peak separation from the bulk component. Confidence in the peak fitting comes from the adoption of this systematic approach in combination with a realistic understanding of what surface chemistry should occur, which has been determined from studies of binary III-V materials such as GaAs and InP. A Shirley type background was employed for all peaks which was modified to account for the secondary electron cascade background at low kinetic energy for certain SRPES spectra where the electrons were emitted with low KE. The residual (number of counts by which the fit differs from the actual experimental data), was required to be within the noise of the data with fit error being less than 3% of the experimental counts. In addition to using the residuals and the $\chi 2$ measures for fit accuracy, a rigorous analysis of all relevant spectral regions (As 3d, Ga 3d, O 1s, In 4d) is performed to ensure a self-consistent analysis. The final criterion for the peak synthesis analysis is that any state identified within the spectral envelope must be explained in terms of the electronegativites of possible bonding arrangements. Initially the spectra were fitted with the minimum number of peaks and additional peaks were only added when it was clear that the spectra could not be fitted without their incorporation after investigating variations in peak widths and positions.

The curve fitting parameters used for the As 3d core level included a doublet ratio of 0.66, a spin orbit splitting of 0.70 eV and the FWHM of the bulk peak was 0.70 eV which was composed of a Gaussian contribution of 0.64 eV and Lorentzian value of 0.07 eV. For In 4d and Ga 3d peaks, doublet ratios of 0.66 were also used, doublet splitting of 0.87 eV (In) and 0.44 eV (Ga), with Gaussian contributions of 0.54 eV and 0.48 eV for In and Ga, respectively and Lorentzian value of 0.20 eV for both peaks. These values were then used throughout the study for the bulk component peaks so that any variations from these parameters would be indicative of changes in the bonding environment.

3.2.2 Atomically Clean InGaAs Surface

The in-situ synchrotron studies of the 100 nm arsenic capped InGaAs surface confirmed the presence of an elemental arsenic overlayer on the substrate. The As 3d peak acquired at a photon energy of 92 eV shown in Figure 3.2 (a) at a binding energy of 41.6 eV confirms the presence of the elemental As cap with no evidence of arsenic oxide which are found at higher binding energies (43-46 eV) [22]. This measurement

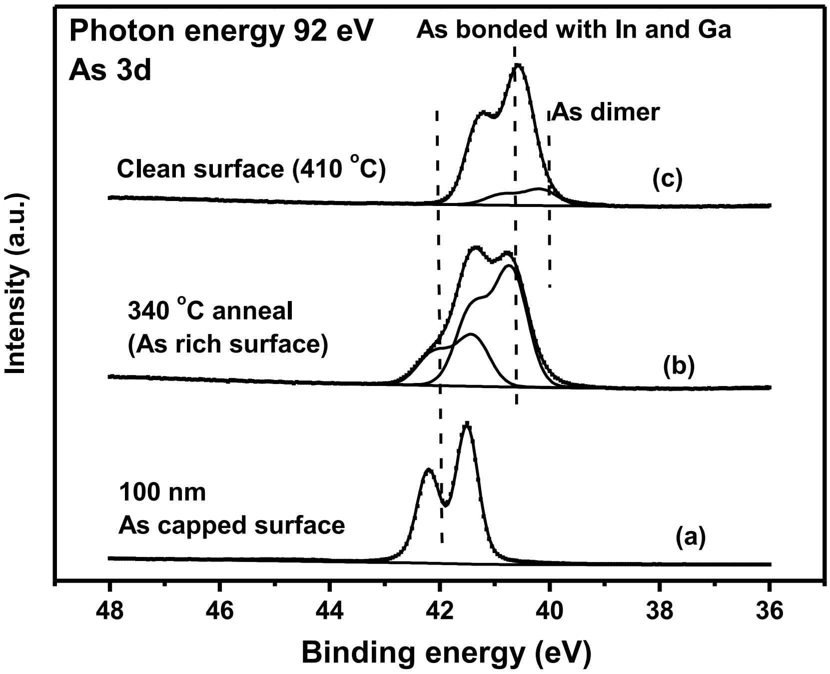

Figure 3.2 Photoemission spectra of As 3d peak acquired at a photon energy of 92 eV of the (a) 100 nm As capped surface (b) annealed at 340 °C showing evidence of elemental arsenic and (c) the atomically clean surface annealed at 410 °C

shows that the As capped surface has not oxidised in the 15 minutes taken to load the samples into the vacuum chamber. The spectra shown in this section are for the p-doped sample. The As cap layer was initially thermally desorbed at 340 °C which removed a substantial amount of the cap. Two component peaks were now necessary to peak fit the As 3d spectrum as shown in Figure 3.2 (b), one component at 40.75 eV binding energy was assigned to the substrate As and the other peak at 41.45 eV was assigned to residual elemental arsenic on the surface. Figure 3.2 (c) shows the As 3d core level spectra acquired at 92 eV, following the removal of the As cap at 410 °C. The As 3d peak can be curve fitted with a bulk As component and an As dimer component shifted by 0.50 eV to lower binding energy in agreement with previous studies [21, 23]. Decapping of InGaAs at this temperature has been reported to result in an arsenic terminated surface [12]. No In 4d /Ga 3d peak was observed on the 100 nm As capped InGaAs surface while Figure 3.3 shows the In 4d/Ga 3d core level spectra acquired at 69 eV, following the removal of the As cap at 340 °C and 410 °C anneals. The core level peaks were curve fitted with an In bonded with As and Ga bonded with As peaks separated by 1.80 eV.

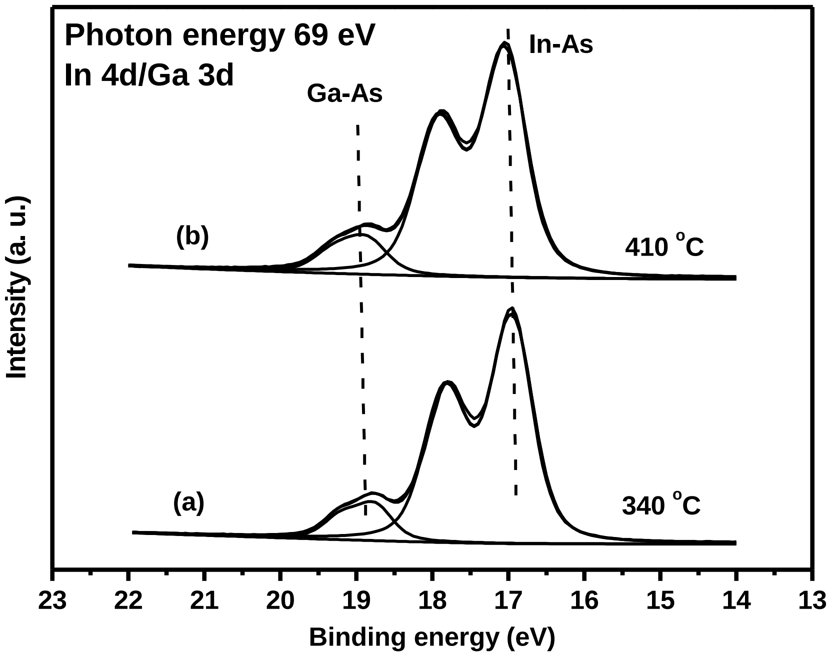

Figure 3.3 Photoemission spectra of the raw data of In 4d/Ga 3d peak acquired at a photon energy of 69 eV of the (a) annealed at 340 ^{o}C (b) atomically clean surface annealed at 410 ^{o}C

3.2.3 Thermal annealing of atomically clean surface at high temperature

In this study atomically clean InGaAs surface was annealed up to high temperature to quantify the effects of high temperature annealing on the surface chemical composition. As 3d spectra at a photon energy of 92 eV and In 4d/ Ga3d spectra at a photon energy of 130 eV and 300 eV were acquired at thermal anneals up to 560 ^{o}C. Normalised spectra of As 3d following thermal anneals are shown in Figure 3.4 and illustrate that no change in the peak shape profile is observed.

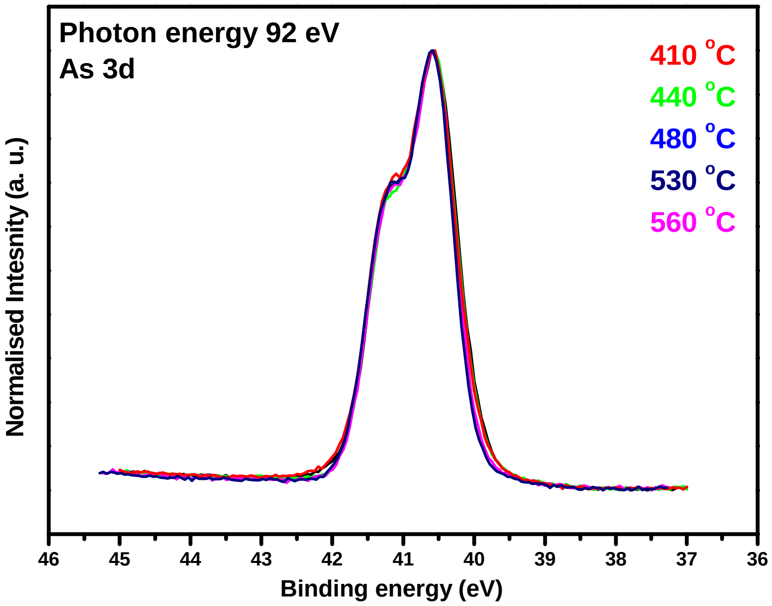

Figure 3.4 Normalised As 3d photoemission spectra acquired at a photon of energy 92 eV during the thermal annealing sequence showing no change in the peak profile

Curve fitted As 3d spectra at a photon energy of 92 eV are shown in Figure 3.5 for the 410 ^{o}C (clean surface), 530 ^{o}C and 560 ^{o}C anneals. The two peak fit is required to curve fit the spectra one is due to bulk As-Ga signal at 40.60 eV and the other is related to the presence of a state at 40.10 eV or -0.50 eV from the bulk peak. This lower binding energy peak is generally reported due to As-As dimer bond formation at the surface [21, 23]. A model has been proposed by Robertson [24] which describes the defect density of the GaAs and InGaAs surfaces in terms of Ga and As dangling bonds at the conduction and valence band edges which would support the assignment of these peaks. The arsenic intensity as a function of anneal is shown in the histogram in Figure 3.5 (b) calculated from the curve fitted peak areas. It is clear from the histogram that no change in the arsenic intensity is observed following thermal anneals, however following the high temperature anneals there is a reduction in the arsenic dimer signal as shown in Figure 3.5 (b) reflecting the loss of the arsenic termination layer at these high temperatures.

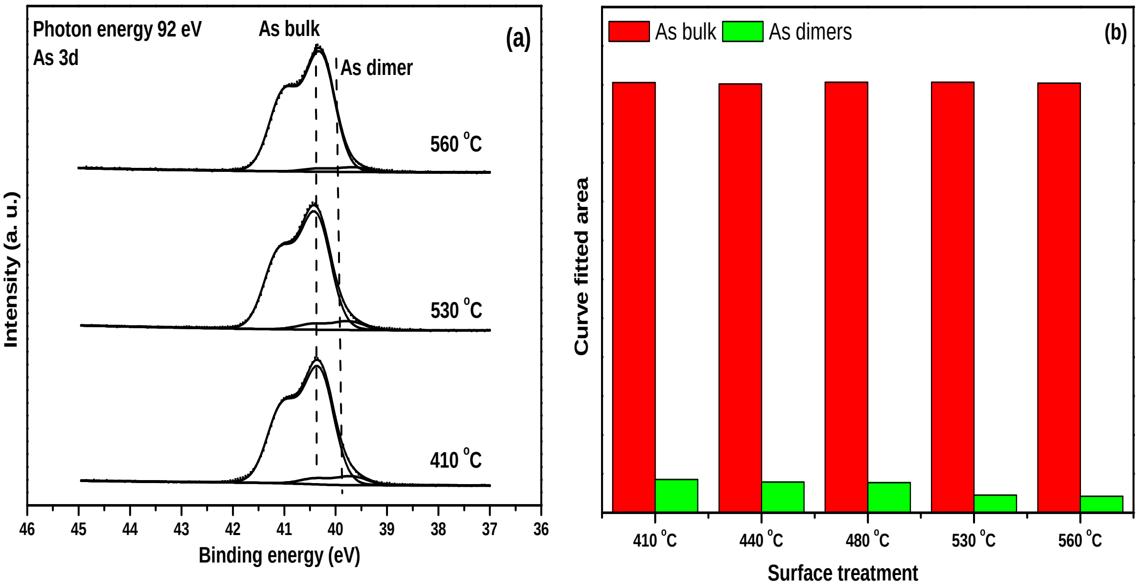

Figure 3.5 (a) Curve fitted As 3d spectra at a photon of energy 92 eV at 410 ^{o}C, 530 ^{o}C and 560 ^{o}C (b) curve fitted area showing the As intensity and As dimer signal as a function of thermal anneals.

Curve fitted spectra for the In 4d/ Ga 3d core levels at photon energies of 130 eV and 300 eV are shown in Figure 3.6 (a) and (b) for the clean surface (410 ^{o}C), and following 530 ^{o}C and 560 ^{o}C anneals. No changes in the intensity of the indium or gallium signals are observed up to 480 ^{o}C. When the surface is annealed at 530 ^{o}C, there is a reduction in the In 4d peak intensity which reflects that at this temperature the InGaAs surface has started to decompose. The areas calculated from curve fitted peaks and the changes induced in the individual peak intensities are more clearly observed in the histogram representation plotted in Figure 3.6 (c) and (d).

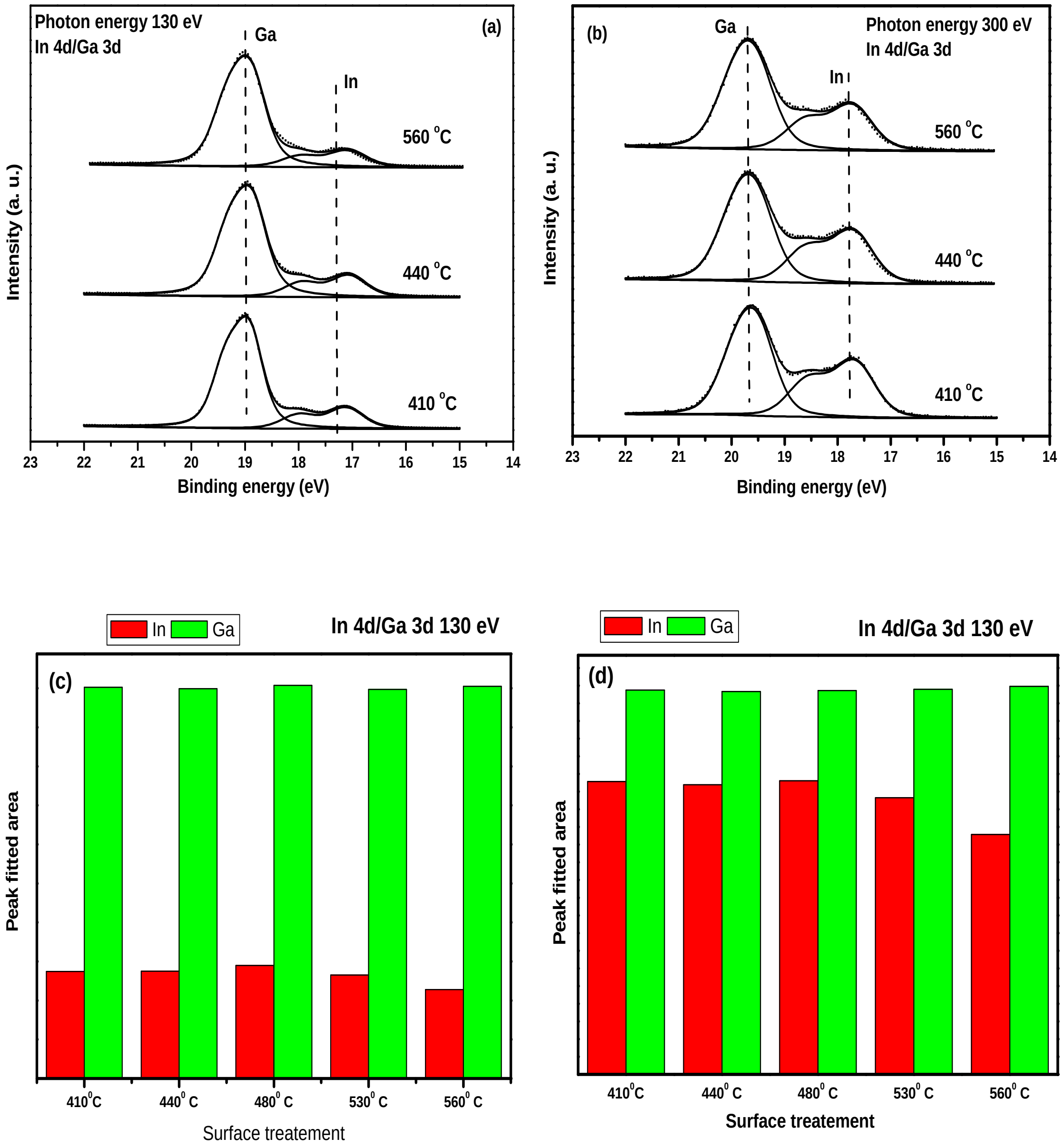

Figure 3.6 Curve fitted spectra of In4d/Ga 3d spectra at a photon energy of (a) 130 eV and (b) 300 eV at 410 °C, 530 °C and 560 ° C , (c) and (d) Curve fitted area of In 4d and Ga 3d signal as a function of thermal anneals.

Annealing at 530 °C leads to a 5% reduction in the intensity of the In 4d core level with no reduction in Ga signal. A further drop in In signal (15%) was measured following a 560 °C anneal, while no corresponding reduction in the Ga or As signals was observed. The work function value for the clean surface was determined to be 4.7 eV.

3.3 In-situ sulphur passivation of InGaAs and thermal anneals

3.3.1 Impact on As 3d spectra

Figure 3.7 shows the normalised As 3d core level spectra acquired at 92 eV photon energy for the clean InGaAs surface decapped at 410 °C, following sulphur deposition and subsequent anneal at 400 °C illustrating the change in the peak shape as a function of surface treatment.

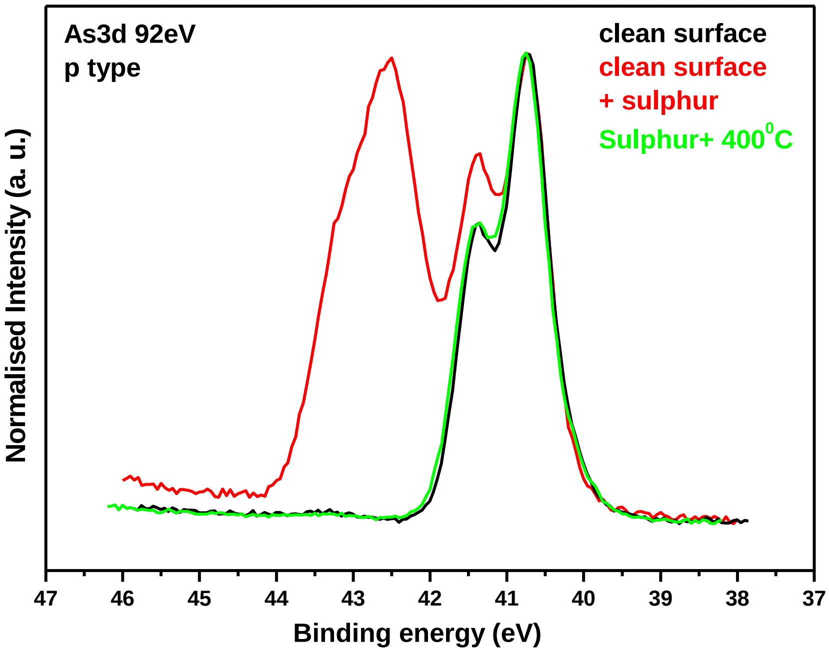

Figure 3.7 Normalised photoemission spectra for the As 3d peaks at 92 eV photon energy showing the evolution of the peak shape with the removal of the As cap, sulphur deposition and anneal.

Figure 3.8 shows the As 3d curve fitted photoemission spectra for p-type InGaAs at 92 eV for (a) the clean InGaAs surface (b) following sulphur deposition and (c) 400 °C anneal, respectively. The clean decapped InGaAs surface had been exposed to a molecular sulphur flux from the electrochemical cell at room temperature for 30 minutes and the changes in the As 3d core level spectrum following this deposition are shown in Figure 3.8 (b). The As 3d peak displays a large chemically shifted component which was curve fitted with two peaks at 1.45 eV and 1.84 eV higher binding energy with respect to the bulk As peak as shown in Figure 3.8 (b). These peaks are interpreted as evidence of significant sulphur – arsenic bond formation and have been previously identified as originating from As-S bond and As(S-S) disulphide bonding interactions, respectively [25-28]. Annealing the sulphur treated surface at 400 °C results in the complete disappearance of the As-S bonding components as shown in Figure 3.8(b) and the As 3d peak can now be curve fitted with two peaks identical to those used to fit the clean surface spectrum as has previously been reported for studies on GaAs [21].

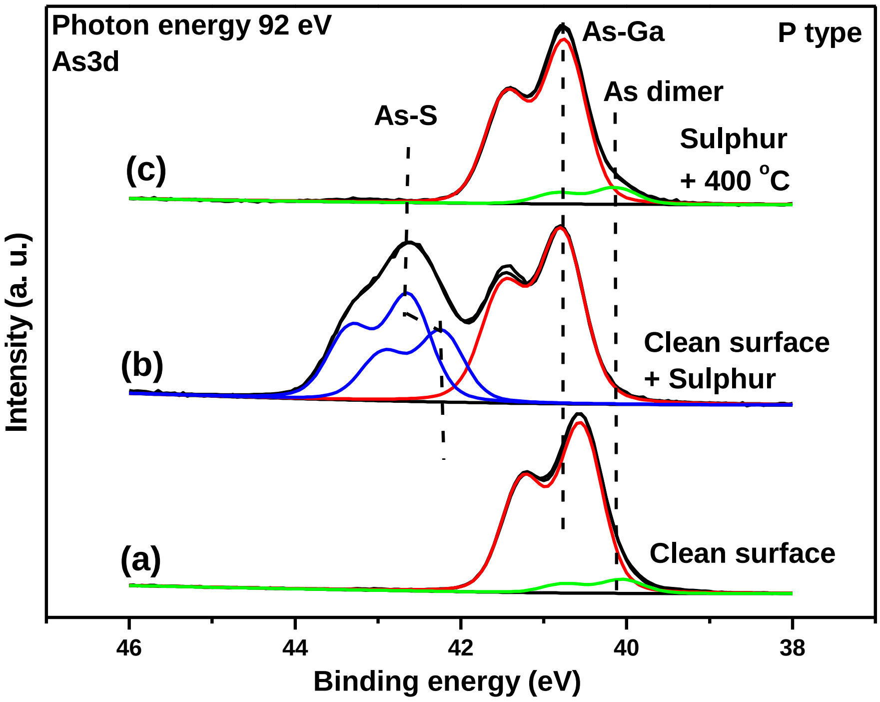

Figure 3.8 As 3d curve fitted photoemission spectra for p-type InGaAs at photon energy 92 eV for (a) Clean surface (b) sulphur exposed at room temperature (c) sulphur + 400 °C anneal.

3.3.2 Impact on In 4d /Ga 3d spectra

Figure 3.9 shows the corresponding normalised In4d/Ga 3d spectra at the three different photon energies with (a) 69 eV, (b) 130 eV, (c) 300 eV on p-type InGaAs for the decapped surface, sulphur deposition and anneal to 400 °C. These spectra show the variation in the relative In and Ga peak intensities due to changes in the photoionization cross section with photon energy resulting in a significantly larger In 4d peak while using 69 eV photon energy and a larger Ga 3d signal at both 130 eV and 300 eV.

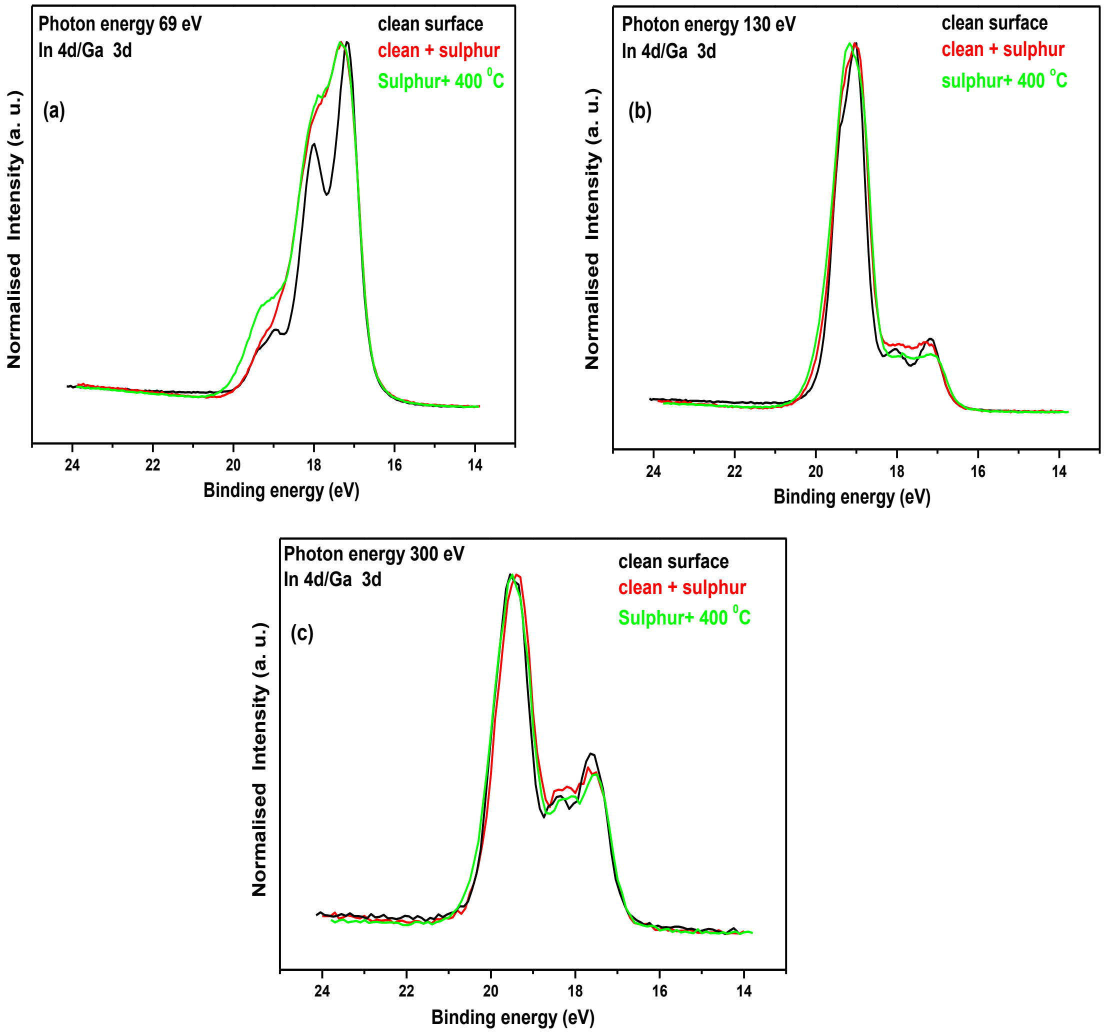

Figure 3.9 Normalised In4d/Ga3d spectra at the three different photon energies of (a) 69 eV, (b) 130 eV, and (c) 300 eV on p-type InGaAs, black : clean surface, red : sulphur exposed at room temperature and green: sulphur + 400 ^{o}C anneal.

The In 4d and Ga 3d core level spectra of the clean decapped surface acquired at 69 eV shown in Figure 3.10 (a) are curve fitted with single spin-orbit split components separated by 1.80 eV binding energy. The changes in the Ga 3d/In 4d composite peak resulting from sulphur deposition shown in Figure 3.10 (b) display evidence of a bonding interaction between the indium and the sulphur as indicated by the presence of a In-S component in the curve fitted spectrum, shifted by 0.45 eV to higher binding energy which is similar to previously reported values [29]. The subsequent 400 ^{o}C anneal also results in the appearance of a Ga-S attributed bonding component shifted by

0.50 eV [30] relative to the bulk Ga 3d peak in the spectrum. Because of the low photoionization cross section of the Ga 3d core level at this photon energy as mentioned in section 3.1.1, it is difficult to detect any evidence of a Ga-S bonding interaction following sulphur deposition. However, acquiring the same core levels at 130 eV and 300 eV as shown in Figure 3.11 for both room temperature sulphur deposition and following the 400 °C anneal allows clear identification of a Ga-S bonding component in agreement with comparable studies of sulphur deposition on GaAs [21, 31].

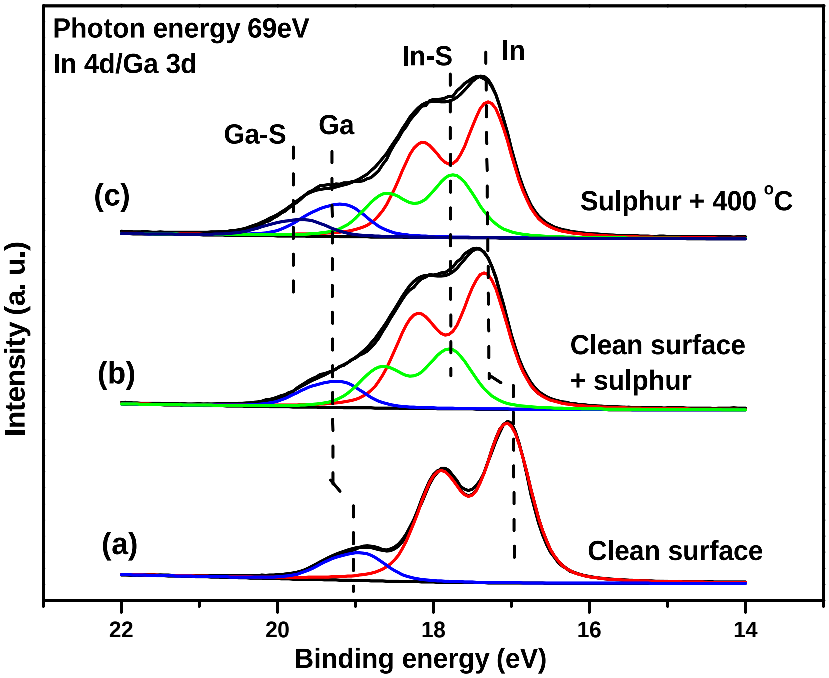

Figure 3.10 In 4d and Ga 3d curve fitted photoemission spectra for p-type InGaAs at photon energy of 69 eV for (a) clean surface, (b) sulphur exposed at room temperature and (c) sulphur + 400 °C anneal

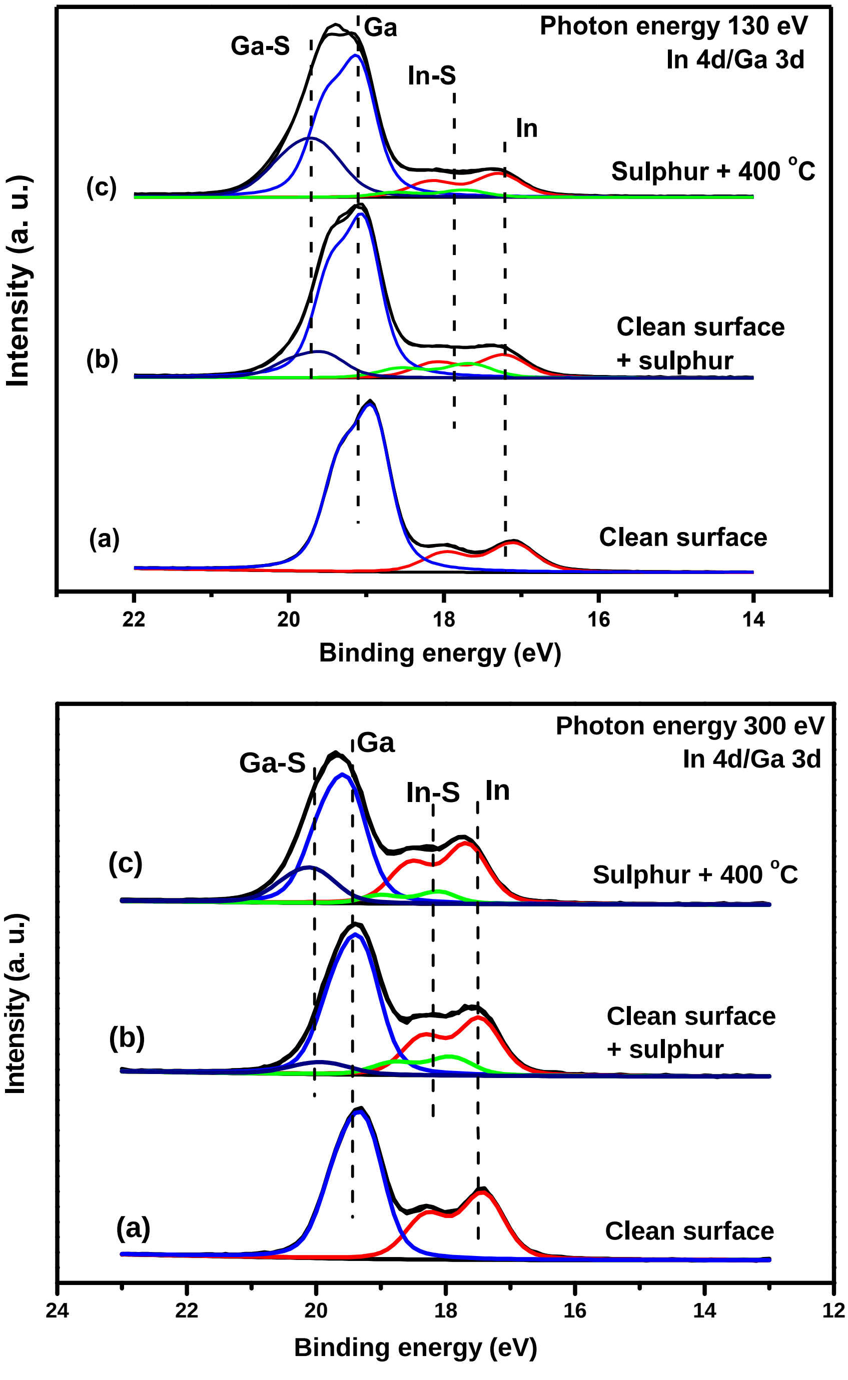

Figure 3.11 In 4d and Ga 3d curve fitted photoemission spectra for p-type InGaAs at photon energies of 130 eV and 300 eV for (a) clean surface, (b) sulphur exposed at room temperature and (c) sulphur + 400 °C anneal.

This dependence can be exploited to accentuate the bonding interactions between sulphur and either Ga or In by selecting the appropriate photon energy for curve fitting. The area of As, As-S, In, InS, Ga and GaS bonding components for the full deposition and annealing temperature sequence have been plotted as a histogram for the differently prepared surfaces as shown in Figure 3.12 (a). The maximum intensity of the As peak following the 340 ^{o}C anneal and the significant decrease in the intensity of the peak following sulphur deposition and anneal at 400 ^{o}C probably reflects desorption from the surface. This is accompanied by the complete removal of all evidence of As-S bond formation as shown in the curve fitted spectra in Figure 3.8 (b). The intensity of the As 3d peak decreases to approximately 1/3 of its original value reflecting the extent of the loss of As from the near surface region as shown in Figure 3.12 (a).

The impact of changes in the photo-ionization cross section on the relative intensities of the In 4d/Ga 3d component peaks is clearly evident from this analysis in Figure 3.12 (b), (c) and (d). At 69 eV photon energy the In signal is a maximum on the decapped surface following the 410 ^{o}C anneal and similar behaviour is exhibited by the Ga 3d intensity in the 130 eV photon energy spectra. Sulphur deposition results in the significant suppression of these intensities and the appearance of an In-S bonding component. As described in earlier section 3.3.2 at 69 eV, the Ga-S bond could not be detected due to low photoionisation cross section while it can be seen at photon energies of 130 eV and 300 eV. Annealing at 400 ^{o}C results in an increase the In/Ga intensity level as well as of the In-S and Ga-S signals as shown in the profiles in Figure 3.12 (b), (c) and (d), resulting from both the desorption of the surface As and excess sulphur on the surface. Further annealing at 480 ^{o}C and 530 ^{o}C results in a reduction in the In signal and a corresponding increase in the Ga and Ga-S intensities were observed.

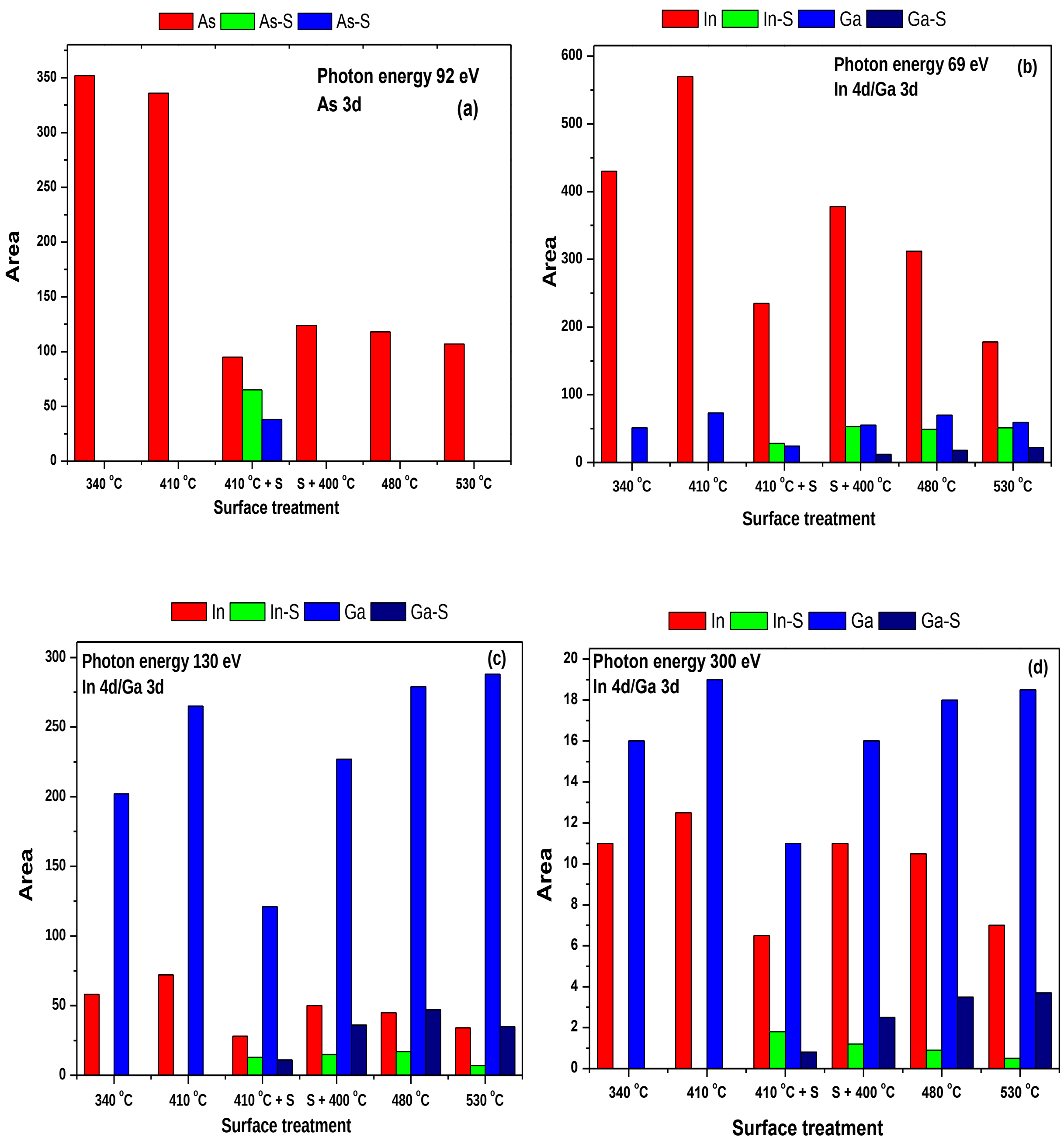

Figure 3.12 Area plot for (a) As 3d at a photon energy of 92 eV, In 4d and Ga 3d for p-type at photon energy (b) 69 eV, c) 130 eV and (d) 300 eV for surface treatment 340 ^{o}C, 410 ^{o}C, 410 ^{o}C +S, S+400 ^{o}C, 480 ^{o}C and 530 ^{o}C

3.3.3 Impact on sulphur spectra following thermal anneals

The broadened nature of the S 2p component peaks for the room temperature deposited spectrum shown in Figure 3.13 reflects the range of chemical environments in which the sulphur exists resulting from As-S, In-S and Ga-S bonding interactions. After the thermal anneal at 400 °C which results in the removal of the As-S bonds, the peak becomes more resolved and can be fitted with two well defined components. The lower BE component is attributed to sulphur bonded to both In and Ga at the surface and the high BE peak is attributed to a subsurface component, consistent with its higher coordination, resulting from the diffusion of sulphur into the top most atomic layers in agreement with previous studies for both sulphur and selenium passivation of GaAs [21,32]. No significant change is seen in the relative intensities of these component peaks at higher temperature anneals of 480 °C or 530 °C (not shown).

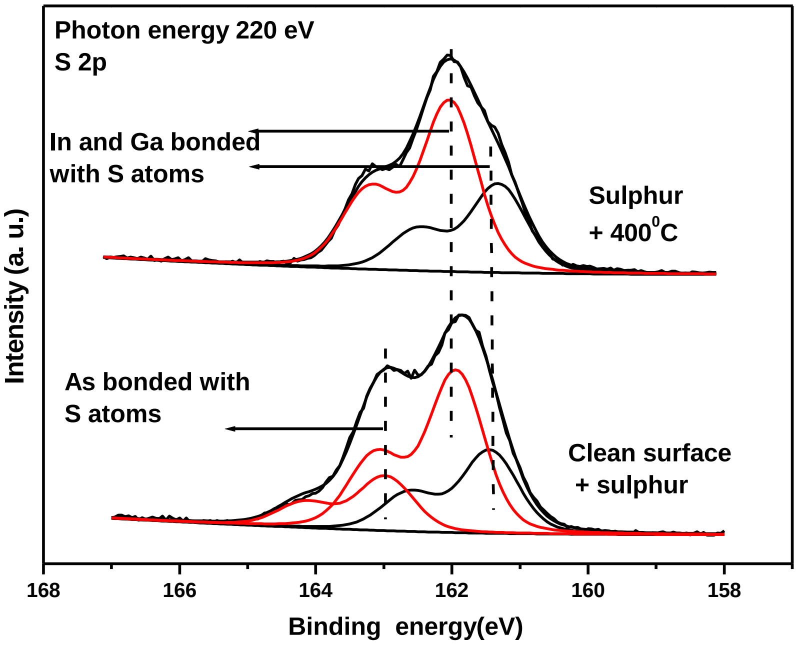

Figure 3.13 S 2p curve fitted spectra acquired at 220 eV photon energy for room temperature deposition and following 400 °C anneal. The high binding energy component peak at 163 eV, which is removed by the 400°C anneal, is attributed to an As-S bonding.

3.3.4 Indium desorption from surface at higher temperature anneals

While these higher temperature anneals have no significant impact on the intensity of the As 3d signal as shown in Figure 3.12 (a), the effect on the Ga 3d/In 4d core level intensities can be seen from normalised and curve fitted spectra in Figure 3.14 (a) and (b), respectively, acquired at a photon energy of 105 eV which gives almost equal intensity to the Ga 3d and In 4d core level peaks for the clean surface. The loss of indium from the surface is more clearly displayed in the histogram in Figure 3.15 reflecting the change in intensity of the component peaks which has previously been observed during the thermal annealing of the atomic hydrogen cleaned InGaAs surface [16].

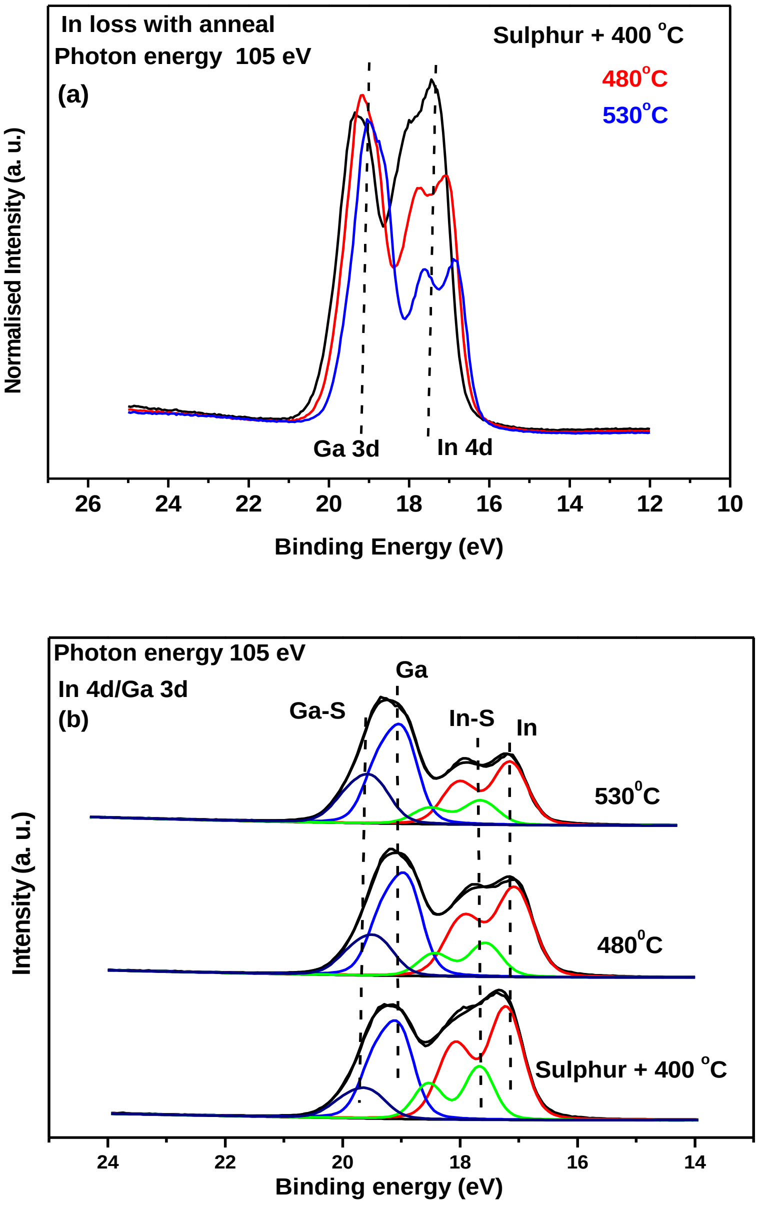

Figure 3.14 The loss of In as a function of thermal anneal is apparent in these spectra acquired at a photon energy of 105 eV (a) normalised spectra (b) curve fitted spectra

These changes in surface chemical composition are also accompanied by a decrease in the intensity of the In-S bonding component and an increase in the intensity of the Ga-S component peak which is consistent with the relative bond energies of In-S and Ga-S calculated by Ohno and Shiraishi [33]. It is also observed that at 530 ^{o}C that the peak width of the Ga 3d becomes narrower which reflects the sulphur desorption taking place at a higher temperature.

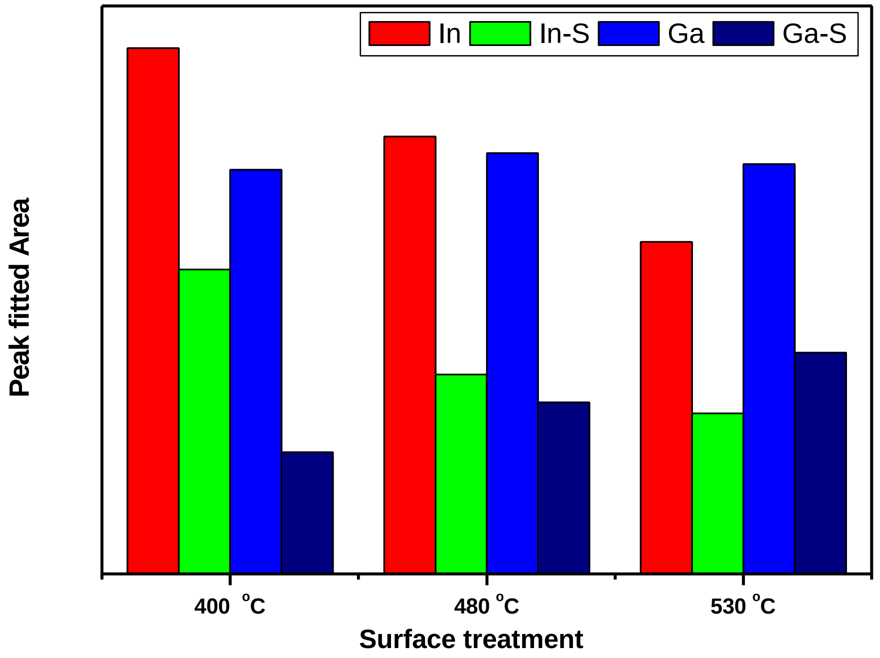

Figure 3.15 The magnitude of the changes in the intensity of the indium bulk, S-In and S-Ga components acquired at a photon energy of 105 eV as a function of thermal anneal

3.3.5 Angle resolved measurements

The photoemission results indicate that there is a strong interaction at room temperature between the deposited sulphur and the atomically clean InGaAs surface. Evidence of a significant bonding interaction between the sulphur and the As 3d and In 4d are clearly observed, while the interaction with Ga 3d is less apparent. Annealing at 400 ^{o}C completely removes the As-S component peaks with the resulting As 3d profile identical to that from the clean surface. However, the resulting change in the intensity of the arsenic signal shown in the bar chart in Figure 3.12 (a) highlights the extent to which the surface arsenic signal has been attenuated by this treatment. The change in the relative intensity of the In, Ga, As peaks following sulphur deposition and anneal are shown in the results of the angle resolved XPS measurements in Figure 3.16 acquired at normal emission and 60° off normal, which corresponds to a factor of two reduction in the sampling depth.

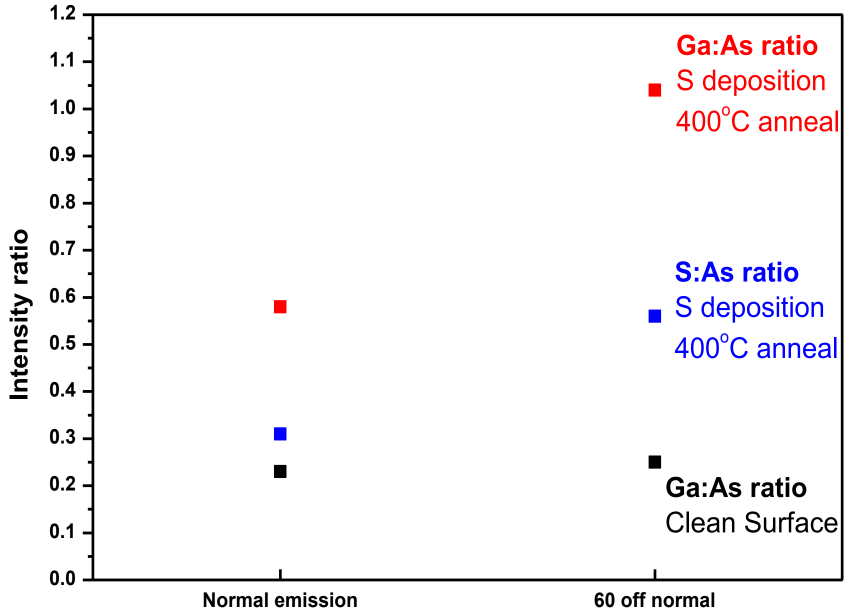

Figure 3.16 Ga : As and S : As ratios at normal emission and 60° off normal showing that sulphur replaces the As in the near surface region

No attempt has been made to quantify the elemental composition by the use of relative sensitivity factors and the ratios displayed are the raw data. The Ga:As intensity ratio of the cleaned InGaAs surface shows almost no dependence on angle indicating that within the sampling depth, the composition is uniform. The clean surface Ga:As intensity ratio of 0.23 increases to 0.58 at normal emission following sulphur deposition and anneal suggesting the loss of As within the photoemission sampling depth (~2.0 nm), as no detectable change in the Ga signal intensity is apparent from Figure 3.16. Acquiring the same spectra at 60° off normal results in a further increase in this ratio to 1.04 indicating that in the upper most atomic layers, the As loss is even more accentuated. The assertion that this change reflects the substitution of As by S in the near surface region is supported by the fact that the S:As ratio increases from 0.32 to 0.57 between the spectra taken at normal emission and 60° off normal. Similarly, on the clean InGaAs surface, there is no change on In:As ratio (not shown) between normal emission and 60^o off normal while on the sulphur deposition + 400^{0}C anneal, the In:As ratio increases from 2.1 to 3.48 consistent with the loss of As from the near surface region. Therefore, when these results are combined with the fact that after the 400 ^{o}C anneal there is no evidence of As-S bonding, this suggests that the surface is composed of an In-S and Ga-S bonded layer with sulphur taking the place of arsenic.

3.3.6 Fermi level position as a function of treatment from valence band measurements

The change in position of the Fermi level in the InGaAs bandgap was monitored as a function of surface treatment for both n and p-doped InGaAs substrates. The position of the Fermi level in the gap was determined by measuring the energy difference between the valence band edge and the metallic Fermi level of the sample holder in contact with the sample. The determination of the valence edge for the clean surface, sulphur deposited and S + 400 ^{o}C surface is shown in Figure 3.17. The valence band maxima indicated in the figure were determined by the linear extrapolation and the Fermi level position is determined from the photon energy. The change in position of the Fermi level in the InGaAs bandgap was monitored as a function of surface treatment from valence band measurement and is displayed in Figure 3.18. For both doping types, the Fermi level position was found to be in midgap on the atomically clean surface in agreement with the recent scanning tunnelling spectroscopy measurements by Shen et al [12] on similarly decapped InGaAs surfaces. The deposition of sulphur results in the Fermi level moving towards the conduction band for both doping types and the subsequent anneal does not significantly alter the positions. This suggests that the initial interaction with sulphur at room temperature primarily determines the electronic impact of the treatment. The identical shifts in Fermi level positions for both doping types confirms that sulphur is essentially doping the near surface region by acting like a shallow donor rather than unpinning the Fermi level. A similar photoemission study by Scimeca et al [32] reported that the maximum Fermi level movement on the GaAs(001) surface following the in-situ adsorption of Se was observed when the surface As atoms had been replaced by Se atoms.

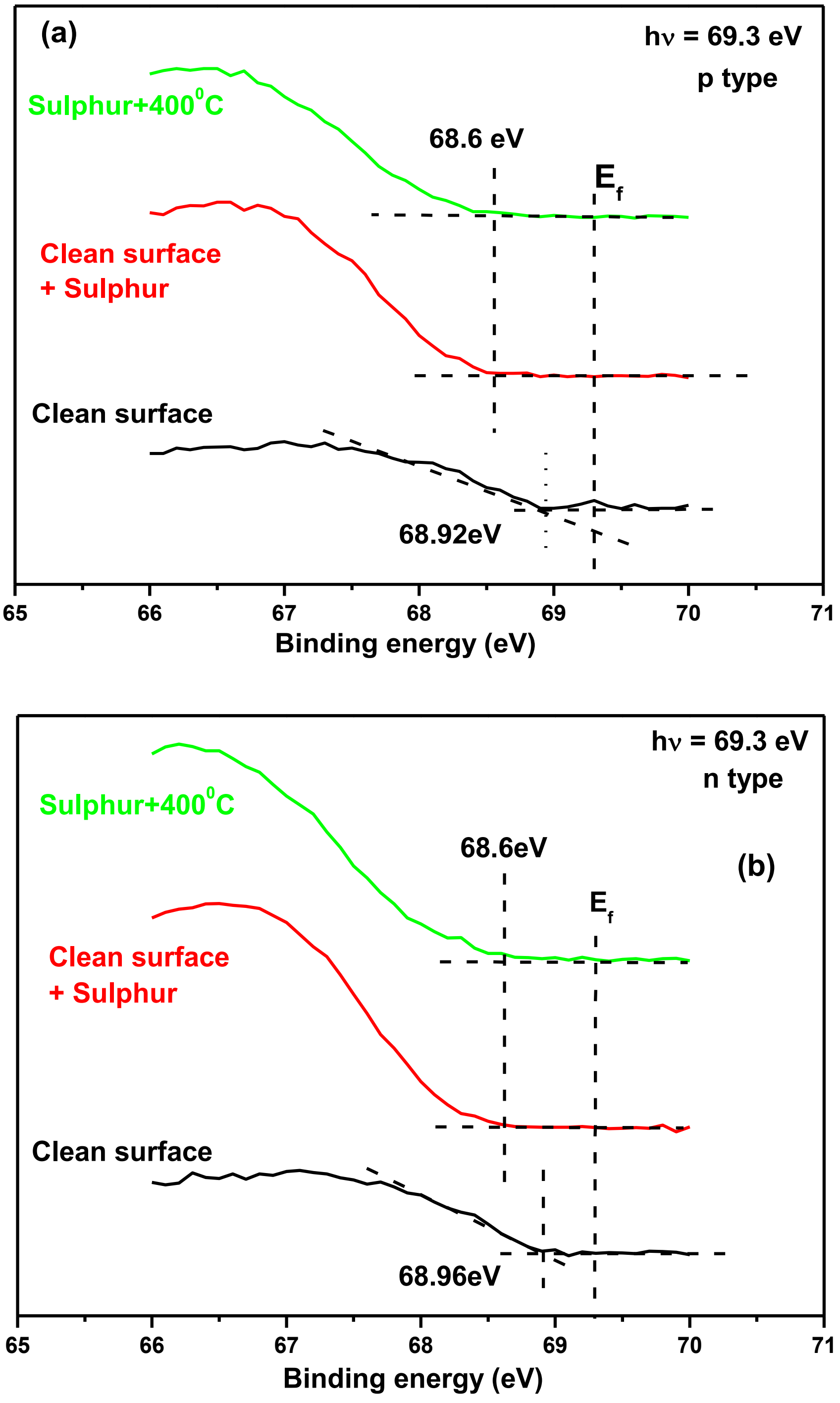

Figure 3.17 Valence band spectra for clean surface, sulphur exposed at RT and sulphur + 400 °C anneal surface : (a) p-type (b) n-type

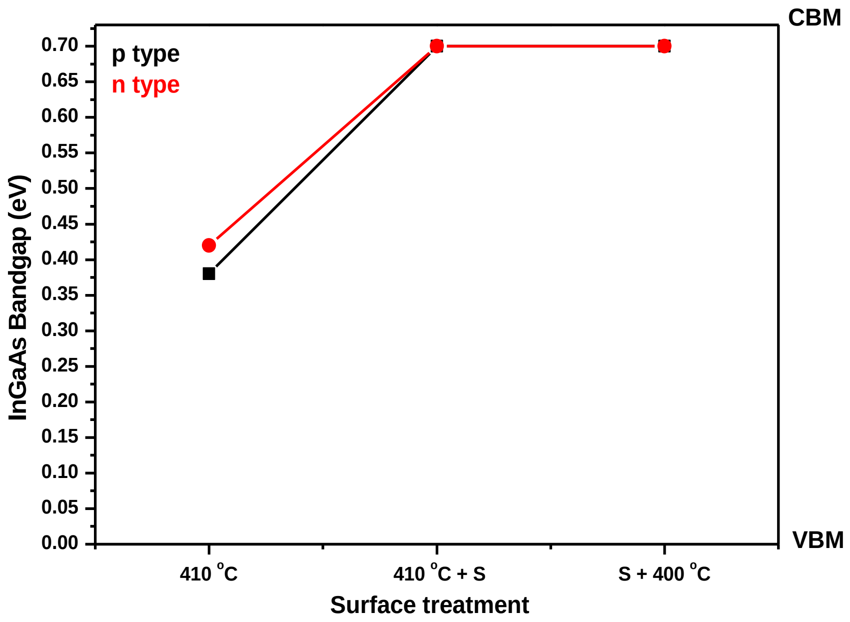

Figure 3.18 Fermi level position relative to VBM for both n and p-doped substrates as a function of surface treatment (From figure 3.17).

Koenders et al. [34] also reported similar Fermi level behaviour for n and p-doped GaAs (110) cleaved surfaces following insitu deposition of high exposures of sulphur from an electrochemical cell. A photoemission study by Zahn et al [35] of both sulphur and selenium passivation of atomically clean GaAs(100) prepared by arsenic decapping found reduced band bending for n-type substrates and an increase in band bending for p-type, consistent with the findings in the current study for InGaAs. Therefore, at a more general level, when the results of this study are taken in conjunction with previous studies on both InGaAs and GaAs semiconductor surfaces [34, 35] it can be concluded that the chalcogenide treatment results in similar trends being observed involving the replacement of the As in the near surface region by the chalcogen and the consequential local n-type doping of the surface, regardless of the initial doping type of InGaAs.

The subsequent anneal does not significantly alter the Fermi level positions suggesting that the initial interaction with sulphur at room temperature primarily determines the electronic impact of the treatment. The resulting band bending configuration is schematically shown in Figure 3.19

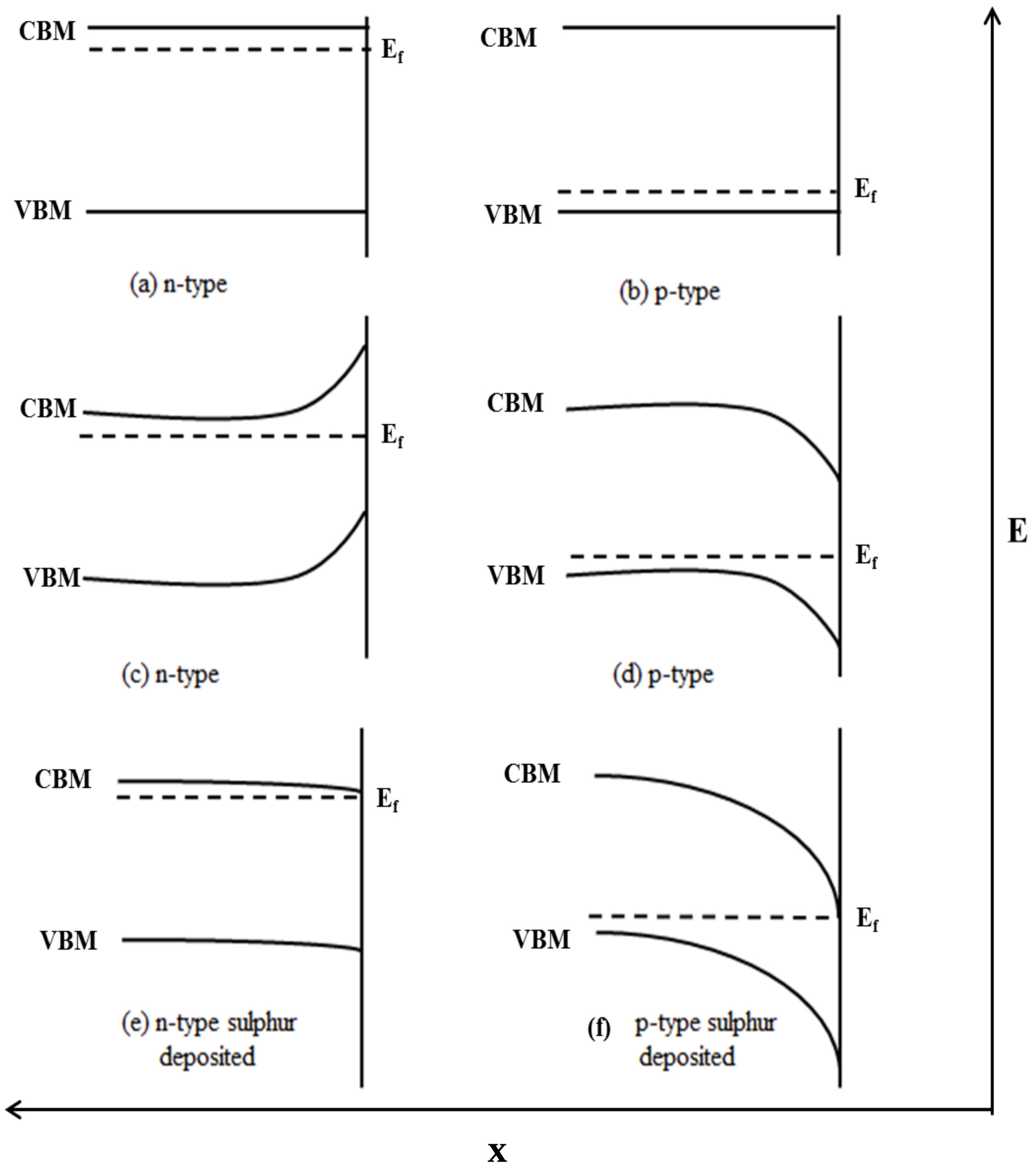

Figure 3.19 Band bending diagram for both doping types (a) and (b) ideal condition, (c) and d) clean surface after As decapping, (e) and (f) sulphur deposited surface

3.3.7 Change in InGaAs work function with sulphur deposition and anneal

The change in work function with sulphur deposition and anneal is shown in Figure 3.20. Work function measurements on both doping types after sulphur deposition and anneal show similar behaviour displaying a value close to 6 eV which is indicative of the formation of a surface dipole layer related to the presence of sulphur on the surface.

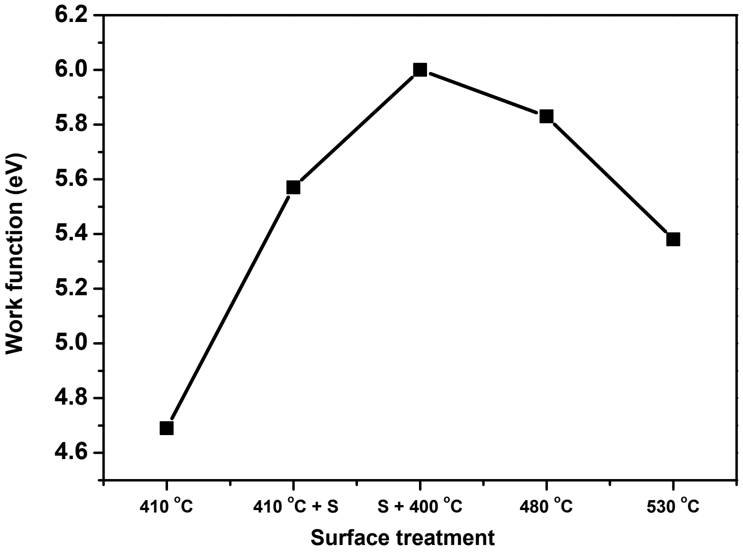

Figure 3.20 Change in work function value on sulphur deposition and following thermal anneals

The change of the work function on a surface can be approximately predicted by knowing the electronegativity of the adsorbates [36]. For the clean InGaAs surface the work function value is 4.7 eV. With the sulphur deposition the value reaches 5.54 eV. As the sulphur atom is more electronegative than the atoms in InGaAs, the charge transfer takes place from substrate to the sulphur layer which generates a surface dipole layer reinforcing the pre-existing dipole on the InGaAs surface. Annealing at 400 ^{o}C increases the work function value towards 6 eV for both doping types which could be the result of increased In-S and Ga-S bond formation in the near surface region. On further annealing at higher temperatures, the work function value decreases, possibly reflecting the disruption of the In-S bond as indium desorbs and the start of the desorption of sulphur from the surface.

Following the sulphur passivation and anneal at 530 ^{o}C the sample was exposed to air for one week, to observe the regrowth of the oxide on the surface. The air exposed surface was compared with the native oxide InGaAs surface. For comparison curve fitted As 3d and In 4d/Ga 3d spectra acquired at a photon energy of 92 eV and 69 eV for exposed surface and native oxide surface are shown in Figure 3.21 (a) and (b). Both spectra reflect the regrowth of oxide on the surface composed of a mixed phase oxide (Ga, In, As). However the As 3d spectra shown in Figure 3.21 (a) shows the level of oxide on the air exposed surface is significantly less than the native oxide surface. The oxide thickness calculated on the native oxide surface was approximately 1.1 nm while on air exposed surface was calculated to be approximately 0.35 nm. It is well known that As in InGaAs surface oxidizes mainly to As_2O_3 and As_2O_5 states. The corresponding chemically shifted peaks in the As 3d spectra from those compounds are shifted by 1.2–4.5 eV [37] to higher binding. Similarly curve fitted spectra for In 4d/Ga 3d shown in Figure 3.21 (b) display the level of indium and gallium oxide growth on the surface.

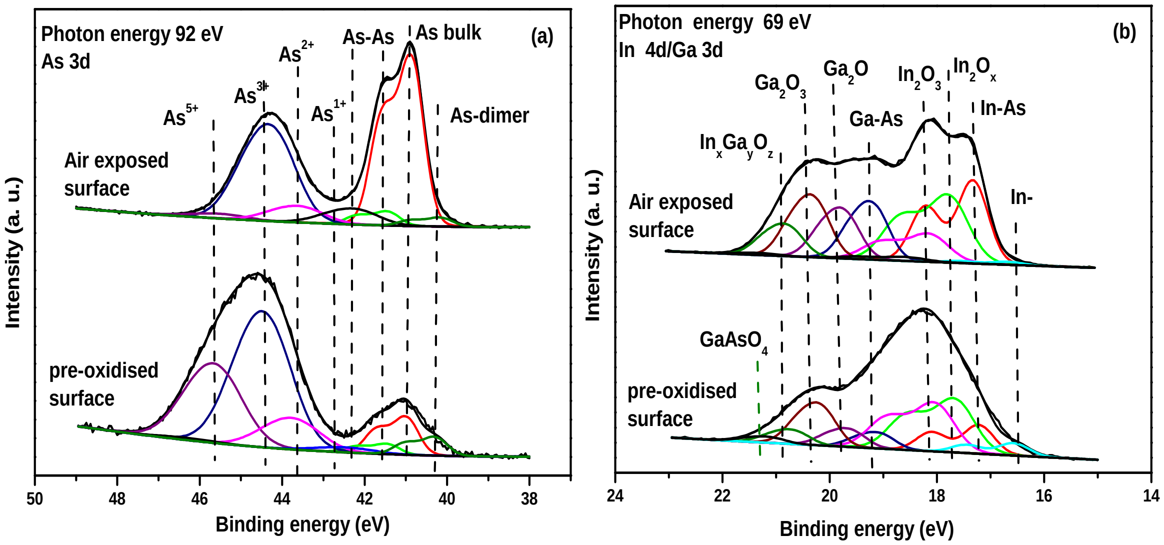

Figure 3.21 Comparison of (a) As 3d and (b) In 4d /Ga 3d curve fitted photoemission spectra acquired at photon energies of 92 eV and 69 eV on native oxide surface and air exposed surface following sulphur deposition and anneal

However the gallium oxide re-growth is significantly larger than the indium oxide re-growth. This oxidation behaviour of the surface is attributed to the decomposition of the surface at higher temperature 530 °C. At this temperature the InGaAs surface was observed to be gallium rich and indium deficient which indicates larger level of gallium oxide re-growth on the surface.

3.4 Native oxide and wet chemical sulphur passivated InGaAs surfaces investigation by synchrotron radiation based photoemission

3.4.1 Sample preparation:

For ex-situ sulphur passivation, an n-type Be doped $In_{0.53}Ga_{0.47}As$ epilayer 0.5 μm thick ($5x10^{17}$ cm^{-3}) lattice matched to an InP substrate was degreased for 1 min in acetone followed by 1 min rinse in methanol prior to being immersed in 10% ammonium sulphide ($(NH_4)_2S$) solution for 20 min at room temperature (290 K). The sample was secured to a molybdenum holder before being loaded into the vacuum system in less than 10 minutes after removal from $(NH_4)_2S$ to minimize both native oxide regrowth and ambient oxidation. In order to provide a consistent fit for the core level peaks, reference spectra were acquired from an atomically clean InGaAs wafer which had been capped with arsenic, in order to obtain the correct curve fitting parameters.

3.4.2 Synchrotron radiation photoemission study of wet chemical sulphur passivated InGaAs surface

3.4.2.1 Impact on As 3d spectra

Figure 3.22 shows the normalised spectra of As 3d at a photon energy of 92 eV for native oxide and sulphur passivated surface. The profile of the As 3d peak shows that there is evidence of a residual arsenic oxide component present on the sulphur passivated surface when comparison is made with the native oxide covered surface spectrum. These spectra show that the sulphur passivation is very effective in removing the surface oxide and preventing re-oxidation even after ambient exposure up to 10 minutes.

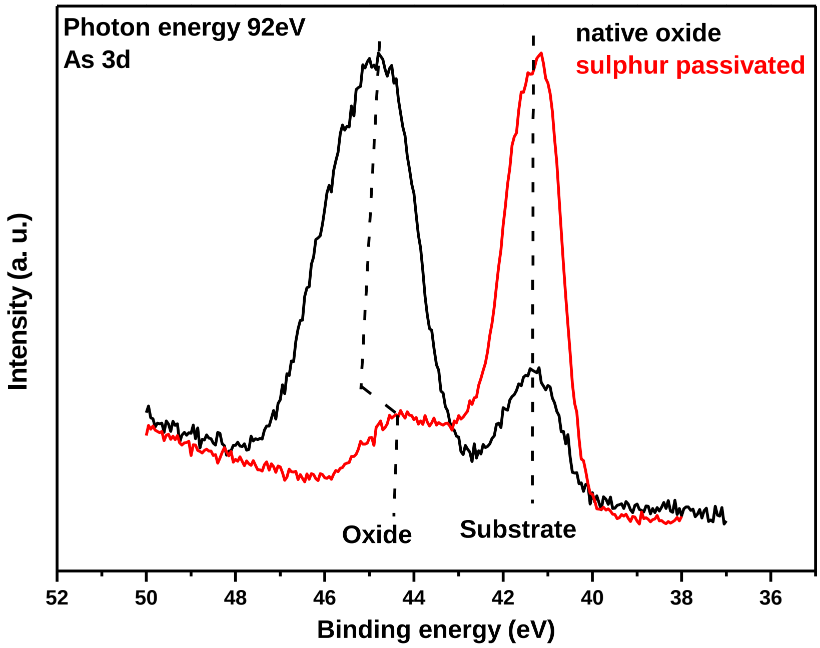

Figure 3.22 Normalised As 3d spectra acquired at a photon energy of 92 eV for native oxide and sulphur passivated surface showing the effectiveness of the $(NH_4)_2S$ treatment in removing the oxides.

The curve fitted spectra for the As 3d peak for native oxide and the wet chemical sulphur passivated surface at a photon energy of 92 eV are shown in Figure 3.23. The sulphur passivated spectrum consists of a bulk As component, an As dimer component at -0.65 eV, elemental arsenic As^{o} (+0.55 eV) and mixed phase of interfacial arsenic oxide composed of As^{1+} (+1.3 eV), As^{2+} (+1.7 eV), AsSO (+2.55 eV) [22] and As^{3+}(+3.4 eV) respectively, A ‘ + ’ or ‘ - ’ sign indicates a shift toward higher or lower binding energy. The peak of native oxide surface wer curve fitted with As dimer component (-0.65 eV), elemental arsenic As^{o} (+0.55 eV) and mixed phase of interfacial arsenic oxide composed of As^{1+} (+1.23 eV) , As^{2+} (2.55 eV), As^{3+} (+3.24 eV) and As^{5+}(+4.44 eV) and $GaAsO_4$ (+5.08 eV). These peaks previously have been reported by Brennan et al. [37] in his synchrotron studies of the native oxide covered InGaAs surface.

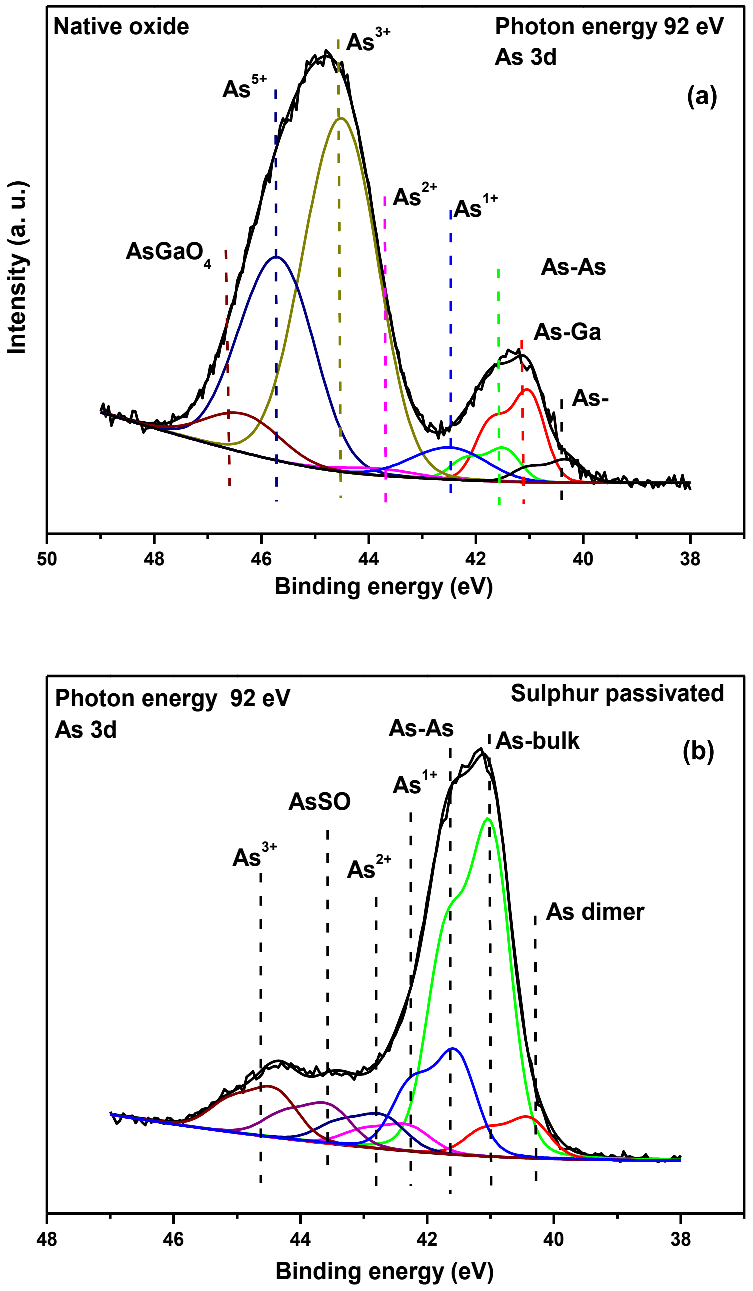

Figure 3.23 Curve fitted As 3d spectra at photon energy of 92 eV for (a) native oxide and (b) wet chemical sulphur passivated surface showing the effectiveness of the treatment in removing the native oxide

O 1s spectra for both surfaces are shown in Figure 3.24 displaying a residual oxygen signal on the sulphur passivated surface. Higher oxygen signal was observed on native oxide surface in comparison to the sulphur passivated surface that also reflects the reduction in the oxide from the sulphur treated surface.

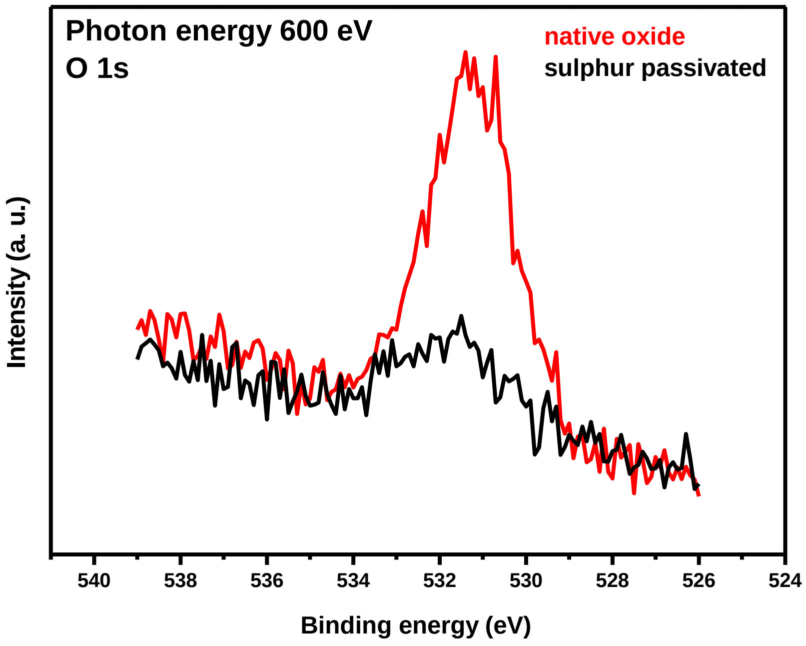

Figure 3.24 Normalised O 1s spectra at a photon energy of 600 eV for native oxide and sulphur passivated InGaAs surface

3.4.2.2 Impact on In 4d/ Ga 3d spectra

Curve fitted spectra at different photon energies of (a) 69 eV (b) 105 eV (c) 130 eV for the sulphur passivated surface are shown in Figure 3.25. In 4d/Ga 3d bulk peaks were curve fitted with single spin-orbit-split components separated by 1.80 eV binding energy and chemically shifted components consisting of the In^{1+} (+0.45 eV) , In^{2+} (0.60 eV), Ga^{1+} (+0.60 eV) and Ga^{3+} (+1.1 eV) oxidation states [22]. Due to the relatively small binding energy separation differences between the In 4d/Ga 3d bulk peak and the various reported sulphur and oxygen oxidation states [22], so no attempt was made to identify these individual component peaks.

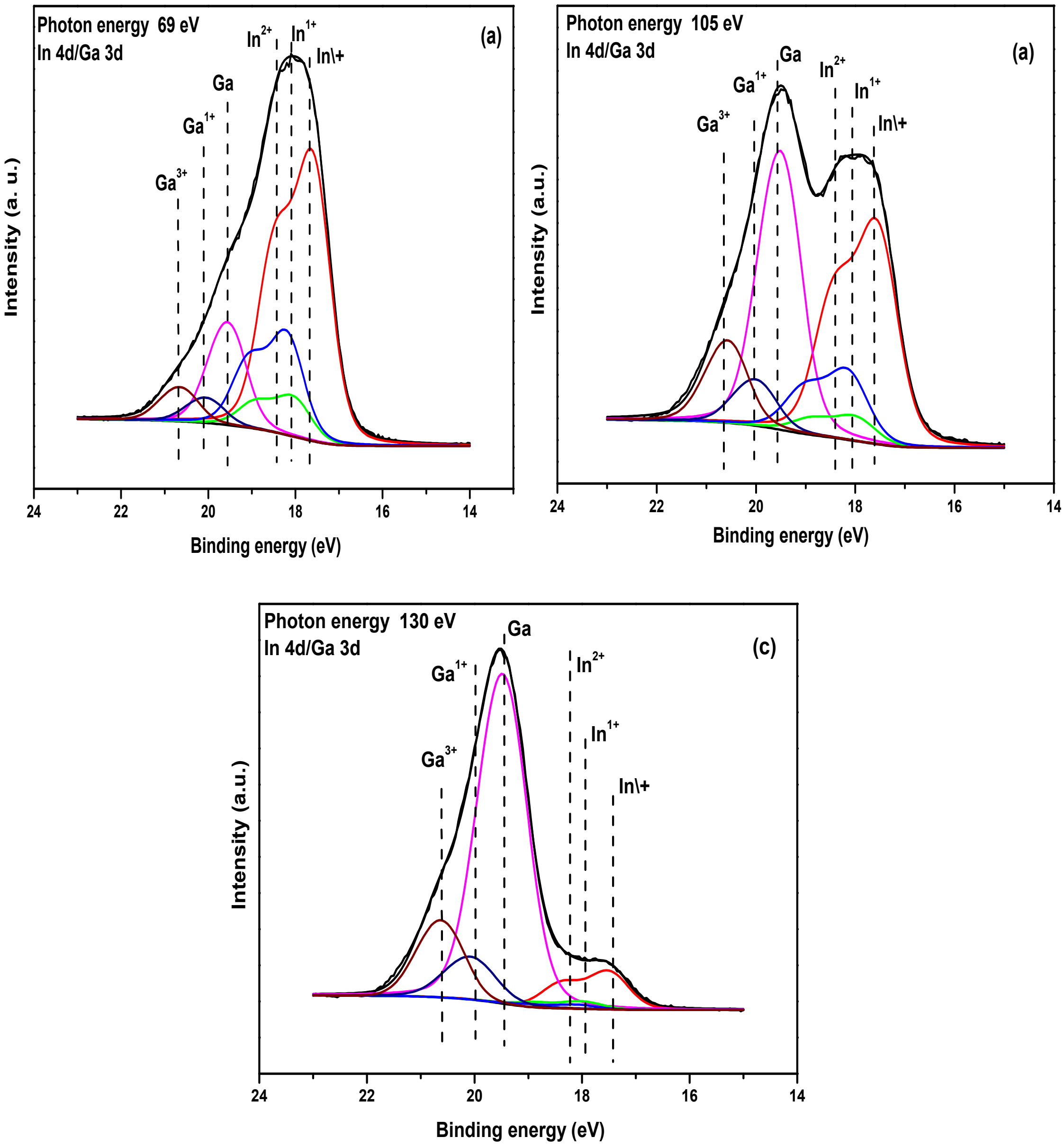

Figure 3.25 Curve fitted spectra for In 4d and Ga 3d at different photon energy of (a) 69 eV (b) 105 eV (c) 130 eV for the sulphur passivated InGaAs surface

At a photon energy of 130 eV while it is difficult to detect the indium oxidation states as the indium signal is small, the gallium signal is very strong making it possible to identify the oxidation states. However, at a photon energy of 69 eV the relative intensities are reversed making it easier to identify the indium oxidation states.

To observe the effectiveness of sulphur passivation, a comparison is made between the ratio of the peak intensities to bulk intensity for both native oxide and sulphur passivated surfaces as shown in Figure 3.26. The change in oxide to bulk ratio can be seen for native oxide and the sulphur passivated surface. Reduction in arsenic oxide was calculated 94 % shown in Figure 3.26 (a). A similar analysis on the indium and gallium oxide to bulk ratios at different photon energies also shows a similar reduction of 93% in indium oxide while 87% reduction in gallium oxide as shown in Figure 3.26 (b) and (c) respectively, indicating the effectiveness of wet chemical sulphur passivation at removing the native oxide layer. These ratios highlight changes in the relative composition of the oxide layer by tracking the trends determined from the peak fitted data.

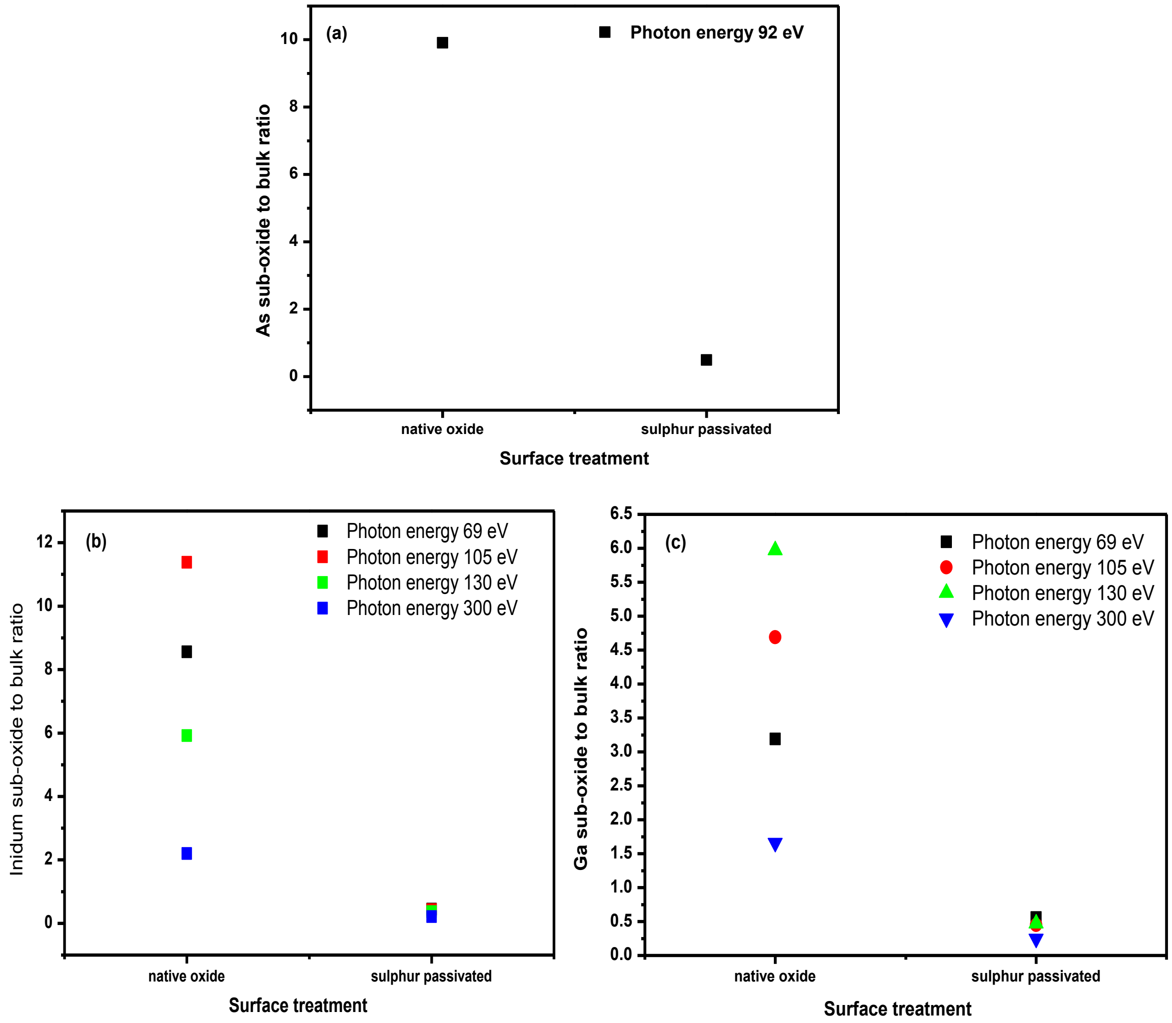

Figure 3.26 Sub-oxide to bulk ratio comparison for native oxide and sulphur pasivated surface (a) arsenic sub-oxide to bulk ratio, (b). indium sub-oxide to bulk ratio and (c) gallium sub-oxide to bulk ratio

3.4.3 Thermal stability of the wet chemical sulphur passivated InGaAs surface at high temperature

3.4.3.1 Thermal annealing

Figure 3.27 shows the As 3d normalised spectra at photon energy of 92 eV after incremental annealing from room temperature (RT) to 700 °C of a sulphur passivated surface. It is clear from these spectra that the residual surface As oxides/sulphides can be completely removed by a thermal anneal at 545 ^{o}C.

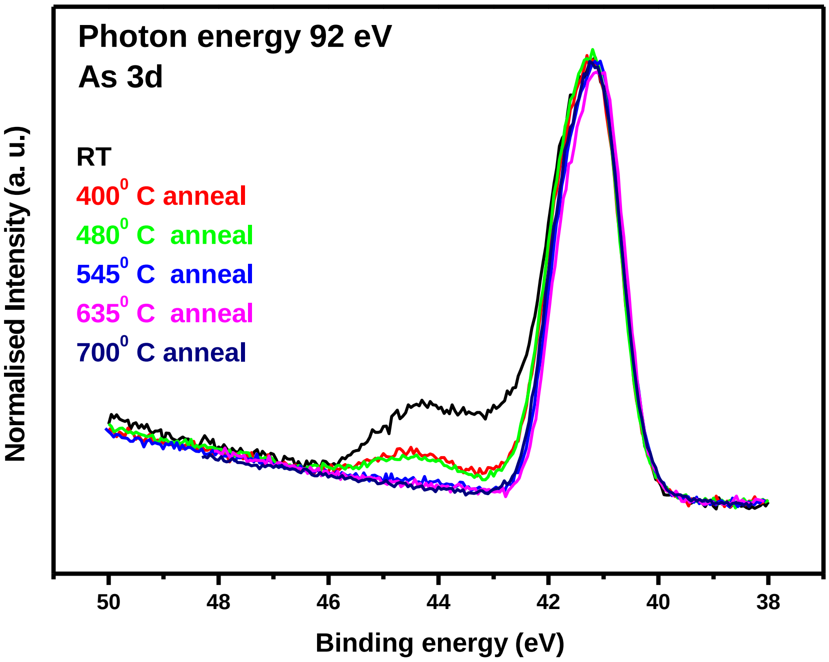

Figure 3.27 Normalised As 3d spectra at a photon energy of 92 eV for wet chemical sulphur passivated surface as a function of thermal

Figure 3.28 (a)-(d) shows the corresponding spectra at the four different photon energies of (a) 69 eV (b) 105 eV (c) 130 eV and (d) 300 eV after incremental annealing up to 700 °C. Again these highlight the variation in the peak intensities of the In and Ga peaks with the change in photon energy. The decrease in the peak widths clearly shows that the increase in annealing temperature has a significant effect in removing the residual surface oxides and sulphides present on the surface.

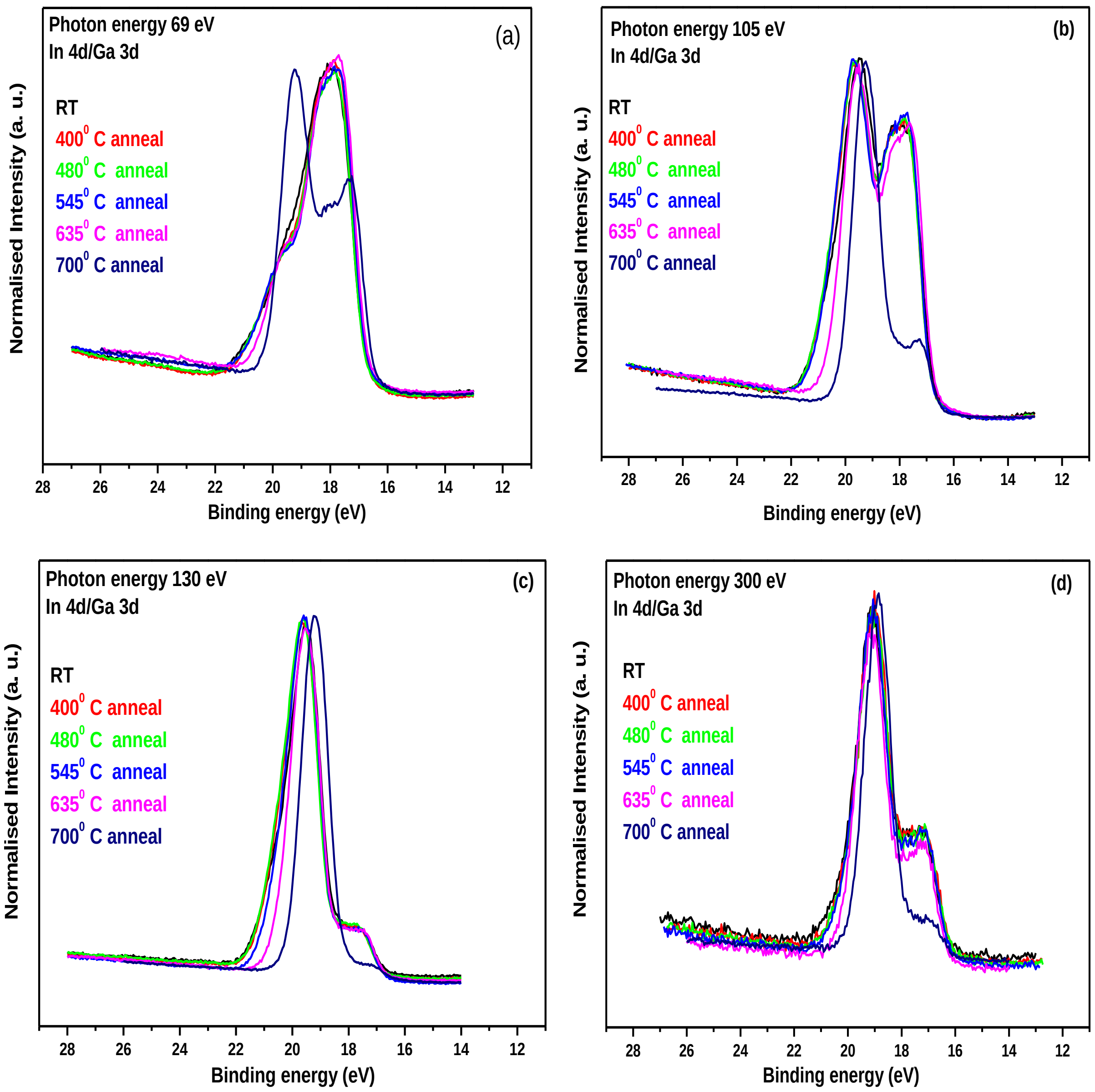

Figure 3.28 Photoemission spectra for the In 4d and Ga 3d peaks at photon energies of (a) 69 eV (b)105 eV (c) 130 eV (d) and 300 eV after annealing up to 700 °C on sample treated by wet chemical sulphur.

3.4.3.2 Impact on As 3d spectra

Figure 3.29 shows the changes in the As 3d curve fitted photoemission spectra at 92 eV as a result of thermal annealing up to 700 °C. Due to the relatively small binding energy separation differences between the As 3d bulk peak and the various reported sulphur and oxygen oxidation states [22,37-42], no attempt has been made to distinguish between the chemical shifts of the two elements in the curve fitted data. At room temperature, the As 3d peak was curve fitted with a bulk As component, an As dimer component (-0.65 eV), elemental arsenic As^o (+0.55 eV) and mixed phase of interfacial arsenic oxide composed of As^{1+} (+1.3 eV) , AsSO (+1.7 eV), As^{2+} (+2.55 eV) and As^{3+}(+3.4 eV). A ‘ + ’ or ‘ - ’ sign indicates a shift toward higher or lower binding energy as described in earlier section. Annealing at 400 °C leads to the removal of the As^{1+} state, a significant reduction in all other cationic arsenic oxidation states and a small reduction in As^o, while the As dimer signal remains constant. Subsequent annealing at 480 °C (not shown) shows a further reduction of higher arsenic oxides and

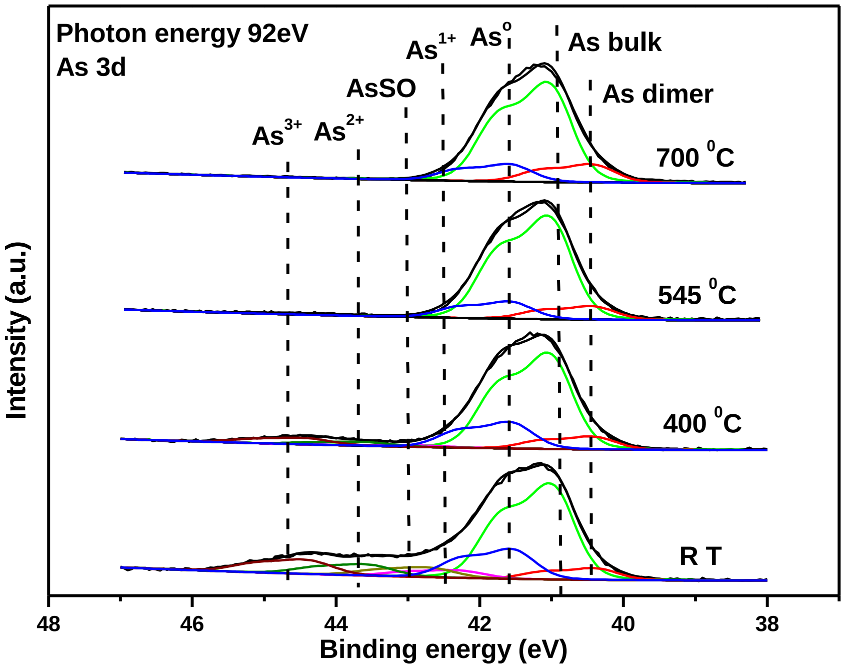

Figure 3.29 Curve fitted core level spectra of As 3d at photon energy of 92 eV on sulphur passivated InGaAs surface following thermal anneal.

states with a removal of the lower oxidation states. Complete arsenic oxide and sulphides removal was observed annealing at a temperature of 545 °C (not shown) with an increase in As bulk signal while arsenic dimers and As^o remains at the surface. An increase in As signal with thermal anneals was observed as a result of the removal of the arsenic oxides which enhance the substrate signal. Further annealing at high temperature shows no change in the arsenic signal. The resulting change in the intensity of the As signal shown in the bar chart in Figure 3.30 highlights the removal of the oxidation states upon annealing and illustrates that the higher temperature anneals have no significant impact on the intensity of the As 3d substrate signal.

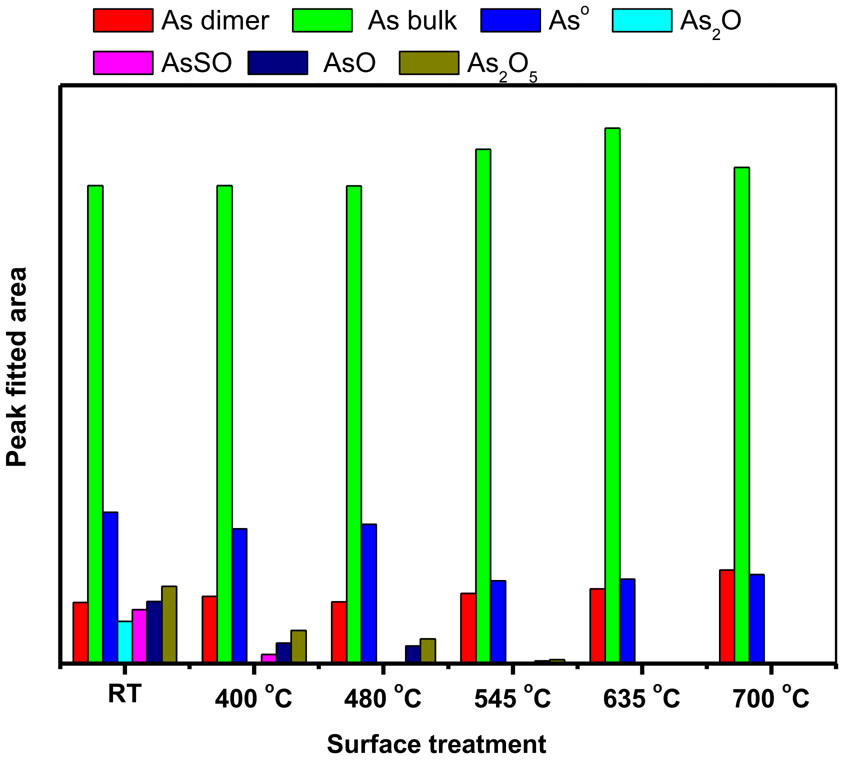

Figure 3.30 Magnitude of the changes in the intensity of arsenic components as a function of thermal anneal are clearly observed.

3.4.3.3 Impact on In 4d/ Ga3d spectra

Figure 3.31 shows the changes in the In 4d/Ga 3d curve fitted photoemission spectra at 69 eV as a result of thermal annealing up to 700 °C. As stated above for the deconvolution of the As peak, similar difficulty occurs here for In and Ga peak oxidation states in making any distinction between oxides and sulphides, so no attempt was made to identify these individual component peaks. At RT, In 4d/Ga 3d bulk peaks were curve fitted with single spin-orbit-split components separated by 1.80 eV binding energy and chemically shifted components consisting of the In^{1+} (+0.45 eV) , In^{2+} (+ .60 eV), Ga^{1+} (+0.60 eV) and Ga^{3+} (+1.1 eV) oxidation states [22].

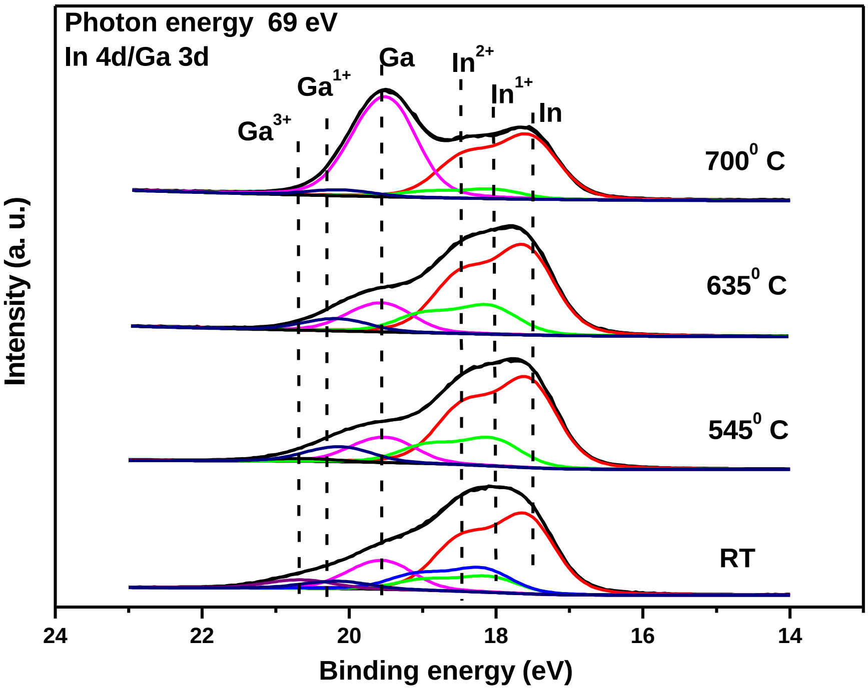

Figure 3.31 Curve fitted core level spectra of In 4d/Ga 3d at a photon energy of 69 eV on sulphur passivated InGaAs surface following thermal anneals at various temperature.

Annealing at 545 °C and 635 °C results in a disappearance of the higher oxidation states of In and a concurrent increase in the lower oxidation states of In. Similarly, an increase in the lower oxidation states of Ga and a complete removal of the higher oxidation states was observed following annealing at 635 °C. The final anneal at 700 °C shows a significant decrease in all oxidation states, loss of In and a substantial increase in the Ga signal consistent with the decomposition of the InGaAs surface. Changes in the intensity of the In and Ga signals were calculated from curve fitted area and plotted in the histogram shown in Figure 3.32. Similar behaviour was observed when the same core levels peaks were acquired at a photon energy of 130 eV as shown in Figure 3.33 (a) which reverse the relative intensities of In and Ga peaks due to changes in cross sectional effects and makes it easier to identify the gallium oxidation states. The magnitude of the changes in the intensity of In and Ga component peaks at a photon energy of 130 eV as a function of thermal anneal are clearly observed in Figure 3.33 (b).

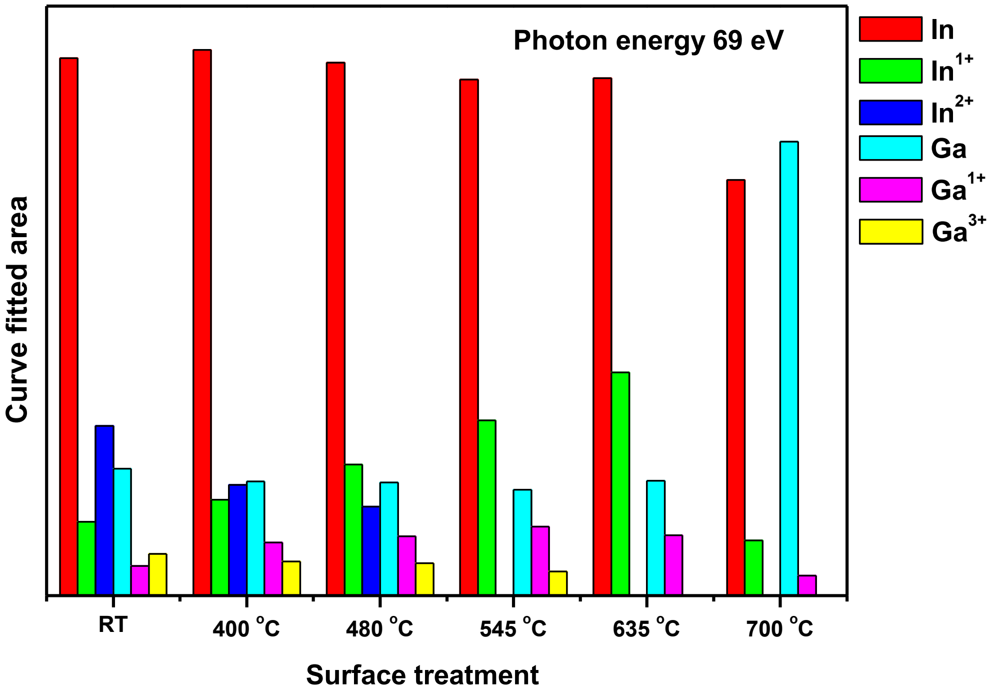

Figure 3.32 Magnitude of the changes in the intensity of In and Ga components as a function of thermal anneal up to 700 °C.

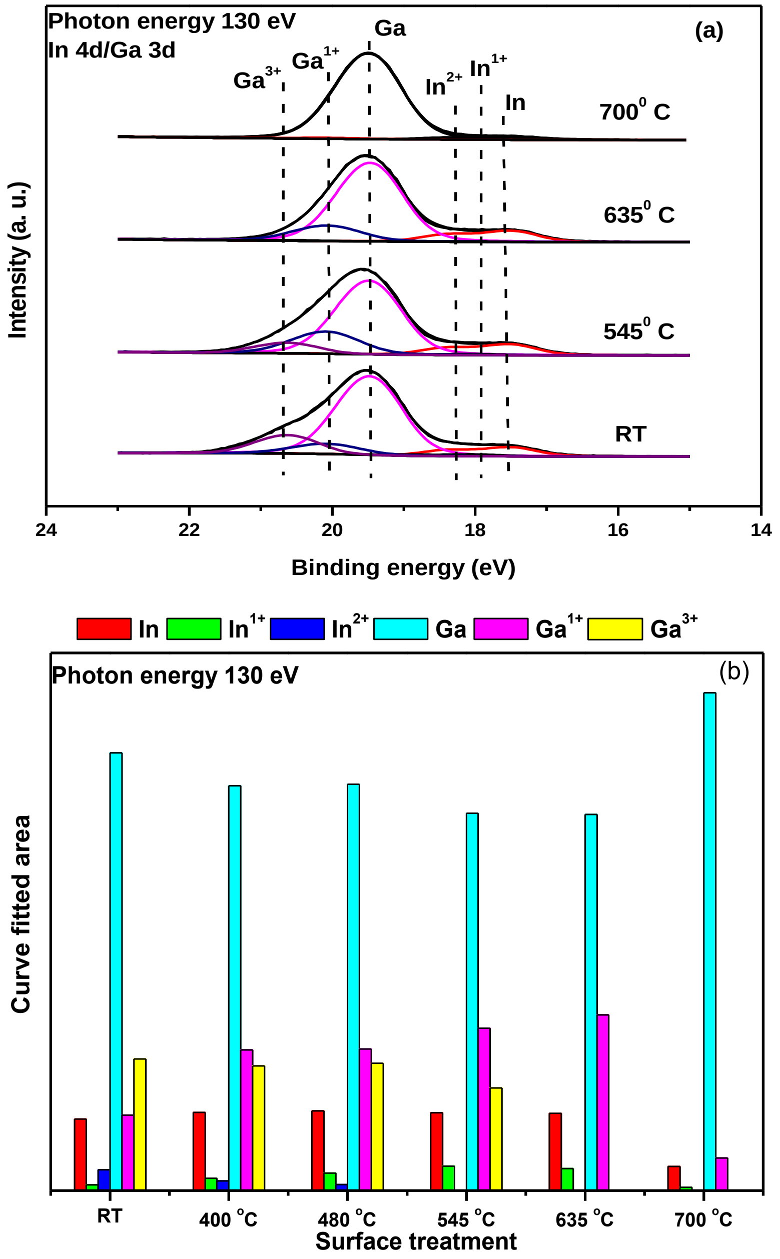

Figure 3.33 (a) Curve fitted core level spectra of In 4d/Ga 3d core levels at a photon energy of 130 eV on sulphur passivated InGaAs surface following thermal anneals (b) the magnitude of the changes in the intensity of In and Ga components as a function of thermal anneal up to 700 °C.

The effect of thermal anneals up to high temperature on the In 4d/Ga 3d core level intensities can be seen from the curve fitted spectra. Again the effects of annealing at 700 °C on the surface chemical composition can be observed as resulting in a substantial loss of the In from the surface. By acquiring these photoemission spectra at a photon energy 105 eV, which gives almost equal signal of the In and Ga core levels, the extent of the indium loss can be quantified. These spectra along with the areas calculated from curve fitted peaks are displayed shown in Figure 3.34 (a) and (b).

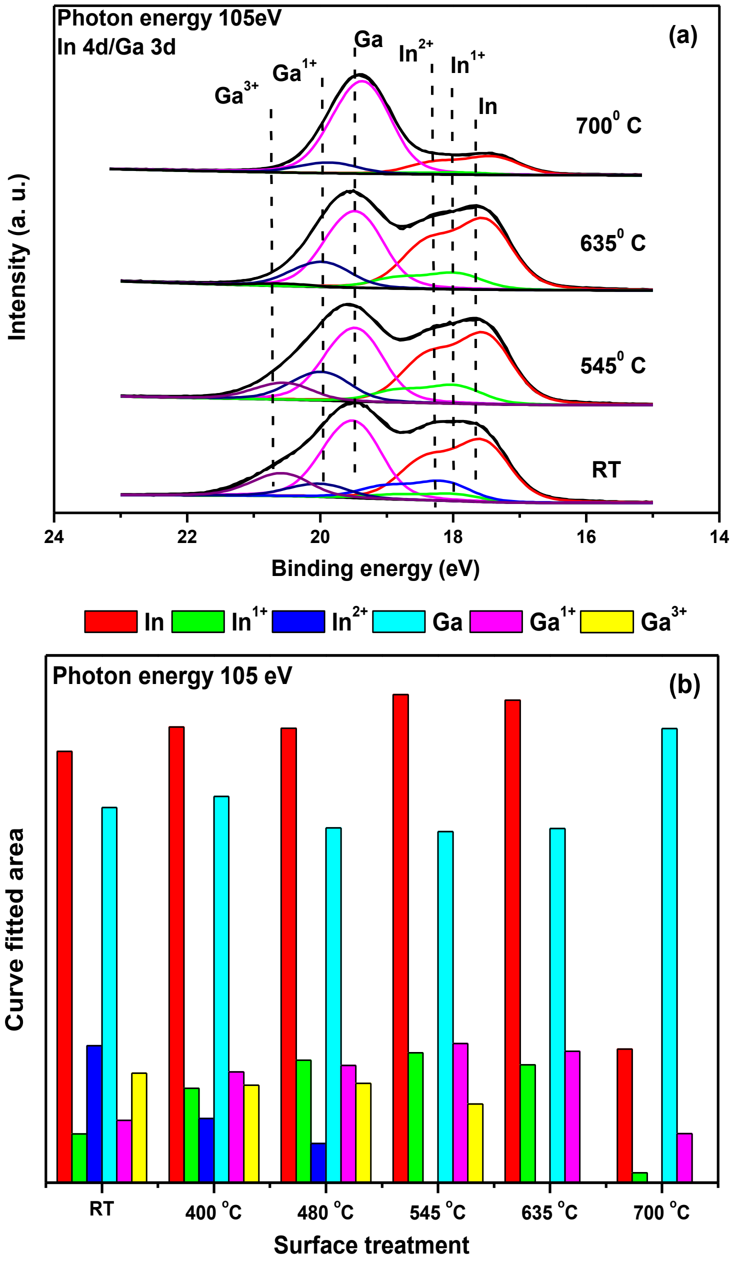

Figure 3.34 (a) Curve fitted core level spectra of In 4d/Ga 3d at photon energy of 105 eV on sulphur passivated InGaAs surface following thermal anneals (b) The magnitude of the changes in the intensity of In and Ga components as a function of thermal anneal are clearly observed.

The wet chemically sulphur treated surface was stable up to the 635 ^{o}C anneal which is attributed to the presence of mixed phase of oxides and sulphides enhancing the thermal stability of the surface. The higher temperature anneals results in the removal of substantial amounts of the residual surface oxides. However, it appears that when these oxides have been removed, the surface becomes chemically unstable and begins to decompose. This loss of indium on the wet chemically prepared sulphur passivated surface will be compared in the next section with the thermal behaviour of the in-situ molecular sulphur passivated atomically clean InGaAs surface and the atomically clean InGaAs surface [43].

Sugahara et al. [30] have shown in a synchrotron radiation photoelectron spectroscopy study that Ga-S, As-S, and S-S bonds are formed on $(NH_4)S$ treated GaAs surface, but Ga-S bonds become dominant after annealing at 360 ^{o}C for 10 mm in vacuum. The O 1s core level spectra were also recorded at a photon energy of 600 eV and the raw data are shown in Figure 3.35 following thermal anneals up to 700 ^{o}C. A weak signal of O 1s peak is observed which indicates that a small amount of oxide is present on the surface. A decrease in O 1s signal was seen as a function of annealing temperature. At 545 ^{o}C a very small signal was observed while no oxygen O 1s signal was observed on further annealing at 635 ^{o}C and 700 ^{o}C.

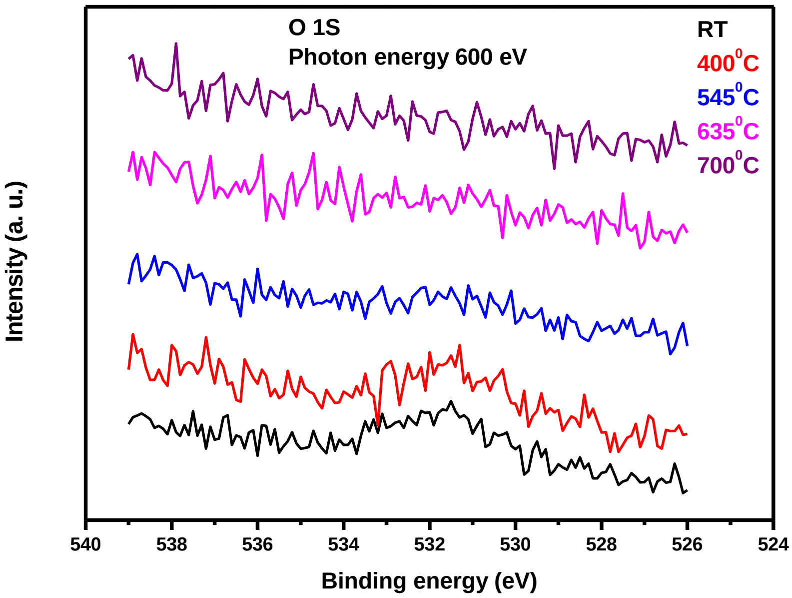

Figure 3.35 Changes in the O 1s at a photon energy of 600 eV signal as a function of thermal anneals up to 700 ^{o}C on a wet chemical sulphur passivated surface.

Figure 3.36 displays changes in the sulphur 2p signal as a function of thermal anneal and illustrates a large drop in sulphur was observed only at 700 °C anneal which reflects desorption of the most of the sulphur from the surface at this temperature.

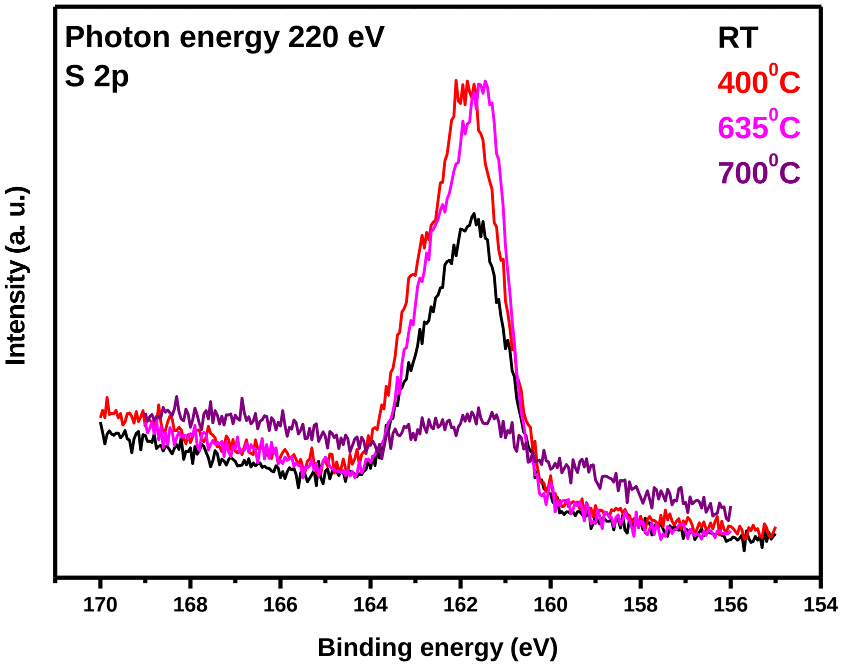

.

Figure 3.36. Changes in the S 2p signal at a photon energy of 220 eV as a function of thermal anneals up to 700 °C.

3.5 Thermal stability comparison between differently prepared InGaAs surfaces

The atomically clean InGaAs surface was prepared by desorbing a 100 nm thick As cap layer from the surface by annealing at 410 °C. To study the effect of high temperature anneals, the atomically clean surface was annealed at high temperature up to 530 °C (section 3.2.3). It was observed that annealing at 530 °C leads to a 5% reduction in the intensity of the In 4d core level with no reduction in Ga signal. A further drop in indium signal (15%) was measured following a 560 °C anneal [44], while no corresponding reduction in the Ga or As signals was observed. No change in the In:Ga ratio was observed up to 480 °C which shows that the surface is stable up to this temperature. The thermal stability of the clean surface favourably compares with the typical InGaAs growth temperature of 500 °C in that the chemical composition is stable even in the absence of an arsenic flux [45]. While the in-situ sulphur passivated surface displayed a significant loss of indium following a 480 ^{o}C anneal (section 3.3.2), the atomically clean InGaAs surface was found to be stable at this temperature. A higher anneal at 530 ^{o}C resulted in a further reduction in the indium signal on the sulphur passivated surface and only a small reduction is seen on the atomically clean surface. No change in the intensity of the As 3d spectrum was observed during these thermal anneals [43]. A summary of the thermal stability for three surfaces prepared in this work is shown in table 1.

Table 1 : Thermal stability of the atomically clean, in-situ dry sulphur and ex-situ wet chemical sulphur passivated InGaAs surface

Surface type	**Initial decomposition temperature (Indium loss in %)**	**Higher temperature anneal (Indium loss in %)**
Atomically clean InGaAs surface	530 ^{o}C (5 %)	560 ^{o}C (15 %)
In-situ sulphur passivated surface	480 ^{o}C (33 %)	530 ^{o}C (50 %)
Ex-situ wet chemical sulphur passivated surface	700 ^{o}C (80 %)	----------

When these two surfaces were compared with ex-situ sulphur passivated surface, it was found that the ex-situ treated surface is stable up to higher temperature (635 ^{o}C) and thereafter an 80 % reduction in the indium signal is observed. Ex-situ wet chemically sulphur passivated InGaAs (section 3.4.3) is more thermally stable than in-situ S-based passivation of atomically clean InGaAs and atomically InGaAs surfaces. The stability of the wet chemical sulphur passivated surface up to 635 ^{o}C is attributed to the presence of thermally stable In and Ga sub-oxides and sulphides. These studies show that the changes induced in surface chemical composition resulting from the incorporation of sulphur in the near surface region of InGaAs by in-situ sulphur passivation significantly impact on the thermal stability of the surface. Given that post deposition annealing treatments at temperatures of 500 ^{o}C have been used to improve the electrical characteristics of Al_2O_3/InGaAs based MOS structures [46] the thermal stability of chemically modified InGaAs is of importance.

3.6 Conclusion

This chapter has compared the thermal stability of the atomically clean InGaAs surface with that of different sulphur passivated surfaces. High temperature thermal annealing studies of atomically clean InGaAs up to 560 ^{o}C were performed to see the effect of thermal anneals on the compositional changes in InGaAs surfaces. In-situ sulphur passivation was carried out on the atomically clean InGaAs surface. The room temperature sulphur adsorption leads to the formation of As, In and Ga bond to sulphur while annealing at 410 ^{o}C results in the complete removal of the As-S bonding states with only sulphur bonds to In and Ga remaining. The important result of this study is the fact that the Fermi level position is in the mid band gap for the clean surface of both doping types and that sulphur adsorption moves the Fermi level close to the conduction band for both materials. The study shows that sulphur is acting as a donor in the near surface region and this has to be considered in its use as a surface passivation layer. There is also an increase in work function observed during sulphur deposition due to the formation of a surface dipole. High temperature annealing studies of in-situ sulphur passivation followed by thermal anneals up to 530 ^{o}C have shown significant changes in the chemical composition of the surface. The important result of this study is the fact that the Fermi level position which is in a mid band gap position on the clean surface of both doping types moves close to the conduction band following sulphur deposition, independent of initial doping type. This indicates that the replacement of arsenic by sulphur in the near surface region results in it acting as a surface dopant

This chapter also investigated the ex-situ wet chemical sulphur passivation of native oxide surface and compared it with the native oxide surface. It was observed that sulphur passivation was very effective in most of removing the oxide from the surface and forming a protective layer to protect it from ambient oxidation. High temperature annealing up to 700 ^{o}C has been carried out to observe the compositional changes as a function of thermal anneals. It was observed that the surface is stable up to 635 ^{o}C which is attributed due to the presence of oxides and sulphides.

The ex-situ treated surface was found to be more thermally stable than the in-situ treated surface at high temperature These findings have important consequences for high temperature annealing of InGaAs based devices as it is important to preserve the InGaAs stoichiometry for applications in high mobility electron channel devices. Since majority carrier mobility in InGaAs scales with indium content, the thermal stability of the InGaAs surface is an important consideration in that preserving the stoichiometry in the near surface region has implications for channel mobility in a device.

3.7 References

[1] Akazawa, M., and Hasegawa, H. Appl. Surf. Sci. 256, 5708,

[2] Bernal Granados-Alpizar, Fee Li Lie, and Anthony J. Muscat, J. Vac. Sci. Technol. A 31, 01A143 (2013)

[3] B. Brennan, M. Milojevic, C.L. Hinkle, F.S. Aguirre-Tostado, G. Hughes, R.M. Wallace Appl. Surf. Sci., 257, 4082 (2011)

[4] R. Driad, W. R. McKinnon, Z. H. Lu, S. P. McAlister, P. J. Poole, and S. Charbonneau, J. Vac. Sci. Technol. A 18, 697 (2000)

[5] Yun Sun, Piero Pianetta, Po-Ta Chen, Masaharu Kobayashi, Yoshio Nishi, Niti Goel, Michael Garner, and Wilman Tsai, Appl. Phys. Lett. 93, 194103 (2008)

[6] S. Ingrey, W. M. lau and R. N. S. Sodhi, J. Vac. Sci. Technol. A 7, 1554 (1989)

[7] E. Martinez, H. Grampeix, O. Desplats, A. Herrera-Gomez, O. Ceballos-Sanchez, J. Guerrero,K. Yckache, F. Martin Chem. Phys. Lett. 539,139 (2012

[8] M. Kobayashi, P. T. Chen, Y. Sun, N. Goel, P. Majhi, M. Garner, W. Tsai, P. Pianetta, Y. Nishi, Appl. Phys. Lett. 93, 182103 (2008)

[9] Hock-Chun Chin, Benzhong Wang, Poh-Chong Lim, Lei-Jun Tang, Chih-Hang Tung, Yee-Chia Yeo J. Appl. Phys. 104, 093527 (2008).

[10] Byungha Shin, Jonathon B. Clemens, Michael A. Kelly, Andrew C. Kummel, Paul C. McIntyre, Appl. Phys. Lett. 96, 252907, (2010)

[11] W. M. Lau, R. N. S. Sodhi, S. Jin, S. Ingrey, N. Puetz, A. SpringThorpe, J. Appl. Phys. 67, 768 (1990)

[12] J. Shen, D. L. Feldwinn, W. Melitz, R. Droopad, and A. C. Kummel, Microelectron. Eng. 88, 377 (2011)

[13] J. Shen, J. B. Clemens, E. A. Chagarov, D. L. Feldwinn, W. Melitz, T.Song, S. R. Bishop, A. C. Kummel, and R. Droopad, Surf. Sci. 604, 1757 (2010)

[14] Hock-Chun Chin, Xinke Liu, Xiao Gong, and Yee-Chia Yeo, IEEE Trans. Elect. Dev., 57, 5 (2010)

[15] Wilhelm Melitz, Jian Shen, Tyler Kent, Andrew C. Kummel, Ravi Droopad, J. Appl. Phys. 110, 013713 (2011)

[16] F. S. Aguirre-Tostado, M. Milojevic, C. L. Hinkle, E. M. Vogel,R. M. Wallace, S. McDonnell, and G. J. Hughes, Appl. Phys. Lett. 92, 171906 (2008)

[17] E. O’Connor, R. D. Long, K. Cherkaoui, K. K. Thomas, F. Chalvet, I. M.Povey, M. E. Pemble, P. K. Hurley, B. Brennan, G. Hughes, and S. B. Newcomb, Appl. Phys. Lett. 92, 022902 (2008)

[18] É. O’Connor, B. Brennan, V. Djara, K. Cherkaoui, S. Monaghan, S. B. Newcomb, R. Contreras, M. Milojevic, G. Hughes, M. E. Pemble, R. M. Wallace, and P.K. Hurley, J. Appl. Physics 109, 024101 (2011).

[19] D Sheela and Nandita Das Gupta, Semicond. Sci. Technol. 23, 035018 (2008)

[20] A. Alian, G. Brammertz, R. Degraeve, M. Cho, C. Merckling, D. Lin, W. Wang, M. Caymax, M. Meuris, K. D. Meyer, and M. Heyns, IEEE Elect. Devi. Lett. 33, 11 (2012).

[21] P. Moriarty, B. Murphy, L. Roberts, A. A. Cafolla, Greg Hughes, L. Koenders, and P. Bailey, Phys. Rev. B 50, 19 (1994).

[22] Surface and interface characterisation of high-κ dielectric materials on silicon and III-V semiconductor substrates, Dublin City University, Barry Brennan ,Chap. 3, 78, (2009)

[23] M. V. Lebedev, E. Mankel, T. Mayer, and W. Jaegermann,J. Phys. Chem. C114, 21385 (2010)

[24] J. Robertson, Appl. Phys. Lett, 94, 152104 (2009)

[25] C. J. Sandroff, M. S. Hegde, and C. C. Chang,J. Vac. Sci. Technol. B7,841 (1989)

[26] D. Paget, J. E. Bonnet, V. L. Berkovits, P. Chiaradia, and J. Avila, Phys. Rev. B53, 4604 (1996)

[27] P. T. Chen, Y. Sun, E. Kim, P. C. McIntyre, W. Tsai, M. Garner, P.Pianetta, Y. Nishi, and C. O. Chui, J. Appl. Phys. 103, 034106 (2008)

[28] C. J. Sprindt, D. Liu, K. Miyano, P. L. Meissnerm, T. T. Chiang, T. Kendelewicz, I. Lmdau, and W. E. Spicer,Appl. Phys. Lett.55, 861 (1989)

[29] L. W. Lai, J. T. Chen, L. R. Lou, C. H. Wu, C. T. Lee, J. Electrochem. Soc. 155, B1270 (2008)

[30] H. Sugahara, M. Oshima, H. Oigawa, H. Shigekawa, and Y. Nannichi, J. Appl. Phys. 69, 4349 (1991)

[31] P. Moriarty, B. Murphy, L. Roberts, A. A. Cafolla, G. Hughes,L. Koenders, P. Bailey, and D. A. Woolf, Appl. Phys. Lett.67, 383 (1995)

[32] T. Scimeca, Y. Watanabe, R. Berrigan, and M. Oshima, Phys. Rev. B46,10201 (1992)

[33] T. Ohno and K. Shiraishi, Phys. Rev. B 42, 11194 (1990)

[34] L. Koenders, M. Blomacher, and W. Monch, J. Vac. Sci. Technol B 6, 1416 (1988)

[35] D. R. T Zahn, T. U. Kampen, S. Hohenecker, and W. Brau, Vacuum 57,139 (2000)

[36] T. C. Leung, C. L. Kao, W. S. Su, Y. J. Feng, and C. T. Chan, Phys. Rev. B 68, 195408 (2003)

[37] B. Brennan and G. Hughes, J. Appl. Phys. 108, 053516, (2010

[38] T. Ishikawa and H. Ikoma, Jpn. J. Appl. Phys. 31, 3981 (1992)

[39] C. J. Sandroff, M. S. Hegde, and C. C. Chang, J. Vac. Sci. Technol. B7, 841 (1989)

[40] N. N. Berchenko and Y. V. Medvedev, Usp. Khim., 63, 655 (1994)

[41] J. Shin, K. M. Geib, and C. W. Wilmsen, J. Vac. Sci. Technol. B9, 2337(1991)

[42] C. J. Spindt, R. S. Besser, R. Cao, K. Miyano, C. R. Helms, and W. E. Spicer, J. Vac. Sci. Technol. A7, 2466 (1989)

[43] L. Chauhan and G. Hughes J. Appl. Phys., 111,114512 (2012)

[44] L. Chauhan, and G. Hughes, Phy. Stat. Sol. (a) 210, 519 (2013)

[45] L.W. Lai, J. T. Chen, L.R. Lou, C.H. Wu, C-T. Lee, J. Electrochem. Soc. 155, B1270 (2008)

[46] H. D. Trinh, E. Y. Chang, P. W. Wu, Y. Y. Wong, C. T. Chang, Y. F. Hsieh, C. C. Yu, H. Q. Nguyen, Y. C. Lin, K. L. Lin, and M. K. Hudait, Appl. Phys. Lett. 97, 042903 (2010)

Chapter 4

Interface characterisation of Al_2O_3 deposition on differently prepared InGaAs surfaces by x-ray photoemission and high resolution synchrotron radiation based photoemission spectroscopy

4.1 Introduction

As mentioned in Chapter 1, high indium content InGaAs is a leading III-V semiconductor candidate to realise high performance for n-channel metal oxide semiconductor (MOS) devices driven by the need for high speed and low power transistors at the nanometre scale. In recent years significant progress has been made in improving the electrical quality of the high-k dielectric-InGaAs interface by the atomic layer deposition (ALD) of high-k materials on passivated surfaces [1-3]. A range of experimental passivation approaches to control D_{it} by removal of the native oxide have been employed [4-8]. One of the more common ex-situ passivation techniques involves the use of sulphur based chemicals such as ammonium sulphide $(NH_4)_2S$ [1,9] which is widely used due to its effectiveness at removing native oxides and passivating the surface thereby improving the electrical characteristics of devices [1,3,10,11].

In the literature it has been reported that different thermal treatments like post deposition forming gas annealing at temperatures of 400-500 ^{o}C can be used to improve the electrical characteristics of Al_2O_3/InGaAs based MOS structures [12,13]. There is therefore a need to understand what effect these high temperature anneals have on the Al_2O_3/InGaAs interface chemistry as some studies have shown evidence of inter-diffusion across the interface [13,14]. In the previous chapter [15,16] our investigations have shown a much higher indium loss from the in situ sulphur passivated InGaAs surface compared to either the ex situ or the atomically clean InGaAs surface at 530 ^{o}C. Also, similar studies of indium lost have been reported by Aguirre-Tostado et al. [17] where the native oxide InGaAs surface was annealed and exposed to atomic hydrogen. Since majority carrier mobility in InGaAs scales with indium content, the thermal stability of the InGaAs surface is an important consideration in that preserving the stoichiometry in the near surface region has implications for channel mobility. Hence, understanding changes in the interface chemistry of the sulphur-passivated InGaAs surfaces capped with insulators, such as Al_2O_3, at high temperature is important for InGaAs based MOS devices.

In this study comparison has been made between XPS and high resolution synchrotron radiation based photoemission spectroscopy (HRSPES) measurements of interface formation between Al_2O_3 and differently prepared InGaAs surfaces. The advantage of using synchrotron based photoemission for this study is the higher surface sensitivity afforded by control of the kinetic energy of the emerging photoelectrons resulting in sampling depths of ~2 nm which is significantly smaller than conventional x-ray photoelectron spectroscopy (XPS).

4.2 Experimental

N-type Be doped $In_{0.53}Ga_{0.47}As$ epilayer 0.5 μm thick (S: $5x10^{17}$ cm $^{-3}$) lattice matched to InP substrates were degreased for 1 min in acetone followed by 1 min rinse in methanol prior to being immersed in 10% ammonium sulphide ($(NH_4)_2S$) solution for 20 min at room temperature (290 K). Both sulphur passivated and native oxide covered samples were then immediately loaded into an atomic layer deposition (ALD) chamber load lock within a minute to minimize the air exposure. The TMA was delivered to an integrated dual chamber ALD reactor with a substrate temperature of 250 °C and a base pressure of ~700 mTorr through heated lines and valve. TMA oven was at 35 ^{o}C , TMA line is at 75 ^{o}C and H_2O oven at room temperature. Approximately 10 cycles of alumina (Al_2O_3) was deposited at 300 ^{o}C using tri-methyl aluminium (TMA) and water as the precursors. Each full cycle consisted of:

0.1 s TMA + 4 s N_2+ 0.1 s H_2O + 4 s N_2

Before the photoemission experiments samples were exposed to air for 15 days. samples were subsequently secured to a molybdenum holder and measured on the soft x-ray photoemission SX700 beam line at the ASTRID synchrotron in the University of Aarhus in an ultra high vacuum (UHV) system which had a base pressure of $5x10^{-10}$ mbar. Photoemission core level spectra were subsequently acquired for In 4d, Ga 3d, As 3d, Al 2p, O1s and S 2p core levels following thermal anneals up to 700 ^{o}C. A photon energy of 92 eV was chosen for As 3d and while a range of photon energies (69 eV, 105 eV and 130 eV) were used to acquire the In 4d/Ga 3d core levels for the photoionization cross-sectional reasons mentioned in Chapter 3. The spectra were curve fitted using Voigt profiles and using a Shirley-type back ground as previously reported [17]. The total energy resolution in these photoemission experiments is estimated to be ~ 0.7 eV.

4.3 Advantage of synchrotron technique over convention XPS

Figure 4.1 displays the comparison of the As 3d spectra acquired at a photon energy of 92 eV for InGaAs using conventional XPS and synchrotron based photoemission for different surfaces/interfaces. Figure 4.1(a) shows the As 3d profile for 1 nm Al_2O_3 layer on sulphur passivated surface (A1), the native oxide surface (A2) and the InGaAs native oxide surface with no dielectric overlayer (A3). The exact same samples were then measured using the MgKα x-ray line for a conventional XPS source and the corresponding spectra are shown in Figure 4.1(b). The Figure shows the advantage of the synchrotron source in terms of surface sensitivity in detecting the extent of interface oxidation in that oxide/sulphides component peaks which are not observed in the XPS measurements can be seen in the synchrotron radiation spectra. With an incident photon energy of 92 eV, the emerging photoemitted electrons have a kinetic energy of ~50 eV which is at the minimum of the inelastic mean free path (IMFP) curve, giving a sampling depth into the material of approximately ~ 2 nm. Using the convention Mg Kα x-ray source, the emerging As 3d photoelectron has a kinetic energy of ~1200 eV giving an total sampling depth of ~ 6-7 nm into the material. On the sulphur passivated sample (A1) no interfacial oxide is observed in the XPS spectrum, however, a clear interfacial oxide signal can be seen in the HRSPES spectrum acquired using 92 eV photon energy.

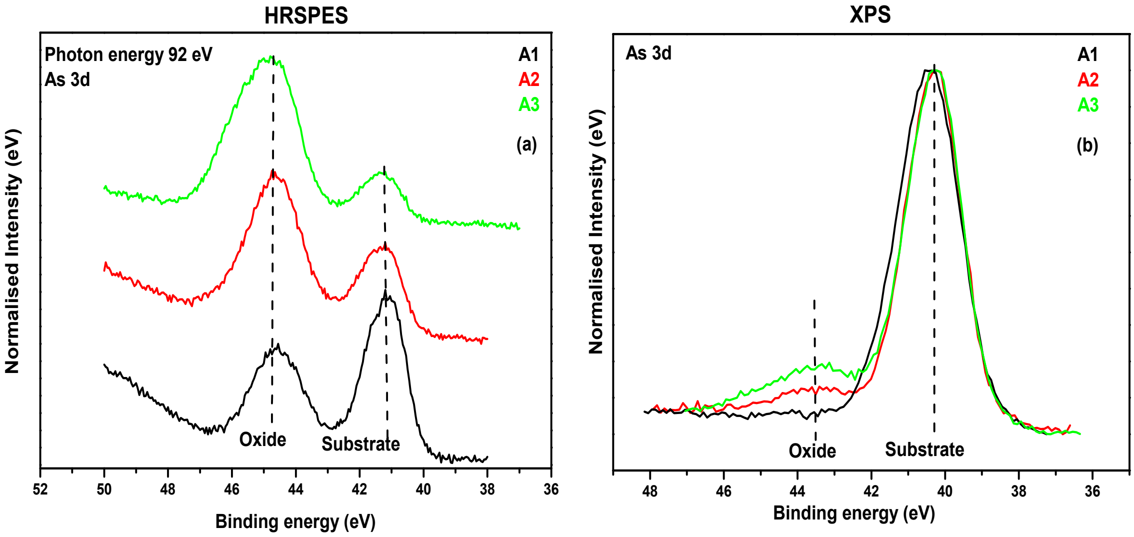

Figure 4.1 Comparison of the As 3d spectra for (a) synchrotron based photoemission (92 eV) photon energy and (b) conventional XPS for different surfaces/interfaces : 1nm Al_2O_3 layer on sulphur passivated surface (A1) and native oxide surface (A2), bare native oxide surface (A3) (no overlayer)

Curve fitted spectra of As 3d and In 4d /Ga 3d are shown in Figure 4.2 for samples A1 and A2, using both the 92 eV photon energy and XPS. For both samples, the As 3d core level XPS spectra are curve fitted with a bulk As component, elemental arsenic (+0.75 eV) and mixed phase of interfacial arsenic oxides composed of As^{2+} (+ 2.7 eV), As^{3+}(+ 3.4 eV) and As^{5+} (+ 4.7 eV). Similarly, the As 3d core level spectra recorded at a photon energy of 92 eV are curve fitted with a bulk As component, As dimer/dangling bond (-0.65 eV) elemental arsenic (+ 0.75 eV) and mixed phase of interfacial arsenic oxides composed of As^{1+} (+1.4 eV) , As^{2+} (+ 2.7 eV) As^{3+}(+ 3.4 eV) As^{5+} (+ 4.7 eV).

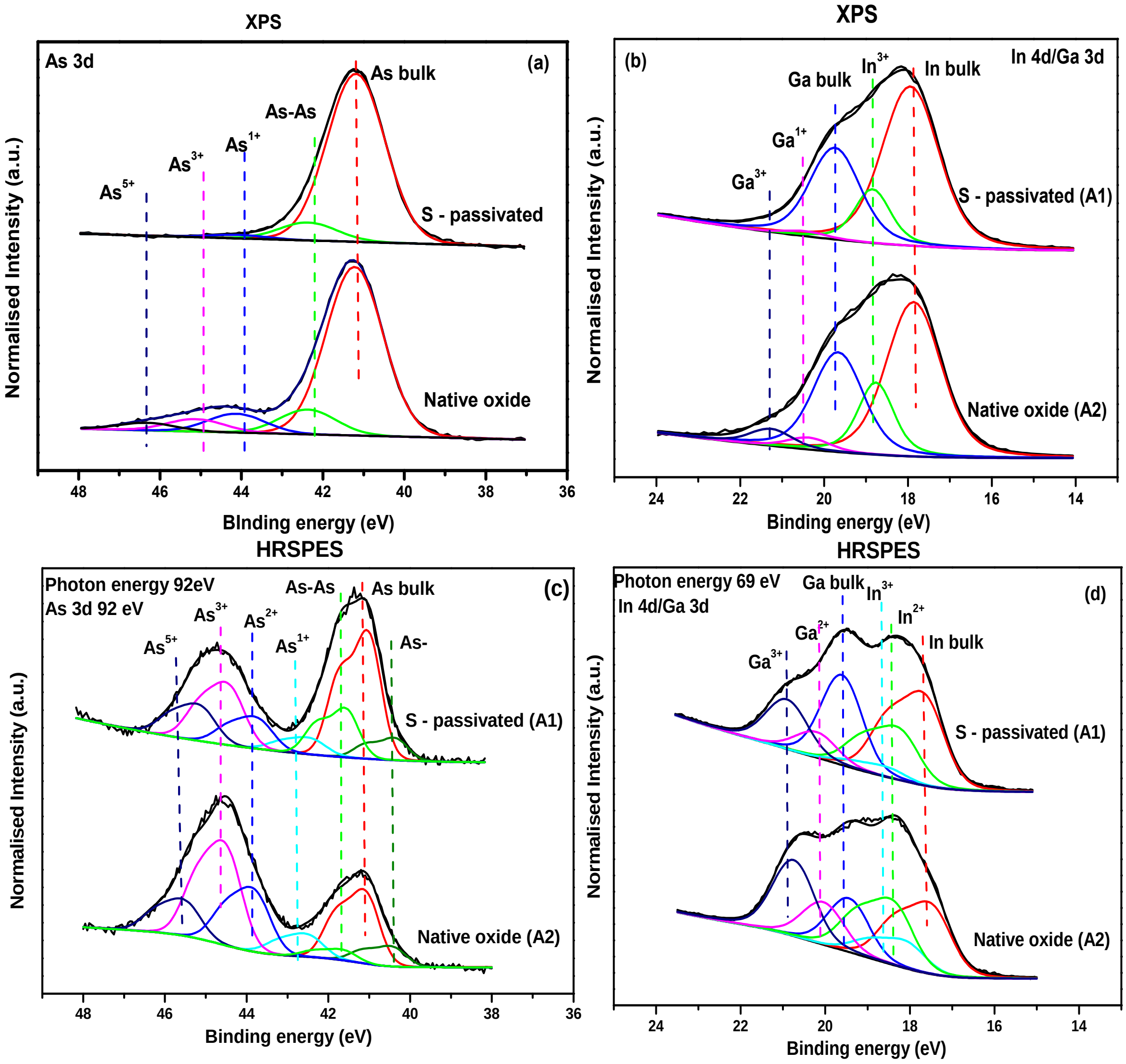

Figure 4.2 Comparison of oxidation states in curve fitted core level spectra of As 3d and In4d/Ga3d by XPS and HRSPES for Al_2O_3 deposited on sulphur passivated and native oxide surface using XPS (a) As 3d and (b) In 4d/Ga 3d and using HRSPES (c) As 3d and (d) In 4d/Ga 3d

Similarly, In 4d/Ga 4d core level XPS spectra are curve fitted with single spin-orbit split components separated by 1.80 eV binding energy and chemically shifted components consisting of the In^{3+} (+ 0.90 eV), Ga^{1+} (+ 0.60 eV) and Ga^{3+}(+ 1.3 eV) oxidation states, respectively. The In 4d /Ga 4d bulk synchrotron spectra at a photon energy 69 eV is curve fitted with single spin orbit split components separated by 1.80 eV binding energy and chemically shifted components consisting of the In^{2+} (+ 0.60 eV) , In^{3+} (+ 0.90 eV), Ga^{1+} (+ 0.60 eV) and Ga^{3+}(+ 1.3eV) oxidation states. The differences in the As 3d curve fitted spectra between the two measurement methods indicate the significantly enhanced surface sensitive of the 92 eV photon synchrotron radiation spectra allowing more accurate identification of the individual oxidation states.

For a clearer picture of the reduction of native oxides by sulphur passivation, the curve fitted area of the oxide and substrate signal is shown in a histogram in Figure 4.3. In Figure 4.3 (a) we see an equal intensity of the As bulk signal on both samples A1 and A2 in XPS measurements as signal is received from bulk while in Figure 4.3 (c) the intensity of the As bulk signal on sulphur passivated sample (A1) is greater than on the native oxide sample (A2). As the native oxide sample (A2) has a thicker interfacial oxide than the sulphur passivated sample, the contribution of the substrate signal to the spectrum is reduced. This is attributed to the fact that the synchrotron radiation based photoemission allows the selection of incident photon energies to enhance signal in near surface region. Sulphur passivation effectively removes the native oxides and protects the surface against regrow of the oxide during Al_2O_3 deposition. Therefore, the interfacial oxide thickness is thinner on sulphur passivated sample (A1) than on the native oxide sample (A2).

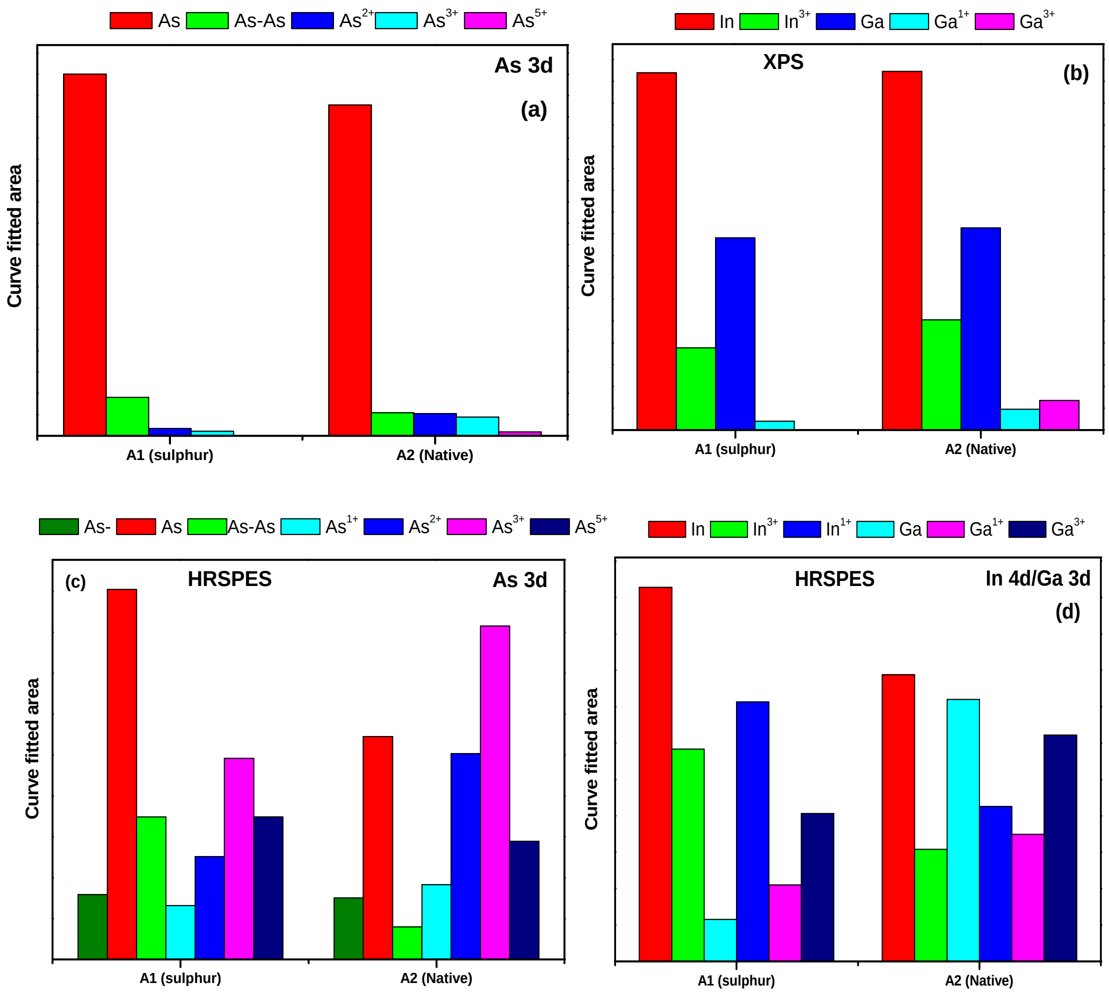

Figure 4.3 Comparison of oxidation states in curve fitted core level spectra of As 3d and In 4d/ Ga3d by XPS and HRSPES for Al_2O_3 deposited on sulphur passivated and native oxide surface (a) As 3d and (b) In 4d/ Ga3d (XPS), (c) As 3d and (d) In 4d/ Ga3d (HRSPES)

Figure 4.4 displays the comparison of the detection level of the interfacial oxides by XPS and HRSPES by calculating the oxide/sulphide to bulk ratio in As 3d and In 4d/Ga 3d spectra on sulphur passivated and native oxide samples. On sample A1, we can see there is substantial amount of interfacial oxide measured by HRSPES while sulphur passivation substantial reduced the oxide level from 0.60 to 0.30, 1.5 to 0.46, 0.92 to 0.22 and 0.26 to 0.16 in the As^{5+}, As^{3+}, As^{2+} and As^{1+} oxidation state ratios, respectively. A rise in As-As signal is observed on the sulphur passivated sample (A1) measured by both techniques and we believe that sulphur passivation removes the oxygen from arsenic oxide and the remaining excess As gives rise to the As-As signal. A drop in the As-dimer/dangling bond is also observed.

Similarly Figure 4.4 (b) displays the In 4d/Ga 3d oxide/sulphide to bulk ratio on sulphur passivated and native oxide sample and comparison of the detection level of the interfacial oxides by XPS and HRSPES.

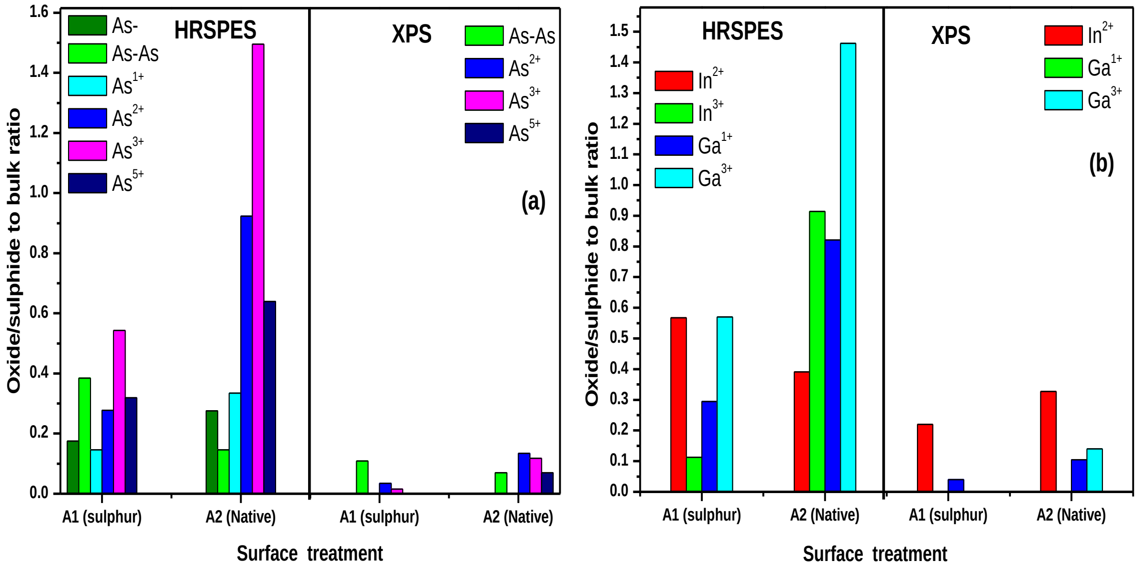

Figure 4.4 Comparison of oxide to bulk ratio measured by HRSPES and XPS for (a) Al_2O_3 on sulphur passivated surface (A1) and (b) native oxide surface (A2)

Similarly, significantly higher levels of oxides or sulphides are observed in the In 4d/Ga 3d core level profiles for measurements made by HRSPES in comparison to XPS. Significant reductions in Ga^{1+} and Ga^{3+} oxidation state ratios are seen after sulphur treatment while a rise in the In^{1+} ratio is observed which we believe to be due to In-S bond formation resulted from the sulphur passivation as sulphur preferentially makes a bond with In as reported in the literature [9,17].

Photoemission spectra of the Al_2O_3 overlayer were acquired using HRSPES at photon energies of 120 eV for the Al 2p and 600 eV for the O 1s core levels as well as with the Al kα source for both sample A1 and A2 and are shown in Figure 4.5 (a)-(d). The binding energy positions of the O 1s and Al 2p core levels are consistent with those expected for Al_2O_3. The intensity of the Al 2p signal acquired by the XPS source is significantly lower than that measured by HRSPES, reflecting the difference in sampling depth related to the kinetic energy of the emerging photoelectrons.

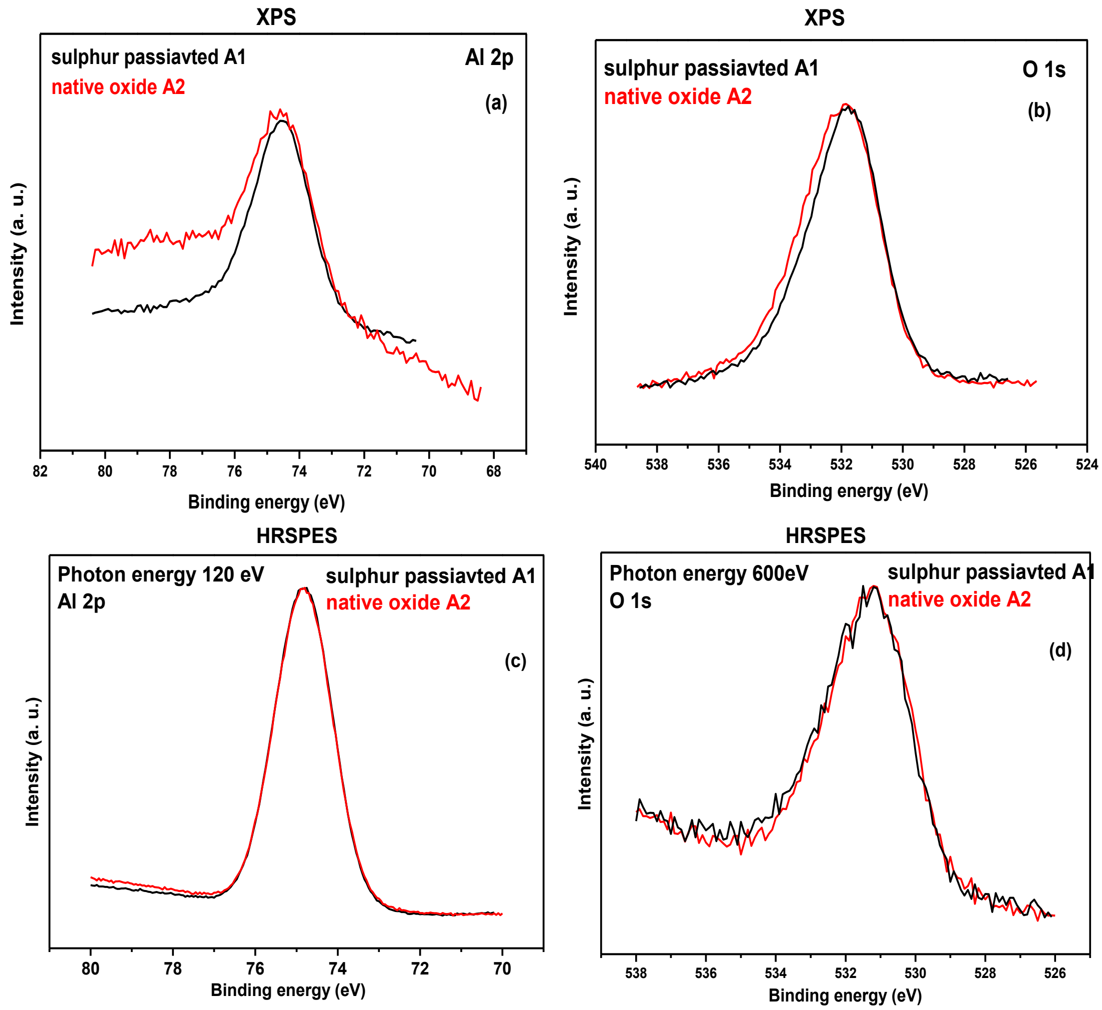

Figure 4.5 Normalised photoemission spectra by HRSPES and XPS for the Al 2p and O1s peaks at photon energies of 120 eV and 600 eV ,respectively, for Al_2O_3 on sulphur passivated (A1) and native oxide (A2) surfaces.

4.4 High temperature thermal stability studies of 1nm Al_2O_3 deposited on native oxide and sulphur passivated InGaAs surfaces

Figure 4.6 (a) and (b) display the As 3d core level spectra for both the sulphur passivated (A1) and native oxide (A2) covered surface following incremental annealing from RT to 700 °C. The spectra highlight the thermally induced reduction of the interfacial oxides for both interfaces. The attenuation in the oxide signal can be seen for annealing temperature above 425 °C with almost complete removal of the oxides at 635 °C and at 700 °C, the surface is arsenic oxide free.

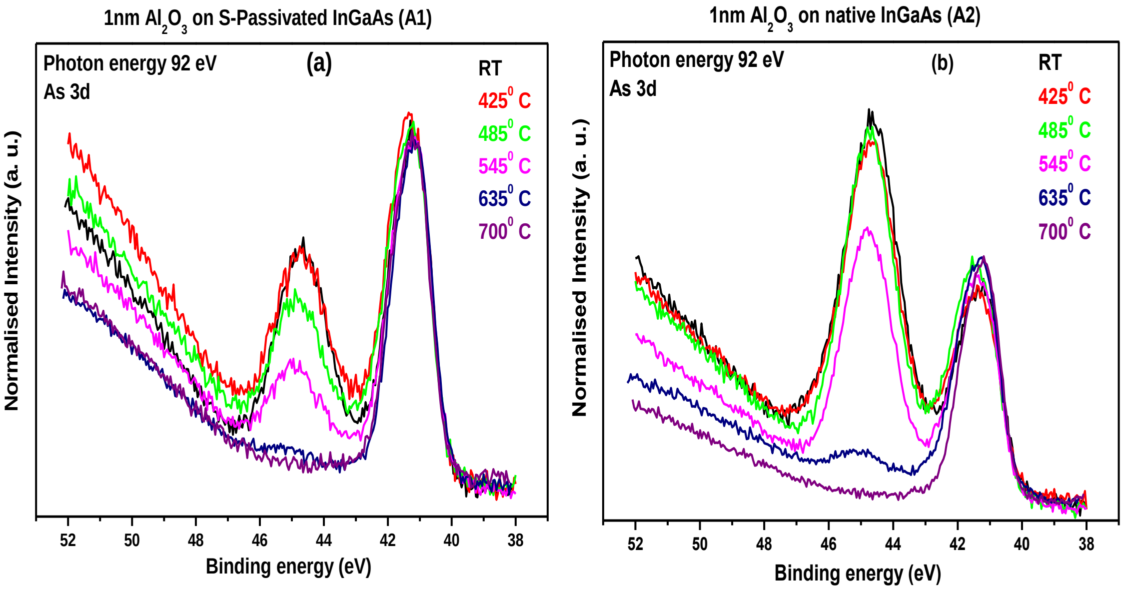

Figure 4.6 Normalised photoemission spectra for As 3d peaks at photon energy 92 eV after annealing at temperatures incrementing from RT to 700 °C for Al_2O_3 on (a) sulphur passivated surface (A1) and (b) native oxide surface (A2)

Similarly, Figure 4.7 (a)-(f) shows the corresponding spectra of In 4d and Ga 3d at the three different photon energies of 69 eV, 105 eV, and 130 eV after incremental annealing from RT to 700 °C for both sulphur passivated (A1) and native oxide (A2) interfaces. The increase in annealing temperature has a significant effect on the composition of the oxides and sulphides present on the surface with changes in the peak intensities and line shapes evident after the first anneal at 425 °C. Annealing at high temperatures has the effect of reducing the interfacial oxide which is apparent from the decreasing width of the composite core level. Significant differences in the relative height of the In 4d/Ga 3d component peaks on the differently prepared surfaces are only apparent following the 700 °C anneal, however detailed analysis of the changes which occur require curve fitting of the spectra which will be presented in the next section. The spectral feature observed at a binding energy of 24 eV is related to the oxygen signal from the Al_2O_3 over layer. Comparison between the differently prepared surfaces indicates that the Al_2O_3 layer is thinner on the native oxide surface reflecting the slower nucleation rate during the ALD growth.

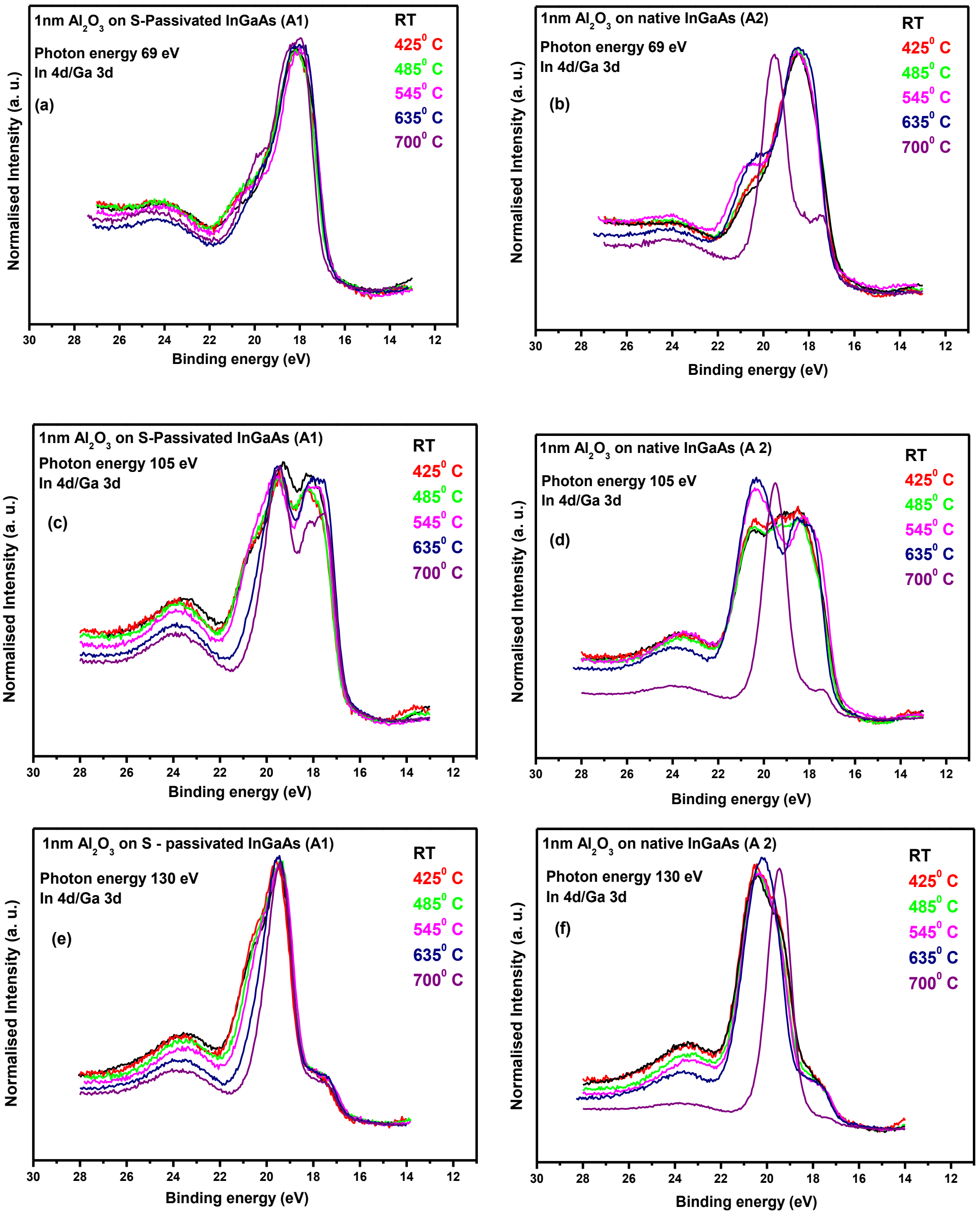

Figure 4.7 Normalised photoemission spectra for the In 4d and Ga 3d peaks at photon energies of 69 eV, 105 eV and 130 eV after annealing at temperatures incrementing from RT to 700 °C for Al_2O_3 on sulphur passivated surface (left) and native oxide surface (right)

4.4.1 Impact on As 3d Spectra

Figure 4.8 shows the changes in the As 3d curve fitted photoemission spectra at 92 eV for 1 nm Al_2O_3 on sulphur passivated (A1) and native oxide InGaAs (A2) surface as a result of thermal annealing up to 700 °C. Due to the relatively small binding energy separation differences between the As 3d bulk peak and the various reported sulphur and oxygen oxidation states [9, 17, 19], no attempt has been made to distinguish between the chemical shifts of the two elements in the curve fitted data. At room temperature, the As 3d peak was curve fitted with a bulk As component, an As dimer or dangling bond related component (- 0.65 eV) [19], elemental arsenic (+ 0.75 eV) and mixed phase of interfacial arsenic oxides composed of As^{1+} ($\Delta \sim +1.4$ eV) , As^{2+} (+ 2.7 eV) As^{3+}(+ 3.4 eV) As^{5+} (+ 4.7eV), respectively. A ‘ + ’ or ‘ - ’ sign indicates a shift toward higher or lower binding energy for both samples A1 and A2.

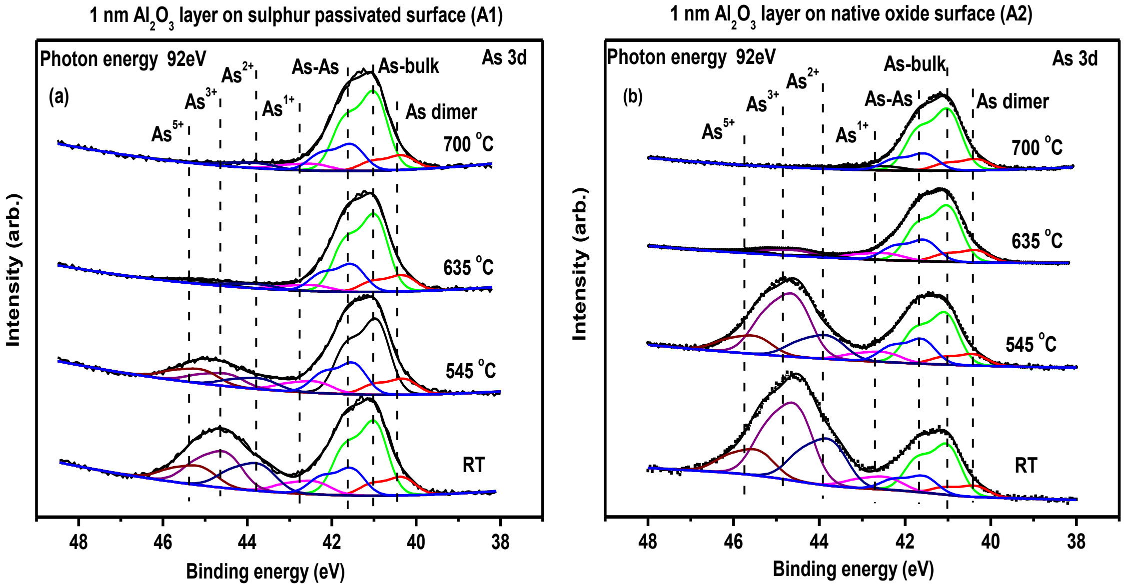

Figure 4.8 Curve fitted photoemission spectra for the As 3d peaks at photon energy of 92 eV after annealing at RT, 545 °C, 635 °C and 700 °C for Al_2O_3 on (a) sulphur passivated sample(A1) and (b) native oxide

Comparison with previous synchrotron radiation photoemission studies of oxidised InGaAs at these photon energies [19], indicate that the thickness of the interfacial oxide on the sulphur passivated surface is estimated to be no more than 0.3 nm while on the native oxide surface, the interfacial oxide is less than 0.7 nm thick. During the initial thermal anneals up to 485 °C for both samples a decrease in the higher oxidation state peak intensities (As^{2+}, As^{3+} and As^{5+}) was recorded with a concurrent increase in lower oxidation states As^{1+}. An increase in the intensity of the elemental As was also observed at this temperature which is attributed to the reduction of the arsenic oxides. This observed preferential removal of the higher oxidation states with thermal annealing is similar to the behaviour previously reported for the thermal anneal of native oxides on InGaAs [19]. Subsequent annealing at 545 ^{o}C shows a decrease in all arsenic oxidation states on both A1 and A2 samples as shown in Figure 4.8. Annealing at 635 ^{o}C removed all the higher As oxidation states (As^{3+}, As^{5+}) on sample A1 with only traces of As^{1+} and As^{2+} states remaining while residual evidence of all arsenic oxidation states was observed on sample A2. Subsequent annealing at 700 ^{o}C shows only a small change in the As interfacial oxides for the sulphur passivated surface with elemental As, As dimers/dangling bond related signal and residual As^{1+} and As^{2+} signals remain at the interface while for sample A2, there is effectively a complete removal of the As interfacial oxides. For a clearer picture of the changes induced by the thermal anneals, the intensity ratio of the individual arsenic oxidation states to the bulk arsenic signals are shown in Figure 4.9 (a) and (b) for both samples.

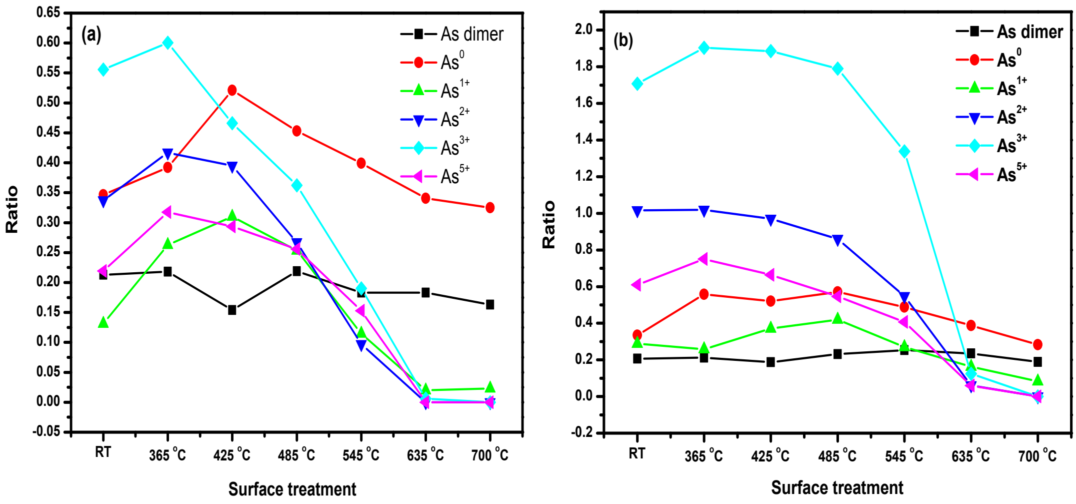

Figure 4.9 Arsenic oxidation states component to arsenic bulk ratio highlighting changes in the oxide composition as a function of thermal anneals (a) for Al_2O_3 on sulphur passivated InGaAs surface (A1) (b) for Al_2O_3 on native oxide InGaAs surface (A2)

The ratios reflect the thicker initial interfacial oxide on sample A2 compared to the sulphur passivated surface which is attributed to the effectiveness of the sulphur treatment at removing the native oxide. As reported in the literature [20,21,22], the

ALD deposition of Al_2O_3 results in the so-called “clean up effect”, which consumes interfacial oxides during the initial stages of Al_2O_3 growth. This is apparent from a comparison between the As 3d spectrum for sample A2 and that of a native oxide covered InGaAs (A3) sample with no Al_2O_3 shown in Figure 4.1(a). While the extent of the clean-up effect depends on the initial native oxide thickness [23] we believe that the interfacial oxide present on sample A1 has grown during the Al_2O_3 deposition process. This is confirmed by the As 3d spectrum of the sulphur passivated InGaAs surface acquired prior to Al_2O_3 deposition also shown in Figure 4.1 (b) which displays a much smaller As oxide component that that observed for sample A1. The observed changes in the As oxides with thermal anneal are in agreement with a recent XPS study by Yoshida et al [2] of the thermal annealing of ALD deposited Al_2O_3 on the InGaAs surface which shows a decrease in higher oxidation arsenic states with increased temperature. They also reported the presence of interfacial oxide at the Al_2O_3/ InGaAs interface after 17 cycles of ALD growth. The high temperature thermal anneals essentially leave both interfaces chemically identical in relation to the As 3d spectrum and there is no evidence of arsenic out diffusion, in contrast to a recently reported study on Al_2O_3 on InGaAs at this temperature [13].

4.4.2 Impact on In 4d/Ga 3d Spectra

Figures 4.10 (a) and (b) show the changes in the In 4d/Ga 3d curve fitted photoemission spectra acquired at a photon energy of 105 eV for 1 nm thick Al_2O_3 on sulphur passivated (A1) and the native oxide InGaAs (A2) surfaces, respectively. As stated above for the deconvolution of the As peak, similar difficulty arises for In and Ga oxidation states in making any distinction between oxides and sulphides, so no attempt has been made to identify these individual component peaks. At RT In 4d/Ga 4d bulk peaks were curve fitted with single spin orbit split components separated by 1.80 eV binding energy and chemically shifted components consisting of the In^{2+} (+0.60 eV), In^{3+} (+ 0.90 eV), Ga^{1+} (+ 0.60 eV) and Ga^{3+} (+1.3 eV) oxidation states, respectively. On sample A1 during the initial thermal anneals up to 485 ^{o}C (not shown) there is a slight decrease in the In^{2+}, In^{3+} and an increase in the Ga^{1+} and Ga^{3+} which is indicative of the transfer of oxygen [19] or sulphur [16] from In to Ga bond. Subsequent annealing

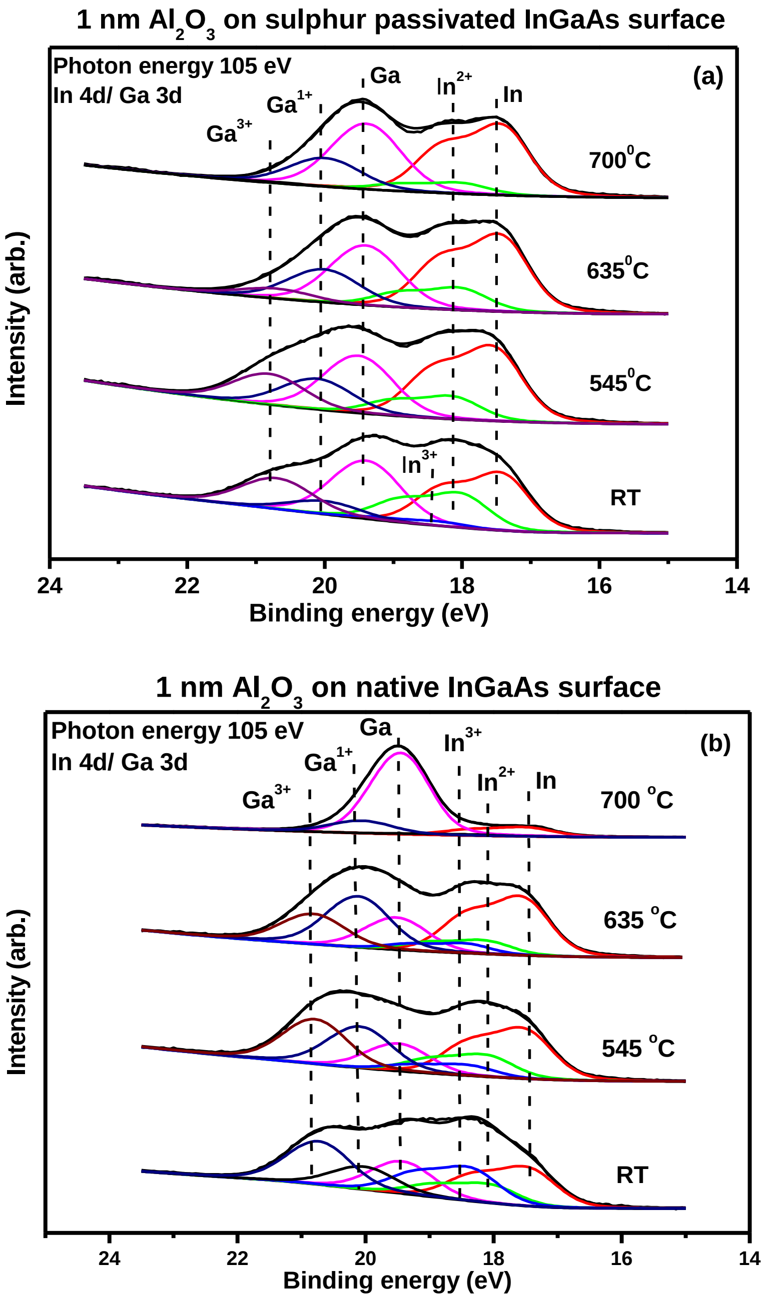
1 nm Al_2O_3 on sulphur passivated InGaAs surface

1 nm Al_2O_3 on native InGaAs surface

Figure 4.10 Curve fitted core level spectra In 4d/Ga 3d at 105 eV following thermal anneals (a) for Al_2O_3 on sulphur passivated InGaAs surface (A1) (b) for Al_2O_3 on native oxide InGaAs (A2)

at 545 °C removes the higher oxidation states of In^{3+}, decreases the In^{2+} states and increases the Ga^{1+} state. Annealing at 635 °C shows a continued decrease in the In^{2+}, and the Ga^{3+} state and the first reduction in the Ga^{1+} oxidation state peak intensity. Annealing at 700 °C effectively reduces the Ga^{3+} state completely with just the In^{2+} and

Ga^{1+} remaining at the interface. Spectra of the sulphur 2p core level shown in Figure 4.11 reveal that it remains throughout the high temperature annealing sequence suggesting that In-S and Ga-S bonding configurations are present at the interface.

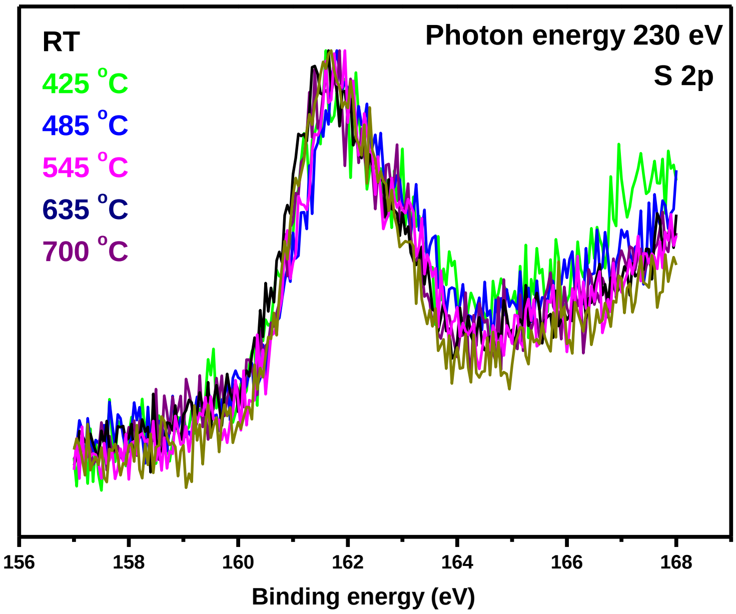

Figure 4.11 Core level spectra of S 2p peak at photon energy of 230 eV for Al_2O_3 on the sulphur passivated surface.

The changes in intensity of the oxide and sulphides peaks as a function of thermal anneal are more clearly seen by plotting the oxide/substrate peak intensity ratios for the individual In and Ga oxidation states as shown in Figure 4.12 (a) and 4.12 (b). Annealing sample A2 up to 545 °C shows a similar trend in terms of the reduction in intensity of the In oxides and a consequential increase in the Ga oxide peak intensities. At 635 °C there is a decrease in the In oxidation state intensities, while the Ga^{1+} state remains constant. Further annealing at 700 °C results in the complete removal of the residual oxides/sulphides, however this is accompanied by a significant change in the chemical composition of the InGaAs surface. A large drop in the In signal was observed following this anneal and a corresponding rise in the Ga signal which indicates that the InGaAs surface region becomes Ga rich. This is in contrast to the observations on the sulphur passivated surface indicating that the sulphur bonding interactions contributes to

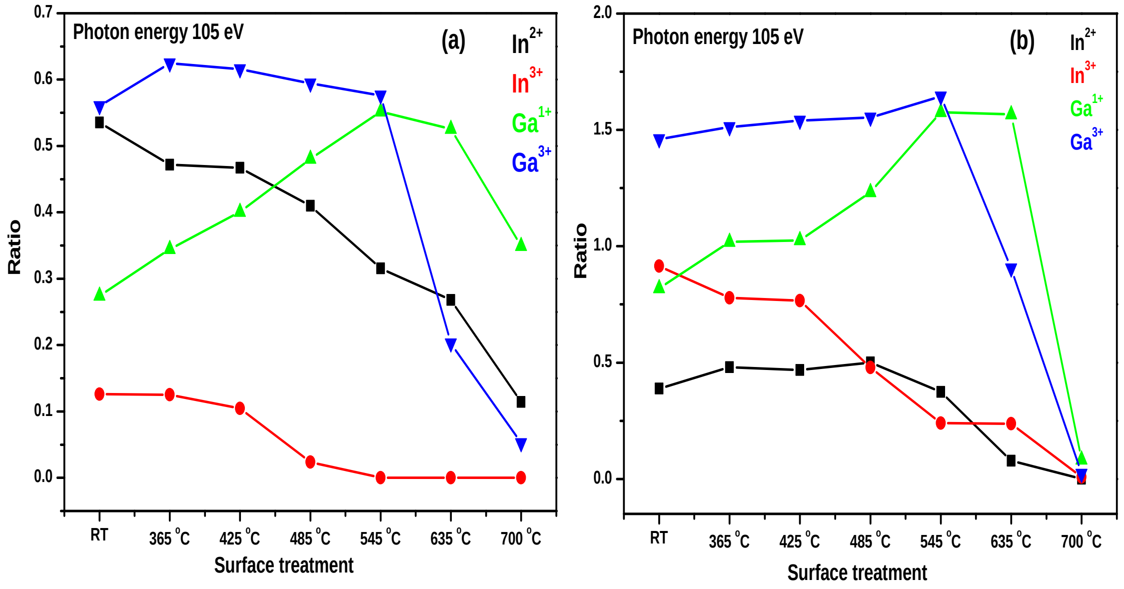

Figure 4.12 In and Ga oxidation states component to bulk ratio highlighting changes in the oxide composition as a function of thermal anneals (a) for Al_2O_3 on sulphur passivated InGaAs surface (A1) (b) for Al_2O_3 on native InGaAs surface (A2)

the surface stability at high temperature. A recent study by Alian et al [9] reported evidence of differences in Indium out diffusion into an ALD deposited Al_2O_3 layer on InGaAs for sulphur passivated and un-passivated InGaAs surfaces. While these differences were observed for Al_2O_3 layers deposited at normal growth temperatures (250 ^{o}C), the beneficial effect of sulphur passivation in increasing the chemical stability of the Al_2O_3/InGaAs interface is reflected in the results obtained in this current work.

Confirmation of the indium loss on sample A1 was also observed when spectra at different photon energies of 69 eV and 300 eV were acquired with the higher photon energy spectra having a larger sampling depth into the surface. The spectra are curve fitted with the individual component peaks having the same binding energy separations as those used to curve fit the spectra acquired at a photon energy of 105 eV. The resultant curve fitted spectra at different photon energies for both samples are shown in Figure 4.13.

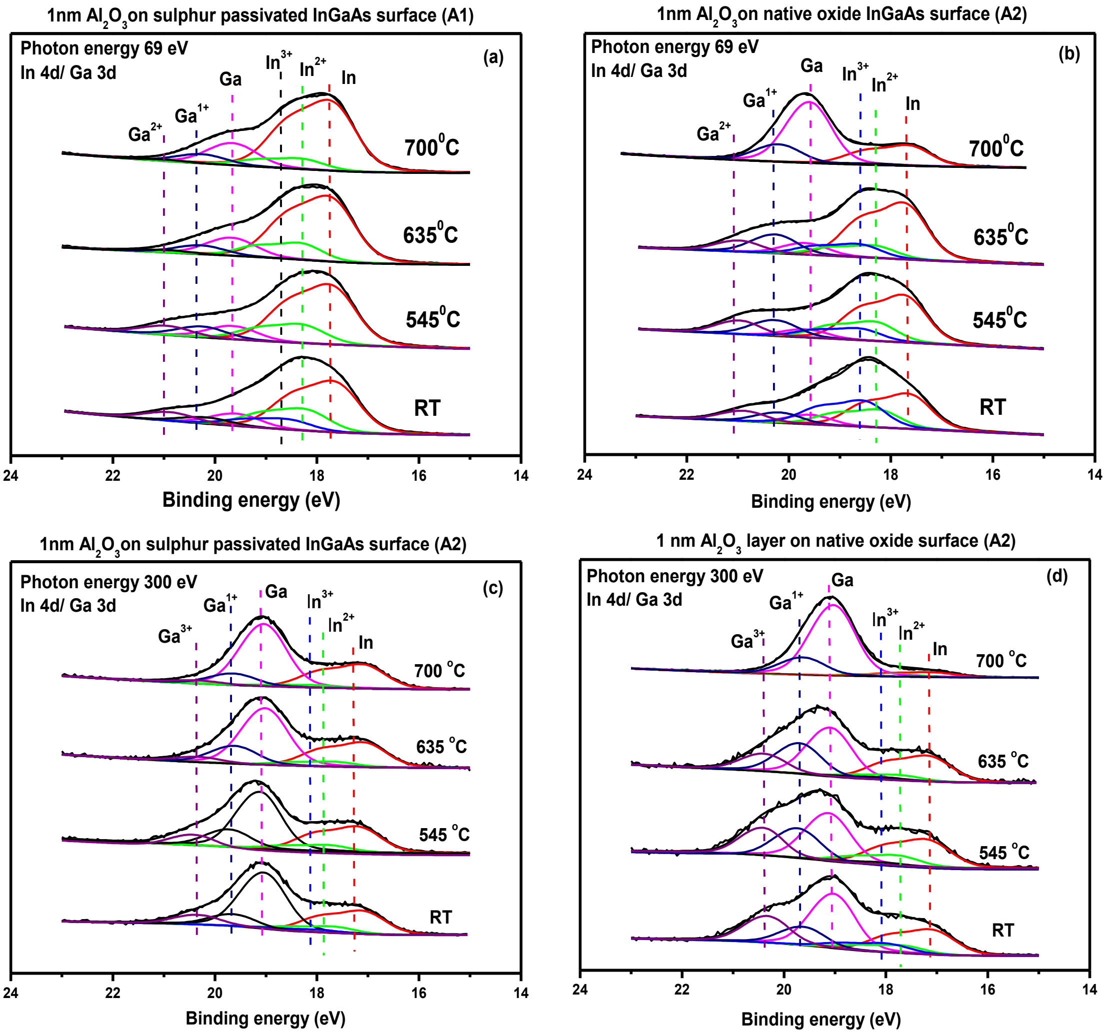

Figure 4.13 Curve fitted photoemission spectra for the In 4d and Ga 3d peaks at photon energy of (a) and (b) 69 eV and (c) and (d) 300 eV after annealing at RT, 545 °C, 635 °C and 700 °C for Al_2O_3 on the sulphur passivated sample (A1) and native oxide surface (A2) respectively.

The effect of annealing on the individual indium and gallium oxidation states compared to the respective bulk signals is shown in Figure 4.14 and follow the general trends observed in the spectra acquired at 105 eV (Figure 4.12). The In^{2+} and In^{3+}ratios decrease with thermal anneal while the gallium oxide peaks increase up to an annealing temperature of 545°C. Thereafter the ratios are seen to decrease with higher temperature annealing. There is very little trace of In^{2+} remaining, whereas no In^{3+} was observed at high temperature on the sulphur passivated surface.

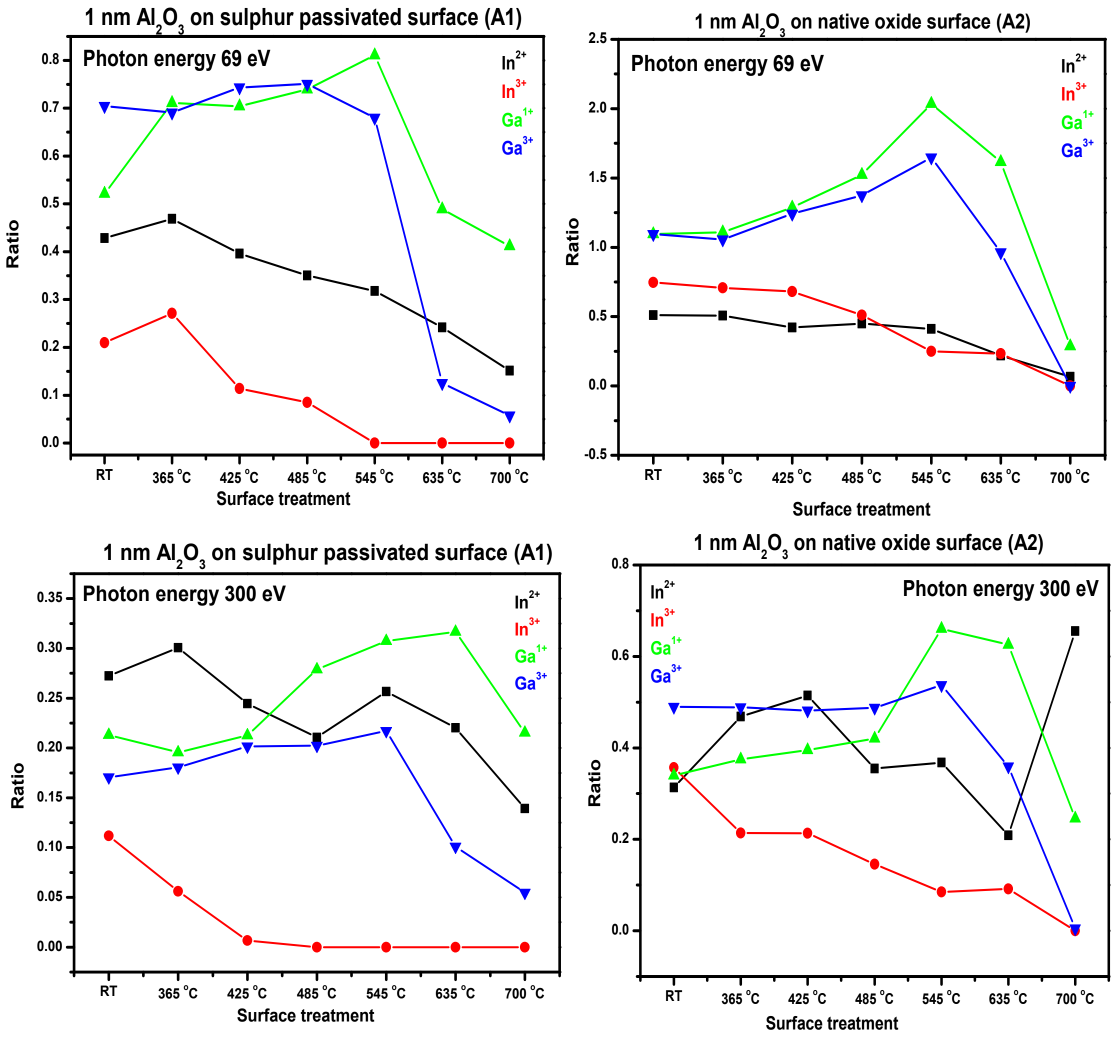

Figure 4.14 Indium and gallium components to bulk ratio highlighting changes in oxide composition and thermal stability at photon energies of 69 eV and 300 eV as a function of annealing temperature for both Al_2O_3 on sulphur passivated surface (A1) and on the native oxide surface (A2).

In contrast to In oxidation states, the Ga oxidation states were seen to increase with the annealing temperature. What is clear from all the plots is that the increase in the total gallium ratio is due to transfer of oxygen from indium oxide to gallium oxide as explained in earlier section 4.4.2. At 545 ^{o}C the decrease in all the oxidation states was observed and at 700 ^{o}C anneal temperature, the Ga^{1+} was found to be the most stable form of oxide which still remains at the surface, while Ga^{3+} ratio drops almost to zero.

The change in Ga : In ratio for Al_2O_3 on sulphur passivated sample is shown in Figure 4.15. The Ga:In ratio was found constant on all photon energies which reflects that InGaAs stoichiometry on the sulphur passivated sample remains preserved. The change in the Ga:In ratios at different photon energies for 1nm Al_2O_3 on native oxide sample are shown in Figure 4.15. These ratios suggest that the Ga : In ratio remain constant up to 635 ^{o}C and the increase in Ga : In is found for all photon energies with different sampling depths. At photon energy 130 eV the Ga : In ratio is highest as indium is lost from the surface which makes the near surface region gallium rich. Higher photon energy at 300 eV causes an increased sampling depth that reflects the loss of indium deep below the near surface region.

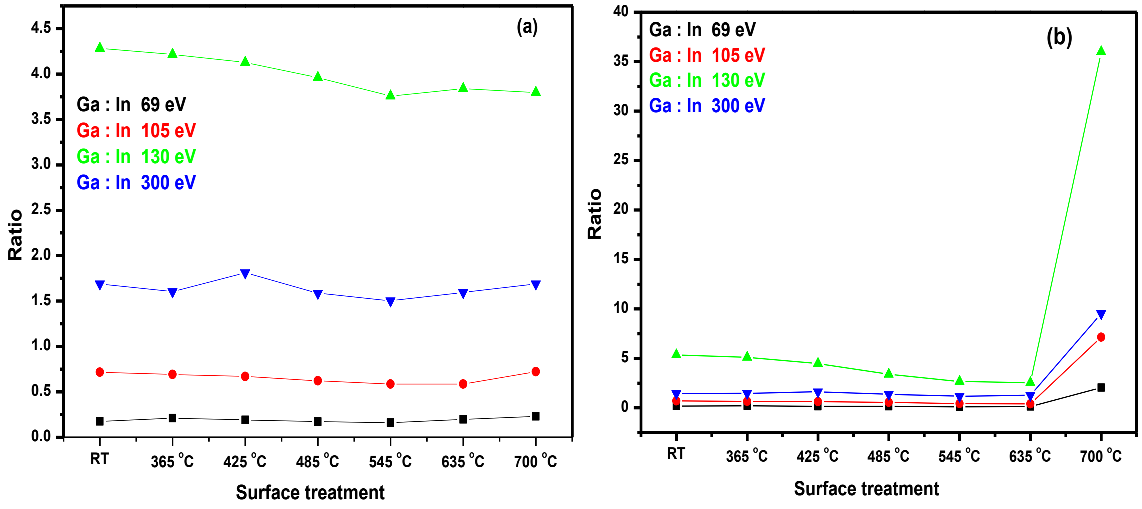

Figure 4.15 Ga : In ratios at different photon energies as a function of annealing temperature for (a) sulphur passivated (b) un-passivated Al_2O_3/InGaAs

4.5 Al_2O_3 film thermal stability

Al 2p and O1s spectra acquired at 120 eV and 600 eV photon energies, respectively, up to 700 ^{o}C are displayed in Figure 4.16 (a)-(d). There was no change in the relative intensities or binding energy positions of either the Al 2p or O 1s peaks as a function of thermal anneal indicating that the chemical composition of the Al_2O_3 layers were unaffected by the high temperature anneals. While the Al 2p peak profile also remained unaltered throughout the anneal sequence, there was a noticeable narrowing of the O1s peak for the highest temperature anneals consistent with the removal of the interfacial InGaAs oxides.

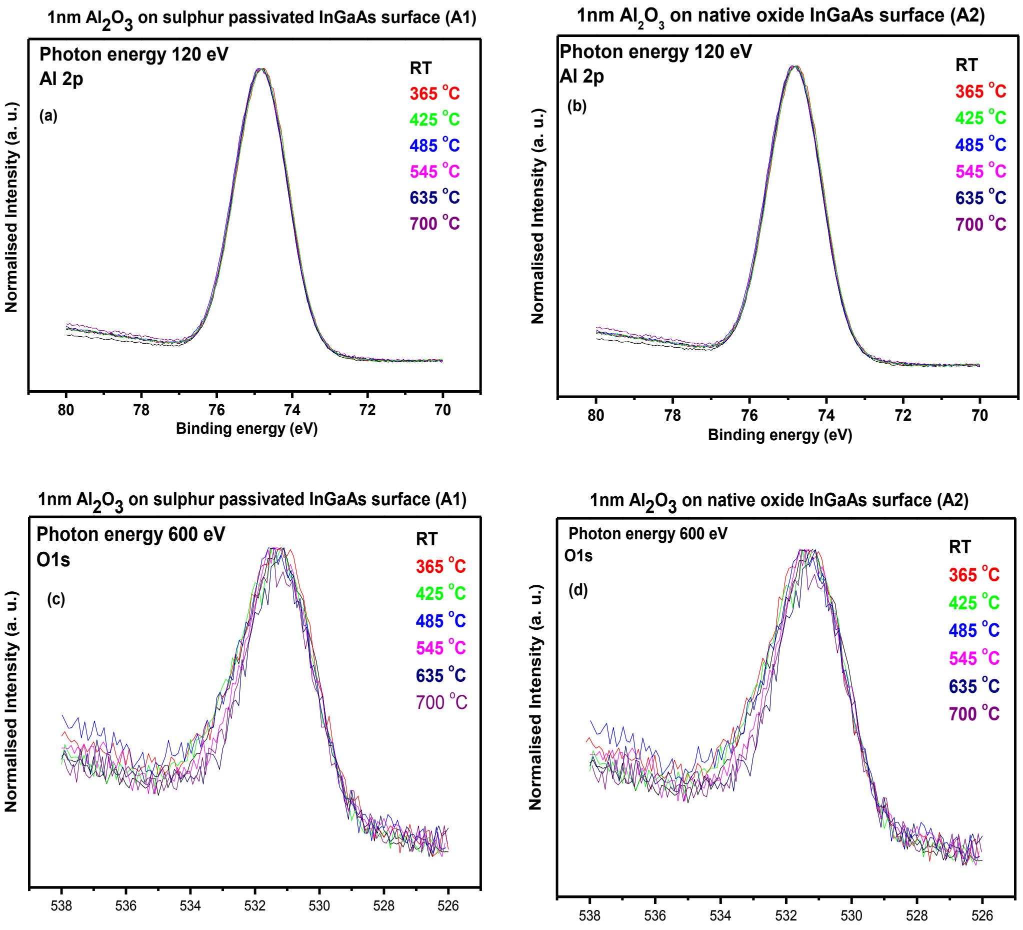

Figure 4.16 Normalised photoemission spectra by HRSPES for the Al 2p (top) and O1s (bottom) peaks at photon energies of 120 eV and 600 eV respectively following thermal anneals for Al_2O_3 on the sulphur passivated surface (A1) and on the native oxide surface (A2).

4.6 Growth of Al_2O_3 layer on InGaAs surface

While details of the interfacial chemistry of Al_2O_3/InGaAs were discussed in chapter 4, in this study more focus was placed on the growth characteristics of Al_2O_3 on different chemically treated InGaAs surfaces. The experimental approach taken was to use XPS to characterise the chemical composition and thickness of the Al_2O_3 layers grown on the differently treated surfaces by depositing on all the surfaces simultaneously. This way, the influence of surface preparation on ALD nucleation and growth can be directly compared. The Al_2O_3 layer was deposited on the following chemically treated surfaces

1) Native oxide surface
2) Pre-clean surface: Prolonged exposure to ambient conditions results in the formation of predominantly carbon based impurities on the surface of semiconducting substrates. This organic pre-cleaning method was used to remove these impurities and consisted of successive 1 minute dips in acetone, methanol and isopropyl alcohol (IPA), with sample being subsequently dried using N_2 gas.
3) 2 stage etch surface: This surface preparation was done in three steps, first surface was pre-cleaned (as pre-clean surface). Thereafter, a two stage piranha etching procedure (4:1:100 H_2SO_4:H_2O_2:H_2O for 2 minutes followed by 1:3 HCl:H_2O for 30 seconds) [24] was used to remove the native oxide without passivating the surface.
4) Sulphur passivated surface: Sample was degreased for 1 min in acetone followed by 1 min in methanol prior to the sulphur passivation. It was then dipped into 10% ammonium sulphide ($(NH_4)_2S$) solution for 20 min at room temperature (290 K) to remove the oxide and passivate the surface.
5) H_2O_2 treated surface: This surface treatment was usedto grow thick native oxide by dipping the sample in 30% H_2O_2 solution for 20 minutes.

The cleaning procedures for all samples were arranged in such a way that samples were then loaded into an atomic layer deposition (ALD) chamber load lock within a minute after the cleaning process to minimize the air exposure to the samples. Approximately 3 nm (30 cycles) of alumina (Al_2O_3) was deposited at 300 ^{o}C using trimethyl aluminium (TMA) and water as the precursors on all the samples. ALD parameters used for deposition were described in experimental section 4.2. These samples were prepared at Queens University Belfast UK as a part of collaboration work.

4.6.1 As 3d spectra

Figure 4.17 shows the profile of As 3d spectra following Al_2O_3 deposited on all treated surfaces. As 3d curve fitted spectra for all samples are shown in Figure 4.18 (a). Spectra consists of As bulk peak, elemental arsenic (+ 0.65 eV) As_2O (+ 1.2 eV) on native oxide, preclean and 2 stage etch sample while As_2O_3 (+ 3.2 eV) was observed only on H_2O_2 treated sample, whereas no oxide was observed on the sulphur passivated sample. The oxide to bulk ratios are plotted in Figure 4.18 (b).

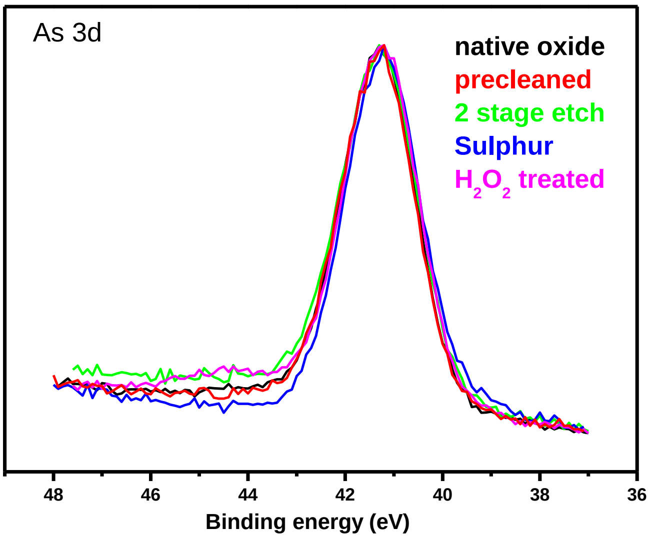

Figure 4.17 Normalised As 3d core level spectra for Al_2O_3/InGaAs interface of different chemically treated surfaces

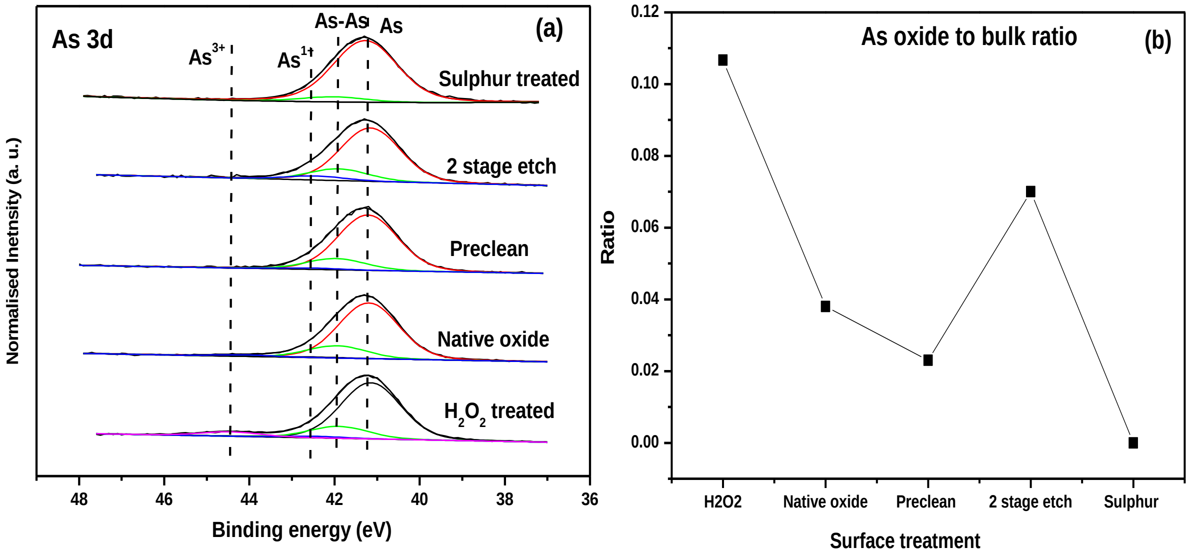

Figure 4.18 (a) Curve fitted As 3d core level spectra (b) oxide to bulk ratio, for Al_2O_3/InGaAs interface of different chemically treated surfaces

As there is no discernable difference between the native oxide and pre-cleaned surface it suggests that the ALD “clean-up” effect has succeeded in removing the As oxide from the surface during ALD growth. However, on the H_2O_2 treated surface and the two stages etched surface traces of arsenic oxide were observed. As H_2O_2 treatment grows the oxide to a thickness greater than the native oxide, it is possible that the self-cleaning effects do not completely consume the oxide from the surface. As reported in the literature self-cleaning depends on the initial level of oxide present on the surface before ALD dielectric deposition [25], whereas the two stage etch treatment makes the surface arsenic rich which results in small residual arsenic oxide formation during the deposition.

4.6.2 In 4d/Ga 3d spectra

Figure 4.19 displays the normalised spectra of In 4d and Ga 3d peaks for all treated surfaces. The fact that the relative intensity of these two peaks is the same for all InGaAs samples, means that they all have the same In:Ga composition ratio - $In_{0.47}Ga_{0.53}As$. When all the samples are compared the broadening of the In 4d/ Ga 3d peak on the higher binding energy (HBE) side (20.7 eV) suggests that there is interfacial oxide present on the H_2O_2 treated surface. On the pre-cleaned surface the peak is narrower than other surfaces which reflect the reduced amount of interfacial oxide present at the interface.

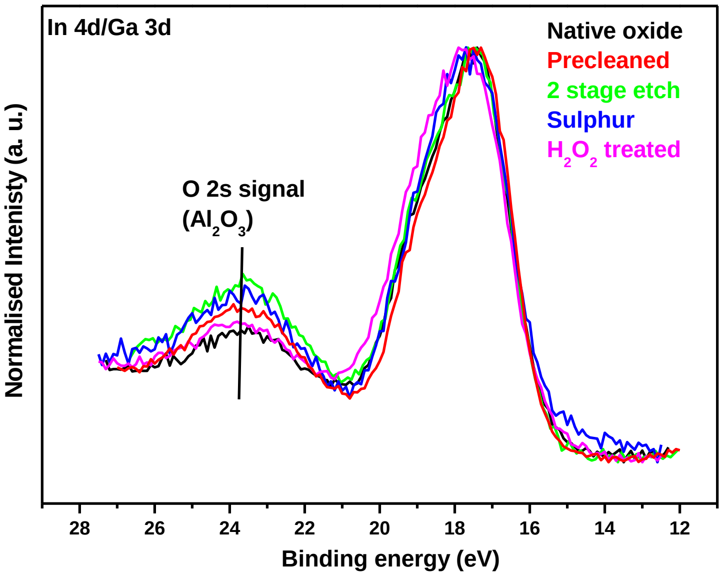

Figure 4.19 Normalised In4d/Ga 3d core level spectra for Al_2O_3/InGaAs interface of different wet chemically treated surfaces

The In4d/Ga3d spectra were curve fitted are shown in Figure 4.20 (a). The spectra consist of In 4d and Ga 3d peak separated by 1.82 eV and InO (+ 0.90 eV) and GaO (+ 0.85 eV). Indium and gallium oxides were seen in all the samples. The oxides to bulk ratio was calculated from curve fitted area and shown in Figure 4.20 (b). Again the highest intensity of the oxide was observed on the H_2O_2 treated surface indicating that the oxide was not completely removed by self-cleaning during ALD deposition. Less oxide signal was observed on native, pre-clean and sulphur treated surfaces. These results reflect the fact that the precleaning and sulphur passivation method helps in reducing the oxide from the interface.

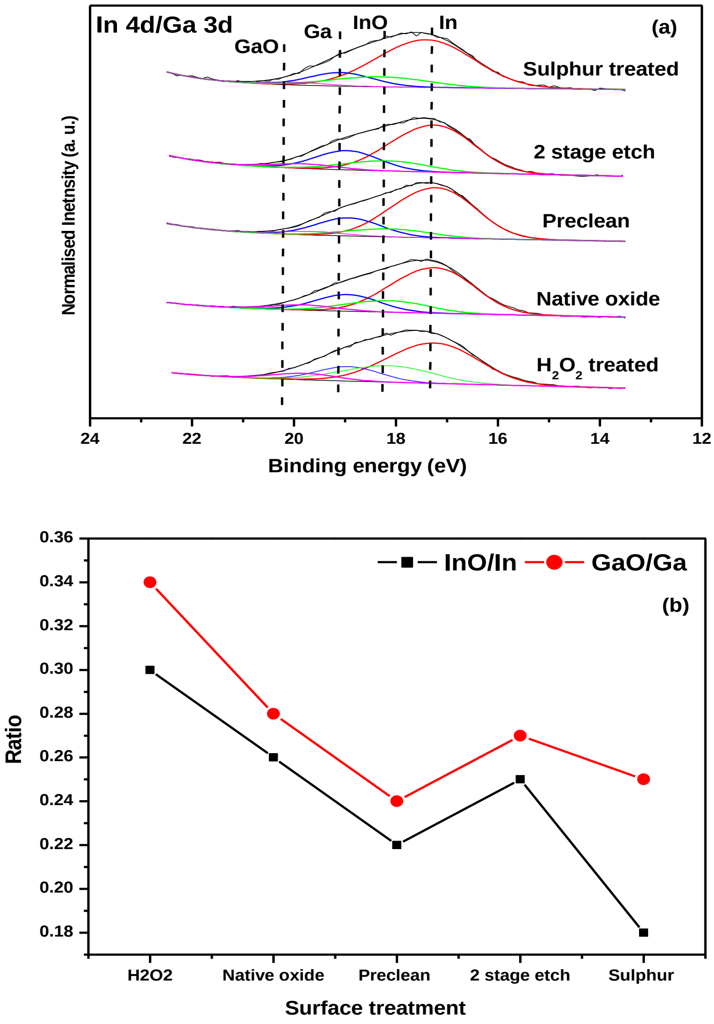

Figure 4.20 (a) Curve fitted In 4d/Ga 3d core level spectra (b) oxide to bulk ratio, for Al_2O_3/InGaAs interface of different chemically treated surfaces

Following Al_2O_3 deposition, there is an additional peak at ~23.8 eV BE which is related to the O 2s core level signal from the overlayer. The intensity of this peak resulting from the presence of residual surface oxides is negligible. It is worth noting that the O 2s signal intensity varies as a function of surface treatments which suggests that the Al_2O_3 film thickness is different on these surfaces. A plot of the curved fitted area of this O 2s peak as a function of surface preparation is shown in Figure 4.21. The O 2s signal is a maximum on the 2 stage etched and sulphur treated surfaces and a minimum on the native oxide and H_2O_2 treated surfaces reflecting the fact that despite the fact that all surfaces were subjected to the same number of ALD cycles, the film nucleation rates were surface dependent. The calculated thicknesses of the ALD overlayers on the sulphur treated and 2 stage etched surface is approximately ~ 3 nm while the on the pre-cleaned surface the thickness is ~ 2.1 nm and on native oxide and H_2O_2 treated surfaces it is ~ 1.2 nm.

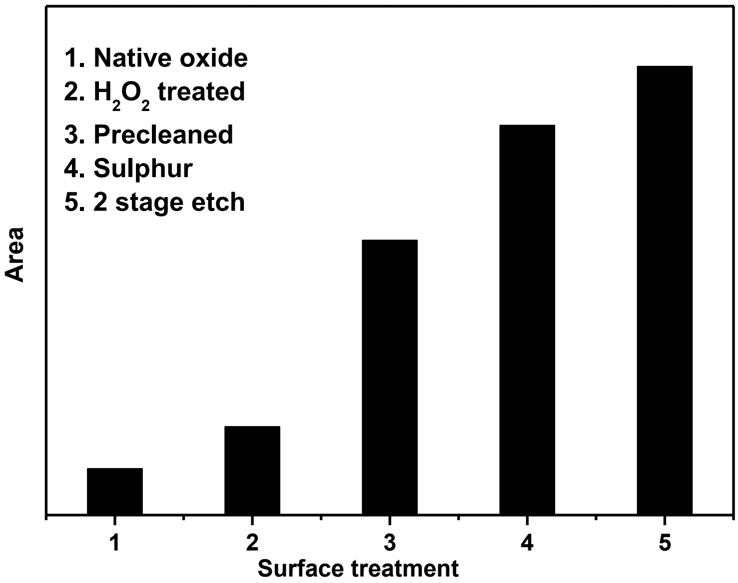

Figure 4.21 Graph display the curve fitted area of O 2s signal verses surface treatments showing the growth rate of Al_2O_3

To confirm the different growth rates of Al_2O_3 layers on the treated surfaces, the intensity ratio of the substrate peak to Al and O peak intensities were calculated and shown in table 4.1.

Table 4.1: Ratio of substrate peak to Al 2p and O 1s peak intensities

Sample	**As3d/ O1s**	**In 4d/ O 1s**	**In3d/ O1s**	**As 3d /Al 2p**	**In3d/ Al 2p**	**In 4d/ Al 2p**	**Al 2p/O1s**
Native oxide	0.05	0.04	**0.22**	0.40	**2.33**	0.40	0.12
H_2O_2	0.04	0.04	**0.26**	0.38	**2.42**	0.37	0.12
Pre-cleaned	0.03	0.03	**0.21**	0.33	**1.34**	0.35	0.12
sulphur passivation	0.02	0.02	**0.09**	0.22	**0.72**	0.18	0.12
2 stage etch	0.02	0.02	**0.08**	0.26	**0.68**	0.28	0.13

As 3d/O 1s, In 4d/O1s and In 3d/O 1s intensity ratios are lower on the sulphur passivated and 2 stage etch in comparison to the native, preclean and H_2O_2 treated surfaces. Similar trend was observed for the As 3d/Al 2p, In 4d/ Al 2p and In 3d/ Al 2p intensity ratios. These ratios confirm the variation in the thickness observed on differently treated surfaces. The Al/O intensity ratio is the same for all the samples which shows the uniformity of the Al_2O_3 layer on InGaAs. The profile of the Al 2p and O 1s peaks are shown in Figure 4.22 and shows that all the samples have similiar chemical composition. The aluminium oxide peak is at 74.3 eV and the energy separation between this peak and the O 1s peak of 457.5 eV, indicative of a stoichiometric Al_2O_3 layer.

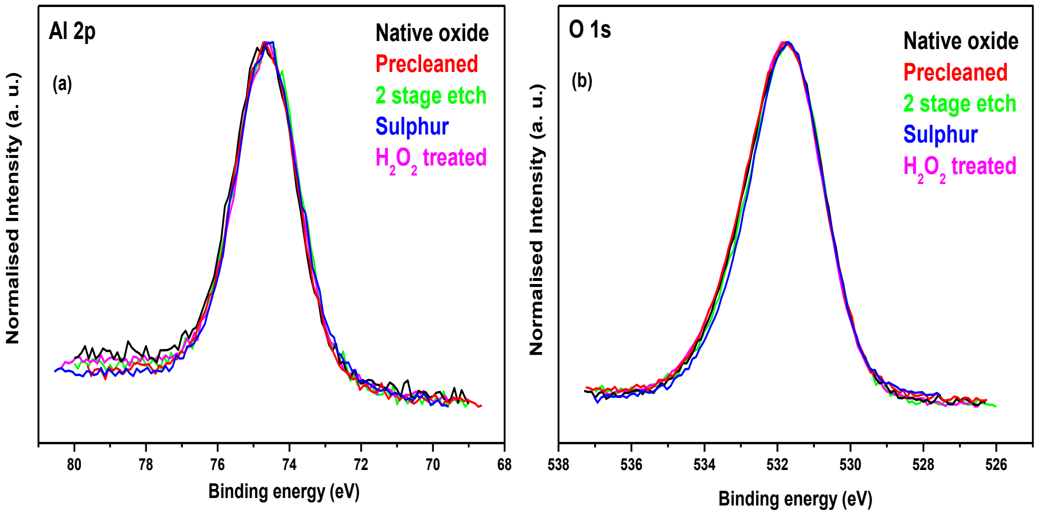

Figure 4.22 (a) Al 2p and (b) O 1s spectra showing the uniform composition on all the samples

The native oxide and H_2O_2 treated covered surfaces has the thinnest Al_2O_3 layer. On two stages etch and sulphur treated surfaces the film thickness is approximately equal and is attributed to the fact that these chemical treatments remove the native oxide present on the surface before Al_2O_3 deposition which helps in forming the nucleation sites and reduces the clean-up requirements. On the pre-cleaned surface which is an organic clean the film thickness is thicker than the native oxide and H_2O_2 treated surfaces, however thinner than the sulphur treated and two stages etch surfaces.

4.7 Conclusions

This chapter has focused on the interfacial chemical characterisation of a high k- Al_2O_3 layer deposited on the sulphur passivated and un-passivated surfaces. The high surface sensitivity advantage of synchrotron based photoemission has been used to show its benefit over conventional XPS. The interfacial oxide at the Al_2O_3/InGaAs interface on differently chemically prepared surface has been detected by the HRSPES which is beyond the XPS detection limit to measure. These results would indicate that the complete removal of the interfacial oxide layer at the unpassivated Al_2O_3/InGaAs interface at 700 °C results in the decomposition of the InGaAs by the loss of In which is assumed to occur by its out diffusion through the Al_2O_3 overlayer and evaporation from the surface. The enhanced thermal stability of the sulphur passivated Al_2O_3/InGaAs interface following the 700 °C anneal meant that it showed a residual gallium oxide signal. While it is not possible to definitively determine whether the oxidised gallium signal composes of oxides and sulphides the fact that the sulphur 2p signal remains throughout the annealing sequence would suggest that the interface stability is enhanced by sulphur bonding configurations. These results therefore set an upper limit on an annealing temperature for the Al_2O_3/InGaAs interface to substantially remove the interfacial oxides without initiating major chemical disruption across the interface. These findings could have implications for optimising MOS device fabrication strategies in that they demonstrate an effective way to remove the interfacial oxide without compromising the substrate composition.

The difference in growth rate of the Al_2O_3 on different chemically treated InGaAs surfaces was investigated by depositing on all surfaces simultaneously. Significant differences in the resulting thickness of the deposited Al_2O_3 film are attributed to different nucleation rates for the layer on the various surfaces. There is evidence of arsenic oxide at the interface at the Al_2O_3 covered H_2O_2 and 2 stage etched InGaAs samples. The O 1s and Al 2p peak shapes and BE positions suggest that both samples have similar chemical composition of Al_2O_3 layers.

4.8 References

[1] É. O'Connor, B. Brennan, V. Djara, K. Cherkaoui, S. Monaghan, S. B. Newcomb, R. Contreras, M. Milojevic, G. Hughes, M. E. Pemble, R. M. Wallace, and P.K. Hurley. J Appl. Phys., 109, 024101 (2011)

[2] T. Yoshida and T. Hashizume, Appl. Phys. Lett. 101, 122102 (2012)

[3] R. Suzuki, N. Taoka, M. Yokoyama, S. Lee, S. H. Kim, T. Hoshii, T. Yasuda, W. Jevasuwan, T. Maeda, O. Ichikawa, N. Fukuhara, M. Hata, M. Takenaka, and S. Takagi Appl. Phys. Lett. 100, 132906 (2012)

[4] N. Goel, P. Majhi, C. O. Chui, and W. Tsai, Appl. Phys. Lett.89, 163517 (2006)M. Akazawa, H. Hasegawa, Appl. Surf. Sci. 256, 5708–5713 (2010)

[5] I. Ok, H. Kim, M. Zhang, F. Zhu, S. Park, and J. Yum, S. Koveshnikov, W. Tsai, V. Tokranov, M. Yakimov, S. Oktyabrsky, J. C. Lee, J. Vac. Sci. Technol. B 25, 1491 (2007)

[6] A. Molle, G. Brammertz, L. Lamagna, M. Fanciulli, M. Meuris, S. Spiga Appl. Phys. Lett. 95, 023507 (2009)

[7] S. Koveshnikov,W. Tsai, I.Ok, J. Lee, V. Torkanov, M. Yakimov, and S. Oktyabrsky, Appl. Phys. Lett. 88, 022106 (2006)

[8] B. Brennan, M. Milojevic, C. L. Hinkle, F. S. Aguirre-Tostado, G. Hughes, and R. M. Wallace Appl. Surf. Sci., 257, 4028 (2011)

[9] A. Alian, G. Brammertz, R. Degraeve, M. Cho, C. Merckling, D. Lin, W. Wang, M. Caymax, M. Meuris, K. D. Meyer, and M. Heyns, IEEE Elect. Devi. Lett., 33, 11 (2012)

[10] H. C. Lin, W. E. Wang, G. Brammertz, M. Meuris, M. Heyns, Microelec. Engg 86, 1554 (2009)

[11] H. D. Trinh, E. Y. Chang, P. W. Wu, Y. Y. Wong, C. T. Chang, Y. F. Hsieh, C. C. Yu, H. Q. Nguyen, Y. C. Lin, K. L. Lin, and M. K. Hudait, Appl. Phys. Lett. 97, 042903 (2010)

[12] J. Hu and H. S. Philip Wong J. Appl. Phys.111, 044105 (2012)

[13] C. Weiland, P. Lysaght, J. Price, J. Huang, and J. C. Woicik, Appl. Phys. Lett.101, 061602, (2012)

[14] O. Ceballos-Sanchez, A. Sanchez-Martinez, M.O. Vazquez-Lepe, T. Duong, R. Arroyave, F. Espinosa-Magaña, and A. Herrera-Gomez, J. Appl. Phys. 112, 053527 (2012)

[15] L. Chauhan, G. Hughes, Phys. Stat. Sol. A, 210, 519 (2013)

[16] L. Chauhan, G. Hughes, J. Appl. Phys. 111,114512 (2012)

[17] F. S. Aguirre-Tostado, M. Milojevic, C. L. Hinkle, E. M. Vogel, R. M. Wallace, S. McDonnell, and G. J. Hughes, Appl. Phys. Lett.92, 171906, (2008)

[18] B. Brennan, D. M. Zhernokletov, H. Dong, C. L. Hinkle, J. Kim, and R. M. Wallace, Appl. Phys. Lett.100, 151603 (2012)

[19] B. Brennan and G. Hughes J. Appl. Phys. 108, 053516 (2010)

[20] C. L. Hinkle, A. M. Sonnet, E. M. Vogel, S. McDonnell, G. J. Hughes, M. Milojevic, B. Lee, F. S. Aguirre-Tostado, K. J. Choi, H. C. Kim, J. Kim, and R. M. Wallace, Appl. Phys. Lett. 92, 071901 (2008)

[21] M. L. Huang, Y. C. Chang, C. H. Chang, Y. J. Lee, P. Chang, J. Kwo, T. B. Wu, and M. Hong, Appl. Phys. Lett. 87, 252104 (2005)

[22] B. Brennan, M. Milojevic, H. C. Kim, P. K. Hurley, J. Kim, G. Hughes, and R. M. Wallace, Electrochemical and Solid State Letters 12 (6) H 205 (2009)

[23] J. J. Gu, Y. Q. Wu, and P. D. Ye J. Appl. Phys. 109,053709 (2009)

[24] L. Zhi, S. Yun, F. Machuca, P. Pianetta, W.E. Spicer, R.F.W. Pease, J. Vac. Sci. Technol. A, 21, 212 (2003)

[25]] B. Brennan, M. Milojevic, H. C. Kim, P. K. Hurley, J. Kim, G. Hughes, and R. M. Wallace, Electrochemical and Solid State Letters 12 (6) H 205 (2009)

Chapter 5

Interfacial oxide formation study of in-situ deposition of MgO on atomically clean InGaAs surface by HRSPES

5.1 Introduction

As mentioned in the introductory chapter, the search for alternative high-κ oxides that could offer stable interfaces on III-V semiconductor substrates with a low density of electrically active defects has become a topic of major interest and intense research efforts have focused on perfecting high-k dielectric/InGaAs interfaces. Recent studies have shown that high quality interfacial properties can be achieved using Al_2O_3 or HfO_2 dielectric layers on InGaAs [1-4]. Magnesium oxide (MgO), which has a similar dielectric constant to Al_2O_3 [6,7], has shown promising results as an interface control(ICL) layer in bilayer studies [8]. MgO is a wide bandgap material and ICL is to be reported as a barrier to tunnelling, oxygen diffusion [9] and provides a high band offset. MgO has been also been reported as an alternative dielectrics and to have promising electrical characteristics on InP [10,11,12], GaAs [13,14] and InGaAs substrates [15]. The reaction chemistry between high-k materials and III-V substrates is more complex than the Si/SiO_2 system, with the possibility for competing bonding configurations comprising more than one substrate element, and associated native oxides, resulting in interface defect formation. Therefore an understanding of the specific bonding arrangements that arise at high-k dielectric / III-V semiconductor interface has great importance for the integration of these high-mobility materials into device fabrication.

The first part of this study focuses on atomically clean InGaAs which has been prepared insitu by the thermal desorption of an As-capping layer. The evolution of the interface chemical interactions resulting from the deposition of an MgO dielectric layer is investigated by high resolution synchrotron radiation based photoemission. The extreme surface sensitivity afforded by this technique allows details of the interfacial oxide growth to be revealed and subsequent changes resulting from thermal annealing and metallic Mg deposition.

In second part the growth rate of Al_2O_3 deposited by ALD on the different chemically prepared InGaAs surfaces was studied by XPS.

5.2 Experimental details

The soft x-ray photoemission experiments were carried out on the SX700 beam line at the Astrid synchrotron in the University of Aarhus in an ultrahigh vacuum (UHV) system which had a base pressure of $5x10^{-10}$ mbar. A 100 nm As capped sample, 0.5μm thick p-type Be doped $In_{0.53}Ga_{0.47}As(100)$ epilayer ($5x10^{17}$ cm^{-3}) lattice matched to the InP substrate was secured to a molybdenum holder before being loaded into the vacuum system. The protective As cap (100nm) was removed by annealing at 410^{o} C for one hour and allowed to cool to room temperature prior to acquiring spectra. After removal of As cap and the acquisition of clean surface spectra, MgO was sequentially deposited insitu by thermally evaporating Mg in an O_2 background pressure of 5 x 10^{-7} mbar as previously reported [15]. The deposited film was subsequently annealed at 400 ^{o}C for 30 minutes prior to the deposition of a metallic Mg overlayer. Photon energies of 69 eV and 92 eV were chosen for the In 4d/Ga 3d and As 3d core level spectra, respectively, to give comparable electron escape depths and high surface sensitivity, as photoemitted electrons from both core levels will have kinetic energies of approximately 50 eV thereby maximizing surface sensitivity. The spectra were curve fitted using Voigt profiles composed of Gaussian and Lorentzian line shapes and using a Shirley-type background. The reference fitting parameters for different core levels were acquired from the atomically clean surfaces and these were used to curve fit the InGaAs spectra following the changes induced by the MgO deposition and anneal. The curve fitting parameters used in the study for the substrate core levels were identical to those previously reported [17].

5.3 MgO growth on atomically clean InGaAs

5.3.1 As 3d spectra

Figure 5.1 displays the curve fitted core level spectra of As 3d at 92 eV for the atomically clean InGaAs surface decapped at 410 ^{o}C and after each MgO deposition. Decapping InGaAs at this temperature has been reported to result in an arsenic terminated surface [16]. The As 3d clean surface spectrum was curve fitted with two component peaks identified as a bulk peak and an As dimer or dangling bond related peak shifted by -0.65 eV to the lower binding energy side [17].

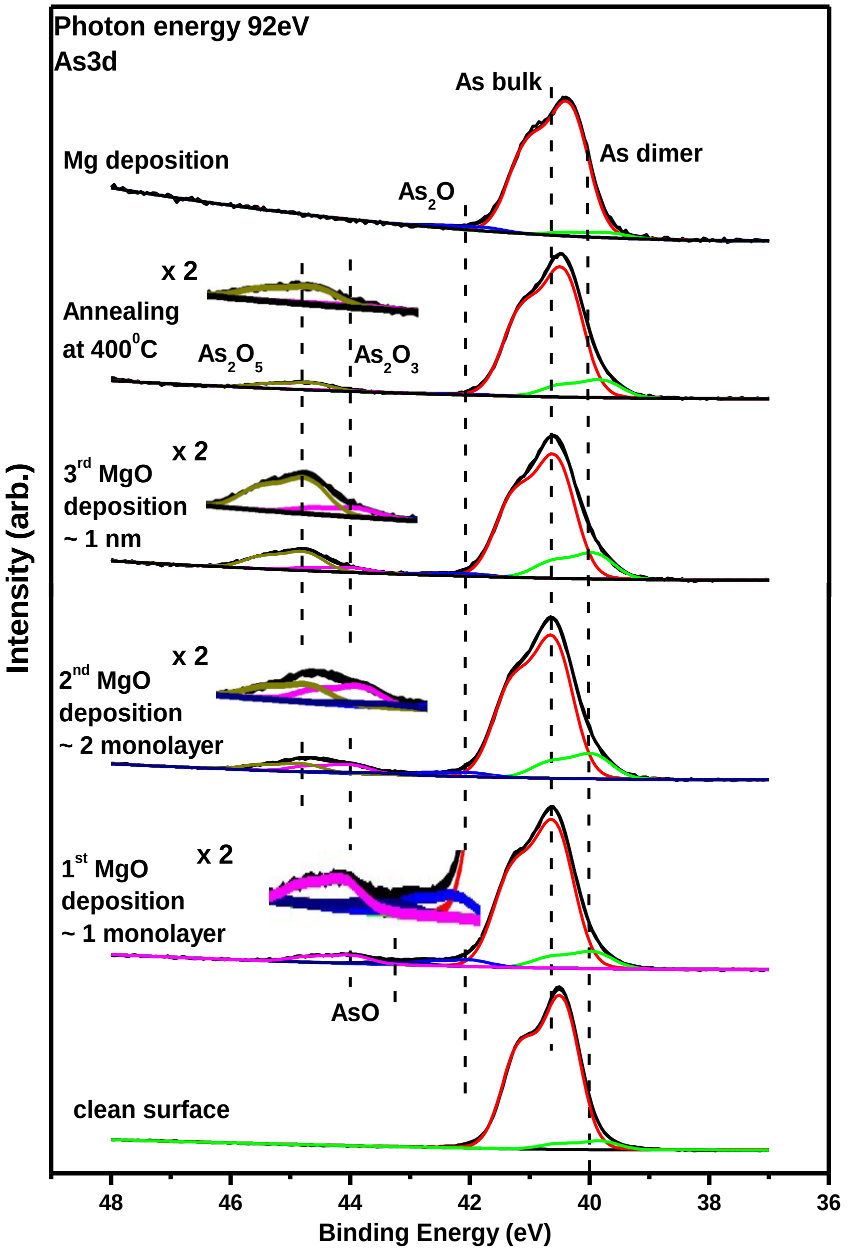

Figure 5.1 Curve fitted core level spectra of As 3d at 92 eV for an atomically clean InGaAs surface and after each MgO deposition, anneal and Mg deposition, To show the actual presence of weak interfacial oxides enlargement (Magnification x 2) of the oxide peaks was used.

The first deposition of MgO results in the observation of three weak, but noticeable oxidation states of arsenic, As^{1+} , As^{2+} and As^{3+} shifted to the higher binding energy side indicating a mixed phase interfacial oxide of As_2O (+1.1 eV), AsO (+2.55 eV) and As_2O_3 (+3.4 eV), consistent with previous studies [17]. The second deposition leads to the appearance of the higher As^{5+} oxidation state consistent with the formation of As_2O_5 (+4.2 eV), an increase in the peak area of the As dimer related peak and a reduction in the areas of the As_2O and AsO component peaks suggesting that the lower As oxidation states are converted into higher oxidation states with increased MgO deposition. A subsequent third MgO deposition results in an increase in the As_2O_5 peak intensity and a further decrease in As_2O and As_2O_3 peak areas, confirming this trend of oxygen transfer. Annealing at 400 °C results in a reduction in the intensity of the As_2O_3 and As_2O_5 however, the persistence of an As^{5+} oxidation signal when the As^{3+} signal has almost been completely attenuated is the reverse of what is observed on the annealing behaviour of native oxide covered InGaAs surface [17]. This annealing treatment appears to result in the formation of a single As_2O_5 oxidized state at the MgO interface. Figure 5.2 plots the attenuation in the intensity of the As 3d substrate signal as a function of the MgO deposition, anneal and final metal Mg deposition. The estimated total thickness of the MgO overlayer prior to thermal anneal was calculated to be approximately 1 nm and the thickness of the interfacial oxide layer is significantly less than one monolayer and is at a level which would not be detected by conventional XPS. The small increase in substrate signal intensity following the thermal anneal reflects both the densification of the film and the attenuation of the interface oxide layer.

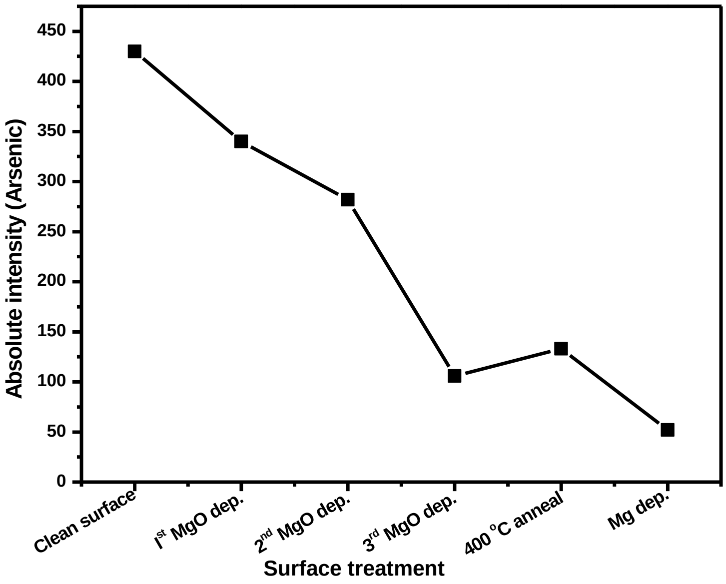

Figure 5.2 As 3d absolute intensity plot as a function of successive MgO depositions and anneal

The change in the intensity of the individual As oxidation states expressed as a ratio of the As substrate signal intensity shown in Figure 5.3 clearly shows the increase in the As_2O_5 oxide component at the expense of the lower oxidation states and the residual presence of this high As oxidation state following the thermal anneal.

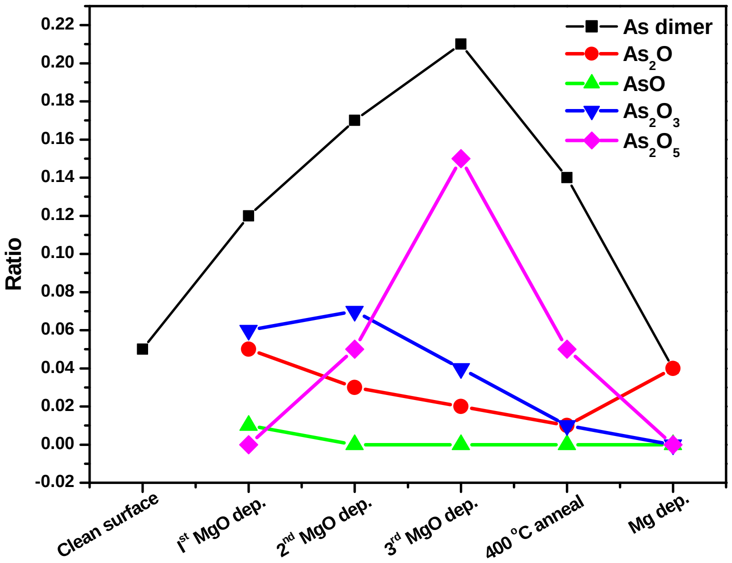

Figure 5.3 Individual As oxide to As substrate intensity ratios for the atomically clean InGaAs surface and after each MgO deposition, anneal and metallic Mg deposition

5.3.2 In 4d/Ga 3d Spectra

The In 4d/Ga 3d spectrum following MgO deposition displayed in Figure 5.4 shows the presence of just one oxidation state, the In^{2+} indicative of the formation of InO (~ +0.45 eV). There is very little evidence of any change in the intensity of the In oxidation state with subsequent MgO deposition consistent with the arsenic rich nature of this surface. The appearance of a significant Ga oxide signal following the 400 °C anneal corresponding to the conversion of In oxides to Ga oxides has been previously reported for the oxidized InGaAs surface [18].

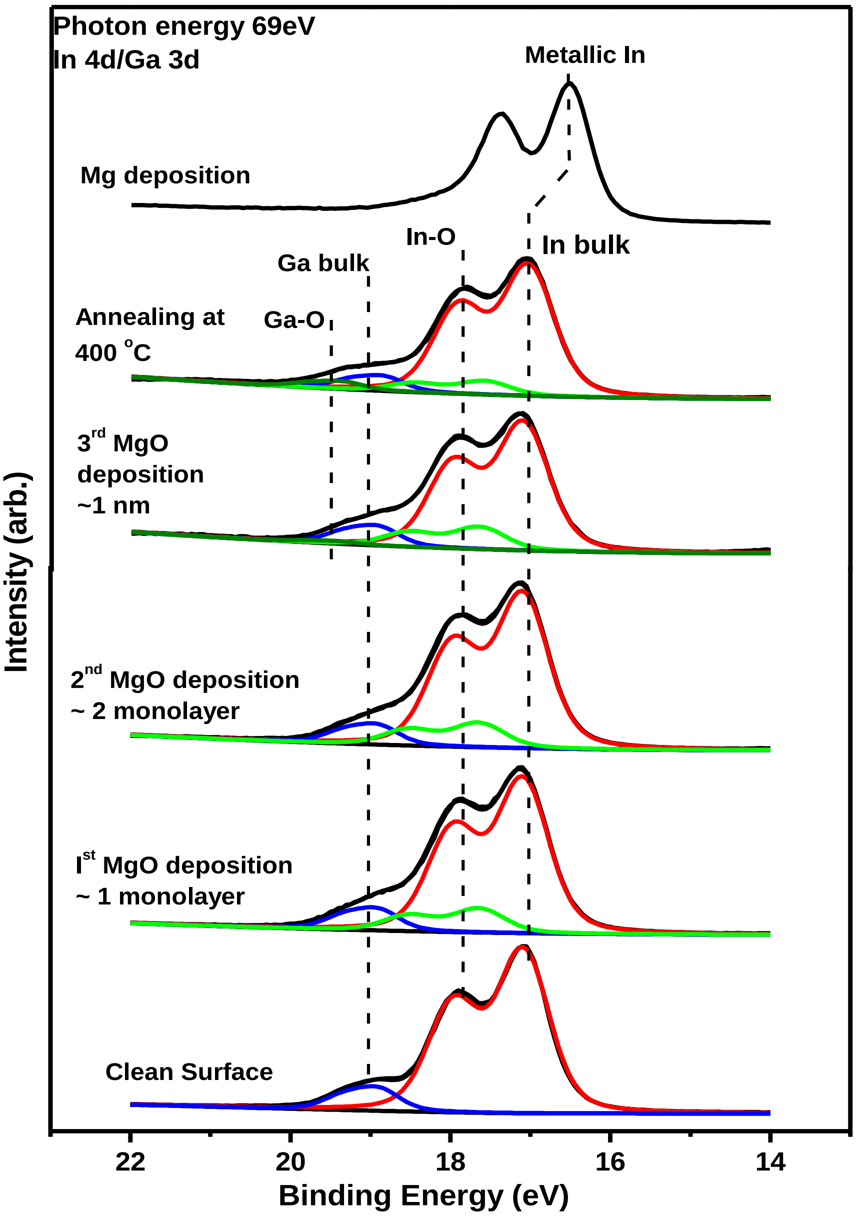

Figure 5.4 Curve fitted core level spectra of In 4d/Ga 3d at 92eV for the atomically clean InGaAs surface and after each MgO deposition, anneal and Mg deposition.

Figure 5.5 (a) plots the absolute intensity of the In 4d substrate signal as a function of the MgO deposition, anneal and final metallic deposition. It is apparent from this plot that there is a similar decrease in the intensity of the bulk signal with MgO deposition as observed for the As 3d peak. The transfer of oxygen from In to Ga oxides following the thermal anneal is clearly observed in Figure 5.5 (b) and may well be a critical interaction in the changes subsequently observed following the deposition of metallic Mg.

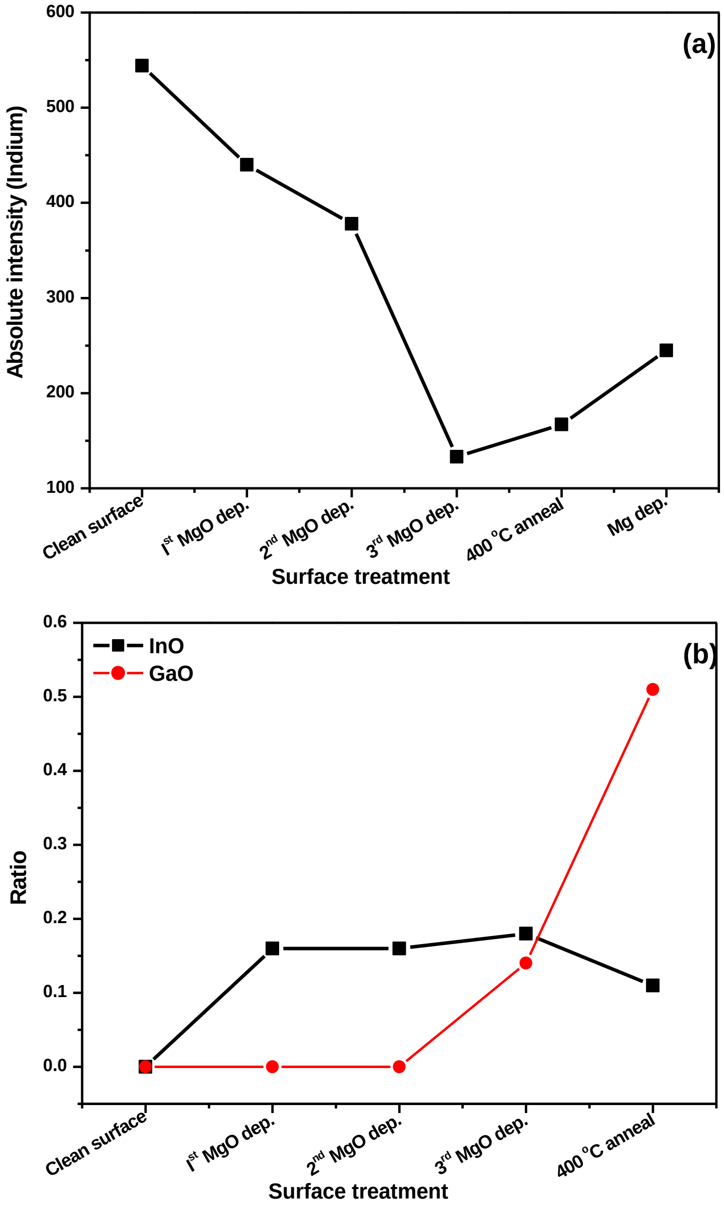

Figure 5.5 (a) In 4d absolute intensity plot as a function of successive MgO depositions and anneal b) InO and GaO to In and Ga substrate ratio respectively, for the atomically clean InGaAs surface and after each MgO deposition, anneal

The As 3d spectrum shown in Figure 5.1 following the deposition of metallic Mg on the MgO surface displays the complete attenuation of the As_2O_5 oxide peak leaving a very small residual As_2O component peak at the MgO/InGaAs interface. This is attributed to a gettering effect resulting from Mg deposition, in that the oxidation of the deposited Mg results in the formation of an oxygen deficient MgO film which can result in the decomposition of the residual interfacial oxide, as no metallic Mg signal was detected. However, the change in the In 4d peak profile in Figure 5.4 provides evidence of a stronger bonding interaction with the indium resulting from the Mg deposition which results in the appearance of a metallic like In 4d signal. This is attributed to the out diffusion of the In which can be observed in both the increase in the absolute intensity of the In signal Figure 5.5(a) and a shift of 0.60 eV in the In 4d peak to lower binding energy.

5.3.3 O 1s spectra

Figure 5.6 shows that the O 1s core level spectrum following the 2^{nd} MgO deposition consists of two components, the lower binding energy (LBE) peak is related to the signal from MgO layer and the higher binding energy (HBE) peak relates to the interfacial oxide.

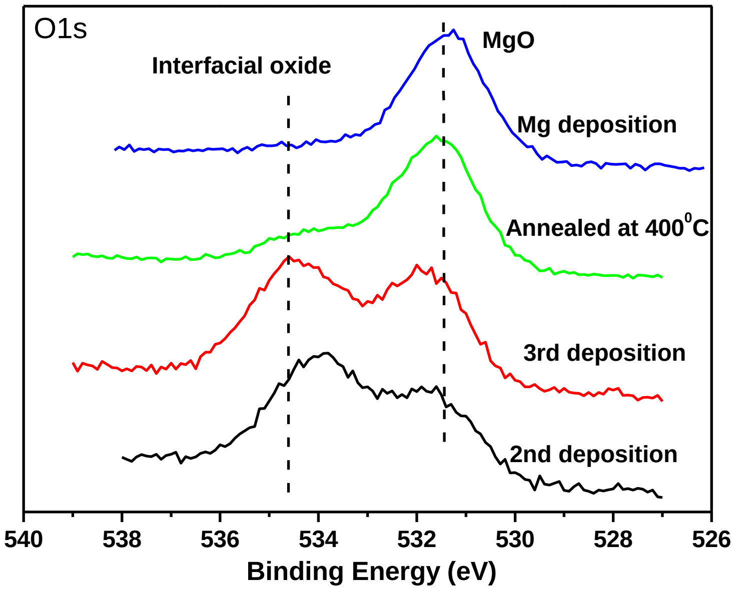

Figure 5.6 O1s core level spectra following MgO deposition, thermal anneal and subsequent Mg deposition.

Annealing results in the reduction of HBE component peak intensity which is consistent with reduction in interfacial oxide as observed in curve fitted As 3d and In 4d/Ga 3d peaks. The further attenuation of the HBE O1s peak after Mg deposition confirms the effective complete removal of the interfacial oxide.

5.3.4 Valence band spectra and energy band diagram

Valence band spectra acquired at 69 eV showing the valence band offset resulting from the MgO deposition on atomically clean InGaAs surface are displayed in Figure 5.7 (a). The valence band (VB) offset was extracted by recording the difference between the VB maximum of clean InGaAs surface and MgO (bandgap ~ 7.8eV). Taking the $In_{0.53}Ga_{0.47}As$ bandgap as 0.75eV, the band diagram of MgO on InGaAs was experimentally constructed as shown in Figure 5. 7 (b)). The valence band offset and conduction band (CB) offsets were calculated to be 3.2 ± 0.3eV and 3.8 ± 0.3eV, respectively. However, the non-abrupt nature of the MgO/InGaAs interface following the removal of the interfacial oxide would be expected to result in non-ideal electrical characteristics for a metal-oxide-semiconductor device fabricated using this approach.

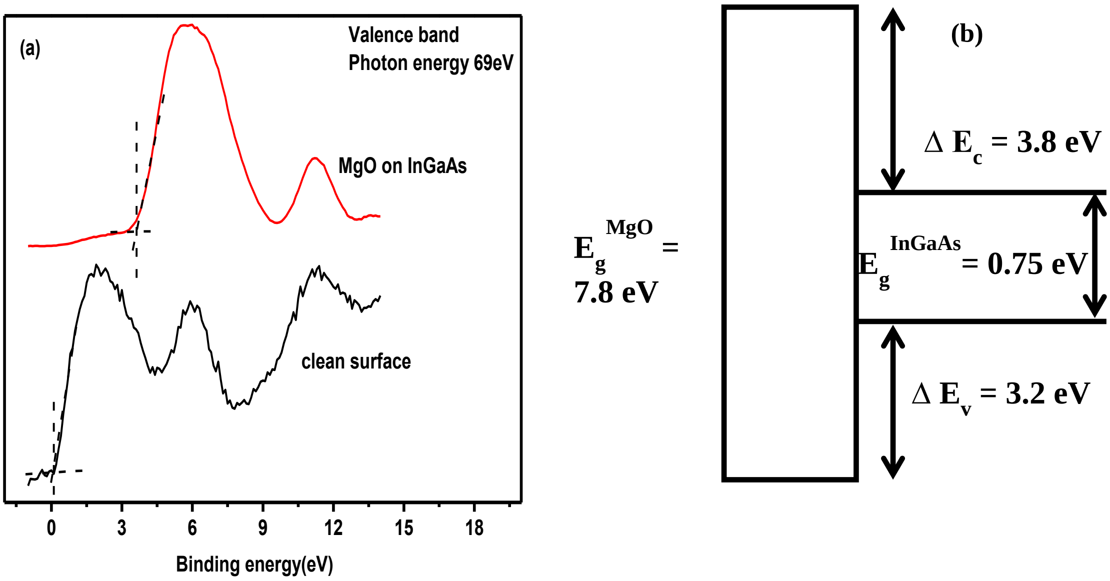

Figure 5.7 (a) Valence band spectra acquired at 69 eV showing the change in the valence band offset resulting from the MgO deposition on atomically clean InGaAs surface. (b) Band diagram of MgO / InGaAs. Valence band (VB) offset is (3.2 ± 0.3) eV and conduction band (CB) offset is (3.8 ± 0.3) eV

5.4 Conclusion

The deposition of an ultrathin MgO dielectric layer on atomically clean InGaAs results in the observation of As_2O, AsO, As_2O_3 and InO interfacial oxides at submonolayer levels. Subsequent MgO deposition leads to the appearance of higher oxidation states of As at the expense of the lower oxidation states without any significant change in the In oxide signal. Annealing leads to the attenuation of the As oxides and transfer of the oxygen from In to Ga. Mg deposition results in the complete removal of the higher oxidation states of As and out diffusion of In. The results suggest that the complete removal of an interfacial oxide layer between the deposited dielectric and the InGaAs surface can result in severe disruption of the interface.

5.5 References

[1] R. Suzuki, N. Taoka, M. Yokoyama, S. Lee, S. H. Kim, T. Hoshii, T. Yasuda, W. Jevasuwan, T. Maeda, O. Ichikawa, N. Fukuhara, M. Hata, M. Takenaka, and S. Takagi Appl. Phys. Lett. 100, 132906, (2012)

[2] É. O'Connor, B. Brennan, V. Djara, K. Cherkaoui, S. Monaghan, S. B. Newcomb, R.Contreras, M. Milojevic, G. Hughes, M. E. Pemble, R. M. Wallace, and P.K. Hurley. J. Appl. Phys. 109, 024101, (2011)

[3] H. C. Chiu, L. T. Tung, Y. H. Chang, Y. J. Lee, C. C. Chang, J. Kwo, and M. Hong, Appl. Phys. Lett., 93, 202903 (2008)

[4] A. O'Mahony, S. Monaghan, G. Provenzano, I. M. Povey, M. G. Nolan, E. O'Connor, K. Cherkaoui, S. B. Newcomb, F. Crupi, P. K. Hurley, and M. E. Pemble, Appl. Phys. Lett. 97, 052904 (2010)

[5] L. Yan, C. M. Lopez, R. P. Shrestha, E. A. Irene, A. A. Suvorova and M. Saunders, Appl. Phys. Lett. 88, 142901(2006)

[6] A. Posadas, F. J. Walker, C. H. Ahn, T. L. Goodrich, Z. Cai and K. S. Ziemer, Appl. Phys. Lett. 92, 233511(2008)

[7] J. Senzaki, K. Kurihara, N. Nomura, O. Mitsunaga, Y. Iwasaki, T. Ueno, Jpn. J. Appl. Phys. 37, 5150 (1998)

[8] A. O’Mahony, et.al ECS Transactions, 33 (2) 69-82 (2010)

[9] B. B. Burton, D. N. Goldstien ans S. M. George, J. Phys. Chem. C 113, 2009, 113, 1939 (2009)

[10] S. W. Robey, J. Vac. Sci. Technol. A 16, 2423 (1998)

[11] T. W. Kim, Y.S. You, Appl. Surf. Sci. 180,162 (2001)

[12] W. Prusseit, S. Corskpius, F. Baudenbacher, K. Hirata, P. Berberich, H. Kinder, Appl. Phys. Lett. 61, 1841, (1992)

[13] L. S. Hung, L. R. Zheng, and T. N. Blanton Appl. Phys. Lett. 60, 3129, (1992)

[14] K. Cherkaoui, E.O'Connor, S. Monaghan, R. D. Long, V. Djara, A. O’Mahony, R. Nagle, Martyn E. Pemble, and P. K. Hurley ECS Trans. 28(2) 181, (2010)

[15] P. Casey, G. Hughes, E. O'Connor, R. D. Long and P. K. Hurley J. Phys.: Conf. Ser. 100, 042046 (2008)

[16] L. Chauhan, G. Hughes, J. Appl. Phys. 111, 114512 (2012)

[17] B. Brennan and G. Hughes J. Appl. Phys.108, 053516, (2010)

Chapter 6

Modification of metal – InGaAs Schottky barrier height by atomic layer deposition of ultrathin Al_2O_3 interlayers and fabrication of MOS structures on InGaAs.

6.1 Introduction

In recent years, great consideration has been given to the high indium content InGaAs which is a leading candidate for n-channel devices in future generations of complementary metal-oxide-semiconductor (CMOS) technology due to its high electron mobility and high saturation velocity. Significant progress has been made in improving the electrical quality of the high-k dielectric InGaAs interface by the atomic layer deposition (ALD) of high-k materials on passivated surfaces [1,2]. An additional technological issue which needs to be addressed for metal oxide semiconductor field effect transistors (MOSFETs) fabrication is the relatively high source/drain (S/D) contact resistance which results from poor dopant activation in III-V semiconductors. Schottky barrier formation at metal/III-V semiconductor interfaces has been of considerable on going interest because of the apparently weak dependence of barrier height on metal work function. One proposed solution to this issue is to fabricate metal S/D Schottky-barrier MOSFET devices which requires control over the barrier height at the metal-InGaAs interface. It has recently been reported [3] that the insertion of an ultrathin layer dielectric layer at the interface between the metal and the semiconductor can help in releasing the Fermi level to obtain a rectifying contact.

In this study we investigate the effectiveness of the insertion of an ultrathin ALD deposited Al_2O_3 dielectric layer on the Schottky barrier height formed at the interface between the metal and the InGaAs. Schottky contacts were fabricated on 1 nm and 2 nm Al_2O_3 layers deposited on native oxide and sulphur passivated $In_{0.53}Ga_{0.47}As$ for both n and p-doped substrates. To investigate the dependence of Schottky barrier height (SBH) on metal work function (WF), both low (Al ~ 4.30 eV) and high (Pt ~ 5.65 eV) WF metals were deposited on these surface. In the later section of the chapter C-V measurements were carried out at a range of frequencies to see the effect of sulphur passivation in reducing the interfacial defect states. The electrical measurements (C-V) can be correlated with the X-ray photoemission spectroscopy (XPS) measurements carried out on the native oxide and sulphur passivated InGaAs surfaces in chapter 4.

6.2 Experiments details

Samples used in this study are 1 μm thick p-type Be doped $In_{0.53}Ga_{0.47}As$ epilayers ($5x10^{17}cm^{-3}$) and 0.5 μm thick n-type Si doped $In_{0.53}Ga_{0.47}As$ epilayers (5×10^{17} cm^{-3}) lattice matched to InP substrates. All samples (twelve p-type and twelve n-type) were degreased for 1 min in acetone followed by 1 min in methanol. For sulphur passivation, $In_{0.53}Ga_{0.47}As$ samples (six p-type and six n-type) were then dipped into 10% ammonium sulphide ($(NH_4)_2S$) solution for 20 min at room temperature (290 K) followed by de-ionized (DI) water rinse and N_2 blow dry. All sulphur passivated and un-passivated samples were then loaded into an atomic layer deposition (ALD) chamber load lock within a minute after the cleaning process to minimize the air exposure to the samples. Approximately 1nm (10 cycles) and 2 nm (20 cycles) of alumina (Al_2O_3) were deposited at 250 ^oC on all these samples. Tri-methyl aluminum (TMA) and water were the precursors used for ALD alumina deposition. The Pt Schottky devices are realized by sputtering through a shadow mask (contact area 350 μm^2), however, Al Schottky devices are realized by evaporation. Aluminum metallization was performed to provide ohmic back-contacts.

6.3 Schottky J-V characteristics

The current-voltage J-V characteristics obtained for the Schottky devices fabricated on passivated p-type and n-type substrates are shown in Figure 6.1, 6.2, 6.3 and 6.4. The thermionic emission current is given as

$$J = A^{*}T^{2}\exp\left(\frac{-q\phi_{B}}{K_{B}T}\right)*\exp\left(\frac{qV}{nK_{B}T}-1\right) \qquad (2.22)$$

Where A^{*} is the Richardson constant, T is the temperature, q is the electron charge, $Ø_B$ is the effective Schottky barrier height (SBH), k is Boltzmann's constant, n is the ideality factor, and V is the applied forward voltage.

From above equation $Ø_{B,}$ (SBH) was calculated for each Schottky junctions formed on n and p-InGaAs.

6.3.1 P-type

Figure 6.1 (a) and (b) displays the J-V characteristics of metal/p-InGaAs junctions with and without the ultrathin layer (1nm and 2nm) of Al_2O_3 for Al contacts on InGaAs. Rectifying behaviour was observed for the p-type substrates (both native and sulphur passivated) for the Al-InGaAs and Al/Al_2O_3/InGaAs junctions indicating that the Fermi level can be moved across the InGaAs bandgap. For metal/p-InGaAs junction the SBH was measured to be ~0.60 eV on sulphur passivated and unpassivated sample. This indicated that when the low WF Al is deposited, on the p-type Fermi level is moved close to the conduction band edge as the barrier height is almost equal to the InGaAs bandgap. For the corresponding Al/1nm Al_2O_3/InGaAs and Al/2 nm Al_2O_3/InGaAs junctions, the SBH was measured 0.55 eV. The effect of insertion of the interlayer shows a small drop of 0.05 eV in SBH on p-type InGaAs irrespective of the thickness of the Al_2O_3 layer which is in agreement with the recent study by Wang et al [3] who reported a similar 0.05 eV decrease in the SBH after insertion of 2 nm thick Al_2O_3 between p-InGaAs and the metal.

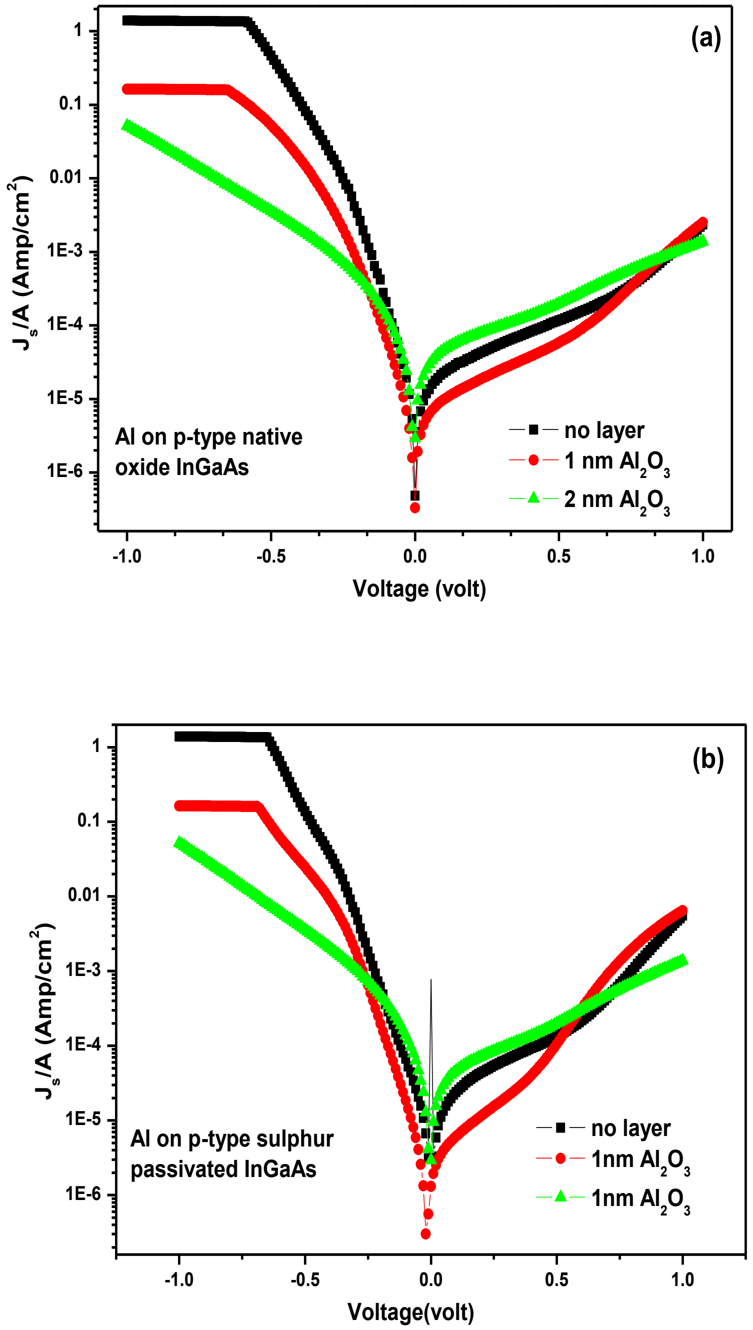

Figure 6.1 Typical J-V characteristics of p-type Al/InGaAs and Al/Al_2O_3/InGaAs junctions (a) native oxide (b) sulphur passivated surface

Figure 6.2 (a) and (b) displays the J-V characteristics of metal/p-InGaAs junctions with and without ultrathin layer (1 nm and 2 nm) of Al_2O_3 for Pt contacts. Ohmic or near ohmic behaviour was observed on the Pt-InGaAs and Pt-Al_2O_3-InGaAs junctions regardless of the dielectric thickness. The high WF metal on the p-type InGaAs substrates would be expected to give rise to a low barrier height which manifests itself as effectively an ohmic contact in these measurements. The reduction in the current with increasing thickness of the Al_2O_3 layer reflects the increase in resistance of the junction.

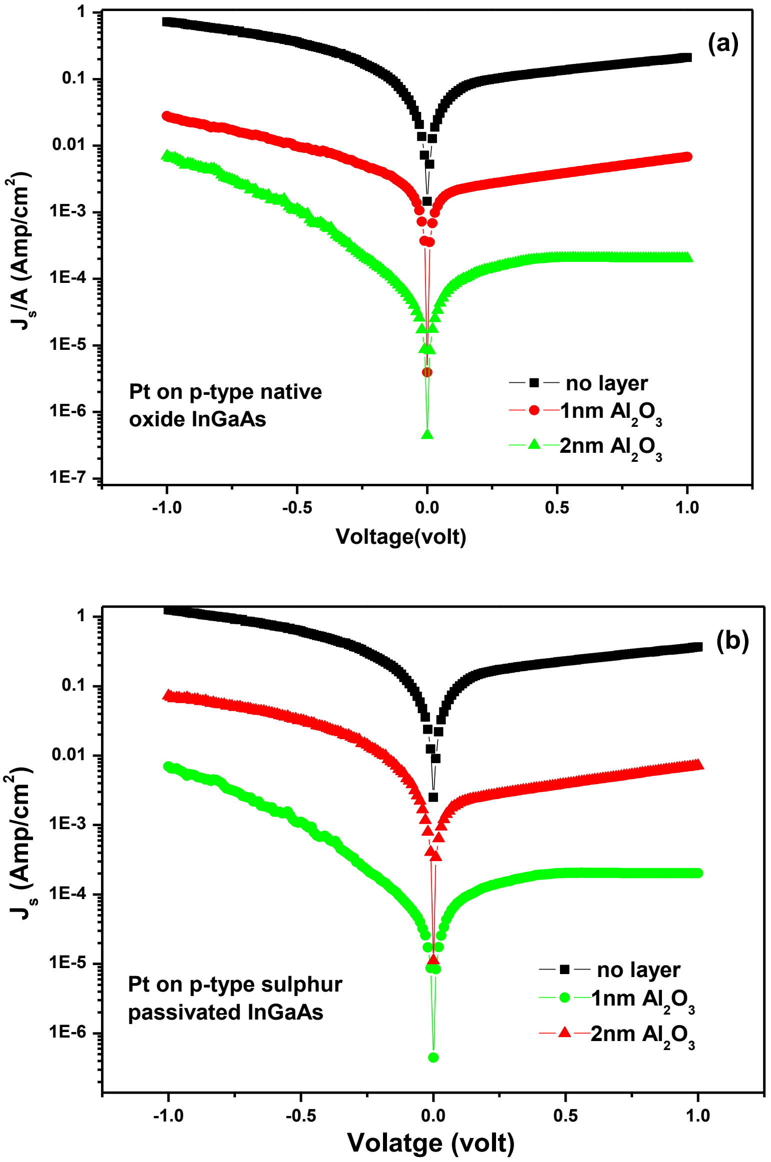

Figure 6.2 Typical J-V characteristics of p-type Pt/InGaAs and Pt Al_2O_3/InGaAs junctions (a) native oxide (b) sulphur passivated surface junctions.

6.3.2 N-type

Figure 6.3 and 6.4 displays the J-V characteristics of metal/n-InGaAs junctions with and without ultrathin layer (1nm and 2nm) of Al_2O_3 for Al and Pt metals, respectively. Ohmic behaviour was observed for all metal/n-InGaAs contacts without the Al_2O_3 interlayer. For the Al_2O_3 interlayers on the native oxide surfaces, again ohmic behaviour was observed regardless of metal WF with the reduction in current for the thicker Al_2O_3 layer attributed to an increase in junction resistance.

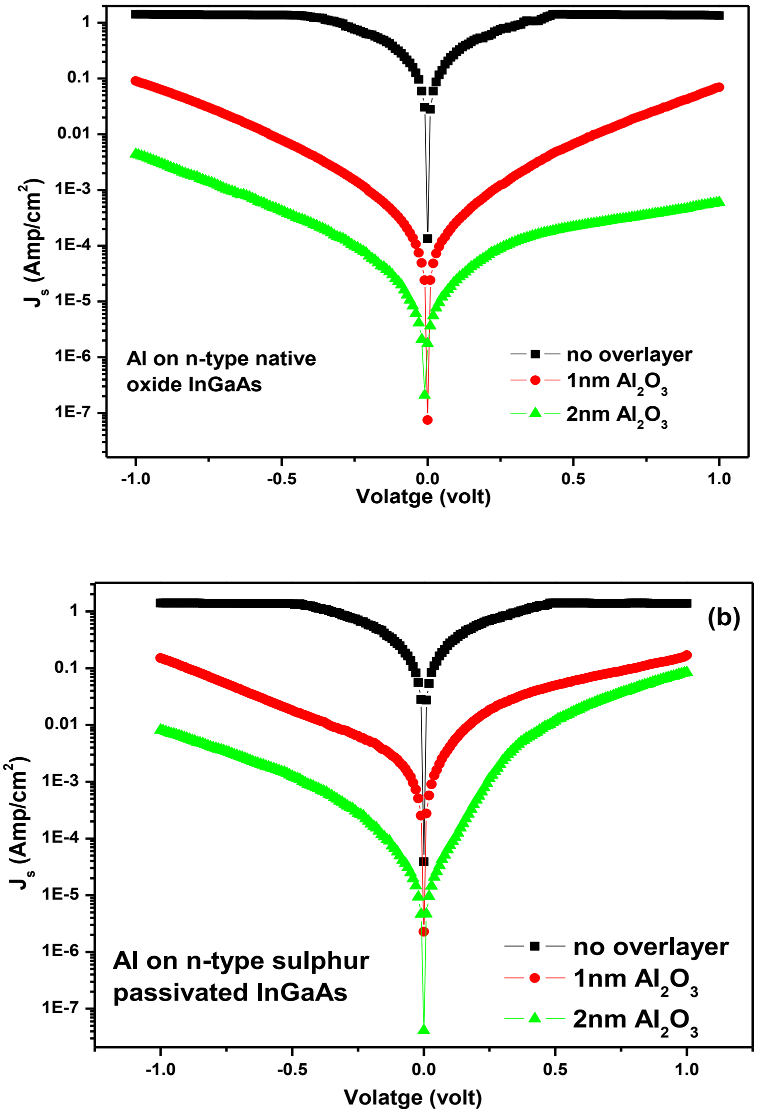

Figure 6.3 Typical J-V characteristics of n-type Al/InGaAs and Al /Al_2O_3/InGaAs junctions (a) native oxide and (b) sulphur passivated surface

Rectifying behaviour was observed for Al and Pt contacts on the 2 nm Al_2O_3/InGaAs junctions on sulphur passivated InGaAs surface and SBH heights of approximately 0.32 eV and 0.42 eV respectively. It is difficult to extract barrier height measurements for the 1 nm Al_2O_3 interlayer as the linear section of the J-V curve is difficult to identify.

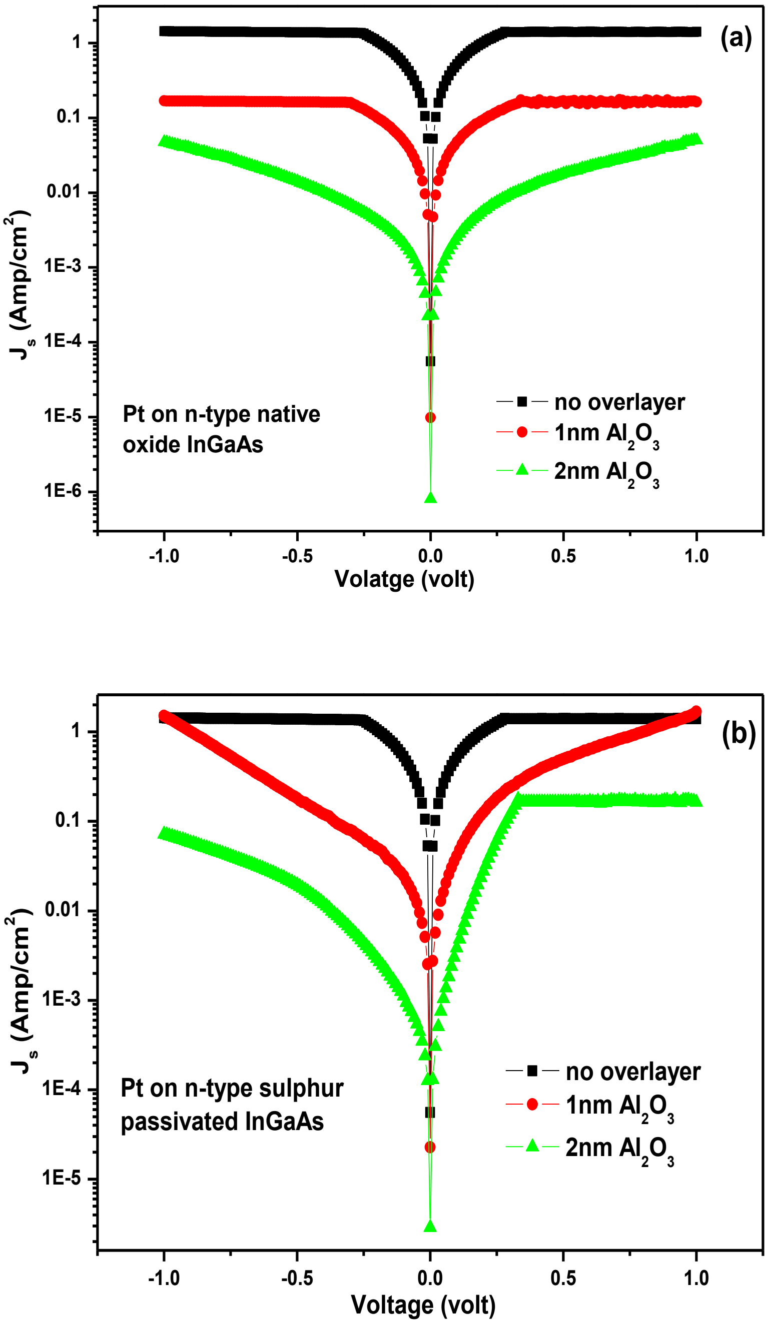

Figure 6.4 Typical J-V characteristics of n-type Pt/InGaAs and Al/ Al_2O_3/InGaAs junctions for the (a) native oxide and (b) sulphur passivated surface.

6.3.3 Discussion

The change in the effective SBH with and without the Al_2O_3 interlayer on Al/p-InGaAs junction is very small, however definite rectification is observed which is consistent with an unpinned Fermi level in the InGaAs layer. This observation didn’t depend on the presence of either a sulphur passivation treatment or a Al_2O_3 interlayer. For the same surface treatments effectively a zero barrier height is observed on the Pt-InGaAs junctions irrespective of presence of the Al_2O_3 interlayer. Al has a low work function (4.3 eV) value and in the case of p-InGaAs, the ideal Fermi level position is close to valence band. Therefore in the case of Al contacts on p-type InGaAs the equilibrium Fermi level position would result in band bending equivalent to the bandgap and hence give rise to a SBH approximately equal to what is measured in this study. In the case of Pt which has a high work function (5.65 eV), when it is in equilibrium with p-type InGaAs, Fermi level alignment would result in a low barrier height as observed in the measurements. However change in the SBH due to Al_2O_3 interlayer is observed to be just 0.05 eV for p-InGaAs indicating that it does not have a major impact on the interface properties. The most interesting result on the n-type InGaAs samples is that rectifying behaviour was only observed on the sulphur passivated samples with a 2 nm Al_2O_3 indicating that both surface treatments were necessary to unpin the Fermi level.

6.4 MOS capacitors

6.4.1 Al/Al_2O_3/n-$In_{0.53}Ga_{0.47}As$/Al capacitor fabrication with and without sulphur passivation

Metal-oxide-semiconductor (MOS) capacitors were fabricated with and without sulphur passivation on n-type InGaAs samples with Al_2O_3 as gate dielectric and aluminum as gate metal. For MOS capacitor fabrication, the 2 µm thick n-type (S: $4x10^{17}$ cm^{-3}) $In_{0.53}Ga_{0.47}As$ layers used throughout this work were grown by metal-organic vapor phase epitaxy (MOVPE) on highly doped n-type (S: 3-$8x10^{18}cm^{-3}$) InP substrates with 0.1 µm thick n-type (S: $4x10^{18}$ cm^{-3}) InP buffered layer in between. All samples were degreased for 1 min in acetone followed by 1 min in methanol prior to the sulphur passivation. $In_{0.53}Ga_{0.47}As$ samples were then dipped into 10% ammonium sulphide ($(NH_4)_2S$) solution for 20 min at room temperature (290 K). All sulphur passivated and un-passivated samples were then loaded into an atomic layer deposition (ALD) chamber load lock within a minute after the cleaning process to minimize the air exposure to the samples. Alumina of thickness 19 nm was deposited on passivated and un-passivated samples in the same ALD run. Thermally evaporated aluminum was used as gate metal and patterned into 1 mm diameter contacts. Figure 6.3 shows the schematic diagram of the InGaAs capacitor.

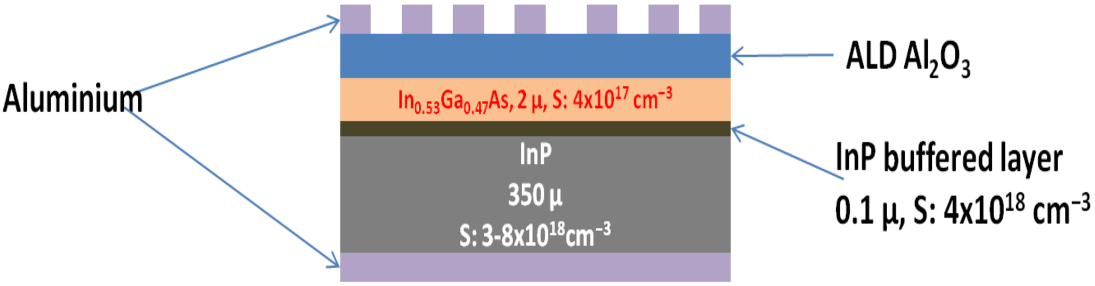

Figures 6.5 Schematic diagram of Al/Al_2O_3/n-InGaAs capacitors

The CV profiles of the capacitor structures at variable frequency are shown in Figure 6.6. The sulphur passivated sample has significantly less hysteresis (300 mV) compared with the un-passivated sample (600 mV) at 1 MHz, which indicates low trap density at the interface for the sulphur passivated sample compared with that of the un-passivated sample.

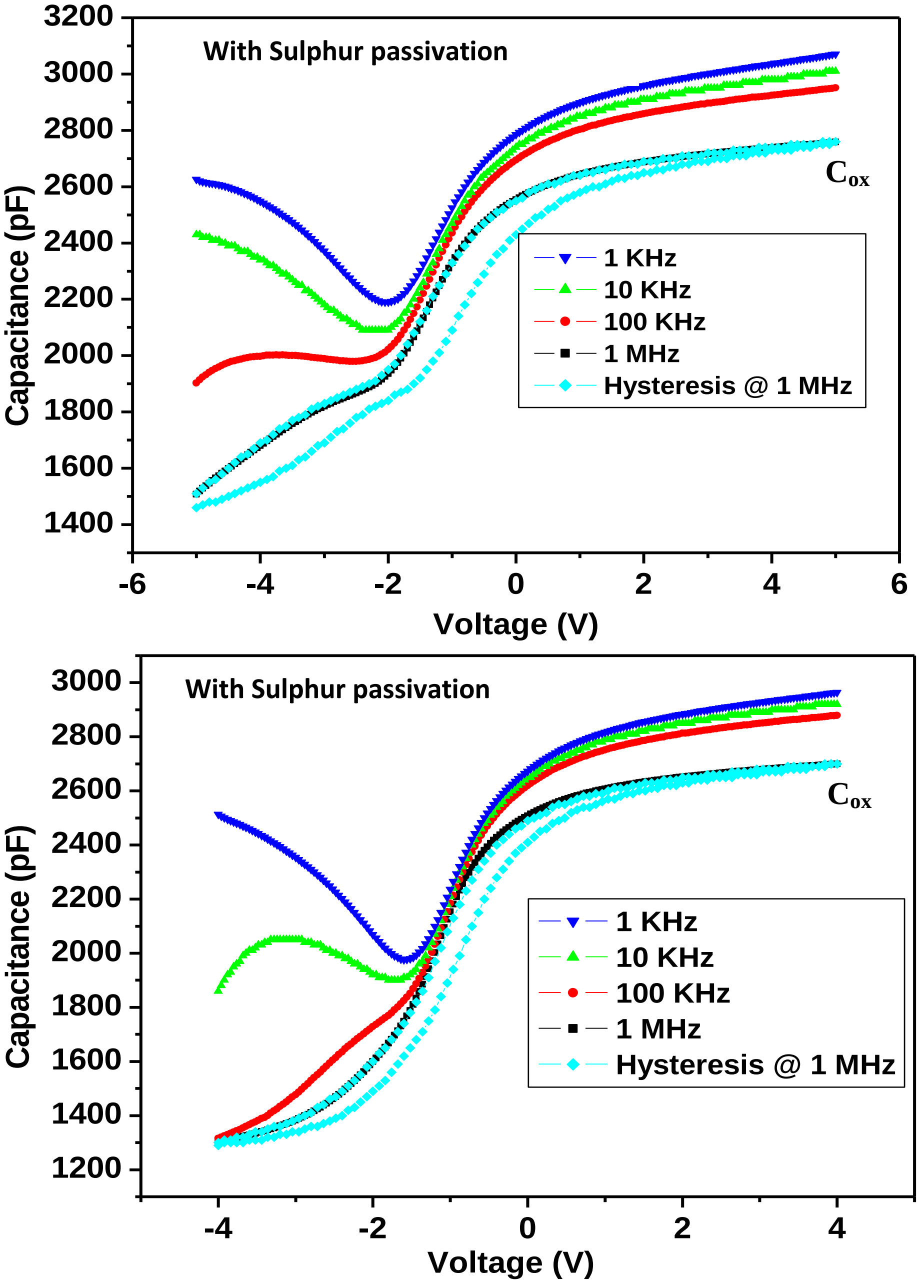

Figure 6.6 show the capacitance-voltage measurements on un-passivated and sulphur passivated Al/Al_2O_3/n-$In_{0.53}Ga_{0.47}As$ capacitors respectively measured at room temperature with a frequency range of 1 KHz-1MhZ. The Hysteresis behaviour at 1 MHz is also shown in these figures

The depletion region is not fully formed for the un-passivated sample, indicating a high trap density. Sulphur passivation is beneficial in forming the depletion region in Al_2O_3/n-$In_{0.53}Ga_{0.47}As$ capacitors. On sulphur passivated sample inversion region starts to form at lower voltage (- 4 V) while on native oxide sample no inversion region was observed even at high voltage (- 5 V). Frequency dispersion was less for the sulphur passivated sample. C_{ox} (C_{max} in accumulation region) is very slightly reduced, possibly due to a thin deposited layer resulting from the passivation treatment.

The interface defect states density (D_{it}) was calculated by the following Terman method [8]

$$\mathrm{D_{it}}(\mathrm{V_g}) = \frac{1}{\mathrm{q}}\,\mathrm{C_{ox}}\left[\left(\frac{d\varphi_s}{dV_g}\right)^{-1} - 1\right] - C_{dep} \qquad 6.2$$

Where C_{ox} is the maximum capacitance, q is charge of the electron, φ_s is the suface potential which is twice of the flatband voltage (V_{FB}), V_g is the gate threshold voltage measured from the CV curve, and C_{dep} is a series capacitance of C_{FB} and and $C_{ox}$where C_{FB} is the capacitance at flat-band voltage.

From equation 6.2 on the native oxide sample, the D_{it} was calculated to be Nss ~ 5.4 x 10^{12} /cm^2 while on sulphur passivated sample it was reduced by approximately 50% to (Nss ~ 2.0 x 10^{12} /cm^2). These values reflect the effect of sulphur passivation in reducing the defect states from the interface.

6.5 Conclusions

The effectiveness of the insertion of ultrathin ALD deposited Al_2O_3 dielectric layers on the Schottky barrier formed at the interface between different work function metals and the InGaAs surface was investigated. The results show that it is easier to form Schottky barriers on p-type InGaAs junctions. The C-V measurements were also carried out on native oxide and sulphur passivated InGaAs surfaces which showed a reduction in the interfacial defect density due to sulphur passivation effects.

6.6 References

[1] Y. Xuan, Y. Q. Wu, and P. D. Ye, IEEE Electron Device Lett. 29,294 (2008)

[2] Y. Sun, E. W. Kiewra, J. P. de Souza, J. J. Bucchignano, K. E. Fogel, D.K. Sadana and G. G. Shahidi, Tech. Dig. - Int. Electron Devices Meet., 367, (2008)

[3] R. Wang, Min Xu, Ye. D. Pedye, R. Huang, J. Vac. Sci. Technol. B 29,4 (2011)

[4] Taoka, N. Yokoyama, M.; Kim, S.H. Suzuki, R. Iida, R. Lee, S. Hoshii, T. Jevasuwan, W.Maeda, T.; Yasuda, T.; Ichikawa, O.; Fukuhara, N.; Hata, M.; Takenaka, M.; Takagi, S. IEDM Tech. Dig., 27, 2.1(2011)

[5] D. Connelly, C. Faulkner, D. E. Grupp, and J. Harris, IEEE Trans. Nano-technol. 3, 98 (2004)

[6] V. Heine, Phys. Rev. A138, A1689 (1965)

[7] J. Tersoff, Phys. Rev. Lett. 52, 465 (1984)

[8] Roman Engel-Herbert, Yoontae Hwang, and Susanne Stemmer, Appl. Phys. Lett. **97**, 062905 (2010)

Chapter 7

Conclusions

The atomically clean InGaAs surface was prepared in the UHV chamber by desorbing 100 nm As cap layer at 410 ^{o}C. Both in-situ and ex-situ sulphur passivation was carried out to observe the difference in chemical bonding and the effectiveness of the passivation. In-situ sulphur passivation of atomically clean surface and ex-situ sulphur passivation were carried out to study the chemical bonding in near InGaAs surface region. Fermi level position was determined on the atomically clean surface and found to be in the midgap of InGaAs band gap. Sulphur was found as a acting donor in near surface region therefore sulphur adsorption moves the Fermi level close to the conduction band. Work function value was also calculated on sulphur adsorbed surface and as a function of thermal anneals. High temperature thermal annealing of the in-situ sulphur passivated atomically clean InGaAs surface was performed which leads to the significant changes in the InGaAs chemical composition as a function of thermal anneals. In-situ sulphur passivated surface was exposed to air to observe the effectiveness of the passivation against air exposure and found to have an increase in the gallium oxide due to the gallium rich surface.

In order to reduce the detrimental impact of native oxides on potential semiconductor device performance, wet chemically ex-situ sulphur passivation using the commonly available aqueous ammonium sulphide was investigated as a method to both remove and prevent the native oxides from forming on the semiconductor surfaces. Ex-situ treated surface was found very effective to remove large amount of the native oxide present on the surface. However during loading the sample it exposed to air and took 10 minutes, traces of oxide were seen on the surface. High temperature thermal annealing studies was carried out to remove the residual oxide from the surface and to observe the compositional changes as a function of thermal anneal upto 700 ^{o}C.

A threshold decomposition temperature was established on all three surfaces which were observed 530 ^{o}C, 480 ^{o}C and 700 ^{o}C with indium loss of 5% , 33% and 80% for atomically clean in-situ and ex-situ sulphur passivated surface respectively. High temperature was established to remove the residual oxide from wet chemically treated surface which was observed thermally stable at higher temperature without impacting the stoichiometry than the atomically and in-situ sulphur passivated surface.

Second chapter has been focused on the advantages of the synchrotron measurements over XPS. Interfacial chemistry of Al_2O_3 on native oxide and sulphur passivated surface was investigated by XPS and HRSPES. Both techniques shows the different level of the oxide present on same surfaces/interfaces, larger level of oxide on HRSPES while smaller level on XPS which suggests oxide present at the interface is beyond the XPS detection limit. A series of thermal annealing upto high temperature 700 ^{o}C was carried out to observe the chemical changes at the interface on both Al_2O_3/InGaAs interface. Thermal annealing at 700 ^{o}C on the unpassivated Al_2O_3/InGaAs interface results in the decomposition of the InGaAs by the loss of In which is assumed to occur by its out diffusion through the Al_2O_3 overlayer without impacting the InGaAs stoichiometry of Al_2O_3 covered sulphur passivated interface while huge amount of indium loss was observed at 700 ^{o}C on Al_2O_3 covered native oxide interface. These results therefore set an upper limit on an annealing temperature for the Al_2O_3/InGaAs interface to substantially remove the interfacial oxides without initiating major chemical disruption across the interface.

The stepwise deposition of ultrathin MgO layer was carried out on the atomically clean InGaAs surface. An evolution of the growth of the interfacial oxides at submonolayers levels was observed as a function of deposition. Annealing results in the reduction in the arsenic interfacial oxide while conversion of InO to GaO was seen. Mg deposition leads to the disappearance of the higher oxidation states and results in the disruption of the interface with indium out diffusion.

Different growth of the Al_2O_3 was observed on differently chemically treated surface. The difference in growth rate is attributed to the different nucleation sites available to grow the layer on various treated surface. Higher growth rate was observed on the 2 stage etch and sulphur passivated surface whereas on the native oxide and H_2O_2 treated surface growth rate was similar but lower than 2 stage and sulphur treated surface. On pre-clean treated surface which helps in removing the organic contamination adsorbed on the surface from air exposure the growth rate was seen higher than the native oxide surface. These treatments provide a nice insight of the growth rate on various treated surfaces which certainly will help in improving the InGaAs surface optimisation process for MOSFET applications.

Modification of Schottky barrier height was examined by inserting of an ultrathin ALD deposited Al_2O_3 dielectric layer on the Schottky barrier formed at the interface between the metal and InGaAs. The results indicate that the SBH modulation is more effective on sulphur passivated n-InGaAs interfaces than on sulphur passivated p-InGaAs interfaces when using the same Al_2O_3 thickness. On n type interface the Fermi level was observed in the midgap and weakly pinned while on p type It was seen close to the conduction band. The change in the SBH is independent of the metal work function and attributed to the formation of the dipole formed at the interface.

In this work in-depth study of in-situ (dry) and ex-situ (wet) sulphur passivation of InGaAs and high temperature annealing have been carried out by using photoemission studies. Sulphur treatment was found to be an effective way to terminate the semiconductor surface leaving a chemical passivation layer to protect the surface against regrow the oxide following air exposure, However sulphur passivation can only slow down the growth rate of the native oxide when exposed to ambient or any dielectric deposition as thermodynamically the oxides are more stable than the sulphides. On an ideal flat III-V semiconductor surface sulphur atoms can act as a termination layer leaving no dangling bonds which are the origin of surface and interface defect states. The other advantage of sulphur passivation shown in this study is that it remains at the interface with a dielectric overlayer up to 700 ^{o}C. Further study is required to produce a good quality interface when deposition of the dielectric layer is performed on the atomically clean surface, in-situ and ex-situ sulphur passivated surfaces. Optimisation of the annealing temperature after dielectric deposition on these surfaces and correlation with the electrical measurements would also be helpful. The Al_2O_3/InGaAs interface chemistry on two different surfaces and their interface thermal stability at high temperature has been described in chapter 4 where results demonstrate an effective way to remove the interfacial oxide without compromising the substrate composition on sulphur passivated sample. However, further study is required to optimized the annealing temperature where sulphur does not contribute any charge which results in the threshold voltage shift reported by Gu et al. [1]. Also, it is needed to distinguish the thermal stability of Al_2O_3/InGaAs interface on sulphur passivated surface is either due to the presence of capping layer or the mixed phase of the sulphides and oxides at the interface at 700^o C as indium lost was observed on Al_2O_3/InGaAs interface on native oxide surface.

In chapter 5, deposition of Al_2O_3 on various chemically prepared InGaAs surfaces shows a different film growth rate and presence of different level of interfacial oxide at the interface. It would also be helpful to use the high surface sensitivity of HRSPES to study the different chemically prepared dielectric/ interface and their high temperature annealing would indeed also be helpful.

By performing forming gas annealing and vacuum annealing at high temperature on different chemically prepared interfaces/surfaces would also be very useful to optimise the interface quality.

An attempt has been made to modulate the SBH of metal/InGaAs and metal/dielectric/InGaAs junctions on native oxide and sulphur passivated surface for making source/drain contact where SBH was found independent of the metal work function and regardless of the dielectric thickness. Therefore further studies is required to modulate the SBH barrier height by using suitable cleaning and passivation method